Experimental and Numerical Studies on Mixed Mode Fracture and Fatigue Using a New Specimen

A thesis

submitted in partial fulfillment of the

requirements for the degree of

DOCTOR OF PHILOSOPHY

by

SHIV SAHAYA SHUKLA

(Roll No: 156103002)

Department of Mechanical Engineering
Indian Institute of Technology Guwahati
Guwahati – 781039, India

October 2023

Department of Mechanical Engineering
Indian Institute of Technology Guwahati
Guwahati – 781039, India

DECLARATION

I hereby declare that the research work embodied in this thesis entitled "**Experimental and Numerical Studies on Mixed Mode Fracture and Fatigue Using a New Specimen**" is the result of original experiments carried out by me at the Department of Mechanical Engineering, Indian Institute of Technology Guwahati, Guwahati, India under the supervision of **Prof. K. S. R. Krishna Murthy**. This thesis has not been submitted to any other Institute/University or elsewhere for the award of any degree or diploma. I have followed the guidelines provided by the Institute in preparing the thesis. I have conformed to the norms and guidelines given in the Ethical Code of Conduct of the Institute. Whenever I have used materials (data, theoretical analysis, figures, and text) from other sources, I have given due credit to them by citing them in the text of the thesis and giving their details in the references. Further, I have taken permission from the copyright owners of the sources, whenever necessary.

Shiv Sahaya Shukla

Date: 5th October 2023

Department of Mechanical Engineering
Indian Institute of Technology Guwahati
Guwahati – 781039, India

CERTIFICATE

It is certified that the work contained in the Thesis titled **“Experimental and Numerical Studies on Mixed Mode Fracture and Fatigue Using a New Specimen”** submitted by **Shiv Sahaya Shukla** to the Indian Institute of Technology Guwahati for the award of the degree of Doctor of Philosophy has been carried out under my supervision in the Department of Mechanical Engineering, Indian Institute of Technology Guwahati. This work has not been submitted elsewhere for the award of any other degree.

5th October, 2023

K. S. R. Krishna Murthy
Professor
Department of Mechanical Engineering
Indian Institute of Technology Guwahati
Guwahati – 781039

Dedicated to My

Father

Mr. Onkar Nath Shukla

Mother

Mrs. Nirmala Shukla

Wife

Mrs. Akanksha


भारतीय प्रौद्योगिकी संस्थान गुवाहाटी
Indian Institute of Technology Guwahati

ACKNOWLEDGEMENTS

First and foremost, I would like to acknowledge the Almighty God, whose divine guidance and grace have been a constant source of strength and inspiration throughout this journey. This thesis is the outcome of eight years of research work, and the exercise was by no means an easy task. During this long period, I have been guided and supported by many people. I would like to extend my heartfelt gratitude to all those individuals and organizations who have nurtured me from childhood and beyond, and to those who have directly or indirectly helped me in various ways during my doctoral study at the Indian Institute of Technology Guwahati. I now have the opportunity to acknowledge my indebtedness to all of them.

I would like to express my deepest respect and gratitude to my supervisor and mentor, Prof. K. S. R. Krishna Murthy, for his support, encouragement, and guidance during my stay at the Indian Institute of Technology Guwahati. I have been immensely benefited from his knowledge, insightful feedback, and constructive criticism. The unexpected and sudden pandemic events added more difficulty to this journey. Nevertheless, his constant encouragement, unwavering support, and friendly discussions in both academic and personal matters played a crucial role in helping me navigate through this challenging period. I sincerely believe that without his support, the research work would not have been possible.

I would also like to thank my doctoral committee members, Prof. P.S. Robi, Prof. Poonam Kumari, and Prof. Amit Shelke, for their time, expertise, and valuable input. Their insightful comments, suggestions, and thorough examination of my work have significantly enriched its quality and contributed to its overall improvement.

My particular appreciation is expressed to all the faculty members of the Mechanical Engineering Department, IIT Guwahati, and the former and present heads of the Department of Mechanical Engineering for providing me with a conducive environment, necessary infrastructure, and laboratory facilities in the Department for the smooth completion of my research work. I sincerely acknowledge the financial support provided by the Ministry of Human Resource Development, Govt. of India, during the entire period of my doctoral program. I am grateful to Mr. N. K. Das (Workshop Superintendent), Mr. Jiten Basumatary (Technical Superintendent, Advanced

Manufacturing Lab), and the entire technical staff of Central Workshop, IIT Guwahati, for their help in preparing experimental specimens. Special thanks to Mr. Sanjib Sarma (Sr. Technical Superintendent) for providing the necessary computational and experimental infrastructure at the Strength of Materials Lab required for this work. I am thankful to the Central Instruments Facility at IIT Guwahati for providing UTM and FESEM facilities for this work. I would like to express my special thanks to Dr. Ashim Malakar (Jr. Technical Superintendent) for allowing me to conduct my experiments during non-office hours in CIF. I express my sincere thanks to my seniors and lab mates in SOM lab and the Fracture Mechanics and Composite Structure lab: Dr. Sajith, Dr. Mirzaul, Dr. Debolena, Dr. Debabrata, and Mr. Pranjol for sharing their valuable and critical inputs during the early phases of my dissertation. I would also like to thank the staff at Tool Room and Training Centre, Amingaon, Guwahati (TRTC Guwahati), especially Mr. Raja Sarkar and Mr. Shiromoni Kumar, for their sincere efforts in fabricating the specimens and fixtures.

I would like to thank my friends Raktim, Karthik, Saptarshi, Avinish, Ajit, Rajdip, Ankan, Atchuta, Sandipan, Bharat, Kbrom, Sarita, Jyotindra, and all other colleagues for their support and friendship that made my stay memorable and joyful. I also wish to thank Dr. Arun Kadian, Dr. Gaurav Goel, Dr. Anshul Garg, Dr. Sibanada Mohanty, Dr. Mohit Mishra, Dr. Ashutosh, Dr. Gaurav Kumar and many more who helped me in different ways and encouraged me during my stay at IIT Guwahati. I would like to thank my elder brother, Mr. Ashutosh Shukla; my elder sister, Mrs. Shiva Mishra; my younger brother Shambhu Shukla, my Bhabhi, Mrs. Kiran Dixit; and my Jijaji, Mr. Manoj Mishra, for their love and affection and for being pivotal in helping me keep a calm state of mind at all times.

Last but most importantly, I express my sincere gratitude to my mother, Mrs. Nirmala Shukla, my father, Mr. Onkar Nath Shukla, and my wife, Mrs. Akanksha, for everything they have done for me, particularly, for their patience, understanding, love, and belief in me. None of this would have been possible without them, and this thesis is dedicated to them.

Date: 5th October 2023 **Shiv Sahaya Shukla**
IIT Guwahati

TABLE OF CONTENTS

Chapter 3 Theoretical background 41

भारतीय प्रौद्योगिकी संस्थान गुवाहाटी
Indian Institute of Technology Guwahati

ABSTRACT

Mixed mode fracture and fatigue failures are one of the most significant causes of failure in materials and structural components. In the present investigation, a simple and efficient specimen geometry and out-of-plane loading fixture that can be used with conventional uniaxial universal testing machines for conducting any combination of mixed mode (I/II/III) fracture and fatigue crack growth studies have been proposed. The proposed specimen is a single edge cracked circular (SECC) specimen which can be employed on both metallic and non-metallic materials under static and fatigue loads.

To examine the efficacy of the proposed SECC specimen and out-of-plane loading fixture, a large number of fracture experiments under quasi-static loading have been conducted on specimens made of PMMA material under two different mixed mode loading configurations, viz., mixed mode (I/II) and (I/III). Furthermore, the efficacy of the SECC specimen to perform mixed fatigue (I/II) fatigue crack growth studies using metallic materials has also been examined by conducting a series of fatigue experiments on two different materials, viz., Al 7075-T6 aluminium alloy and AISI 304 steel. Along with the aforementioned experimental studies, a large number of three-dimensional finite element analyses of the full loading assembly have been performed in ANSYS® to aid the present experimental results.

The present results of the mixed mode fracture experimental studies have been compared with widely used mixed mode fracture criteria, specifically in terms of fracture toughness, critical fracture load, crack kink angle, and crack twist angle, to support the effectiveness of the proposed specimen for fracture and fatigue studies. More than one specimen has been employed in all the present experiments to understand the repeatability and correctness of the adopted experimental procedures.

Another aspect of the present research work focuses on the prediction of crack length versus the number of loading cycles curve (or fatigue life curve) under mixed mode (I/II) loading conditions using modified Paris's law with different ΔK_{eq} models. Currently, these ΔK_{eq} models are essentially used for two purposes: firstly, correlating the mixed mode (I/II) fatigue crack growth rate (FCGR), and secondly, predicting the mixed mode fatigue

life using numerical methods. Clearly, different ΔK_{eq} models can result in varied FCGR characteristics and different fatigue life predictions under mixed mode cyclic loading. Therefore, the performance evaluation and potential applications of various ΔK_{eq} models have been investigated using the proposed SECC specimen setup. Further, in the present work, for the first time, a novel ΔK_{eq} model based on the GMTS criterion has been proposed for correlating the mixed mode FCGR and predicting fatigue life. For this purpose, mixed mode (I/II) fatigue crack growth experiments have been carried out using the SECC specimen made of AISI 304 steel and Al 7075-T6 alloy under different loading angles.

Another important issue related to the numerical estimation of mixed mode (I/II) fatigue life while using various ΔK_{eq} models in the modified Paris law has also been addressed in detail in the present work. The current practice of estimating the fatigue life is to consider a ΔK_{eq} model and employ the mode I Paris' constants in the modified Paris law. Different sets of Paris' constants can be obtained directly from the mixed mode fatigue crack growth experiments, apart from the values obtained from mode I tests. Therefore, the influence of all these different types of Paris' constants in the prediction of fatigue life while using various ΔK_{eq} models has been studied in depth and presented with important observations.

The results of the present work clearly show that (a) the GMTS criterion has shown superior performance while predicting the crack kink angles and fracture locus, similar to some other criteria in mixed mode fracture tests; (b) for a given loading angle and a set of the Paris' constants, the performance of all the ΔK_{eq} models is nearly the same; (c) the results of life prediction using mixed mode Paris constants are in excellent agreement with the experimental mixed mode fatigue life for all the ΔK_{eq} models; (d) the results clearly show that the influence of the Paris' constants has significant effect on the prediction of the mixed mode life than the selection of a ΔK_{eq} model; (e) excellent repeatability of the static and fatigue experimental results have been noticed when more than one SECC specimen is employed, and finally (f) the results of the present investigation clearly demonstrate that the proposed specimen setup can be used to study the mixed mode (I/II), (I/III), and (I/II/III) behavior of linear elastic materials under static and fatigue loading.

LIST OF FIGURES

LIST OF TABLES

NOMENCLATURE

Latin characters

a	Crack length
a_0	Initial crack length
A_0, A_1	Coefficients of the Generalized Westergaard for opening mode
C	Mode I Paris constant
C_{eq}	Mixed mode Paris constant
$C*$	Modified Paris constant
C_0, C_1	Coefficients of the Generalized Westergaard for in mode II
E	Young’s modulus
G	Energy release rate
J	J-Integral
k	Double exponential model constant
$K_{\text{I}}, K_{\text{II}}, K_{\text{III}}$	Mode I, mode II and mode III, stress intensity factor
$K_{\text{If}}, K_{\text{IIf}}, K_{\text{IIIf}}$	Mode I, mode II and mode III, stress intensity factor at critical load
$K_{\text{Ic}}, K_{\text{IIc}}, K_{\text{IIIc}}$	Mode I, mode II and mode III fracture toughness
K_v	Comparative stress intensity factor
$K_{\text{II,max}}$	Mode II stress intensity factor corresponding to the maximum load
$K_{\text{II,min}}$	Mode II stress intensity factor corresponding to the minimum load
$K_{\text{I,th}}, K_{\text{II,th}}$	Mode I and Mode II threshold stress intensity factor
M	Triaxial stress factor
m, m_{I}	Mode I Paris exponent
m_{eq}	Mixed mode Paris exponent
$m*$	Modified Paris exponent

N	Number of loading cycles
p	Double exponential model exponents
P	Applied load
$P_1, P_2,$ and P_3	Punctual loads
$P_{\max}, P_{\min}$	Maximum and minimum applied load, respectively
r^2	Goodness of fit
R	Load ratio
u, v	Displacement in x and y directions, respectively
$\overline{W}$	Averaged strain energy density
W_{c}	Critical strain energy density
$x-y$	Cartesian coordinate system
x_i, y_i	Crack tip coordinates in i^{th} step
z	Complex number
Z, H	Complex stress functions

Greek letters

α	In-plane loading angle
β	The ratio of mode I and mode I fracture toughness
$\gamma_{xy}, \gamma_{yz}, \gamma_{zx}$	Shear strain in $x, y,$ and z plane, respectively
Δa	Crack increment
ΔK_{eq}	Equivalent stress intensity factor range
$\Delta K_{\mathrm{eq\text{-}max}}$	Maximum equivalent stress intensity factor range
$\Delta K_{\mathrm{I}}, \Delta K_{\mathrm{II}}, \Delta K_{\mathrm{III}}$	Mode I, mode II and mode III, stress intensity factor range
Δv	Crack opening displacement
Δu	Crack sliding displacement
$\varepsilon_{xx}, \varepsilon_{yy}, \varepsilon_{zz}$	Normal strain in $x, y,$ and z direction, respectively
θ	Polar coordinate component
θ_0	Crack kink angle
κ	Kolosov's constant

μ	Shear modulus
ν	Poisson’s ratio
ξ, η	Natural coordinates of finite element
$\sigma_{xx}, \sigma_{yy}, \sigma_{zz}$	Normal stress along $x, y,$ and z direction, respectively
$\sigma_{rr}, \sigma_{\theta\theta}$	Normal stresses in polar coordinate system
σ_e	Equivalent stress
σ_u	Ultimate stress
σ_y	Yield stress
$\sigma_{\theta,c}$	Critical tangential (circumferential) stress
$\sigma_{\theta,\max}$	Maximum tangential (circumferential) stress
$\tau_{xy}, \tau_{yz}, \tau_{zx}$	Shear stress in $x, y,$ and z plane, respectively
ϕ	Out-of-plane loading angle
Φ	Airy stress function
ψ_0	Crack twist angle

Abbreviations

ASED	Averaged strain energy density
ASTM	American society for testing and materials
COD	Crack opening displacement
CT	Compact tension
CTS	Compact tension shear
ECT	Edge cracked triangular
EDM	Electrical discharge machining
FCG	Fatigue crack growth
FCGR	Fatigue crack growth rate
FE	Finite element
FESEM	Field emission scanning electron microscopy
GMTS	Generalized maximum tangential stress
MMPS	Maximum mean principal stress
MPS	Maximum principal stress

MTS	Maximum tangential stress
PMMA	Polymethylmethacrylate
Q8	Eight noded quadrilateral
QPE	Quarter point element
RMS	Root mean square
SCB	Semi-circular bend
SECC	Single edge cracked circular
SED	Strain energy density
SIF	Stress intensity factor
UTM	Universal testing machine

Chapter 1

Introduction

This chapter explores the importance of the present work, on mixed mode fracture and fatigue crack growth studies in the context of current technological advancement. A quick note on the definition of fundamental modes of failure, fatigue crack growth, and damage tolerance design approach to fatigue are given. Furthermore, the current status of the mixed mode fatigue crack growth studies in terms of numerical and experimental methods and fatigue life prediction models has been briefly discussed. Based on these discussions, the motivation behind undertaking the present research has been presented. Organization of the thesis has been presented at the end of this chapter.

1.1 Mixed mode fracture

In the industrial world, man-made metal structures have not always operated as intended; unanticipated catastrophic failures like fractures have been observed repetitively. Fracture is one of the important structural failure modes and poses challenges to the use of high strength metals. Fractures are usually caused by a flaw or a crack. A crack can be envisaged as a fine slit, with the radius of curvature approaching zero at the crack tip. Due to repeated service loads, a crack may start developing from a structural flaw or stress concentration zone. Static fractures occur when the applied load reaches its critical value for a given crack length or when the crack length is critical enough for the given applied load.

Fractures are often classified into brittle and ductile types. A brittle fracture is one that is associated with either very little or no plastic deformation ahead of the crack tip. On the other hand, large plastic deformation precedes the fracture in the case of a ductile fracture. The former fracture is considered to be the most dangerous mode of failure, as it does not give any prior warning and occurs suddenly at stresses considerably lower than the design stresses. Fracture mechanics as an engineering discipline is the study of deformable solid bodies containing cracks or crack-like singularities.

In the context of fracture mechanics, the identification of the mode of failure is critical as it helps in developing the proper methodology to predict and prevent catastrophic failures in real-world structures. Depending on the direction and orientation of a crack relative to the applied load, fracture mechanics defines three fundamental modes of failure (or loading) as follows:

Mode I: This is also called *opening mode* or *tensile mode* (Fig. 1.1a). It occurs when the crack plane is normal to the direction of the applied load, and the crack propagates in a self-similar manner.

Mode II: This is also called *sliding mode* or *in-plane shear mode* (Fig. 1.1b). It occurs when the crack plane and direction of the applied load remain parallel, and crack surfaces slide along the applied load's direction.

Mode III: This is also called *tearing mode* or *anti-plane shear mode* (Fig. 1.1c). It occurs when the loading direction is out-of-plane and parallel to the crack front, and the crack faces move in opposite directions.

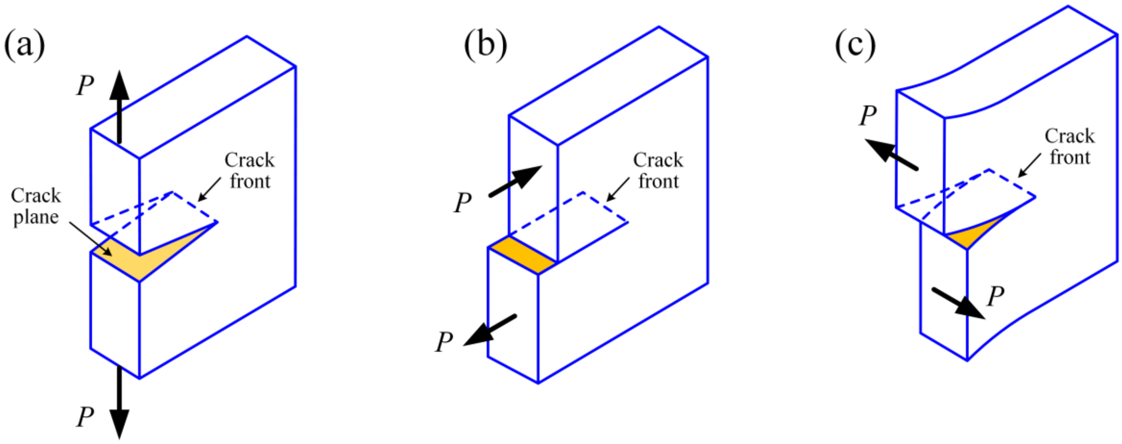

Fig. 1.1 Three fundamental modes of loading. (a) Mode I or opening mode. (b) Mode II or in-plane shear mode. (c) Mode III or tearing mode.

In addition to these three fundamental modes of failure, there are mixed mode failures, which involve a combination of two or all of these three basic modes of loading. Mixed mode failures or fractures can be further classified according to the relative contribution of each mode to the overall loading. For example, mixed mode (I/II) fracture refers to a situation where both tensile and in-plane shear stresses are present, while mixed mode (I/III) fracture involves both tensile and out-of-plane shear stresses. Similarly, mixed mode (II/III) fracture involves both sliding and tearing modes, and mixed mode (I/II/III) fracture involves all three modes of failure.

Engineering structures and components are generally designed to sustain complex multiaxial loading conditions. Under such situations, the cracks in these structures are often subjected to a combination of tensile, compressive, shear, and bending stresses. Such loadings can lead to one of the above types of mixed mode fractures. Due to the ease of mathematical formulations or, more importantly, due to the lack of standard mixed mode fracture testing procedures, fractures of cracked engineering components are attempted to idealize as pure mode I, II, or III conditions. However, it has been reported that using design parameters based on pure mode I testing in mixed mode loading conditions can yield dangerously optimistic and overly conservative results [1–4]. Therefore, it becomes essential to develop better experimental procedures for studying the mixed mode fracture behavior of materials. An important aspect here is that a crack under this loading conditions advances in a complex manner, and an original straight crack continuously tilts and twists, resulting in a tortuous fracture surface [5]. Some examples, which are believed to be mixed mode failures, are shown in Fig. 1.2.

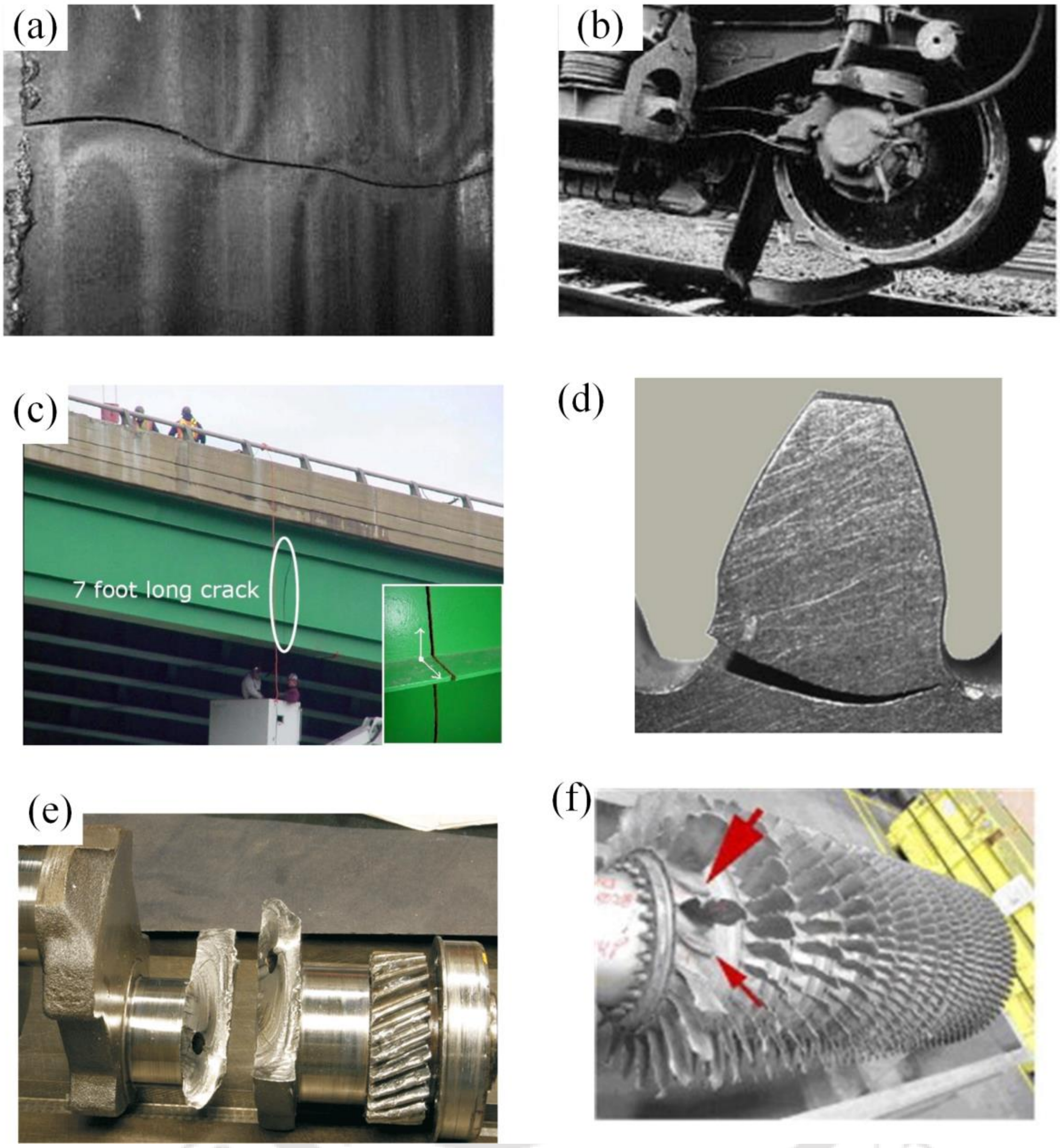

Fig. 1.2 Examples of fractures caused by mixed mode fatigue loading. (a) Curved crack path at the back side of a structure of an agricultural machine [6]. (b) Broken wheel tyre of a railway wheel [6]. (c) Fatigue cracking in a bridge girder starting from weld defects [7]. (d) Curved crack path in tooth root breakage in gear (https://tinyurl.com/fatigue-gear). (e) Failure of crankshaft under bending and torsion loading (https://tinyurl.com/fatigue-crankshaft). (f) Fatigue failure of gas turbine blades under extreme loading conditions (https://tinyurl.com/fatigue-turbine).

Different modes of failure result in distinctive fracture surfaces. For example, under the mode I loading, a crack grows in a self-similar manner, and a flat fracture surface is obtained (Fig. 1.3a)). While, under mixed mode (I/II) loading, depending upon the relative magnitude of mode I and mode II, the crack kinks and grows in a direction making an angle θ_0 with the original crack plane (Fig. 1.3b). More complex fracture surfaces (as shown in

Fig. 1.3c and Fig. 1.3d) are obtained when a material is subjected to mixed mode (I/III) and (I/II/III) loading conditions (Fig. 1.3d).

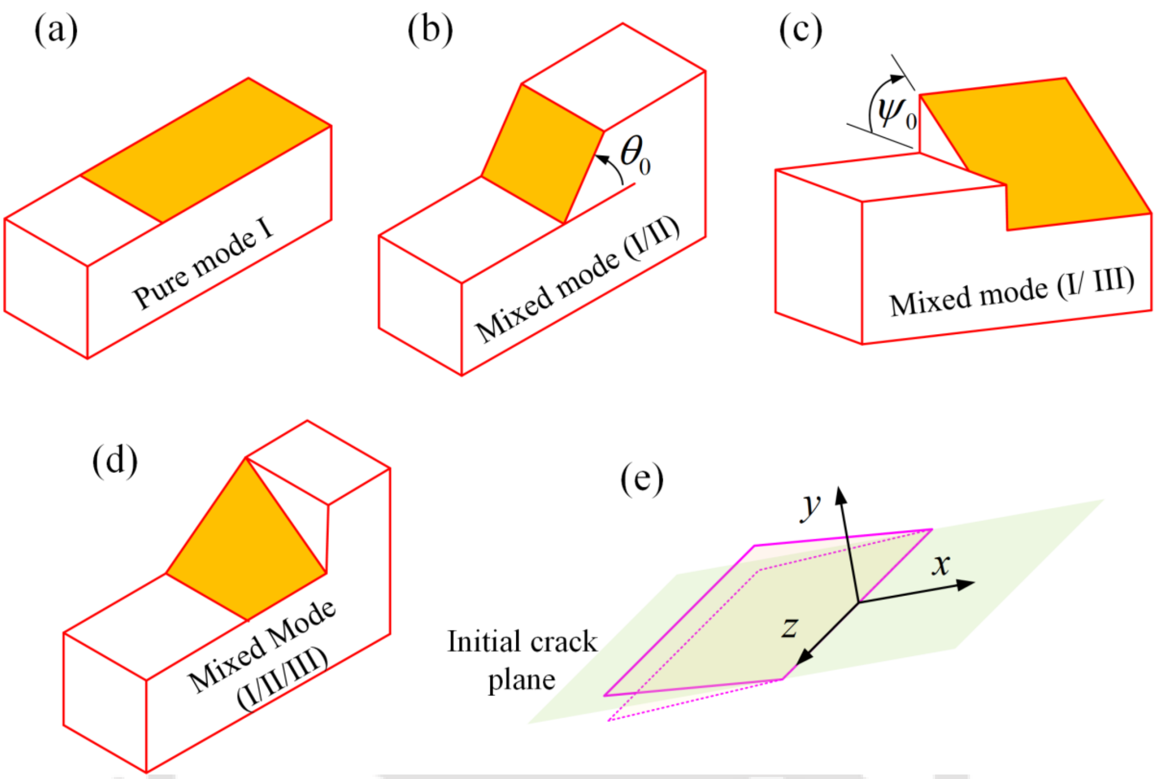

Fig. 1.3 Typical mixed mode fracture surfaces under different loading conditions. (a) Pure mode I. (b) Mixed mode (I/II). (c) Mixed mode (I/III). (d) Mixed mode (I/II/III). (e) Location of the local coordinate system at the crack front.

In the present work, the crack kink angle θ_0 is defined as the rotation of the initial crack plane about the $z-$axis, and the crack twist angle ψ_0 is defined as the rotation of the crack front about the $x-$axis (Fig. 1.3e).

1.2 Fatigue fractures

Fatigue fracture is one of the most common and significant cause of failure in materials and structural components. Fatigue failure occurs when a material or structure is subjected to repeated loading and unloading cycles, causing microscopic cracks to form and grow over time. Once a crack reaches the critical length, the strength becomes so low that the service loads cannot be carried any more by the structure, and a fracture occurs. Thus, these critical cracks can lead to catastrophic failures, even though the applied stresses may be well below the material's yield or ultimate strength. Fatigue failure can occur in a wide range of materials and structures, including metals, composites, and even biological tissues. It frequently occurs in various applications such as aircrafts, automobiles, locomotives, bridges, pressure vessels, and offshore structures, etc. Fig. 1.4 shows two recent examples of catastrophic accidents opined to be caused by fatigue in aircraft engines.

(a)

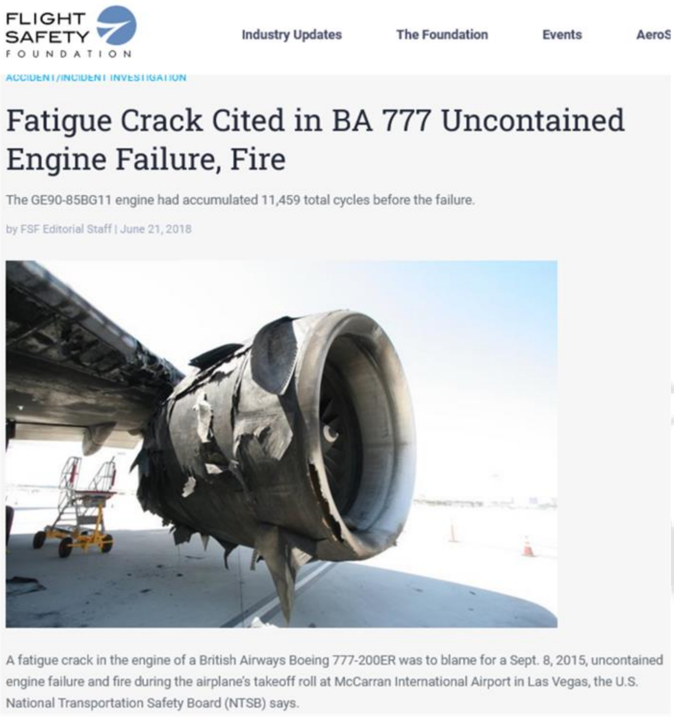

ACCIDENT/INCIDENT INVESTIGATION

Fatigue Crack Cited in BA 777 Uncontained Engine Failure, Fire

The GE90-85BG11 engine had accumulated 11,459 total cycles before the failure.

by FSF Editorial Staff | June 21, 2018

A fatigue crack in the engine of a British Airways Boeing 777-200ER was to blame for a Sept. 8, 2015, uncontained engine failure and fire during the airplane's takeoff roll at McCarran International Airport in Las Vegas, the U.S. National Transportation Safety Board (NTSB) says.

(b)

Metal Fatigue Caused Airbus A380 Engine Breakup, BEA Says

Thierry Dubois October 05, 2020

France's BEA investigation bureau describes the AF066 event as an accident because it was more

Fig. 1.4 (a) Inflight breakup of turbofans of Airbus A380 because of dwell fatigue on Sept. 30, 2017 (https://tinyurl.com/fatiguefailure-fig1). (b) A fatigue crack in the engine of a Boeing 777-200ER was the cause of uncontained engine failure and fire during the airplane's take off on Sept. 8, 2015 (https://tinyurl.com/fatigue-fig-1).

According to a survey by Fonte et al. [8], fatigue failures are responsible for approximately 80–90% of all mechanical service failures, specifically in the aircraft industry, where more than 50% of structural failures are caused by fatigue [9]. Thus, as far as mechanical engineering components are concerned, generally more attention is focused on fatigue failures than static fractures.

Fatigue failure is a complex process, and a detailed investigation of fatigue involves understanding the mechanisms by which cracks form and grow under repeated loading and developing methods to predict and prevent fatigue failure. Engineers and researchers use different techniques to mitigate fatigue failures, such as designing materials and structures with improved fatigue resistance, developing non-destructive testing methods to detect and monitor fatigue damage, and applying appropriate inspection and maintenance procedures. Overall, fatigue studies play a crucial role in ensuring the safety, reliability, and efficiency of a wide range of engineering applications.

1.3 Stages of fatigue crack growth

As the number of loading cycles increases, cracks grow and may eventually lead to sudden and catastrophic failure of the material or structure. There are several stages in the development of a fatigue crack before it leads to the separation of a material into two or more number of pieces, i.e., a fracture. The complete fatigue crack growth (FCG) process can be divided into three major stages, viz., crack initiation (stage I), stable crack propagation (stage II), and final unstable fracture (stage III). The crack growth mechanism under each stage is explained below.

Stage I: Initially, microscopic cracks can form at the material's surface or internal defects due to cyclic loading. These cracks grow and coalesce, forming larger cracks that can be detectable. In this stage, the crack growth is very slow.

Stage II: As the detectable crack grows, it changes the local stress distribution in the material, leading to further crack growth at higher rates and a decrease in the load-carrying capacity of the structure. This constitutes a stable crack growth period until the crack reaches its critical size.

Stage III: After reaching a critical size, the crack may become unstable and propagate rapidly, leading to sudden and catastrophic failure of the material or structure without giving a prior warning. This stage continues only for a very short period of time.

Among the above three stages of fatigue crack propagation, the stable crack propagation period contributes significantly to the overall lifetime of an engineering component. The period of crack initiation is usually neglected, as man-made structures are assumed to contain cracks of a certain length. The number of loading cycles to crack initiation is characterized by the threshold values and depends on various factors like the material's microstructure, mechanical properties, loading direction, and crack orientation. Therefore, the main emphasis of the FCG studies is given to the stable crack growth region, i.e., stage II.

1.4 Design against fatigue failure

For the design against fatigue, the *total life approach* ($S-N$ and $\varepsilon-N$ approaches) and the *fracture mechanics approach* are commonly used. Generally, the *total life approach* is employed in designs where the crack initiation life is emphasized more. On the other hand, the *fracture mechanics* approach focuses explicitly on growing cracks, and more emphasis is given to the crack propagation life. In the former approach, flawless specimens are used for experimental studies, whereas specimens with pre-existing flaws are used in the fracture mechanics approach. The experimental data obtained from the flawless specimens do not distinguish between crack initiation life and crack propagation life, and provide limited information to assess the fatigue life quantitatively. On the other hand, the fracture mechanics approach provides a better understanding of fatigue crack initiation and propagation and allows a structure to be designed around pre-existing flaws. Further, it also incorporates non-destructive evaluation techniques.

1.4.1 Fracture mechanics approach to fatigue design

This approach uses fracture mechanics concepts like stress intensity factor (SIF), J-integral and crack tip opening displacement (CTOD) to predict the crack growth rate and residual fatigue life under cyclic loading. The fracture mechanics approach follows the philosophy of damage-tolerant design, which safely allows the presence of dormant cracks in the material until their sizes reach above some prescribed values. When the material deforms elastically up to the point of crack initiation and propagation, and satisfies small-scale yielding assumptions, the concepts of LEFM can be applied, and the SIF (K)

becomes the most important fracture parameter which is used to characterize the crack growth. The LEFM approach is mainly applied to the case of brittle or quasi-brittle fracture of materials. When a material exhibits both elastic and plastic deformation behavior (for example, in highly ductile materials), the concepts of EPFM are applicable, and a path-independent integral termed as $J-$integral is used to characterize the fracture.

It is desirable that a component in-service should continue to operate for at least a million load cycles. In other words, the component design should have a high cycle fatigue life. Under such conditions, the material must undergo an elastic deformation during subcritical crack growth. Consequently, the fracture mechanism is considered brittle in the engineering sense. The present research is mainly focused on high-cycle fatigue failures and adopts the fracture mechanics approach, specifically LEFM, for all numerical and experimental analyses.

1.4.2 Damage tolerance and inspection interval

Damage tolerance refers to the ability of a structure/component to withstand the presence of flaws or damage without catastrophic failure. It involves designing and analyzing engineering components to ensure structural integrity in the presence of defects or damage. It is particularly important in critical applications such as aerospace, automotive, and structural engineering. This design philosophy establishes an inspection interval to ensure that potential flaws or damage are detected before they reach a critical size that could lead to a catastrophic failure. It is an iterative design method that starts at the design level and continues until the component is removed from service. A brief description of the damage tolerance design methodology is given below.

This design approach starts with detecting a crack using a reliable non-destructive testing (NDT) method. The inspection interval depends upon the resolution capacity (or precision) of the NDT technique, i.e., a high-precision NDT method can detect a crack of very small length and thus leads to a longer inspection interval, whereas a low-precision NDT method can only detect a crack of large size and thus leads to shorter inspection intervals (Fig. 1.5). However, the cost of the NDT method is directly related to its precision.

The previous discussion implies that finding a balance between the inspection interval and the associated costs is necessary. In order to implement fracture control measures like replacement or repair, it is essential to follow the inspection interval with the crack growth time determined through damage tolerance analyses [10]. The process of determining the inspection interval is shown in Fig. 1.6.

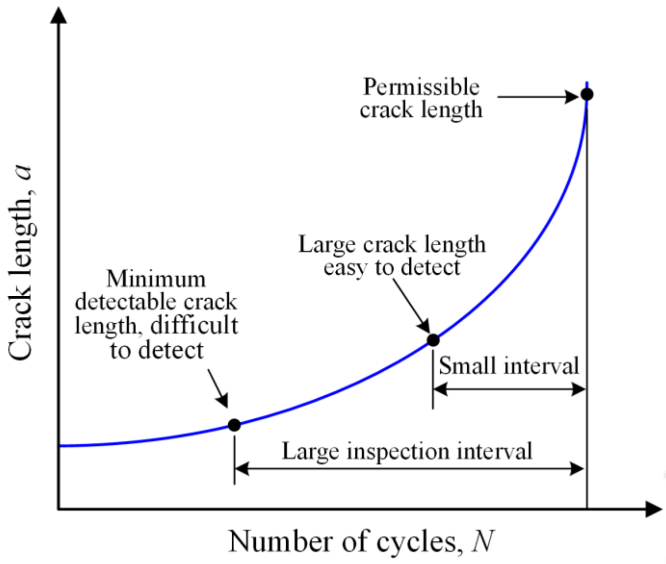

Fig. 1.5 Illustration of determining inspection interval using the crack length versus the number of cycles plot [11].

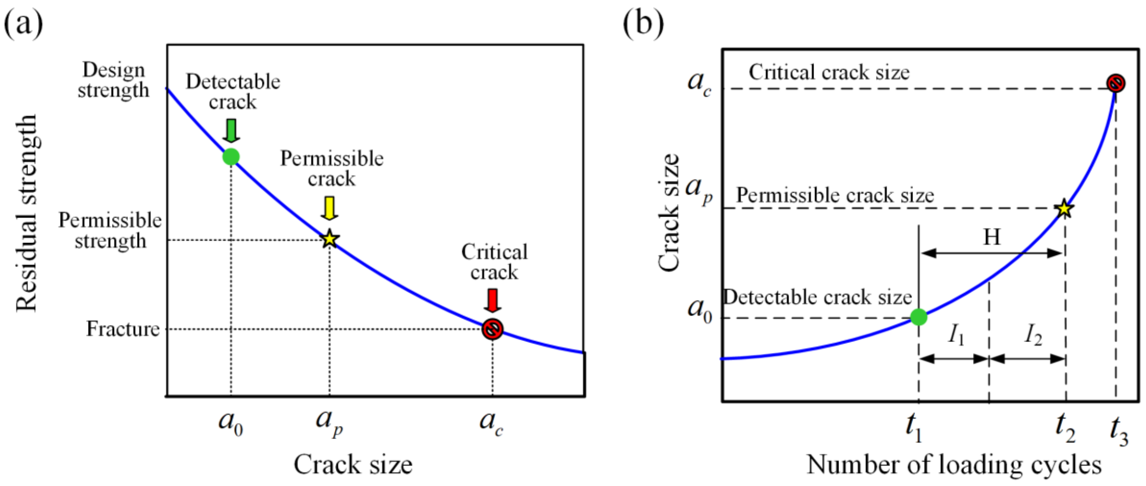

Fig. 1.6 Illustration of the principle of damage tolerance: (a) Residual strength diagram. (b) Crack growth curve [12].

Prior to entering into service, the intended component or structure is inspected to identify any potential flaws or defects. If no cracks are detected during this inspection, the size of the smallest crack that can be detected by the NDT technique is considered as the initial crack size a_0 (Fig. 1.6) [12,13]. And the prediction of safe fatigue life and the time to subsequent inspection are based on this initial crack size a_0. As shown in Fig. 1.6b, the number of load cycles H required for the crack to propagate from the initial crack size a_0 to the allowable crack size a_p are then calculated by fatigue crack growth laws. It is recommended that the first inspection interval I_1 should be set shorter than the number of loading cycles required for the crack to grow from a_0 to a_p. A common guideline is to consider the first inspection interval I_1 to be equal to $H/2$ [10].

The damage tolerance design philosophy combines non-destructive inspections with fatigue crack growth principles to simulate and predict fatigue life. The objective of employing the NDT method is to detect cracks in a timely manner. However, it is important to note that the probability of crack detection is not 100 percent and varies depending on the crack size and the specific inspection technique employed. Increasing the frequency of inspections improves the chances of detecting cracks within a reasonable time frame [14,15]. Even if a crack remains undetectable during initial inspections, subsequent inspections have a higher probability of detecting it due to the increased crack size between inspections.

The preceding discussion highlights the importance of having predicted or estimated fatigue life curves (or $a-N$ curves), which depict the relationship between crack length a and the number of loading cycles N, for accurate estimation of inspection intervals. While an experimental determination of fatigue life curves is feasible for simple benchmark specimens and loading configurations, it becomes challenging for practical components with complex geometries, loading, and boundary conditions. In such cases, numerical methods are employed to determine the fatigue life curves. Techniques like the finite element method (FEM) and the boundary element method (BEM) are commonly used for this purpose. These numerical tools analyze the actual geometry of the component and estimate the fatigue life with the help of an appropriate crack growth model.

1.5 Mixed mode fracture and fatigue theories

Mixed mode fractures usually occur under complex loading conditions and have been frequently studied by considering various combinations such as mixed mode (I/II), mixed mode (II/III), mixed mode (I/III), and mixed mode (I/II/III). For example, in mixed mode (I/II) fracture, both the direction of the crack growth (or crack kink θ_0 (Fig. 1.3b)) and the critical load (P_cr) at which unstable crack growth occurs are important parameters. Similarly, under general mixed mode (I/II/III), crack kink angle (θ_0), crack twist angle (ψ_0 (Fig. 1.3c)), and critical load (P_cr) need to be determined.

Under mixed mode (I/II) loading, the crack kink angle θ_0 and condition for unstable static fracture are generally calculated using a suitable fracture criteria [16], like the maximum tangential stress (MTS) criterion [17], maximum energy release rate (G) criterion [18], and Richard's criterion [19]. Similarly, in mixed mode (I/II/III) loading conditions, the crack kink angle, twist angle, and critical load at unstable fracture are calculated using fracture criteria like maximum principal stress criterion [20], Richard criterion [21], maximum tangential strain energy density (MTSED) criterion [22], and maximum mean principal stress criterion [23].

Moreover, to study mixed mode fractures and the corresponding fracture criteria, both the specimen configuration and material of the specimen play an indispensable role in laboratory experiments. Previous studies indicate that several specimens have been developed to characterize the mixed mode (I/II) fracture behavior of different materials like metals, rocks, acrylic, and marbles. For example, compact tension shear (CTS) specimen [24], semi-circular bend specimen [25], Arcan specimen [26], and T-specimen [27] have been widely used for the mixed mode (I/II) fracture studies of metals [28,29], rocks and composite materials. Similarly, for mixed mode (I/II/III), specimens like all fracture mode (AFM) specimen [30], compact tension shear rotation (CTSR) specimen [31], and CTS specimen with additional loading fixtures [32,33] have been used. Many of these specimens can be tested using generally available uniaxial universal testing machines (UTM). Issues like complicated specimen geometry, complex loading fixture, and unsuitability to conduct both fatigue and quasi-static fracture tests limit the application of many of these specimens. And there is a persistent need to develop better specimens for an in-depth understanding of mixed mode fracture.

As far as mixed mode fatigue crack growth studies are concerned, while many mixed mode (I/II) FCGR correlation laws are available [16], the modified Paris law by Tanaka [34] in terms of an equivalent stress intensity factor range (ΔK_{eq}) is very popular due to its simplest form and direct relevance with the Paris law in the mode I loading. The modified Paris law is expressed as: $da/dN = C(\Delta K_{\mathrm{eq}})^m$. Wherein, da/dN is FCGR, C and m are the Paris material constants, and ΔK_{eq} is a function of both the mode I stress intensity factor range ΔK_{I} and mode II ΔK_{II}. Subsequently, many ΔK_{eq} models, like Irwin's model [35], Richard's model [21], Demir's model [36], Yan's model [37], Hussain's model [18], etc., have been developed in the last few years [16,38]. On the other hand, the crack kink angle θ_0 in mixed mode FCG studies is estimated using the static fracture criteria mentioned earlier.

Currently, the above ΔK_{eq} models are basically used for two purposes: firstly, for correlating the mixed mode (I/II) FCGR da/dN with ΔK_{eq}, and secondly, for predicting the mixed mode fatigue life using numerical methods. Clearly, the use of different ΔK_{eq} models in the modified Paris law may result in varied FCGR characteristics and different fatigue life predictions for cracked components [39]. Therefore, the performance evaluation of existing ΔK_{eq} models is essential in establishing their potential applications to damage tolerance and structural integrity analyses [29]. To the authors' knowledge, only a few works (Sajith et al. [28,29,40]) have been aimed at comparing the performance of various ΔK_{eq} models and this particular aspect has been scarcely investigated.

1.6 Motivation of the present research work

Mixed mode fracture and fatigue crack growth is an open topic of remarkable significance to the engineering community [41]. In general, it is a complex design problem that involves the interaction of different modes of loading. This interaction can lead to crack deflection, branching, and twisting, which can affect the critical load, rate of crack growth, and the direction of crack propagation. Therefore, understanding the behavior of materials under mixed mode loading (both static and fatigue) is paramount important because it allows for the design of more reliable and safer structures. Mixed mode fatigue crack growth studies can provide insight into the mechanisms that govern crack initiation and growth in complex loading conditions. This knowledge can then be used to develop more accurate models and methods for predicting the useful fatigue life of components and structures.

In the past few decades, researchers have continued to develop and refine experimental and numerical techniques to better understand the behavior of materials under complex mixed mode loading conditions. Researchers have developed various experimental and numerical techniques to study mixed mode fracture and fatigue. This includes testing methods that allow for different combinations of loading modes and analytical models that can predict the behavior of cracks under mixed mode loading. However, unlike mode I loading, no standardized test methods are currently available for mixed mode static and fatigue loading situations. A large number of specimens and loading setups have been used by various researchers in the last few decades. Among them, CTS and Arcan specimens have been widely employed. But these specimens require additional complex and heavy loading fixtures to induce the desired mode mixities. It has been reported that using such fixtures limits their testing capabilities in terms of the repeatability of results, loading frequency, and testing time. An important limitation of many specimen configurations is that they are not suitable to conduct both static and FCG studies.

Due to the complexities involved in existing mixed mode fracture and fatigue testing methods, a limited number of experimental studies are available using selected specimen geometries. As a consequence, the existing theories or models are only validated with limited experimental data. Clearly, the role of a mixed mode specimen setup cannot be overemphasized in such experiments in providing valid and useful data. Therefore, a simple experimental setup and testing strategies are required to facilitate the extensive mixed mode fracture and FCG studies so that a better understanding of the existing theoretical framework can be achieved.

Another important development needed in the mixed mode fatigue studies is the evaluation of predictive models that can accurately predict the crack growth rate and fatigue life under different combinations of modes. These models can help engineers and designers in optimizing structures' and components' designs to maximize integrity and reliability. In addition, predictive models can be used to develop strategies to prevent fatigue failure, such as deciding the periodic inspections of the engineering components to monitor the crack growth or using materials that are more resistant to mixed mode fatigue crack growth. Among the various available mixed mode (I/II) fatigue crack growth laws, the modified Paris law, based on the equivalent SIF, ΔK_{eq} is widely employed for numerical predictions of fatigue life of engineering components. Clearly, different ΔK_{eq} models may result in varied FCGR characteristics and different fatigue life predictions under mixed mode cyclic loading. Therefore, the performance evaluation of various ΔK_{eq} models is very essential in establishing their potential applications. To the authors' knowledge, this aspect has been scarcely investigated. No serious attempts are available to provide the answer to the question: *Does the available* ΔK_{eq} *model(s) severely affect the mixed mode (I/II) FCGR correlations and predict the fatigue life (using numerical methods) close to the experimental results or provide conservative estimates?*

The current practice in numerical prediction of mixed mode fatigue life is to employ the mode I Paris' constants in the modified Paris law with an arbitrarily selected ΔK_{eq} model [1,29,34,36,37,42–45]. However, it was reported that the use of mode I Paris constants in mixed mode loading conditions can yield dangerously optimistic and overly conservative results [1–4]. As a consequence, researchers have arrived at proposing different Paris' constants in the stable crack propagation region. To the knowledge of the author, no serious attempts are available to provide the answer to the question: *What is the effect of the Paris' constants on the prediction of the mixed mode fatigue life using the modified Paris law?* Therefore, these ΔK_{eq} models must be tested (in a common experimental program) to see whether they provide nearly accurate or conservative predictions (with the different Paris' constants) as compared with the experimental data. The availability of such knowledge will help engineers and designers in developing better experimental and numerical techniques, fatigue life predictive models, and new materials that can better resist fatigue damage under complex loading conditions.

1.7 Organization of the thesis

This thesis is organized into 9 chapters.

Chapter 1 briefly introduces the importance of present research work, i.e., mixed mode fatigue crack growth studies, in the context of current technologies, followed by the basics of fatigue failures, the fundamental modes of loading/failure, and types of mixed mode loading. And an overview of the current approaches of mixed mode fracture and fatigue studies has been provided briefly. The motivation behind the present study has also been presented in this chapter.

Chapter 2 reviews relevant literature on different analytical, theoretical, and experimental methods adopted for mixed mode fracture and fatigue studies. Subsequently, a summary of the literature is presented. Based on this summary, the objectives of the present investigation have been outlined.

Chapter 3 presents the necessary theoretical background for the computation of stress intensity factors and various mixed mode fracture criteria to calculate the fracture locus, crack kink angle, crack twist angle, and critical loads. Additionally, a brief mathematical formulation of various crack tip elements employed in the present finite element analyses has also been presented in this chapter.

Chapter 4 describes the complete design and development of the newly proposed single edge cracked circular specimen and the new out-of-plane loading fixture. It also discusses the specimen fabrication and experimental procedures adopted for conducting experimental studies in the present work.

Chapter 5 presents the numerical and experimental results of the mixed mode (I/II) fracture studies (under static loading conditions) performed on the proposed SECC specimen made of PMMA material.

Chapter 6 presents the numerical and experimental results of the mixed mode (I/III) fracture under static loading conditions performed on the SECC specimen made of PMMA material. This chapter also presents an extensive 3D finite element analyses of the proposed loading setup. The results of experimental studies are validated with the theoretical fracture criteria in terms of fracture locus, and crack twist angle. The influence of mode III loading on crack propagation and crack growth mechanisms is also investigated in detail.

Chapter 7 presents the results of the mixed mode (I/II) FCG studies on the SECC specimen made of Al 7075-T6 alloy. Furthermore, a study on the influence of mixed mode Paris constants and ΔK_{eq} models on the FCGR correlation, and fatigue life prediction of the Al 7075-T6 alloy is presented in detail. Fractographic studies have also been presented to support the results.

Chapter 8 presents the experimental and numerical results of the mixed mode (I/II) FCG studies performed on the SECC specimen made of AISI 304 steel. Furthermore, the influence of ΔK_{eq} models and Paris constants on the FCGR correlation and fatigue life prediction of AISI 304 steel is discussed. The fractographic studies on fractured AISI 304 steel specimens are also discussed.

Chapter 9 concludes the present dissertation with the key conclusions drawn from the present research work. The recommendations for future studies that might be performed as possible extensions of this study have also been presented.

Chapter 2

Literature review

Mixed mode fracture and fatigue crack growth studies have been an ongoing and evolving areas of research in the last few decades. A large number of theoretical and experimental studies are available in the literature. Survey of several pertaining works have been carried out in the present work. The present literature review is broadly categorized into three domains: first, the theoretical framework that includes the development of various mixed mode (I/II), (I/III), and (I/II/III) fracture criteria to predict the incipient crack growth conditions. Second, the development of various specimen geometries and loading fixtures to induce mixed mode (I/II), (I/III), and (I/II/III) loading conditions using uniaxial testing machines. And third, the development of various mixed mode (I/II) fatigue crack growth laws have been reviewd. This includes critical review of existing equivalent SIF ΔK_{eq} models and their application in numerical prediction of fatigue life. Finally, based on the presented literature, important research gaps have been highlighted, and objectives and the scope of the present investigation have also been presented.

2.1 Review of various mixed mode fracture criteria

This section reviews some of the important fracture criteria that have been developed under LEFM conditions to study the mixed mode fracture of materials. These theories are applicable under static loading conditions. These criteria play an important role in accessing the structural integrity of engineering components as they provide a systematic and quantitative approach to predict the crack growth direction and the fracture load, or critical load for an unstable fracture. Various criteria corresponding to mixed mode (I/II), (I/III), and (I/II/III) loadings have been reviewed in this section.

2.1.1 Mixed mode (I/II) fracture criteria

In the past few decades, several theoretical and empirical fracture criteria have been established to predict the crack initiation, unstable failure, and fracture toughness of different materials under mixed mode (I/II) loading [17,18,20,21,38,46–53]. These criteria can be broadly classified into three categories: stress-based, strain-based, and energy-based as given in Table 2.1.

Table 2.1 Summary of theoretical criteria used for mixed mode (I/II) fracture studies.

Category	Criteria
Stress-based	Maximum tangential stress (MTS) criterion [17]
	Maximum tangential principal stress (MPTS) criterion [54]
	Generalized maximum tangential stress (GMTS) criterion [50]
	Modified Maximum tangential stress (MMTS) criterion [55]
	Triaxial stress or M-criterion [56]
Strain-based	Maximum tangential strain (MTSN) criterion [46]
	Extended maximum tangential strain (EMTSN) criterion [47,48] [57]
	Generalised maximum tangential strain (GMTSN) criterion [58]
Energy-based	Strain energy density (SED) criterion [59]
	Generalized strain energy density (GSED) criterion [60]
	Averaged strain energy density (ASED) criterion [49]
	Generalized averaged strain energy density (GASED) criterion [61]
	Maximum energy release rate criterion [62]
	Generalised maximum energy release rate (GMERR) criterion [63]
	Maximum strain energy release rate (G) criterion [18]

The MTS criterion [17], SED criterion [59], and $G-$criterion [18] are considered classical fracture criteria. Due to their elegant formulation, these criteria have been implemented in standard software like ANSYS® and ABAQUS® codes, and are widely employed in fracture studies of various materials such as metals [64,65], rocks [66], glass [67,68], marbles [69–72], polymeric foam materials [73,74] and polymeric glasses [67,68,75].

However, many researchers have also reported a significant difference between the theoretical predictions of these classical criteria and the experimental results [25,60,72,76–81]. This difference is probably attributed to the fact that all these criteria only consider the leading stress intensity factor (SIFs) terms but ignore the effect of higher order terms of William's series expansion [82] of the crack tip stress field [50]. Several researchers [60,61] have emphasized that the negligence of higher order terms, importantly the first non-singular term (called $T-$stress) in William's stress field solution, can cause a significant difference between the approximated stress field and the actual stress field. This can possibly result in the non-agreement of the experimental results with the fracture behavior predicted using classical criteria, particularly for mode II dominant failures [47,48,60,61,68].

It is now well established that the $T-$stress has a significant influence on the prediction of crack initiation angle and fracture toughness of materials [50,83–87]. Therefore, to improve these aspects in brittle/quasi-brittle materials, many modified fracture criteria, viz., GMTS criterion [50,55], EMTSN criterion [47,48,68], GMTSN criterion [58], GSED criterion [60] and GASED criterion [61] have been developed that consider the effect of both SIFs and $T-$stress. Smith et al.[50] proposed the GMTS criterion and studied the influence of $T-$-stress on the mixed mode (I/II) fracture of brittle materials. The experimental results of several studies [72,75,76,78,88–90] confirmed the applicability of the GMTS criterion for predicting mixed mode fracture behaviors of quasi-brittle materials under static loading conditions.

Furthermore, strain-based and energy-based criteria have also been modified by considering the effect of $T-$stress. For example, the EMTSN criterion [47,48,81], GSED criterion [60], and GASED criterion [61] accounted the effect of $T-$stress in their energy formulations. Mirsayar [47] proposed the EMTSN criterion and studied the effect of $T-$stress on crack initiation and fracture toughness of PMMA using experimental data of Ref. [91,92]. Similarly, Ayatollahi et al. [60] proposed the GSED criterion by accounting for the

$T-$stress in the formulation of the strain energy density factor and found good agreement between the theoretical predictions of the GSED criterion and the experimental results of Ref. [76,93]. Hou et al. [63] modified the conventional $G-$criterion [18] and proposed the GMERR criterion by considering the influence of $T-$stress in its formulation. Hou et al. [63] have found a very good agreement between the theoretical predictions of the GMERR criterion with the experimental results of rock materials [93].

Some criteria, like the MMTS criterion [55] have also considered the singular stress terms (SIFs) and the first three non-singular stress terms, viz., $T-$stress, A_3 and B_3, in their formulation. Akbardoost and Ayatollahi [55] have verified the MMTS criterion by conducting fracture experiments on Neyriz marble samples. As per the author's knowledge, no further studies using this criterion are available in the open literature. A review of various other brittle fracture criteria can be found in Ref. [21,64,94].

2.1.2 Mixed mode (I/II/III) fracture criteria

In the last few decades, there has been a growing interest in developing fracture criteria for unstable crack growth under mixed mode (I/II/III) loading [19,23]. For example, Sih and Cha [95] extended the classical energy-based SED criterion [59] to the 3D crack geometry. According to this criterion, a crack under mixed mode loading initiates along the direction of minimum strain energy density. Based on Griffith's theory of crack propagation, Yishu [96,97] proposed the energy release rate criterion for mixed mode (I/II/III) failure. Lazarus et al. [98] investigated the predictive capability of local and global mixed mode fracture criteria. Furthermore, several publications have also appeared in recent years on the development of various fracture criteria. For instance, the maximum principal stress (MPS) criterion [20], principal of local symmetry [99], Richard's empirical criterion [21], maximum potential energy release rate (MPERR) criterion [100], maximum mean principal stress (MMPS) criterion [23], maximum tangential strain energy density (MTSED) criterion [22] and the three-dimensional GMTS criterion [86] have been developed for the determination of fracture load P_{cr} and propagation angles (θ_0,ψ_0) under mixed mode (I/II/III) loading.

Wang et al. [23] reported that criteria like MPERR [100], maximum strain energy (MSE) criterion [96], generalized maximum energy release rate (GMERR) criterion [97], and 3D SED criterion [101] could predict the crack kink angle θ_0 under mixed mode

(I/II/III) loading. But these criteria cannot predict the non-planar crack growth due to the mode III component of loading. In other words, although these criteria include the K_{III} in their formulation, the calculation of crack twist angle ψ_0 is not affected by mode III. On the other hand, criteria like MPS, MMPS, Richard's, and MTSED criterion are more popular because of their capability of predicting the non-planar crack growth under mixed mode (I/II/III) loading, i.e., these criteria can predict both the crack kink angle θ_0 and crack twist angle ψ_0.

2.1.3 Mixed mode (I/III) fracture criteria

The mixed mode (I/II/III) fracture criteria have been applied to the case of mixed mode (I/III) loading by considering mode II SIF and crack kink angle equal to zero, i.e., $K_{\mathrm{II}} = 0$ and $\theta_0 = 0$. For example, Aliha and Bahmani [102] have used the MTSED and MTS criteria for validating the mixed mode (I/III) experimental results of marble rock. Aliha et al. [103] have used the MTSED criterion to study the mixed mode (I/III) fracture toughness of PUR foam and found a good agreement with the experimental results. Seifi and Omidvar [104] have used Richard's empirical criterion to correlate the FCGR under mixed mode (I/III) fatigue. Apart from these studies, various other criteria have also been developed for mixed mode (I/III) fracture studies. Lin et al. [5], and Pham and Ravi-Chandar [105,106] have studied crack growth under mixed mode (I/III) loading and concluded that a crack subjected to mixed mode (I/III) loading undergoes abrupt fragmentation and results in daughter cracks. Berto et al. [107] have developed an averaged strain energy density (ASED) criterion for mixed mode (I/III) fracture and applied it to the study of fracture toughness of PMMA specimens under combined tension and torsion loading.

2.1.4 Review of various types of materials used for mixed mode fracture experiments

As the mixed mode fracture criteria are developed under small-scale yielding conditions [19,21], PMMA (Polymethylmethacrylate or Perspex) material has been frequently employed as the model material of the specimens in the above experimental studies of various criteria [25,76,78]. Linear elastic behavior at room temperature, easy-to-fabricate specimens with sharp pre-cracks, and optical transparency for easy observation of the crack growth path are among the advantages of the PMMA that have made it the most favorable material for conducting experimental studies to validate mixed mode fracture criteria [79,108–113]. In addition to PMMA, metallic materials [64,65], brittle materials such as rocks [66], glass [67,68], and marbles [71] have also been employed to study the aforementioned mixed mode fracture criteria.

2.2 Review of various specimens used for mixed mode fracture experiments

This section critically reviews some of the existing specimens and loading fixtures employed for the mixed mode (I/II), (I/III), (I/II/III), and (II/III) fracture studies under static and cyclic loading conditions.

2.2.1 Specimens used for mixed mode (I/II) fracture studies

The specimens employed in the mixed mode (I/II) fracture studies can be classified into two categories:

(a) Specimens that produce desired mode mixities, including the pure mode I and pure mode II configurations (Fig. 2.1), and

(b) Specimens that produce desired mode mixities but without the pure mode II configurations (Fig. 2.2).

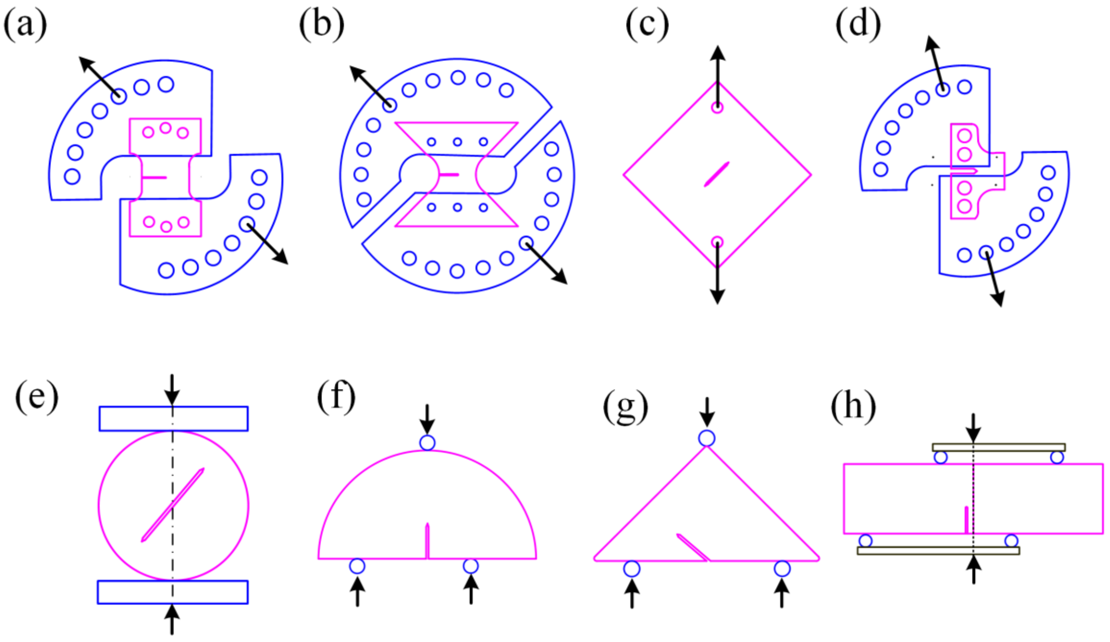

Fig. 2.1 Schematics of various mixed mode (I/II) specimens and loading fixtures that also produce pure mode II. (a) CTS specimen. (b) Arcan specimen. (c) DLSP specimen. (d) T-

specimen. (e) Brazilian disk specimen. (f) Asymmetric SCB specimen. (f) ECT specimen. (h) Asymmetric FPB specimen.

The first category includes the compact tension shear (CTS) specimen [114] (Fig. 2.1a), Arcan specimen [115] (Fig. 2.1b), diagonally loaded square plate (DLSP) specimen [78] (Fig. 2.1c), and T-specimen [27,116] (Fig. 2.1d). Apart from these specimens, some simple specimens geometry, like the centrally cracked Brazilian disk specimen [72,117] (Fig. 2.1e), symmetric and asymmetric semi-circular bend (SCB) specimen [25,118] (Fig. 2.1f), edge cracked triangular (ECT) specimen [93] (Fig. 2.1g), and four-point bend (FPB) specimen [119] (Fig. 2.1h), are also capable of producing pure mode II configurations. These specimens (Fig. 2.1e-h) are mainly used for mixed mode (I/II) fracture studies of brittle materials under static loading.

The second category of specimens includes a rectangular plate containing an inclined center crack subjected to uniform tension (Fig. 2.2a) [17,91,92], symmetric three-point bend (TPB) specimen (Fig. 2.2b) [120], modified compact tension (CT) specimen (Fig. 2.2c) [121,122], and modified CT specimen with micro defect (Fig. 2.2d) [123–125].

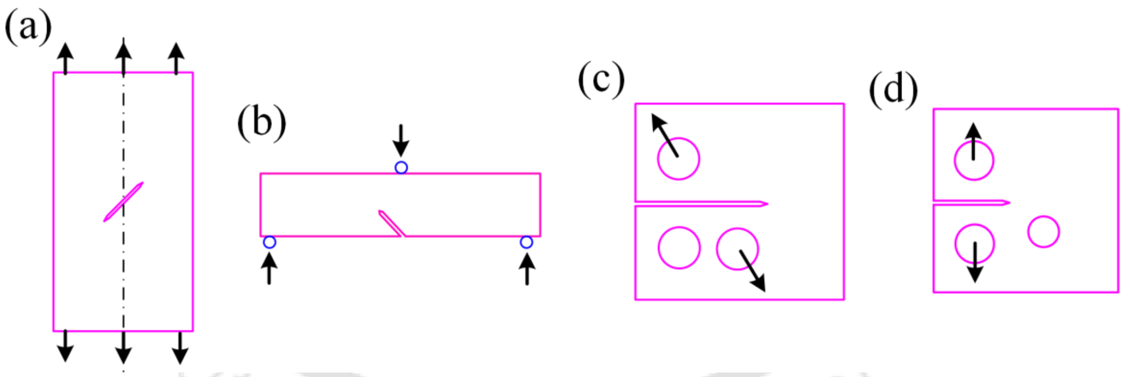

Fig. 2.2 Schematics of various mixed mode (I/II) specimens which do not have pure mode II configuration. (a) Inclined center crack specimen. (b) Symmetric TPB specimen. (c) Modified CT specimen. (d) Modified CT specimen with microdefect.

Previous studies [24,25,78] indicate that each of the aforementioned test specimens has its own merits and demerits. For example, some of these test specimens can provide only limited combinations of the mode I and mode II loadings (Fig. 2.2), and some require complicated and sensitive additional test fixtures (Fig. 2.1a, b, d). Experiments were found to become expensive and prone to produce errors in the test results due to these additional complicated fixtures. In some specimens, the orientation of the crack for producing pure mode II is not straightforward to locate and requires numerical analyses to determine the precise orientation (Fig. 2.1e-h). Sometimes this results in inconvenient orientations [25]. Some specimens are also found to produce undesirable forces on the actuator [126]. It is also well known that it is easier to pre-crack edge notched specimens than center notched specimens. The possibility of producing inconsistent results from both the tips of a center cracked specimens is also well-known (Fig. 2.1c,e and Fig. 2.2a).

Notably, only some of the above specimens are found suitable with the metallic materials for the mixed mode (I/II) experimental and fatigue crack growth studies. Another essential requirement for a specimen to be used in fatigue crack growth studies is that it should be able to provide a large, unobstructed viewing area near the crack tip for manual observation of the growing crack using an optical method. It has been found that only a few of the available specimens could meet the above requirement.

2.2.2 Specimens used for mixed mode (I/III) fracture studies

Three types of specimens have been employed for mixed mode (I/III) fracture experiments, viz:

a) Specimens with through-the-thickness inclined crack under tensile or bending loads (Fig. 2.3a, b),
b) Circumferentially cracked cylindrical specimens under tension and torsion loads (Fig. 2.3c), and
c) Specimens with additional loading fixtures that can impart all combinations of the mixed mode (I/II/III) loading such that (I/III) loading becomes a special case of these specimens (Fig. 2.4).

The specimens with a through-the-thickness inclined crack under tensile and bending loads like modified CT specimen (Fig. 2.3a) [104,127,128] and single edge notched beam (SENB) specimen (Fig. 2.3b) [129] can produce only limited range of mixed mode (I/III) ratios. Furthermore, the fabrication of through-the-thickness inclined crack is very challenging. Moreover, generating an inclined fatigue precrack in such specimens may not be easy to achieve. Some other specimens, like edge notched disc bend (ENDB) specimen (Fig. 2.3c) [130] and asymmetric disc bend specimen [131], have also been utilized to test the mixed mode (I/III) fracture toughness of brittle materials like rock [102] and asphalt concrete [131,132]. To the authors' knowledge, the suitability of these specimens to perform mixed mode (I/III) fatigue analysis using metallic specimens has not been investigated till now, and the applications have been limited to the fracture toughness testing of brittle materials.

A critical analysis of circumferentially cracked cylindrical specimen (Fig. 2.3d) reveals that in-situ measurement of crack growth in cylindrical specimens is not possible with the existing crack measuring technologies. Also, expensive biaxial testing machines capable of applying torsion and tension load are required for achieving mixed mode (I/III) loading configurations.

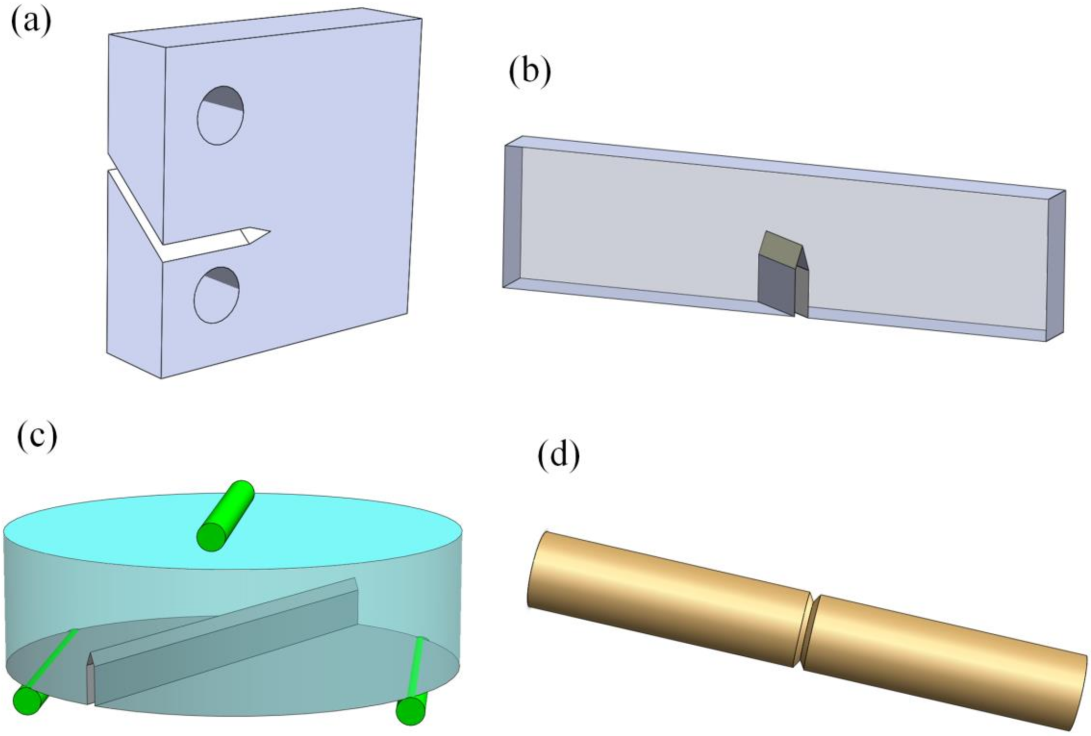

Fig. 2.3 Various mixed mode (I/II) specimens. (a) Modified CT specimen. (b) Single edge notched beam. (c) ENDB specimen. (d) Circumferentially cracked cylindrical specimen.

As far as the third category of the specimens is concerned, the specimens like compact tension shear rotation (CTSR) specimen (Fig. 2.4a), compact tension shear (CTS) specimen, all fracture mode (AFM) specimen (Fig. 2.4d), compact tension tearing (CTT) specimen, and compact tension shearing and tearing (CTST) specimen, along with their corresponding out-of-plane loading fixtures, have been used for mixed mode (I/III) and (I/II/III) fracture studies. The CTSR specimen [30] and its corresponding loading device are shown in Fig. 2.4a and Fig. 2.4b, respectively. The CTSR loading setup has a rotating turret mechanism that enables it to produce any combination of Mode I, Mode II, and Mode III [30]. The CTSR specimen has been used by Richard et al. [133] to study the fracture behavior of PMMA material. Fig. 2.4c shows the loading setup for the CTS specimen which was used by Razavi and Berto [33] for studying the mixed mode (I/II/III) fracture behavior of PMMA. This setup combines an out-of-plane loading fixture (J-fixture), C-fixture, and the CTS specimen. The complete loading assembly is connected to the testing machine using a fork-shaped fixture (Fig. 2.4c). The AFM specimen and its loading device are shown in Fig. 2.4d. The applicability of this loading setup has also been confirmed by static tests on PMMA material [134]. Further, Zeinedini [32] studied the complete range of mixed mode (I/II/III) failures in epoxy polymer using a testing assembly which was a combination of CTS specimen, out-of-plane loading fixture, and arcan fixture, as shown in Fig. 2.4e.

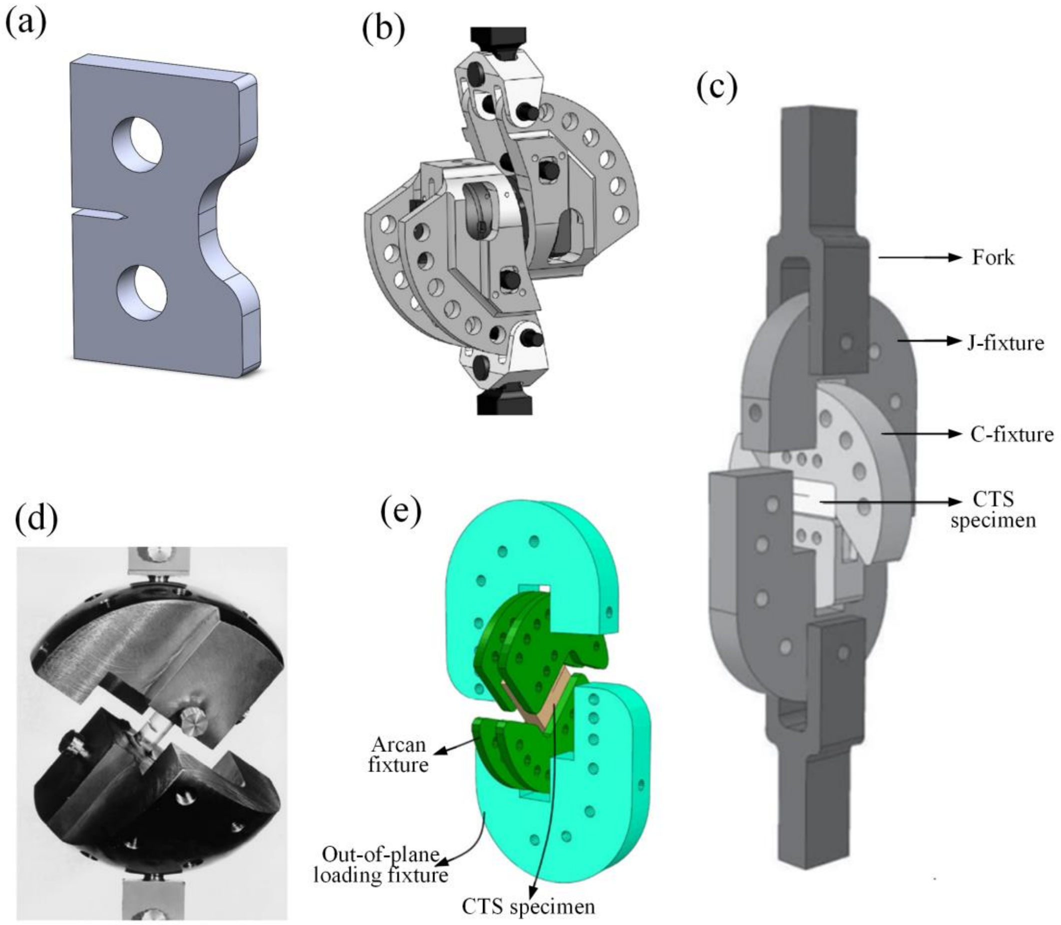

Fig. 2.4 Various mixed mode (I/II/III) specimens and loading fixtures. (a) CTSR specimen. (b) Loading device for CTSR specimen [19]. (c) Loading setup using CTS specimen, J-fixture, and C-fixture [33] (d) Loading device for AFM specimen [19]. (e) Loading setup using J-fixture, Arcan fixture, and CTS specimen [32].

Fig. 2.5 shows the loading setup for the recently developed CTST [135] and CTT [136] specimens. It can be seen that the geometry of the CTST and CTT specimens are the same. The different name is because of their loading devices. In the CTST specimen, the loading device is capable of generating mixed mode (I/II/III) by applying tension, shearing, and tearing load simultaneously. On the other hand, the loading device for the CTT specimen is capable of applying only the mixed mode (I/III) loading. The CTST specimen and loading device have been introduced by Ayhan and Demir [137] (Fig. 2.5a). They performed the mixed mode (I/II/III) fatigue fracture experiments on Al 7075-T651 aluminum alloy using the CTST specimen. Khatammanesh et al. [135] and Demir et al. [138] have performed the mixed mode (I/II/III) fracture studies on Al 2024-T351 alloy and Al 7075-T651 alloy, respectively, using the CTST specimen. As far as the CTT specimen is concerned, Wei et al. [139] have used the CTT specimen to study the mixed mode (I/III) crack growth in Al 6061-T6 allloy. Bozkurt et al. [136] have studied the mixed mode (I/III) fracture toughness of Al 7075-T651 alloy. Other than these studies using mixed mode (I/II/III) loading setups, Ayatollahi and Saboori [140] have studied the mixed mode (I/III) fracture of PMMA using an out-of-plane loading fixture and rectangular specimen.

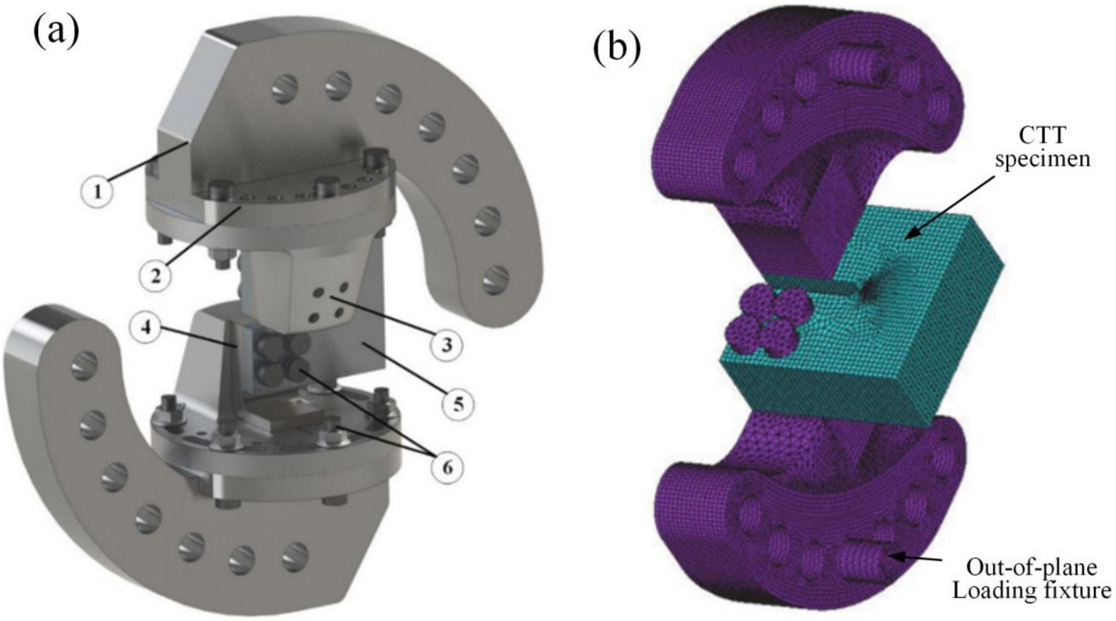

Fig. 2.5 (a) Compact Tension Shear Tearing (CTST) specimen [135]. (b) Compact Tension Tearing (CTT) specimen [136].

The above-mentioned testing assemblies are very suitable for mixed mode (I/II/III) quasi-static fracture testing, and a complete range of mode mixities from pure mode I to pure mode III, including pure mode II can be achieved. But due to very large inertia (weight) and complicated loading arrangement, these testing assemblies find limited application in the fatigue testing of metallic specimens.

In summary, the first category specimens provide a limited range of mixed mode (I/III) configurations, and creating an inclined pre-crack crack is a difficult and challenging task [64]. On the other hand, the circumferential cracked cylindrical specimen cannot show the crack twist angle under different mode mixities and requires more complicated and expensive testing machines [64]. While the third category of specimens is promising, their loading capacity, the heavy weight of the additional fixtures [64], and the availability of limited area in the specimen for observing the fatigue crack growth pose big challenges while conducting mixed mode (I/III) fatigue crack growth studies.

2.2.3 Specimens used for mixed mode (II/III) fracture studies

To the author's knowledge, in the context of mixed mode (II/III) fracture, only a few works are available in the open literature [141–144]. Hellier et al. [141] developed a test rig to investigate the mixed mode (II/III) fatigue fracture problem in steels. Merati et al. [145] investigated the fatigue threshold behavior of two structural aluminum aerospace alloys, Al 2014-T6 and Al 7075-T6, using the test rig developed by Hellier et al. [141]. Saboori and Ayatollahi [143] have designed a rotating four-point bend testing fixture to study the mixed mode (II/III) fracture. Further, Ayatollahi et al. [144] have used this jig plate to study the mixed mode (II/III) behavior of PMMA. The authors believe that the problem of mixed mode (II/III) fracture is very important for a comprehensive understanding of mixed mode fracture. Therefore, further studies on mixed mode (II/III) are required.

2.3 Review of mixed mode fatigue crack growth models

Mixed mode fracture and fatigue crack growth studies have been an area of research for several decades. Researchers began investigating the mixed mode fatigue failure in metals around the 1970s-1980s. The first study on mixed mode (I/II) fatigue was conducted by Iida and Kobayashi [146] by using an inclined center crack rectangular specimen made of Al 7075-T6 alloy. Based on these experimental results, they concluded that a crack under mixed mode (I/II) loading grows in a way which minimizes the mode II component, and also rate of crack growth increases with the increase in mode II loading component. Later, Roberts and Kibler [147] conducted mixed mode (I/II) fatigue crack growth experiments in Al 2024-T3 alloy and found that under certain conditions, a crack under mixed mode (I/II) loading grows considerably in a direction in which mode II SIF component does not reduce.

Tanaka [34] equated the mixed mode crack growth rate with the equivalent SIF range, which later became the most widely used approach for fatigue life prediction. During this period (1970-1980s), the experimental data were generally obtained from inclined center cracked specimens.

Paris et al. (1961) [148] showed that the FCGR, plotted as a function of the SIF range ΔK in a log-log plot, can be fitted with a straight line, and the FCGR for mode I loading can be represented as:

$$\frac{da}{dN} = C\left(\Delta K\right)^m \tag{2.1}$$

where C and m are called the Paris' material constants and $\Delta K = K_{\max} - K_{\min}$. The literature review shows that in the beginning, most of the fatigue crack growth studies were performed under mode I loading conditions. However, as explained earlier, the cracks in real structures are often subjected to a case of mixed mode loading for which $K_{\mathrm{I}}, K_{\mathrm{II}}$ and K_{III} should be considered. Notably, the work of Tanaka [34] was a major breakthrough in the area of mixed mode (I/II) fatigue crack growth studies. Tanaka extended the Paris law for mode I (Eq. (2.1)), and proposed a modified Paris law for mixed mode (I/II) loading conditions. According to modified Paris law, the mixed mode FCGR can be correlated with an equivalent SIF ΔK_{eq} model as given in Eq. (2.2).

$$\frac{da}{dN} = C\left(\Delta K_{\mathrm{eq}}\right)^m \tag{2.2}$$

where $\Delta K_{\mathrm{eq}} = f(\Delta K_{\mathrm{I}}, \Delta K_{\mathrm{II}})$. Similarly, by considering different fracture parameters, various other crack growth laws have also been developed, such as the effective SIF model by Chen and Keer [149], ΔS-model [150,151], J-integral model [152–154], and equivalent strain intensity factor $\Delta \varepsilon_{\mathrm{eq}}$ model [155–157]. In the context of LEFM, the equivalent SIF ΔK_{eq} models are generally used to characterize the mixed mode FCGR.

Due to the straightforward form of the modified Paris law (Eq. (2.2)) and its relation with the Paris law, it is extensively used in mixed mode (I/II) FCG studies. Consequently, various ΔK_{eq} models based upon different fracture criteria have been introduced for the last four decades to be used in Eq. (2.2). For example, Tanaka's ΔK_{eq} model [34] is based on the dislocation-based crack initiation theory, Hussain's [18] and Yan's ΔK_{eq} models

[37] are based on the static fracture theories under mixed mode (I/II) loading, while some models are empirically formulated. These existing ΔK_{eq} models and their application in mixed mode FCG studies are critically reviewed in this section.

2.3.1 Tanaka's model

Based upon Lardner's and Weertman's theory of crack propagation under fatigue loading, Tanaka [34] proposed two different forms of ΔK_{eq} models as given below:

$$\Delta K_{\text{eq}} = \left(\Delta K_{\text{I}}^{2} + 2\Delta K_{\text{II}}^{2}\right)^{1/2} \tag{2.3}$$

$$\Delta K_{\text{eq}} = \left(\Delta K_{\text{I}}^{4} + 8\Delta K_{\text{II}}^{4}\right)^{1/4} \tag{2.4}$$

In the present work, Eq. (2.3) and (2.4) will be referred to as 'Tanaka 1' and 'Tanaka 2' models, respectively. Tanaka studied the FCG behavior of an aluminum alloy using a CCP specimen under four different loading angles (30°, 45°, 72°, and 90°) and found that the FCG rate da/dN from different loading angles falls on a straight line in log-log scale when plotted with one of the proposed ΔK_{eq} models.

Tanaka's models has been widely used for characterizing the mixed mode fatigue crack behavior of various materials [42,158–163]. Qian and Fatemi [2] conducted the numerical and experimental mixed mode (I/II) FCG studies on an asymmetric FPB specimen and used one of the Tanaka's ΔK_{eq} models to calculate the fatigue life. Ingraffea et al. [164] developed an automatic numerical scheme using BEM, and Portela et al. [165], Yan and Nguyen-Dang [166], and Leite and Gomes 2019 [167] used a dual boundary element method to simulate the FCG and used the Tanaka's ΔK_{eq} models for the fatigue life prediction under mixed mode (I/II) loading conditions.

Additionally, Tanaka's ΔK_{eq} model was employed for the fatigue life prediction of various real engineering components, e.g., fatigue crack path in an anti-return valve of a high-pressure machine [168], rail [169] and railways bridges [158,170,171]. Many other studies like FCG in friction stir welded zone [172,173], subsurface crack growth in gears [174], the effect of plastic anisotropy on crack growth behavior [175], the effect of biaxial load ratios on FCGR in the cruciform specimen [176] were also employed Tanaka's ΔK_{eq} model. This model has also been employed in the XFEM-based numerical studies of mixed mode FCG [177]. Dirik and Yalçinkaya [178] performed the XFEM-based crack path and life prediction studies and used Tanaka's ΔK_{eq} model for calculating the fatigue life

2.3.2 Irwin's model

Based upon the Irwin's theory of fracture, Liu et al. [179] proposed a new ΔK_{eq} model (called as Irwin's model) in which equal weights were assigned to each mode (ΔK_{I} and ΔK_{II}).

$$\Delta K_{\text{eq}} = \sqrt{\Delta K_{\text{I}}^2 + \Delta K_{\text{II}}^2} \tag{2.5}$$

Liu et al. [179] reported that this ΔK_{eq} model could not correlate the fatigue results of biaxially stretched cruciform specimens (made of 7075-T352 and 2024-T351 alloys) under various biaxial stress ratios. Later, Biner [35] conducted the mixed mode (I/II) FCG studies using the CTS specimen (made of AISI 304 stainless steel) under different loading angles (0°, 30°, 45°, and 75°) and found that the FCGR for all the loading angles correlates well with Irwin's ΔK_{eq} model.

The application of Irwin's model has also been extended to the case of general mixed mode (I/II/III) fracture. The 3D version of Irwin's model has been employed in the FCG study of helicopter lift frames [180], web stiffeners of ships [159], CFRP patch-repaired panels [181], pressured pipes [182], and XFEM-based FCG simulations of surface cracks [183].

2.3.3 Richard' model

Richard et al. [24] defined a fracture limit curve and proposed a ΔK_{eq} model (Eq. (2.6)) comparable to the equivalent stress in the classical stress hypothesis [184] for static failure under mixed mode (I/II) loading conditions.

$$\Delta K_{\text{eq}} = \frac{\Delta K_{\text{I}}}{2} + \sqrt{\Delta K_{\text{I}}^2 + 5.3361 \Delta K_{\text{II}}^2} \tag{2.6}$$

In further studies, Richard et al. [185] verified the applicability of this model by comparing it with the fracture limit curves of other available criteria. This model has been used for the prediction of fatigue life in several numerical and experimental FCG studies. For example, Sander and Richard [186,187], and Seifi and Eshraghi [188] utilized Richard's model in the study of the effect of overload on the mixed mode FCG rate using a CTS specimen made from Al 7075-T651 alloy. Borrego et al. [189] studied the crack closure effect in mixed mode FCG using the CTS specimen made from Al 6082-T6 and used Richard's model for correlating the FCG rate.

Similarly, Mohanty et al. [190,191] used Richard's model for correlating the FCGR in the study of the FCG retardation due to overloads in the SENT specimen made of Al 7020-T6 and introduced an exponential FCG model for estimating the crack length. Varfolomeev et al. [192] and Zarrinzadeh et al. [193] used this model in the experimental and XFEM-based numerical analyses of FCG of an aluminum pipe repaired by a composite patch. Other applications of Richard's ΔK_{eq} model in mixed mode FCG studies include: the work of Li et al. [194] on the development of a cyclic cohesive zone model for predicting FCGR in CTS specimen made of AISI 304 steel, a study of mixed mode FCGR in high-speed rail steel [195], finite element based numerical study of various possible configuration of the cracks in railway axel geometries [196,197]. The 3D version of Richard's ΔK_{eq} model was also applied in the FCG simulations of crack initiation and propagation in gear tooth [198]. Schöllmann et al. [199] used this generalized Richard's ΔK_{eq} model for FCG simulation of a crack under mixed mode (I/II/III) loading conditions and determined the progress of a crack surface in an arbitrary 3D geometry.

2.3.4 Demir's model

Demir et al. [116,200] proposed an empirical ΔK_{eq} model (Eq. (2.7)) by using the experimental results of CTS and T-shaped specimens made from Al 7075-T6 alloy.

$$\Delta K_{\mathrm{eq}} = \left[1.0519\Delta K_{\mathrm{I}}^{4} - 0.035\Delta K_{\mathrm{II}}^{4} + 2.3056\Delta K_{\mathrm{I}}^{2}\Delta K_{\mathrm{II}}^{2}\right]^{0.25} \tag{2.7}$$

Demir and Ayhan [116] tested this model to predict the critical fracture load of the statically loaded T-specimen. The authors have claimed that this model is useful for higher mode mixity levels. The efficacy of this model has been demonstrated using the experimental results of CTS and T-shaped specimens [27,36]. In this study, Demir et al. [27] compared the fatigue life predictions of Demir's model with other ΔK_{eq} models. This model is found to be highly accurate for the higher mode mixity levels for the CTS specimen by Sajith et al. [29].

2.3.5 Hussain’s model

Hussain et al. [18] computed the parametric form of energy release rate for crack growth under mixed mode (I/II) loading conditions and proposed that “the incipient crack will grow in a direction along which the elastic energy release per unit extension will be maximum, and the crack will start to grow when this energy release rate reaches to a critical value.” The ΔK_{eq} model corresponding to Hussain’s fracture criteria can be written as

$$\Delta K_{\text{eq}} = \sqrt{\frac{4}{\left(3+\cos^2\theta_0\right)^2}\left(\frac{1-\frac{\theta_0}{\pi}}{1+\frac{\theta_0}{\pi}}\right)^{\frac{\theta_0}{\pi}}\left\{\begin{matrix}\left(1+3\cos^2\theta_0\right)\Delta K_{\text{I}}^2+8\sin\theta_0\cos\theta_0\Delta K_{\text{I}}\Delta K_{\text{II}}+\\ \left(9-5\cos^2\theta_0\right)\Delta K_{\text{II}}^2\end{matrix}\right\}} \tag{2.8}$$

This model was originally derived for the static fracture under mixed mode (I/II) loading. Later, Miranda et al. [201] suggested using this model for FCG studies. Sajith et al. [28,29,40] have used this model for calculating fatigue life for the CTS specimens fabricated from Al 6061 alloy and AISI 316 steel. As per the author’s knowledge, this model has found limited application to the mixed mode (I/II) FCG studies except for a few studies.

2.3.6 Yan’s model

Similar to Hussain’s model, Yan’s ΔK_{eq} model is also defined as a function of SIFs (ΔK_{I} and ΔK_{II}) and the crack kink angle θ_0. Yan et al. [37] extended the application of the MTS criterion proposed by Erdogan and Sih [17] to the case of fatigue loading. They derived a new ΔK_{eq} model (Eq. (2.9)) from the expression of maximum hoop stress at the crack tip and used it to correlate the FCGR under mixed mode (I/II) loading conditions.

$$\Delta K_{\text{eq}} = \frac{1}{2}\cos\frac{\theta_0}{2}\left[\Delta K_{\text{I}}\left(1+\cos\theta_0\right)-3\Delta K_{\text{II}}\sin\theta_0\right] \tag{2.9}$$

This model has been applied to a large number of FCG studies. For example, Leonel and Venturini [202] developed a BEM-based numerical method to analyze the crack growth in multiple random cracks and used this model for fatigue life prediction. Ayatollahi et al. [203] employed Yan’s ΔK_{eq} model to study the effect of FCG retardation caused by hole drilling at the crack tip. Jameel and Harmain [159] developed an element-free Galerkin method to study the FCG in cracked specimens and employed Yan’s model for calculating the fatigue life. Singh et al. [204] and Grbović et al. [205,206] have conducted mixed mode

(I/II) FCG studies using the XFEM method and applied Yan's ΔK_{eq} model for fatigue life predictions, numerically. Furthermore, Martins et al. [207], Yang and Vormwald [208], and Vormwald et al. [209] have utilized the 3D version of Yan's model to verify the experimental results of FCG studies in thin-walled hollow cylinders subjected to fatigue axial tension-torsion loading.

2.4 Review of performance evaluation of ΔK_{eq} models for fatigue life prediction

The previous literature review indicates that currently, ΔK_{eq} models are essentially used for two purposes: firstly, correlation of the mixed mode (I/II) FCGR, i.e., da/dN with ΔK_{eq}, and secondly, prediction of the mixed mode fatigue life using numerical methods. Clearly, different ΔK_{eq} models can result in varied FCGR characteristics, critical loads, and different fatigue life predictions [39] under mixed mode fracture and cyclic loading.

Only a few works are available in open literature devoted to comparing the competence of available ΔK_{eq} models for the numerical prediction of fatigue life under mixed mode loading conditions. For example, Demir et al. [36] studied the predictive capabilities of available ΔK_{eq} models by comparing the predictions of fatigue life using selected ΔK_{eq} models with the experimental results of the CTS specimen. However, their findings did not provide any definitive conclusions.

Recently, Sajith et al. [28,29,40] have performed a comprehensive investigation on the effect of different ΔK_{eq} models in fatigue life estimation under mixed mode (I/II) loading. They conducted experimental studies on the CTS specimen made of two different materials (Al 6061-T6 alloy [29] and AISI 316 steel [28]), and performed numerical analyses using the finite element method. They considered large number of ΔK_{eq} models for their study. Based on the extensive experimental and numerical studies, they concluded that Irwin's model and Tanaka's model predict fatigue life close to the experimental results.

Xie et al. [210] have investigated the efficacy of selected ΔK_{eq} models for mixed mode (I/II) FCG studies at high temperatures. They conducted the FCG experiments on the CTS specimen made of Nickel-based superalloy GH4169 and found that at high temperatures, FCGR did not show a strong linear relationship with Hussain's ΔK_{eq} models. However, the fatigue life estimation using Hussain's model has shown the highest accuracy with the experimental results.

While it is very important to know the performance of various ΔK_{eq} models, the previous discussion clearly demonstrates that research in this direction has been scarcely addressed. Therefore, the performance evaluation of various ΔK_{eq} models on a common experimental scheme is very essential in establishing their potential applications [29].

2.5 Review of the effect of Paris' material constants in the estimation of mixed mode (I/II) fatigue life

Predicting crack length a as a function of the number of loading cycles N (or fatigue life curve) has become an essential requirement for practical applications like inspection schedule planning [205,211,212] and damage tolerant designs. As stated earlier, the mixed mode fatigue life is commonly predicted using the modified Paris law that requires the Paris constants (C and m) and a ΔK_{eq} model. It is well-known that these constants significantly affect the fatigue life prediction. As stated earlier, the current practice in numerical approaches is to employ the mode I Paris constants and an arbitrarily selected ΔK_{eq} model [1,29,34,36,37,42–45]. However, it has been reported that the use of mode I Paris constants in mixed mode loading conditions can yield dangerously optimistic and overly conservative results [1–4].

In several mixed mode (I/II) FCG tests conducted on high-strength structural steels and similar materials indicated that the slope m of the FCGR curve in mixed mode (I/II) and mode I is nearly the same. On the other hand, the parameter C differed for each mode mixity [1,35,161–163]. Ma et al. [162], in their mixed mode FCG experiments on aluminum alloys and steels, observed that the mode I C parameter can be correlated with the mode mixity parameter M^{e}, to obtain the mixed mode C^*. To the authors' knowledge, no work is reported till date to check the usefulness of the modified Paris constants $C^*, m^*(=m)$ proposed by Ma et al. [162]. Furthermore, the Paris constants obtained directly from the mixed mode tests ($C_{\mathrm{eq}}, m_{\mathrm{eq}}$) are also found to be considerably different from the mode I Paris constants (C, m) [43–45,169,189,210,213,214].

Despite knowing the importance of the Paris' constant, to the knowledge of author, no work is available to date on the effect of using the above different Paris constants, i.e., (C, m), (C^*, m^*) and $(C_{\text{eq}}, m_{\text{eq}})$ in prediction of the fatigue life. Interestingly, numerical fatigue life predictions using the mixed mode C_{eq} and m_{eq} in the modified Paris law has also been scarcely investigated.

2.6 Summary of literature review

The present literature review can be summarised into three broad domains as shown in Fig. 2.6: (a) Theoretical framework, (b) experimental framework, and (c) FCG models, particularly ΔK_{eq} models and their application in predicting mixed mode (I/II) fatigue life.

Theoretical fracture criteria

Three types of criteria have been utilized to predict the fracture under mixed mode (I/II) loading conditions:

1. Stress-based e.g., MTS, GMTS and MMTS.
2. Strain-based, e.g., MTSN, EMTSN and GMTSN.
3. Energy based, e.g., SED, GSED, ASED, *G*, and GMERR.

- For mixed mode (I/III) and (I/II/III) loading conditions, fracture criteria like, MPS, Richard, MPERR, MMPS and MTSED have been widely used predict the incipient crack growth.

Experimental setup for fracture tests

- Two types of specimen have been used to conduct the mixed mode (I/II) fracture experiments.
  1. Specimens with pure mode II configurations, e.g., CTS, Arcan, DLSP, T, BD, SCB, ECT and FPB.
  2. Specimens without pure mode II configuration, e.g., CCP, TPB and Modified CT.
- Three types of specimens have been used to study the mixed mode (I/III) fracture
  1. Through-the-thickness inclined crack
  2. Circumferentially cracked cylindrical
  3. Specimens with additional loading fixtures

Equivalent SIF models for mixed mode (I/II) fatigue life prediction

- A large number of equivalent SIF models have been developed to be used with the modified Paris law for the fatigue life prediction under mixed mode (I/II) loading, e.g.,
  1. Tanaka's model, Irwin's model, Richard's model, Demir's model, Hussain's model and Yan's model
  2. Performace eavaliation of these models in terms of fatigue life prediction is scarcely available.
  3. Effect of different Paris mateiral constants on the fatigue life estimation is not studied.

Fig. 2.6 Domains of literature review carried out in the present investigation.

The theoretical framework includes the development of various mixed mode (I/II), (I/III), and (I/II/III) fracture criteria. The experimental framework includes the development of various specimen geometries and loading fixtures to conduct mixed mode (I/II), (I/III), and (I/II/III) fracture and fatigue crack growth studies. Summary of the literature review of the three domains stated above is as follows:

- The classical fracture criteria like MTS, MTSN, G and SED consider only the SIFs in their formulation and have been found to be useful for predicting the brittle fracture under mode I dominated loading conditions only. For mode II dominated loading, a noticeable deviation between the experimental and theoretical predictions of classical criteria has been reported by various researchers.

- By considering the effect of the first non-singular terms (called $T-$stress) along with the SIFs terms in William's stress field solutions, a better prediction of the fracture load and crack initiation angle has been achieved by GMTS, EMTSN, GMTSN, GSED, and GASED criteria.

- The stress-based GMTS criteria have shown promising results in predicting the mixed mode fracture behavior of various types of specimen geometries, and materials. It has been found that the GMTS criterion can predict the critical fracture load (P_{cr}) and crack kink angle (θ_0) close to the experimental results under mode II dominated loading conditions.

- After the success of GMTS, many other criteria also included $T-$stress in their formulation.

- Many fracture criteria, such as SED, MPS, Richard's empirical criterion, MPERR MMPS, MTSED, and 3D-GMTS, are currently available for mixed mode (I/II/III) fracture.

- No standard test procedure has been developed to date for conducting mixed mode fracture and fatigue tests.

- Due to a lack of standard test procedures, many different specimen geometries and loading fixtures have been used to study the mixed mode fracture and fatigue behaviour of materials. Among them, CTS, CCP, and Arcan specimens have been extensively used for mixed mode (I/II) fracture and fatigue studies.

- Literature reviews indicate that each of the aforementioned test specimens has its own merits and demerits. Some of them can provide only limited combinations of the mode I and mode II loadings, and some require complicated and sensitive additional test fixtures. In some specimens, a priori numerical analysis is needed to determine the orientation of the specimen. Only a few specimens have been found suitable with the metallic materials for conducting both the mixed mode fracture and fatigue tests. The focus of recent research has been on the development of new specimen configurations to meet various challenges involved in mixed mode testing.

- As compared to mixed mode (I/II), a very limited number of specimen set-ups are available for mixed mode (I/II/III) loading conditions.

- Based on the above literature review, it can be envisaged that a suitable mixed mode loading setup should have the following desirable properties:
  - ✓ It should have a simple specimen, crack geometry, and loading arrangement to introduce the desired mode mixities.
  - ✓ It should be fabricated using simple manufacturing techniques.
  - ✓ It should have the ability to introduce a wide range of mode mixities, such as (I/II), (I/III), and (I/II/III).
  - ✓ It should accommodate both brittle materials and metals for fracture tests under static loading.
  - ✓ The specimen should also be capable of conducting mixed mode fatigue tests on metals.
  - ✓ It should have sufficient visible area for capturing the curvilinear crack path using a digital microscope.
  - ✓ The most vital requirement for testing with metallic materials (whether in static or fatigue loading) is the arrangement in the specimen for creating fatigue pre-cracks. Thus, the specimen should have an efficient and simple arrangement for the creation of fatigue pre-cracks for testing metals.
  - ✓ Importantly, it should be able to be used with a conventional UTM.

- The literature review on mixed mode (I/II) fatigue crack growth studies shows that due to the popularity of the modified Paris law, a large number of ΔK_{eq} models have been developed to be used for mixed mode (I/II) fatigue life prediction.

- The ΔK_{eq} models are essentially used for two purposes: firstly, correlation of the mixed mode (I/II) FCGR, i.e., da/dN with ΔK_{eq}, and secondly, prediction of the mixed mode fatigue life using numerical methods.
- Prediction of crack length, a vs. number of loading cycles, N (fatigue life) is an important requirement in the damage tolerance design philosophy.
- The fatigue life is commonly predicted using the modified Paris law that requires the Paris constants (C and m) and a ΔK_{eq} model. The current practice is to employ the mode I Paris constants and an arbitrarily selected ΔK_{eq} model.
- The finite element method is widely employed for fatigue crack growth simulations under mixed mode loading conditions. During FCG simulations, the MTS and SED criteria are generally employed to predict the crack path. For the correlation between ΔK_{eq} and da/dN, one needs to rely on numerical methods to calculate the SIFs along the experimental crack path.

2.7 Research Gap

Based on the above literature review in the broad area of mixed mode fatigue crack growth, some of the important gaps which deserve to be addressed are as follows:

- Although several specimen configurations are available for testing, they inherently have some serious limitations when working in mixed mode loading conditions. Thus, there is a need for the development of a new specimen configuration to meet the desirable features (mentioned in the previous section) in order to mitigate the challenges posed in mixed mode fracture and fatigue tests with metallic materials.
- Due to the unavailability of a suitable specimen, the existing theoretical framework to predict the fracture under mixed mode (I/II, I/III) loading has been validated only with a limited number of experimental data. Therefore, it is indispensable to study the applicability of existing mixed mode fracture criteria using a new specimen configuration.
- Except for the work of Sajith et al. [215], no significant efforts are being devoted in understanding the competence of various ΔK_{eq} models in fatigue life estimation under mixed mode (I/II) loading conditions.

- Although the effect of $T-$stress on the calculation of fracture toughness and crack kink angle is studied extensively using the GMTS criterion, no study is available on the effect of $T-$stress on the fatigue crack growth rate correlation and fatigue life estimation under mixed mode (I/II) loading conditions. Conversely, no ΔK_{eq} model based on the GMTS criterion is available to date.
- The current practice in predicting mixed mode (I/II) fatigue life is to employ the mode I Paris constants along with a selected ΔK_{eq} model. While it is very convenient to use the modified Paris law for the above purpose, no work is available to date on the effect of using different Paris constants i.e., (C, m), (C^*, m^*) and ($C_{\mathrm{eq}}, m_{\mathrm{eq}}$).
- It is also not evident to date whether a ΔK_{eq} model or the Paris' constants have the more profound effect on the prediction of mixed mode (I/II) fatigue life using the finite element method.

2.8 Objectives of the present study

In view of the research gaps discussed in the previous section, the objectives of the present investigation are set as follows:

1. To design and develop a simple specimen geometry and loading setup for investigating the mixed mode (I/II/III) failures of brittle materials and metals at room temperature under static tensile and fatigue loads.
2. To study the mixed mode (I/II) and (I/III) fracture of linear elastic isotropic materials under static tensile loads using the proposed specimen setup.
3. To study the mixed mode (I/II) fatigue fracture of metals such as Al 7075-T6 alloy and AlSI 304 steel using the proposed specimen setup and extend this study (a) to understand the effect of Paris' material constants in prediction of mixed mode (I/II) fatigue life using modified Paris law and (b) to recommend a ΔK_{eq} model and Paris constants for accurate and conservative numerical prediction of mixed mode (I/II) fatigue life of metallic components.

Chapter 3

Theoretical background

This chapter presents the theoretical framework of the various concepts used in the present investigation. First, a brief derivation of the crack-tip stress field equations using the generalized Westergaard approach has been presented. Then the formulation of selected mixed mode (I/II), (I/III), and (I/II/III) fracture criteria are explained in detail. Furthermore, the formulation of a new GMTS-based ΔK_{eq} model and the theoretical foundation for the prediction of the residual fatigue life under mixed mode (I/II) loading conditions are presented in detail. A quick note on the basics of the finite element method for modeling a two-dimensional and three-dimensional cracked component using quarter point elements and wedge elements is briefly discussed. Finally, the formulation of two SIF determination techniques, viz., interior collocation technique and interaction integral technique are presented.

3.1 Stress field for mixed mode (I/II/III) loading

Under a general mixed mode (I/II/III) loading condition, a crack is more often subjected to a superposition of all three modes of crack extension (Mode I, Mode II and Mode III). For such cases, a complex form of stress field having all the six stress components, i.e., σ_{ij} with $i, j = r, \theta, z$, exists at the crack tip. Using the principle of superposition, the stress field for the case of a general mixed mode (I/II/III) loading in cylindrical coordinate system can be written as

$$
\begin{aligned}
\sigma_{rr} &= \frac{K_{\mathrm{I}}}{4\sqrt{2\pi r}}\left\{5\cos\frac{\theta}{2}-\cos\frac{3\theta}{2}\right\}-\frac{K_{\mathrm{II}}}{4\sqrt{2\pi r}}\left\{5\sin\frac{\theta}{2}-3\sin\frac{3\theta}{2}\right\}+T\cos^{2}\theta \\
\sigma_{\theta\theta} &= \frac{K_{\mathrm{I}}}{4\sqrt{2\pi r}}\left\{3\cos\frac{\theta}{2}+\cos\frac{3\theta}{2}\right\}-\frac{K_{\mathrm{II}}}{4\sqrt{2\pi r}}\left\{3\sin\frac{\theta}{2}+3\sin\frac{3\theta}{2}\right\}+T\sin^{2}\theta \\
\tau_{r\theta} &= \frac{K_{\mathrm{I}}}{4\sqrt{2\pi r}}\left\{\sin\frac{\theta}{2}+\sin\frac{3\theta}{2}\right\}+\frac{K_{\mathrm{II}}}{4\sqrt{2\pi r}}\left\{\cos\frac{\theta}{2}+3\cos\frac{3\theta}{2}\right\}-T\sin\theta\cos\theta \\
\tau_{rz} &= \frac{K_{\mathrm{III}}}{\sqrt{2\pi r}}\sin\frac{\theta}{2} \\
\tau_{\theta z} &= \frac{K_{\mathrm{III}}}{\sqrt{2\pi r}}\cos\frac{\theta}{2} \\
\sigma_{zz} &= \nu\left(\sigma_{rr}+\sigma_{\theta}\right)=\frac{8\nu}{4\sqrt{2\pi r}}\left\{K_{\mathrm{I}}\cos\frac{\theta}{2}-K_{\mathrm{II}}\sin\frac{\theta}{2}\right\};\text{plane strain} \\
\sigma_{zz} &= 0\ ;\quad \text{plane stress}
\end{aligned}
\tag{3.1}
$$

where, r, θ, z are the cylindrical coordinates originated at the crack front). K_{I}, K_{II} and K_{III} are the Mode I, Mode II, and Mode III SIFs, and ν is the Poisson's ratio. The leading singular terms in Eq. (3.1) are the SIFs, and the first non-singular term, called $T-$stress, is a constant term that is independent of the distance from the crack tip. The SIFs (leading terms of Eq. (3.1)) dominate the stress field near the crack tip and govern the mechanics of brittle fracture. Therefore, in the context of LEFM, SIFs are the most critical parameters which characterize brittle fracture. Derivations of crack-tip field equations under mode I, mode II, and mode III loading conditions are given in Appendix A.

3.2 Mixed mode (I/II) fracture criteria

The fracture criteria are used to predict the condition for stable or unstable crack growth. This section presents theoretical formulations of selected mixed mode (I/II) fracture criteria which are used to verify the present experimental results.

3.2.1 Maximum tangential stress (MTS) criterion

According to the MTS criterion [17], a crack under mixed mode (I/II) loading grows in the direction normal to the maximum tangential stress $\sigma_{\theta\theta\max}$, and the brittle fracture initiates when this maximum tangential stress reaches a critical value. This criterion considers only the leading terms (K_{I} and K_{II}) of the tangential stress $\sigma_{\theta\theta}$ in Eq. (3.1). The maximum of tangential stress can be determined by satisfying the following relations: $\partial\sigma_{\theta\theta}/\partial\theta = 0$ and $\partial^2\sigma_{\theta\theta}/\partial\theta^2 < 0$. Accordingly, the crack kink angle θ_0 can be determined from Eq. (3.2).

$$\begin{aligned}
\theta_0 &= 2\tan^{-1}\left[\frac{1}{4}\frac{K_{\mathrm{I}}}{K_{\mathrm{II}}} - \frac{1}{4}\sqrt{\left(\frac{K_{\mathrm{I}}}{K_{\mathrm{II}}}\right)^2 + 8}\,\right] \quad \text{for} \quad K_{\mathrm{II}} > 0 \\
\theta_0 &= 2\tan^{-1}\left[\frac{1}{4}\frac{K_{\mathrm{I}}}{K_{\mathrm{II}}} + \frac{1}{4}\sqrt{\left(\frac{K_{\mathrm{I}}}{K_{\mathrm{II}}}\right)^2 + 8}\,\right] \quad \text{for} \quad K_{\mathrm{II}} < 0
\end{aligned} \tag{3.2}$$

where positive θ_0 is defined as the angle measured in the anticlockwise direction with respect to the initial crack orientation (Fig. 3.1). This angle θ_0 can then be used to calculate the onset of mixed mode (I/II) fracture as $\sigma_{\theta\theta}(\theta_0) = \sigma_{\theta\theta C}$, which yields,

$$\sqrt{2\pi r}\,\sigma_{\theta\theta C} = K_{\mathrm{Ic}} = \cos\frac{\theta_0}{2}\left[K_{\mathrm{I}}\cos^2\frac{\theta_0}{2} - \frac{3}{2}K_{\mathrm{II}}\sin\theta_0\right] \tag{3.3}$$

The fracture locus (fracture limit curve) for the MTS criterion can be written as:

$$\begin{aligned}
\frac{K_{\mathrm{I}}}{K_{\mathrm{Ic}}} &= \left[\cos\frac{\theta_0}{2}\left(\cos^2\frac{\theta_0}{2} - \frac{3}{2}\frac{K_{\mathrm{II}}}{K_{\mathrm{I}}}\sin\theta_0\right)\right]^{-1} \\
\frac{K_{\mathrm{II}}}{K_{\mathrm{Ic}}} &= \left[\cos\frac{\theta_0}{2}\left(\frac{K_{\mathrm{I}}}{K_{\mathrm{II}}}\cos^2\frac{\theta_0}{2} - \frac{3}{2}\sin\theta_0\right)\right]^{-1}
\end{aligned} \tag{3.4}$$

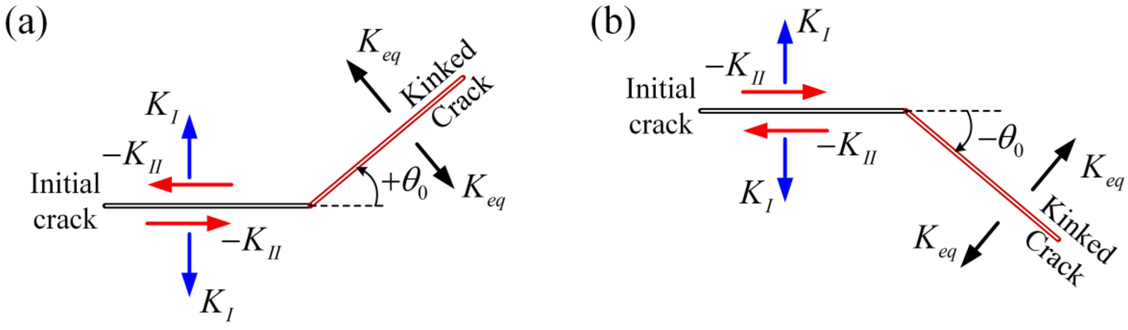

Fig. 3.1 Direction of K_{II} and the crack kink angle. (a) Positive θ_0. (b) Negative θ_0.

3.2.2 Generalized maximum tangential stress (GMTS) criterion

The GMTS criterion is the modified MTS criterion wherein the effect of both the SIFs (K_{I} and K_{II}) and the $T-$stresses near the crack tip is considered [50]. According to this criterion, the crack kink angle θ_0 can be predicted as

$$\left.\frac{\partial\sigma_{\theta\theta}}{\partial\theta}\right|_{\theta=\theta_0}=0\Rightarrow\left[K_{\mathrm{I}}\sin\theta_0+K_{\mathrm{II}}(3\cos\theta_0-1)\right]-\frac{16T\sqrt{2\pi r_{\mathrm{c}}}}{3}\sin\frac{\theta_0}{2}\cos\theta_0=0 \tag{3.5}$$

The angle θ_0 calculated from Eq. (3.5) can then be used to calculate the onset of mixed mode (I/II) fracture as $\sigma_{\theta\theta}\left(r_{\mathrm{c}},\theta_0\right)=\sigma_{\theta\theta\mathrm{c}}$, which yields,

$$\sqrt{2\pi r_c}\,\sigma_{\theta\theta C}=K_{\mathrm{Ic}}=\cos\frac{\theta_0}{2}\left[K_{\mathrm{I}}\cos^2\frac{\theta_0}{2}-\frac{3}{2}K_{\mathrm{II}}\sin\theta_0+\sqrt{2\pi r_{\mathrm{c}}}T\sin^2\theta_0\right] \tag{3.6}$$

The mixed mode (I/II) fracture locus of the GMTS criterion can be written as

$$\begin{aligned}\frac{K_{\mathrm{I}}}{K_{\mathrm{Ic}}}&=\left[\cos\frac{\theta_0}{2}\left(\cos^2\frac{\theta_0}{2}-\frac{3}{2}\frac{K_{\mathrm{II}}}{K_{\mathrm{I}}}\sin\theta_0\right)+\sqrt{2\pi r_{\mathrm{c}}}\sin^2\theta_0\frac{T}{K_{\mathrm{I}}}\right]^{-1}\\\frac{K_{\mathrm{II}}}{K_{\mathrm{Ic}}}&=\left[\cos\frac{\theta_0}{2}\left(\frac{K_{\mathrm{I}}}{K_{\mathrm{II}}}\cos^2\frac{\theta_0}{2}-\frac{3}{2}\sin\theta_0\right)+\sqrt{2\pi r_{\mathrm{c}}}\sin^2\theta_0\frac{T}{K_{\mathrm{II}}}\right]^{-1}\end{aligned} \tag{3.7}$$

here r_{c} may be considered as the length of the localized damage zone for a material [25]. For accurate prediction of the fracture load and crack kink angle, using the GMTS criterion requires an appropriate value of r_{c}. It is to be noted here that if the $T-$stress term is ignored in Eqs. (3.5) to (3.7), the GMTS criterion simplifies to the classical MTS criterion.

3.2.3 Maximum energy release rate criterion (*G*-criterion)

According to the maximum energy release rate criterion [18], the crack under mixed mode (I/II) loading propagates in the direction along which the strain energy release rate $G(\theta)$ is maximum, and the crack will propagate when this maximum energy release rate reaches a critical value. The energy release rate for a crack under mixed mode (I/II) loading for any given angular coordinate θ can be calculated [18] as

$$G(\theta)=\frac{4}{E}\left(\frac{1}{3+\cos^2\theta}\right)^2\left(\frac{1-\dfrac{\theta}{\pi}}{1+\dfrac{\theta}{\pi}}\right)^{\theta/\pi}\left\{\begin{array}{c}\left(1+3\cos^2\theta\right)K_{\mathrm{I}}^2+8\sin\theta\cos\theta\,K_{\mathrm{I}}K_{\mathrm{II}}\\ +\left(9-5\cos^2\theta\right)K_{\mathrm{II}}^2\end{array}\right\} \tag{3.8}$$

where θ is in radians. In this criterion, the strain energy release rate, $G(\theta)$ is computed under mixed mode (I/II) loading for a series of angular coordinates θ and found the crack initiation angle θ_0 corresponding to the maximum value of the $G(\theta)$. The fracture load for a given mode mixity can also be calculated using Eq. (3.8) by equating $G(\theta_0)$ to the critical energy release rate G_{c} which is given for plane stress conditions as

$$G_{\mathrm{c}}=\frac{K_{\mathrm{Ic}}^2}{E} \tag{3.9}$$

The mixed mode (I/II) fracture locus for $G-$criterion can be written as

$$\begin{aligned}\frac{K_{\mathrm{I}}}{K_{\mathrm{Ic}}}&=\left[\left(\frac{2}{3+\cos^2\theta_0}\right)^2\left(\frac{1-\dfrac{\theta_0}{\pi}}{1+\dfrac{\theta_0}{\pi}}\right)^{\theta_0/\pi}\left(\begin{array}{c}\left(1+3\cos^2\theta_0\right)+\left(8\sin\theta_0\cos\theta_0\right)\dfrac{K_{\mathrm{II}}}{K_{\mathrm{I}}}\\ +\left(9-5\cos^2\theta_0\right)\left(\dfrac{K_{\mathrm{II}}}{K_{\mathrm{I}}}\right)^2\end{array}\right)\right]^{-1/2}\\ \frac{K_{\mathrm{II}}}{K_{\mathrm{Ic}}}&=\left[\left(\frac{2}{3+\cos^2\theta_0}\right)^2\left(\frac{1-\dfrac{\theta_0}{\pi}}{1+\dfrac{\theta_0}{\pi}}\right)^{\theta_0/\pi}\left(\begin{array}{c}\left(1+3\cos^2\theta_0\right)\left(\dfrac{K_{\mathrm{I}}}{K_{\mathrm{II}}}\right)^2+\left(8\sin\theta_0\cos\theta_0\right)\dfrac{K_{\mathrm{I}}}{K_{\mathrm{II}}}\\ +\left(9-5\cos^2\theta_0\right)\end{array}\right)\right]^{-1/2}\end{aligned} \tag{3.10}$$

3.2.4 *M*-criterion

This criterion postulates that the crack would grow in the direction along which the triaxial stress factor, M as given by Eq. (3.11) reaches a maximum value along a circular contour around the crack tip [56].

$$M=\frac{\sigma_{kk}}{3\sigma_e}=\frac{F_1}{F_2} \tag{3.11}$$

$$F_1 = 2\sqrt{2}\left(1+\nu\right)\left\{K_{\mathrm{I}}\cos\frac{\theta}{2} - K_{\mathrm{II}}\sin\frac{\theta}{2}\right\}$$

$$F_2 = 3\left\{\begin{array}{c}\left(\frac{3}{2}K_{\mathrm{I}}^2 - \frac{9}{2}K_{\mathrm{II}}^2\right)\sin^2\theta + \left[2K_{\mathrm{I}}^2\left(1-2\nu\right)^2 + 6K_{\mathrm{II}}^2\right]\cos^2\frac{\theta}{2} \\ +8K_{\mathrm{II}}^2\left(1-\nu+\nu^2\right)\sin^2\frac{\theta}{2} + K_{\mathrm{I}}K_{\mathrm{II}}\left[3\sin 2\theta - 2\left(1-2\nu\right)^2\sin\theta\right] + 6K_{\mathrm{III}}^2\end{array}\right\}^{1/2} \tag{3.12}$$

where $\sigma_{kk} = \sigma_{rr} + \sigma_{\theta\theta} + \sigma_{zz}$ is the normal stresses and σ_e is the equivalent stress. According to this criterion, the crack growth direction can be predicted as [56]

$$\begin{array}{l}\tan^4\frac{\theta_0}{2} - 3\frac{K_{\mathrm{I}}}{K_{\mathrm{II}}}\tan^3\frac{\theta_0}{2} - \left\{1-2\left(\frac{K_{\mathrm{I}}}{K_{\mathrm{II}}}\right)^2\right\}\tan^2\frac{\theta_0}{2} \\ +\frac{1}{2}\left\{1-\left(\frac{K_{\mathrm{I}}}{K_{\mathrm{II}}}\right)^2\right\}\frac{K_{\mathrm{I}}}{K_{\mathrm{II}}}\tan\frac{\theta_0}{2} - \frac{1+(K_{\mathrm{I}}/K_{\mathrm{II}})^2}{2} = 0\end{array} \tag{3.13}$$

To the author's knowledge, this criterion is only available to predict the crack kink angle but not the fracture loads.

3.2.5 Average strain energy density (ASED) criterion

According to the ASED criterion [49,216], for a crack under mixed Mode (I/II) loading, brittle failure occurs when the strain energy density averaged $\left(\overline{W}\right)$ over a circular control volume (defined by radius R_{c}) reaches a critical value of W_{c} . These are given by

$$\overline{W} = \frac{e_1}{E}\times\frac{K_{\mathrm{I}}^2}{R_{\mathrm{c}}} + \frac{e_2}{E}\times\frac{K_{\mathrm{II}}^2}{R_{\mathrm{c}}} \quad \text{and} \quad W_{\mathrm{c}} = \frac{\sigma_u^2}{2E} \tag{3.14}$$

For the specific case of the plane stress crack problems and for the Poisson's ratio of $\nu = 0.38$ $e_1 = 0.1536$, $e_2 = 0.373$ [80] and the value of R_c is given by

$$R_{\mathrm{c}} = 0.307\left(\frac{K_{\mathrm{Ic}}}{\sigma_u}\right)^2 \tag{3.15}$$

where σ_u is the ultimate strength of the material. According to this criterion, the mixed mode fracture locus can be obtained as

$$\frac{K_{\mathrm{I}}}{K_{\mathrm{Ic}}}=\left[1+2.43\left(\frac{K_{\mathrm{II}}}{K_{\mathrm{I}}}\right)^{2}\right]^{-1/2}$$
$$\frac{K_{\mathrm{II}}}{K_{\mathrm{Ic}}}=\left[\left(\frac{K_{\mathrm{I}}}{K_{\mathrm{II}}}\right)^{2}+2.43\right]^{-1/2} \tag{3.16}$$

To the author's knowledge, this criterion predicts only the fracture load and is not formulated for the prediction of the crack initiation angle.

3.3 Mixed mode (I/II/III) fracture criteria

The complete solution to the problem of mixed mode (I/II/III) loading involves the accurate prediction of unstable fracture load P_{cr}, the crack kink angle θ_0, and the crack twist angle (ψ_0). Among various existing mixed mode (I/II/III) fracture criteria, only those criteria which consider the effect of mode III loading in the calculation of the crack twist angles ψ_0 and fracture loads are presented in this subsection. It should be noted that these criteria are frequently used for mixed mode (I/III) loading.

3.3.1 Maximum principal stress (MPS) criterion

Schollman et al. [20] proposed the MPS criterion, which states that a crack under mixed mode (I/II/III) loading propagates in a direction perpendicular to the maximum principal stress σ_1' , which depends on the stress components $\sigma_{\theta\theta}$, σ_{zz}, $\tau_{\theta z}$. The maximum principal stress can be written as:

$$\sigma_1'=\frac{\sigma_\theta+\sigma_z}{2}+\sqrt{\left(\sigma_\theta-\sigma_z\right)^2+4\tau_{\theta z}^2} \tag{3.17}$$

For plane stress conditions, $\sigma_{zz}=0$, putting the expressions of $\sigma_{\theta\theta}$ and $\tau_{\theta z}$ from Eq. (3.1) , the maximum principal stress σ_1' can be written as

$$\begin{aligned}\sigma_1'=\frac{1}{8\sqrt{2\pi r}}\Bigg\{&K_{\mathrm{I}}\left(3\cos\frac{\theta}{2}+\cos\frac{3\theta}{2}\right)-K_{\mathrm{II}}\left(3\sin\frac{\theta}{2}+3\sin\frac{3\theta}{2}\right)\\&+\Bigg[\left[K_{\mathrm{I}}\left(3\cos\frac{\theta}{2}+\cos\frac{3\theta}{2}\right)-K_{\mathrm{II}}\left(3\sin\frac{\theta}{2}+3\sin\frac{3\theta}{2}\right)\right]^2\\&+64K_{\mathrm{III}}^2\cos^2\frac{\theta}{2}\Bigg]^{1/2}\Bigg\}\end{aligned} \tag{3.18}$$

The crack kink angle θ_0, can be calculated by setting: $\partial\sigma_1'/\partial\theta\big|_{\theta=\theta_0}=0$ and $\partial^2\sigma_1'/\partial\theta^2\big|_{\theta=\theta_0}<0$, which yields

$$\begin{aligned}&-6K_{\mathrm{I}}\tan\frac{\theta_0}{2}-K_{\mathrm{II}}\left(6-12\tan^2\frac{\theta_0}{2}\right)+\left\{\left[4K_{\mathrm{I}}-12K_{\mathrm{II}}\tan\frac{\theta_0}{2}\right]\right.\\&\left[-6K_{\mathrm{I}}\tan\frac{\theta_0}{2}-K_{\mathrm{II}}\left(6-12\tan^2\frac{\theta_0}{2}\right)\right]\\&\left.-32K_{\mathrm{III}}^2\tan\frac{\theta_0}{2}.\left(1+\tan^2\frac{\theta_0}{2}\right)^2\right\}\\&.\left\{\left[4K_{\mathrm{I}}-12K_{\mathrm{II}}\tan\frac{\theta_0}{2}\right]^2+64K_{\mathrm{III}}^2\left(1+\tan^2\frac{\theta_0}{2}\right)^2\right\}^{-1/2}\end{aligned}\qquad(3.19)$$

And the crack twist ψ_0 angle can be determined by Eq. (3.20)

$$\psi_0=\frac{1}{2}\tan^{-1}\left(\frac{2\tau_{\theta z}}{\sigma_{\theta\theta}-\sigma_{zz}}\right)\Bigg|_{\theta=\theta_0}\qquad(3.20)$$

According to the MPS criterion, the three-dimensional fracture surface can be written as

$$\begin{aligned}&\frac{1}{8}\left\{\frac{K_{\mathrm{If}}}{K_{\mathrm{Ic}}}\left(3\cos\frac{\theta_0}{2}+\cos\frac{3\theta_0}{2}\right)-\frac{K_{\mathrm{IIf}}}{K_{\mathrm{Ic}}}\left(3\sin\frac{\theta_0}{2}+3\sin\frac{3\theta_0}{2}\right)\right.\\&\left.+\left[\left[\frac{K_{\mathrm{If}}}{K_{\mathrm{Ic}}}\left(3\cos\frac{\theta_0}{2}+\cos\frac{3\theta_0}{2}\right)-\frac{K_{\mathrm{IIf}}}{K_{\mathrm{Ic}}}\left(3\sin\frac{\theta_0}{2}+3\sin\frac{3\theta_0}{2}\right)\right]^2+64\frac{K_{\mathrm{III}}^2}{K_{\mathrm{Ic}}^2}\cos^2\frac{\theta_0}{2}\right]^{1/2}\right\}=1\end{aligned}\qquad(3.21)$$

From Eq. (3.21), the comparative SIF K_{v} can be defined as

$$K_{\mathrm{v}}=\frac{1}{2}\cos\frac{\theta_0}{2}\left\{K_{\mathrm{I}}\cos^2\frac{\theta_0}{2}-\frac{3}{2}K_{\mathrm{II}}\sin\theta_0+\sqrt{\left[K_{\mathrm{I}}\cos^2\frac{\theta_0}{2}-\frac{3}{2}K_{\mathrm{II}}\sin\theta_0\right]^2+4K_{\mathrm{III}}^2}\right\}\qquad(3.22)$$

For the special case of mixed mode (I/III) loading conditions, i.e., $K_{\mathrm{II}}=0,\theta_0=0$, the crack twist angle ψ_0 can be obtained as

$$\psi_0=\begin{cases}\dfrac{1}{2}\tan^{-1}\left(\dfrac{2K_{\mathrm{IIIf}}}{K_{\mathrm{If}}}\right) & ;\text{plane stress}\\[2ex]\dfrac{1}{2}\tan^{-1}\left(\dfrac{2K_{\mathrm{IIIf}}}{K_{\mathrm{If}}(1-2\nu)}\right) & ;\text{plane strain}\end{cases}\qquad(3.23)$$

Following the procedure of [25], the fracture locus for the case of mixed mode (I/III) can be derived as

$$\begin{aligned}
\frac{K_{\mathrm{If}}}{K_{\mathrm{Ic}}}&=\left[\frac{1}{2}+\frac{1}{2}\sqrt{1+\left(2\frac{K_{\mathrm{IIIf}}}{K_{\mathrm{If}}}\right)^{2}}\right]^{-1}\\
\frac{K_{\mathrm{IIIf}}}{K_{\mathrm{Ic}}}&=\left[\frac{K_{I}}{2K_{\mathrm{III}}}+\frac{1}{2}\sqrt{\left(\frac{K_{\mathrm{If}}}{K_{\mathrm{IIIf}}}\right)^{2}+4}\right]^{-1}
\end{aligned}\tag{3.24}$$

3.3.2 Maximum mean principal stress (MMPS) criterion

Wang et al. [23] proposed that fracture occurs when the characteristic fracture length L_{fr} parameter given in Eq. (3.25) reaches its critical value.

$$\begin{aligned}
L_{fr}\left(\theta_0\right)=\frac{2}{\pi\sigma_t^2}\Bigg\{&\frac{1}{4}K_{\mathrm{I}}\cos\frac{\theta_0}{2}\left(1+\cos\theta_0+4\nu\right)-\frac{3}{4}K_{\mathrm{II}}\sin\frac{\theta_0}{2}\left[1+2\nu+\left(1-2\nu\right)\cos\theta_0\right]\\
&+\Bigg[\left\{\frac{1}{4}K_{\mathrm{I}}\cos\frac{\theta_0}{2}\left(1+\cos\theta_0-4\nu\right)-\frac{3}{4}K_{\mathrm{II}}\sin\frac{\theta_0}{2}\left[1-2\nu+\left(1+2\nu\right)\cos\theta_0\right]\right\}^2\\
&+\left(K_{\mathrm{III}}\cos\frac{\theta_0}{2}\right)^2\Bigg]^{1/2}\Bigg\}^2
\end{aligned}\tag{3.25}$$

where, σ_t is the tensile strength of the material. According to the MMPS criterion, the crack kink angle θ_0 can be calculated by Eq. (3.26)

$$\theta_0=K_{2n}\left(81.4^\circ k_{1n}-77.2^\circ k_{1n}k_{2n}+275.5^\circ k_{2n}-107.5^\circ k_{2n}^2-238.5^\circ\right)\tag{3.26}$$

where, $k_{1n}+k_{2n}+k_{3n}=1$ and

$$k_{1n}=\frac{K_{\mathrm{I}}}{K_{\mathrm{I}}+\left|K_{\mathrm{II}}\right|+\left|K_{\mathrm{III}}\right|};\quad k_{2n}=\frac{\left|K_{\mathrm{II}}\right|}{K_{\mathrm{I}}+\left|K_{\mathrm{II}}\right|+\left|K_{\mathrm{III}}\right|};\quad k_{3n}=\frac{\left|K_{\mathrm{III}}\right|}{K_{\mathrm{I}}+\left|K_{\mathrm{II}}\right|+\left|K_{\mathrm{III}}\right|}\tag{3.27}$$

Similarly, the crack twist angle ψ_0 can be calculated by Eq. (3.28)

$$\psi_o=\frac{1}{2}\tan^{-1}\left(\frac{4K_{\mathrm{III}}}{K_{\mathrm{I}}\left(1-4\nu+\cos\theta_o\right)-K_{\mathrm{II}}\left(3-4\nu+\cos\theta_o\right)\tan\left(\theta_o/2\right)}\right)\tag{3.28}$$

Theoretically, the twist angle ψ_o varies between 0° and 45°. For the special case of mixed mode (I/III) loading, i.e., $K_{\mathrm{II}}=0,\theta_0=0$, the crack twist angle ψ_0 can be written as

$$\psi_0 = \frac{1}{2}\tan^{-1}\left(\frac{2K_{\mathrm{III}}}{K_{\mathrm{I}}(1-2\nu)}\right) \tag{3.29}$$

And the fracture locus can be written as

$$\begin{aligned} \frac{K_{\mathrm{I}}}{K_{\mathrm{Ic}}} &= \frac{\sqrt{\left(1+f_{\mathrm{III,I}}\dfrac{K_{\mathrm{III}}}{K_{\mathrm{I}}}\right)\Big/\left(1+f_{\mathrm{III,I}}^{-1}\dfrac{K_{\mathrm{III}}}{K_{\mathrm{I}}}\right)}}{(0.5+\nu)+0.25\sqrt{(2-4\nu)^2+16\left(\dfrac{K_{\mathrm{III}}}{K_{\mathrm{I}}}\right)^2}} \\ \frac{K_{\mathrm{III}}}{K_{\mathrm{Ic}}} &= \frac{\sqrt{\left(\dfrac{K_{\mathrm{I}}}{K_{\mathrm{III}}}+f_{\mathrm{III,I}}\right)\Big/\left(\dfrac{K_{\mathrm{I}}}{K_{\mathrm{III}}}+f_{\mathrm{III,I}}^{-1}\right)}}{\dfrac{K_{\mathrm{I}}}{K_{\mathrm{III}}}(0.5+\nu)+0.25\sqrt{\left(\dfrac{K_{\mathrm{I}}}{K_{\mathrm{III}}}(2-4\nu)\right)^2+16}} \end{aligned} \tag{3.30}$$

where $f_{\mathrm{III,I}} = K_{\mathrm{IIIc}} / K_{\mathrm{Ic}}$.

3.3.3 Richard's criterion

Richard et al. [19] proposed that a crack under mixed mode (I/II/III) loading propagates suddenly if the comparative SIF K_{v}, reaches the critical value K_{Ic}.

$$K_{\mathrm{v}} = \frac{K_{\mathrm{If}}}{2}+\frac{1}{2}\sqrt{K_{\mathrm{If}}^2+4(\zeta_1 K_{\mathrm{IIf}})^2+4(\zeta_2 K_{\mathrm{IIIf}})^2} = K_{\mathrm{Ic}} \tag{3.31}$$

where $\zeta_1 = K_{\mathrm{Ic}} / K_{\mathrm{IIc}}$ and $\zeta_2 = K_{\mathrm{Ic}} / K_{\mathrm{IIIc}}$. It has been found that Eq. (3.31) conforms with the mixed mode (I/II/III) experiments for $\zeta_1 = 1.155$ and $\zeta_2 = 1.0$ [133]. Due to the complexity involved in analytical solutions, Richard et al. [19] proposed an empirical relation to predict the crack kink angle θ_o and twist angle ψ_o for the mixed mode (I/II/III) loading conditions as given in Eqs. (3.32) and (3.33), respectively.

$$\theta_0 = \mp\left[140^\circ\frac{|K_{\mathrm{II}}|}{K_{\mathrm{I}}+|K_{\mathrm{II}}|+|K_{\mathrm{III}}|}-70^\circ\left(\frac{|K_{\mathrm{II}}|}{K_{\mathrm{I}}+|K_{\mathrm{II}}|+|K_{\mathrm{III}}|}\right)^2\right] \tag{3.32}$$

where $\theta_o < 0^\circ$ for $K_{\mathrm{II}} > 0$ and $\theta_o > 0^\circ$ for $K_{\mathrm{II}} < 0$.

$$\psi_o = \mp\left[78^\circ\frac{|K_{\mathrm{III}}|}{K_{\mathrm{I}}+|K_{\mathrm{II}}|+|K_{\mathrm{III}}|}-33^\circ\left(\frac{|K_{\mathrm{III}}|}{K_{\mathrm{I}}+|K_{\mathrm{II}}|+|K_{\mathrm{III}}|}\right)^2\right] \tag{3.33}$$

where $\psi_o < 0°$ for $K_{\mathrm{III}} > 0$ and $\psi_o > 0°$ for $K_{\mathrm{III}} < 0$. It should be noted here that Richard criterion fits very well with the prediction of the MPS criterion. For the special case of mixed mode (I/III) loading conditions, i.e., $K_{\mathrm{II}} = 0, \theta_0 = 0$, the fracture locus of Richard's criterion can be expressed as

$$\frac{K_{\mathrm{I}}}{K_{\mathrm{Ic}}} = \left[0.5 + 0.5\sqrt{1 + 4\left(\zeta_2 \frac{K_{\mathrm{III}}}{K_{\mathrm{I}}}\right)^2}\right]^{-1}$$
$$\frac{K_{\mathrm{III}}}{K_{\mathrm{Ic}}} = \left[0.5\frac{K_{\mathrm{I}}}{K_{\mathrm{III}}} + 0.5\sqrt{\left(\frac{K_{\mathrm{III}}}{K_{\mathrm{I}}}\right)^2 + 4\left(\zeta_2\right)^2}\right]^{-1} \tag{3.34}$$

According to this criterion, the crack twist angle ψ_o for the mixed mode (I/III) is given by the empirical formula Eq. (3.35).

$$\psi_o = \mp\left[78°\frac{|K_{\mathrm{III}}|}{K_{\mathrm{I}} + |K_{\mathrm{III}}|} - 33°\left(\frac{|K_{\mathrm{III}}|}{K_{\mathrm{I}} + |K_{\mathrm{III}}|}\right)^2\right] \tag{3.35}$$

where $\psi_o < 0°$ for $K_{\mathrm{III}} > 0$ and $\psi_o > 0°$ for $K_{\mathrm{III}} < 0$.

3.4 Prediction of mixed mode (I/II) fatigue life

This section describes the formulation of a new GMTS-based ΔK_{eq} model to be used for the mixed mode (I/II) fatigue crack growth studies. Further, it also presents all ΔK_{eq} models employed in the present investigation. The algorithm for mixed mode FCG simulations for fatigue life prediction is also explained in detail.

3.4.1 GMTS-based equivalent SIF (ΔK_{eq}) model

GMTS based ΔK_{eq} has been proposed for the first time here. As previously explained in subsection 3.2.2, according to the GMTS criterion, the onset of unstable fracture can be calculated by Eq. (3.36). (Note: Eq. (3.36) is same as Eq. (3.6))

$$K_{\mathrm{Ic}} = \cos\frac{\theta_0}{2}\left[K_{\mathrm{I}}\cos^2\frac{\theta_0}{2} - \frac{3}{2}K_{\mathrm{II}}\sin\theta_0 + \sqrt{2\pi r_{\mathrm{c}}}T\sin^2\theta_0\right] \tag{3.36}$$

According to the GMTS criterion as given in above Eq. (3.36), a new ΔK_{eq} model can be formulated as given below Eq. (3.37).

$$\Delta K_{\mathrm{eq}} = \cos\left(\frac{\theta_0}{2}\right)\left[\Delta K_{\mathrm{I}} \cos^2\left(\frac{\theta_0}{2}\right) - \frac{3}{2}\Delta K_{\mathrm{II}} \sin\left(\theta_0\right)\right] + \sqrt{2\pi r_{\mathrm{c}}}\,\Delta T \sin^2\left(\theta_0\right) \tag{3.37}$$

where $\Delta T = T_{\max} - T_{\min}$. In the present work, the authors have attempted, for the first time, to verify the applicability of the GMTS-based ΔK_{eq} model for the mixed mode (I/II) FCG studies. It is to be noted here that the value of r_{c} depends upon the material.

3.4.2 Equivalent SIF ΔK_{eq} models

The theoretical background of various available ΔK_{eq} models has already been explained in previous chapter (Section 2.3, Page 28). But for the sake of completeness and easy reference, the expression for selected ΔK_{eq} are again presented here in Table 3.1.

Table 3.1 List of selected ΔK_{eq} models used in the present work.

Model	Expression
Tanaka 1	$\Delta K_{\mathrm{eq}} = \left(\Delta K_{\mathrm{I}}^2 + 2\Delta K_{\mathrm{II}}^2\right)^{1/2}$
Tanaka 2	$\Delta K_{\mathrm{eq}} = \left(\Delta K_{\mathrm{I}}^4 + 8\Delta K_{\mathrm{II}}^4\right)^{1/4}$
Yan	$\Delta K_{\mathrm{eq}} = \frac{1}{2}\cos\frac{\theta_0}{2}\left[\Delta K_{\mathrm{I}}\left(1+\cos\theta_0\right) - 3\Delta K_{\mathrm{II}}\sin\theta_0\right]$
Hussain	$\Delta K_{\mathrm{eq}} = \sqrt{\frac{4}{\left(3+\cos^2\theta_0\right)^2}\left(\frac{1-\frac{\theta_0}{\pi}}{1+\frac{\theta_0}{\pi}}\right)^{\frac{\theta_0}{\pi}}\left\{\begin{array}{r}\left(1+3\cos^2\theta_0\right)\Delta K_{\mathrm{I}}^2 + 8\sin\theta_0\cos\theta_0\Delta K_{\mathrm{I}}\Delta K_{\mathrm{II}}\\ +\left(9-5\cos^2\theta_0\right)\Delta K_{\mathrm{II}}^2\end{array}\right\}}$
Irwin	$\Delta K_{\mathrm{eq}} = \sqrt{\Delta K_{\mathrm{I}}^2 + \Delta K_{\mathrm{II}}^2}$
Richard	$\Delta K_{\mathrm{eq}} = \frac{\Delta K_{\mathrm{I}}}{2} + \sqrt{\Delta K_{\mathrm{I}}^2 + 5.3361\Delta K_{\mathrm{II}}^2}$
Demir	$\Delta K_{\mathrm{eq}} = \left[1.0519\Delta K_{\mathrm{I}}^4 - 0.035\Delta K_{\mathrm{II}}^4 + 2.3056\Delta K_{\mathrm{I}}^2\Delta K_{\mathrm{II}}^2\right]^{0.25}$
GMTS (present)	$\Delta K_{\mathrm{eq}} = \cos\left(\frac{\theta_0}{2}\right)\left[\Delta K_{\mathrm{I}}\cos^2\left(\frac{\theta_0}{2}\right) - \frac{3}{2}\Delta K_{\mathrm{II}}\sin\left(\theta_0\right)\right] + \sqrt{2\pi r_{\mathrm{c}}}\,\Delta T\sin^2\left(\theta_0\right)$

3.4.3 Fatigue life simulation

Fig. 3.2 shows the threshold, stable and unstable regions in a typical mixed mode (I/II) fracture limit curve. It has been experimentally observed that the crack initiation happens under fatigue loading only if the equivalent SIF ΔK_{eq} exceeds the fatigue threshold K_{th} value of the material [19,217], i.e., $\Delta K_{\text{eq}} \geq K_{\text{I,th}}$, and the crack grows unstably when the maximum equivalent SIF ΔK_{eq} exceeds the fracture toughness K_{Ic} of the material, i.e., $K_{\text{eq}-\max} \geq K_{\text{Ic}}$.

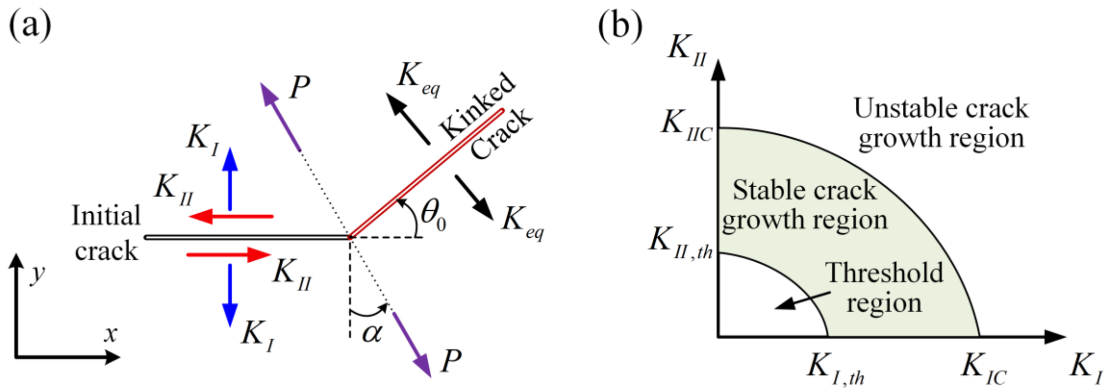

Fig. 3.2 (a) ΔK_{eq} as a function of K_{I} and K_{II}. (b) Fracture limit curve under mixed mode (I/II) loading.

The number of load cycles required to increase the existing crack length a_i to the next crack length a_{i+1} by a finite increment Δa, can be estimated by integrating the modified Paris law (Eq. (2.2)) as

$$\int_0^{\Delta a} \frac{da}{C\left(\Delta K_{\text{eq}}\right)^m} = \int_0^{\Delta N} dN = \Delta N \tag{3.38}$$

Assuming that the crack growth occurs discretely and the crack increment $\Delta a_i \, (= a_{i+1} - a_i)$ is very small, the associated number of load cycles ΔN for this crack increment can be estimated from Eq. (3.38) for the i^{th} step of crack growth as

$$\frac{\Delta a_i}{C\left(\Delta K_{\text{eq}}^i\right)^m} = \Delta N_i \tag{3.39}$$

In the present work, the residual fatigue life ΔN for a crack increment Δa is calculated numerically by the incremental crack extension method [29] using Eq. (3.39). In this approach, a pre-defined crack increment value (Δa) is used to calculate the residual fatigue life (ΔN) of a cracked component. Fig. 3.3 illustrates the flow diagram of various steps involved in the incremental crack growth approach for predicting fatigue life.

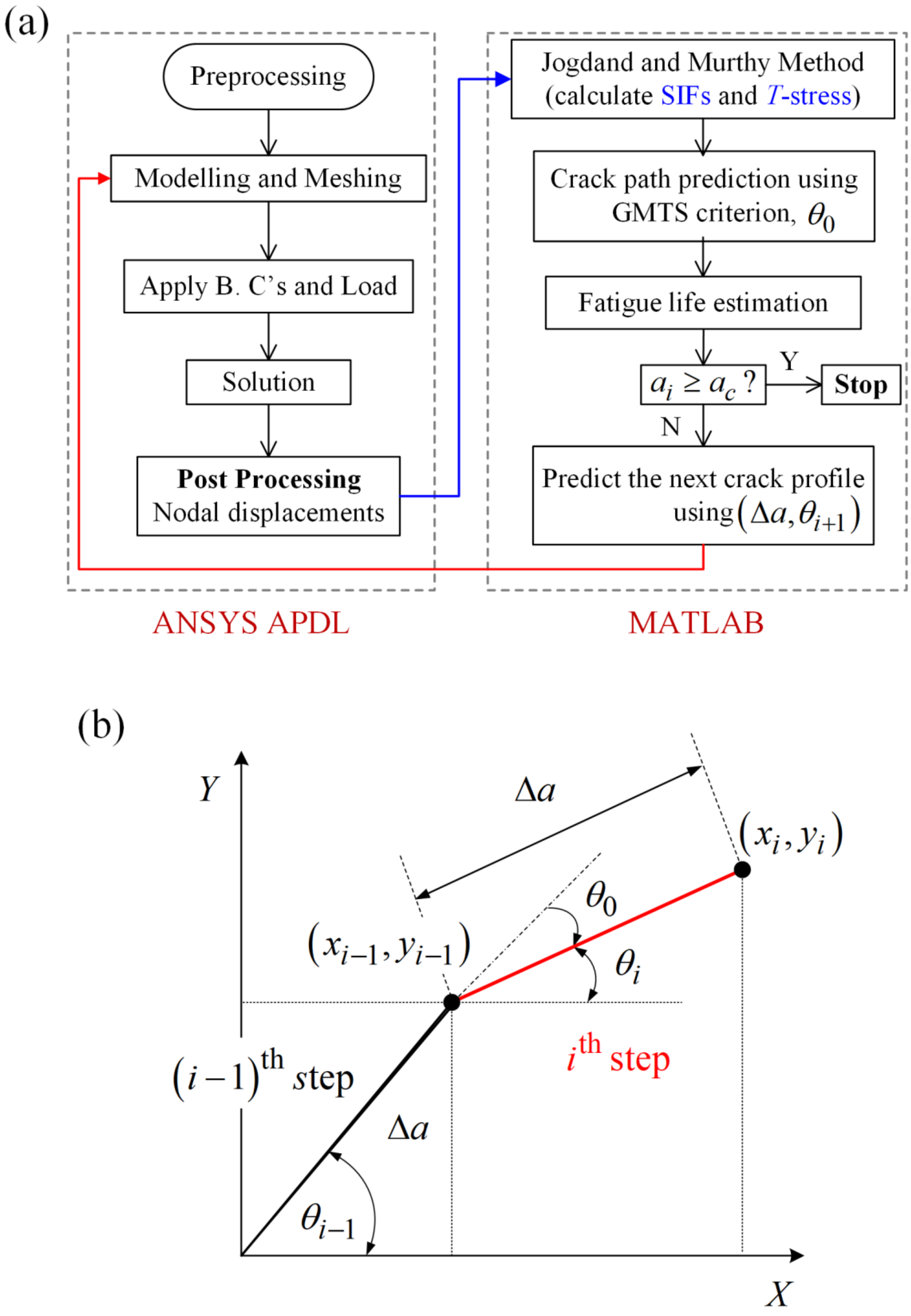

Fig. 3.3 Incremental crack growth approach adopted for the FCG simulation.

The details of each step involved during crack growth simulations using the incremental crack extension method are explained below.

Step 1. First, the initial crack configuration is modeled, and the FE mesh is created in the ANSYS APDL®.

Step 2. Using the appropriate boundary conditions, the FE model of the cracked component is solved, and crack flank nodal displacements are extracted.

Step 3. Then the SIFs (K_I and K_II) and $T-$stress are calculated in MATLAB® using the interior collocation technique proposed by Jogdand and Murthy [218].

Step 4. Using a suitable fracture criterion, the crack kink angle θ_0 is calculated. The present investigation uses the GMTS criterion to determine the crack path.

Step 5. By assuming a suitable crack increment Δa size, the fatigue life ΔN is calculated using Eq. (3.39).

Step 6. Then the existing crack tip is extended to the new location $(\Delta a, \theta_0)$ (Fig. 3.3b)

Step 7. Finally, a new mesh is generated for the updated crack configuration.

Step 8. Repeat Step 2 to Step 7 until the current crack length a_i reaches the critical crack length a_c.

3.5 Finite element formulation

This section focuses on the brief details of two different types of elements that are used for finite element modeling in the present investigation. First, details of the 8-noded isoparametric plane element for 2D modeling are explained. Subsequently, details of the 20-noded isoparametric element for 3D modeling are presented.

3.5.1 Eight noded quadrilateral element (PLANE183 element)

The eight-noded isoparametric quadrilateral elements (Q8) allow the modeling of complicated geometries, and generally, this element is also employed to solve fracture mechanics problems. The general shape of the Q8 element is shown in Fig. 3.4. This element is called PLANE183 element in ANSYS®. The advantage of an isoparametric formulation is that the geometric variables and the dependent field variables are approximated using the same order shape functions.

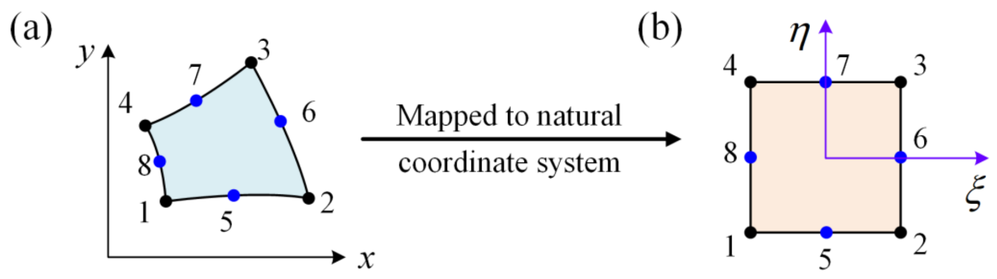

Fig. 3.4 Eight-noded quadrilateral element represented in natural coordinates.

The shape functions for a Q8 element can be expressed in the natural coordinates as

$$\begin{aligned}
N_1 &= \frac{1}{4}(1+\xi)(1-\eta)-\frac{1}{2}(N_8+N_5) & N_5 &= \frac{1}{2}(1-\xi^2)(1-\eta)\\
N_2 &= \frac{1}{4}(1-\xi)(1+\eta)-\frac{1}{2}(N_5+N_6) & N_6 &= \frac{1}{2}(1+\xi)(1-\eta^2)\\
N_3 &= \frac{1}{4}(1-\xi)(1-\eta)-\frac{1}{2}(N_6+N_7) & N_7 &= \frac{1}{2}(1-\xi^2)(1-\eta)\\
N_4 &= \frac{1}{4}(1+\xi)(1-\eta)-\frac{1}{2}(N_7+N_8) & N_8 &= \frac{1}{2}(1+\xi)(1-\eta^2)
\end{aligned} \tag{3.40}$$

where (ξ,η) are the natural coordinates (Fig. 3.4b). The displacements of the element $\{U\}$ can be expressed in terms of shape function matrix $[N]$ and nodal displacements $\{X\}_e$, as

$$\{U\}=\begin{Bmatrix} u \\ v \end{Bmatrix}=[N]\{X\}_e \tag{3.41}$$

Finally, the stress-strain relationship in element matrix form can be written as

$$\{\sigma\}=\begin{Bmatrix} \sigma_{xx} \\ \sigma_{yy} \\ \tau_{xy} \end{Bmatrix}=[D]\{\varepsilon\}=[D][B]\{X\}_e \tag{3.42}$$

where $\{\varepsilon\}$ is the strain matrix, $[B]$ is the strain-displacement matrix. For homogeneous, isotropic materials, under plane stress condition, elasticity matrix $[D]$ is the defined as:

$$[D]_{Plane-Stress}=\begin{bmatrix} \frac{E}{1-\nu^2} & \frac{\nu E}{1-\nu^2} & 0 \\ \frac{\nu E}{1-\nu^2} & \frac{E}{1-\nu^2} & 0 \\ 0 & 0 & \mu \end{bmatrix} \tag{3.43}$$

Here E, ν, and μ are Young's modulus, Poisson's ratio, and shear modulus, respectively.

3.5.2 Quarter point elements (QPEs)

The QPEs are generated from the elements that containing mid-side nodes [219,220]. The one edge of the conventional Q8 elements is first collapsed to 6-noded triangular elements (Fig. 3.5). The QPEs are generally arranged in a standard spider-web pattern circumferentially around the crack tip. The square root singularity in the QPE is achieved by shifting the mid-side nodes on edges by an amount of quarter of the length towards the crack tip. The ANSYS automatically perform all these steps using an inbuilt command 'KSCON'.

Fig. 3.5b shows a 6-noded element obtained from the Q8 element, in which the edge $\xi = -1$ is collapsed, i.e., nodes 1 and 4 are collapsed at node 8. The resultant collapsed node (shown in red color) is usually kept at the crack tip.

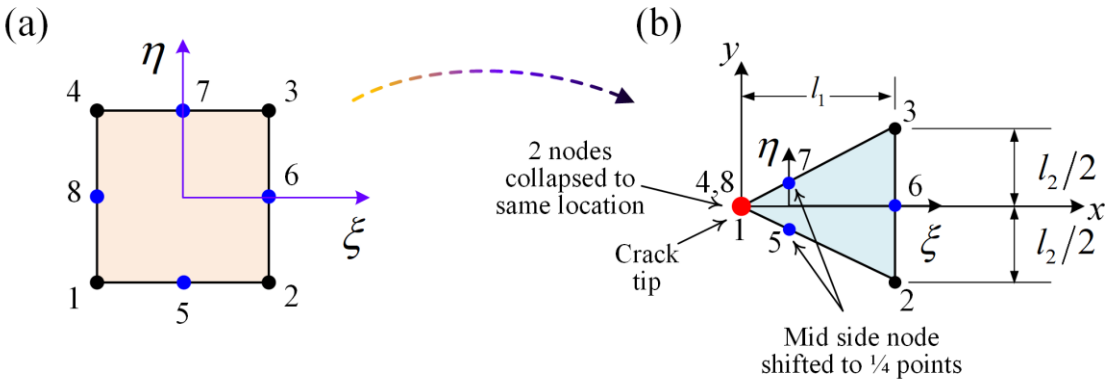

Fig. 3.5 The transformation of an 8-noded isoparametric element into a 6-node QPE.

3.5.3 Three-dimensional wedge element

Fig. 3.6a shows the 20-noded isoparametric element, and Fig. 3.6b illustrates the corresponding quarter-point singular wedge element with one face collapsed. This element is termed as SOLID186 in ANSYS®. Similar to the 2D QPE, Barsoum [220] showed that the square root singularity at the crack tip is embodied in the quarter point wedge element. Using the same command KSCON, the wedge element can be formed in the ANSYS®. The complete details of the formulation of the quarter-point wedge element can be read from Ref. [220–222]. Fig. 3.6c shows the higher order 3D, 10 node tetrahedral solid element termed as SOLID 187 element in ANSYS®. This element is widely employed to mesh irregular shapes.

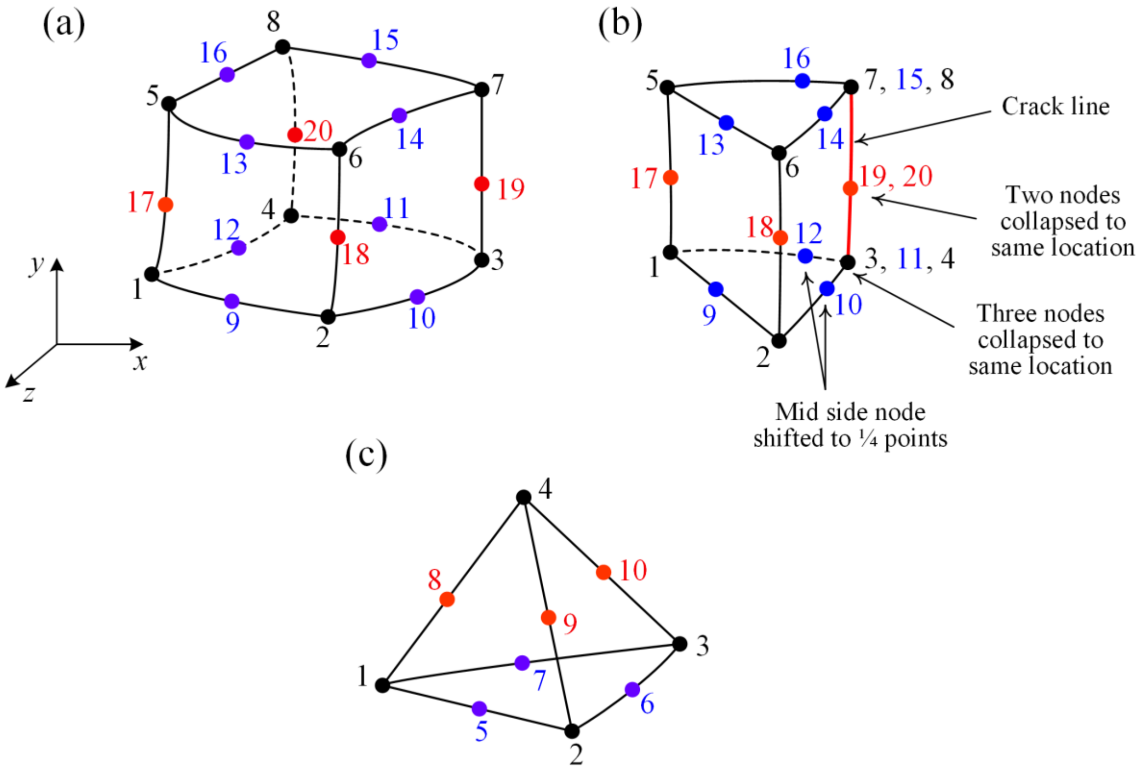

Fig. 3.6 (a) 20-node solid element (SOLID 186). (b) A 3D wedge crack tip element. (c) 10-node solid element (SOLID 187).

3.6 Determination of SIFs using finite element method

In the present work, $K_{\mathrm{I}}, K_{\mathrm{II}}$ and $T-$stress for the planar mixed mode (I/II) analyses are determined using an interior collocation method proposed by Jogdand and Murthy [218]. On the other hand, for the case of 3D mixed mode (I/II/III) crack modeling, an integral interaction technique is used for calculating the $K_{\mathrm{I}}, K_{\mathrm{II}}$, and K_{III}. The overview of both of these techniques is explained briefly in this section.

3.6.1 Interior collocation technique

The interior collocation technique involves solving an overdetermined system of equations. In the present work, the method proposed by Jogdand and Murthy [218] has been used to determine the coefficients A_0 (Eq. (A.18)), B_0 (Eq. (A.19)), and C_0 (Eq. (A.26)). The procedure for calculating SIFs and $T-$stress using FE analysis is explained briefly here. Further details of this method can be read from Ref. [218].

At a point $P(x, y)$, the displacement components obtained from the FE solution can be decomposed into opening mode and shear mode displacements as

$$\begin{Bmatrix} u_{\mathrm{I}}^{FE} \\ v_{\mathrm{I}}^{FE} \end{Bmatrix} = \frac{1}{2}\begin{Bmatrix} u+u' \\ v-v' \end{Bmatrix} \quad \text{and} \quad \begin{Bmatrix} u_{\mathrm{II}}^{FE} \\ v_{\mathrm{II}}^{FE} \end{Bmatrix} = \frac{1}{2}\begin{Bmatrix} u-u' \\ v+v' \end{Bmatrix} \tag{3.44}$$

where $u_{\mathrm{I}}^{FE}, v_{\mathrm{I}}^{FE}$ and $u_{\mathrm{II}}^{FE}, v_{\mathrm{II}}^{FE}$ are Mode I and mode II displacements obtained from the FE solution (Fig. 3.7). In Eq. (3.44), (u,v) and (u',v') are the finite element displacement components at points $P(x,y)$ and $P(x,-y)$, respectively. By using Eqs. (A.15), (A.24) and (3.44) one can obtain

$$\begin{aligned} v_{\mathrm{I}}^{FE} &= \frac{A_0}{2\mu} r^{1/2}\left[(\kappa+1)\sin\frac{\theta}{2} - \sin\theta\cos\frac{\theta}{2}\right] \\ &+ \frac{A_1}{2\mu} r^{3/2}\left[\frac{\kappa+1}{3}\sin\frac{3\theta}{2} - \sin\theta\cos\frac{\theta}{2}\right] - \frac{B_0 v(\kappa+1)}{4\mu} r\sin\theta \end{aligned} \tag{3.45}$$

$$\begin{aligned} u_{\mathrm{II}}^{FE} &= \frac{C_0}{2\mu} r^{1/2}\left[(\kappa+1)\sin\frac{\theta}{2} + \sin\theta\cos\frac{\theta}{2}\right] \\ &+ \frac{C_1}{2\mu} r^{3/2}\left[\frac{(\kappa+1)}{3}\sin\frac{3\theta}{2} + \sin\theta\cos\frac{\theta}{2}\right] + \frac{D_0(\kappa+1)}{4\mu} r\sin\theta \end{aligned} \tag{3.46}$$

The unknown coefficients A_0, A_1, B_0, C_0, C_1 and D_0 have been estimated by solving an overdetermined system of linear equations, which are obtained by employing Eqs. (3.45) and (3.46) at various nodes of the elements of the first and second layer at the crack tip, as shown in Fig. 3.7.

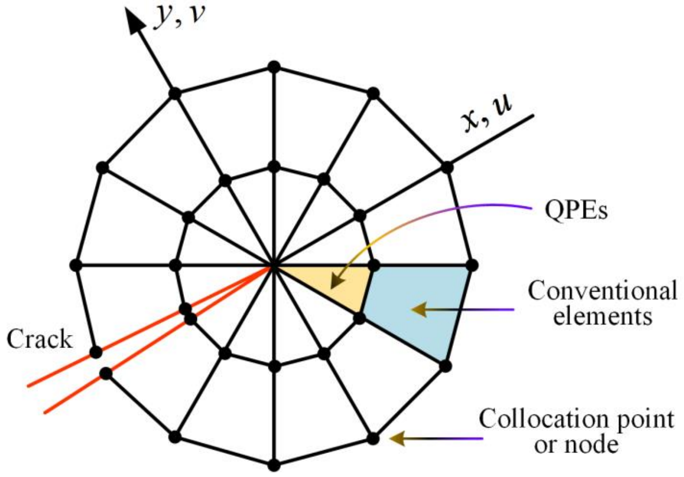

Fig. 3.7 The collocation nodal points used to calculate SIFs and T – stress.

3.6.2 Interaction Integral Method

The interaction integral provides a direct way to calculate the SIFs ($K_\mathrm{I}, K_\mathrm{II}$ and K_III) under general mixed (I/II/III) loading conditions. This method is based on the calculation of a path independent $J-$integral along the crack front as

$$J(s)=\lim_{\Gamma\to 0}\int_{\Gamma}\left(W\delta_{li}-\sigma_{ij}u_{jl}\right)n_i\,d\Gamma \tag{3.47}$$

where $\Gamma(s)$ is contour integral around the crack tip, σ_{ij} is the Cauchy stress, W is the strain energy density and u_{jl} are the components of the displacement gradient tensor, and δ_{ij} is the Kronecker delta. In the interaction integral method, the auxiliary field is superimposed on the actual field, and the associated $J-$integral is calculated as

$$J_{total}=J^{actual}+J^{aux}+I \tag{3.48}$$

where, J^{actual} and J^{aux} are the $J-$integral corresponding to the actual and auxiliary fields, respectively. The term I correspond to the interaction integral and can be expressed as

$$I(s)=\lim_{\Gamma\to 0}\int_{\Gamma}\left(\sigma_{ik}\varepsilon_{ik}^{aux}\delta_{li}-\sigma_{ik}\varepsilon_{il}^{aux}-u_{il}\sigma_{ij}^{aux}\right)n_j\,d\Gamma \tag{3.49}$$

where $\sigma_{ij}^{aux},\varepsilon_{ik}^{aux}$ and u_{il} are the auxiliary stress, strain, and displacement fields, respectively. The interaction integral as a function of actual and auxiliary fields of stress intensity factors can be obtained as

$$I(s)=\frac{2\left(1-\nu^2\right)}{E}\left(K_\mathrm{I}K_\mathrm{I}^{aux}+K_\mathrm{II}K_\mathrm{II}^{aux}\right)+\frac{1}{\mu}K_\mathrm{III}K_\mathrm{III}^{aux} \tag{3.50}$$

The SIF corresponding to each mode can be obtained by setting other auxiliary SIFs equal to zero. For example, for mode I, putting $K_\mathrm{I}^{aux}=1, K_\mathrm{II}^{aux}=0$ and $K_\mathrm{III}^{aux}=0$ gives

$$K_\mathrm{I}(s)=\frac{E}{2\left(1-\nu^2\right)}I(s) \tag{3.51}$$

Similarly, K_II and K_III can be obtained as:

$$\begin{gathered}K_\mathrm{II}(s)=\frac{E}{2\left(1-\nu^2\right)}I(s)\\ K_\mathrm{III}(s)=\mu I(s)\end{gathered} \tag{3.52}$$

Further details on interaction integral can be read from Ref. [223–226].

3.7 Summary

This chapter discussed the theoretical background required for determining the crack tip stress field by using the generalized Westergaard approach. The crack tip stress field exhibits square root singularity, which is characterized by the stress intensity factor (SIFs). The crack tip under mixed mode (I/II/III) loading is characterized by the combination of K_{I}, K_{II} and K_{III}. The $T-$stress is the first non-singular term in the crack tip field equations and can strongly influence the stress field approximation. The mathematical expressions for determining the crack propagation angles (i.e., kink angle θ_0 and twist angle ψ_0) and fracture locus under mixed mode (I/II) and (I/III) have been presented. These expressions will be used in the context of experimental analyses in subsequent chapters. Furthermore, the crack incremental technique for fatigue simulations has been explained in detail, which will again be utilized in the chapter dealing with the investigation of fatigue crack growth analyses in metals under mixed mode (I/II) loading conditions.

Chapter 4

Design of proposed specimen and experimental setup

This chapter first presents the design and development of the proposed single edge cracked circular (SECC) specimen and a new out-of-plane loading fixture (called J-fixture). In the present experimental work, three different types of materials, viz., Polymethylmethacrylate (PMMA), AISI 304 steel, and Al 7075-T6 aluminum alloy, have been utilized for the fracture and fatigue experiments. The complete specimen fabrication process using PMMA, Al 7075-T6 alloy, and AISI 304 steel is described in detail. Furthermore, different test setups utilized for conducting mixed mode (I/II), (I/III), and (I/II/III) fracture and fatigue crack growth studies have been presented. The details of the setup employed for measuring crack kink angle θ_0, crack twist angle ψ_0 from fractured PMMA specimens, pre-cracking of metallic specimens, and the crack length measuring procedure for mixed mode (I/II) FCG studies have been explained in detail. Additionally, the details of the field emission scanning electron microscope (FESEM) machine used for fractographic studies have been given.

4.1 Proposed specimen: Single edge cracked circular specimen

Sections 4.1-4.3 describes the proposed specimen setup for general mixed mode loading. The geometry and dimensions of the proposed single edge cracked circular (SECC) specimen are shown in Fig. 4.1. The specimen has a circular shape with a diameter equal to D_o, a single edge-crack of length a (notch length plus the pre-crack length), and three holes A, B and C of equal diameter d. The centers of all these three holes lie on a circle of diameter D_i as shown in Fig. 4.1a. The hole B is diametrically opposite to that of the hole A. First, a horizontal edge notch OS of length $a-\Delta a_{\mathrm{p}}$ (Fig. 4.1a) can be created easily using standard fabrication methods. If the specimen is used to test the metallic materials, then fatigue precracking can be made for a length of Δa so that the final crack length is a. On the other hand, suitable method can be adopted to create Δa if the material is non-metallic. Depending on a desired mode mixity angle β, centers of the loading holes A and B can be easily located and drilled (Fig. 4.1a). Center of the hole C can be located in such a way that the center of C and A lie on a vertical line perpendicular to the axis of the edge notch OS and located at an equal distance of h from the notch axis (Fig. 4.1a). The holes A and C are used for creating the fatigue precracking of length Δa_{p} when the specimen material is a metal.

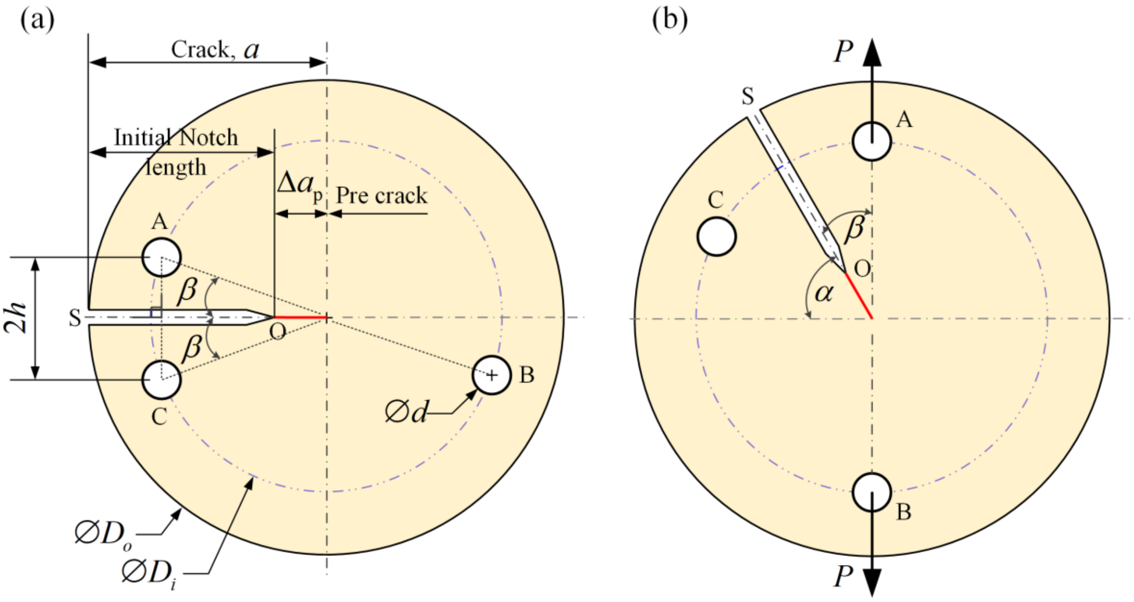

Fig. 4.1 Geometry of the proposed SECC specimen and its loading configurations: (a) details of the specimen. (b) Specimen orientation for conducting the mixed mode (I/II) tests.

If the material of the specimen is Polymethylmethacrylate or Perspex (PMMA), hole C is not required as the precracking of length Δa_p in such material can be easily created by pressing a razor blade or a fine jewelry saw [25] from the tip of the notch OS. After the pre-cracking, the specimen can then be easily rotated such that the holes A and B are aligned in the direction of actuators of the UTM, and tensile loading can be easily applied to the specimen using the clevis pins through the holes A and B. Thus, the horizontally created edge crack now automatically makes an angle β with the loading axis, as shown in Fig. 4.1b.

The angular position of holes A and B can be varied to achieve a range of mode mixity, ranging from the pure mode I to any desired mixed mode (I/II) loading (Fig. 4.1b). Defining angle $\alpha = 90° - \beta$ as shown in Fig. 4.1; $\alpha = 0°$ leads to the pure mode I loading, while $\alpha \neq 0°$ produces desired mixed mode (I/II) loading. Six different mixed mode (I/II) loading configurations of the SECC specimen ranging from pure mode I to mixed mode (I/II) with an angular increment of $15°$ are shown in Fig. 4.2. As can be seen in Fig. 4.2, with an increase in angle α, the in-plane shear component of load increases and the mode I component at the crack-tip decreases.

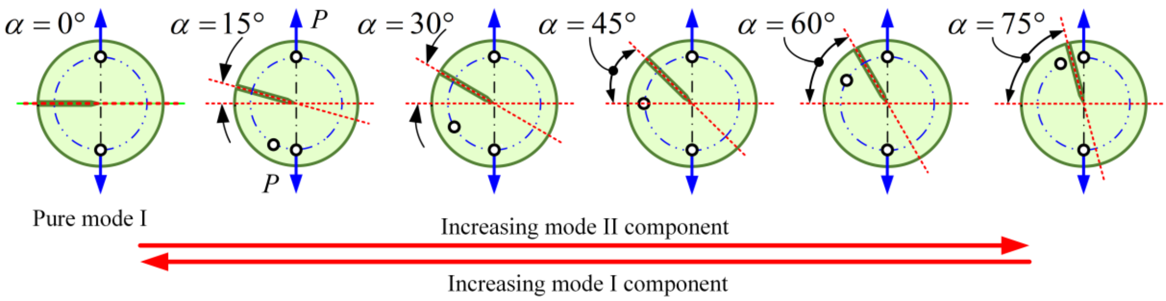

Fig. 4.2 Different mixed mode (I/II) loading configurations of the SECC specimen.

Thus, the proposed specimen can be used with both metallic and non-metallic brittle materials such as PMMA, and the specimen provides an integral arrangement for creating the fatigue precrack. Selected dimensions of the proposed specimen have been presented in Table 4.1.

Table 4.1 Geometrical dimensions of the SECC specimen.

Description	Dimensions (mm)
Diameter of the specimen, D_o	160
Location of the center of holes, D_i	118
Size of the hole, d	12.8
Crack size, a	80

These sizes have been arrived based on the dimensions of a standard compact tension (CT) specimen described in ASTM E399 and desired properties of a mixed mode specimen (Section 4.4). The following steps have been followed for fixing the dimensions of the specimen:

Step 1. Fig. 4.3a shows the standard CT specimen and its recommended dimensions as per the ASTM E399 code. The diameter of holes A, B and C (i.e., $d = 12.8$ mm) of the proposed specimen are almost equal to clevis pin sizes corresponding to the half inch CT specimen.

Step 2. Keeping in view of the static and fatigue crack growth tests, the outside diameter of the D_o has been set at 160 mm based on our past experience. This has also been chosen to ensure that the loading holes are at enough distance from the crack tip to avoid any influence on the crack tip stress field. Further, sufficient viewing area should be available for measuring and observing the mixed mode fatigue crack propagation using the optical microscope. Moreover, the selected D_o value is useful in extending the present specimen to include mode III and all three modes simultaneously as well.

Step 3. A standard one inch thick and $W = 60$ mm CT specimen have been widely used. As shown in Fig. 4.3a the recommended distance between the center of the loading hole and outer edge of the standard one-inch thick CT specimen is $0.325W$ which equals to 19.5 mm for $W = 60$ mm. Thus, a distance of 21 mm has been maintained between the center of the holes A, B, and C and the outer boundary of the proposed specimen. Based on the experience for a desired mixed mode specimen, this distance is increased from 19.5 mm to 21 mm as shown in Fig. 4.3b.

Step 4. Following the recommendations of the ASTM for the CT specimen, the crack tip has been located at the center of the disk. With the crack tip (not the notch tip) at the center of the disk, D_{i} can then be easily obtained as 118 mm as shown in Fig. 4.3b. The other dimensions can be easily found from the geometry.

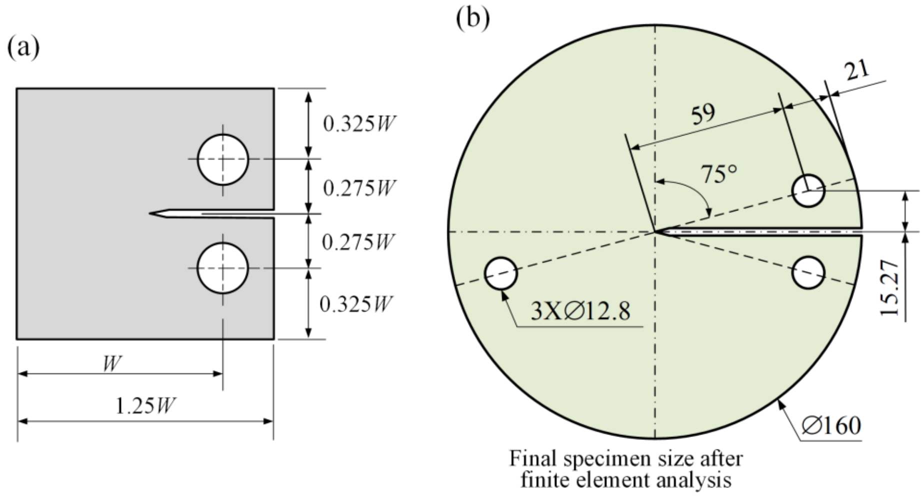

Fig. 4.3 Comparison of dimensions of the standard CT specimen and the proposed specimen. (a) Dimensions of CT specimen. (b) Final dimensions of SECC specimen.

4.2 New out-of-plane loading fixture: J-fixture

A new out-of-plane loading fixture or (J-fixture) has been developed in the present work to impart mode III loading onto the SECC specimen. Using this fixture, a desired mixed mode (I/II/III) loading can be applied to the SECC specimen by a conventional uniaxial universal testing machine. Fig. 4.4a shows the connection sequence of the loading assembly using the J-fixture and SECC specimen. The fixture contains two identical loading plates as shown in Fig. 4.4a. Top J-fixture and bottom J-fixture, are required to load the SECC specimen with the UTM (Fig. 4.4a). The geometric dimensions of one of the two identical plates of the new J-fixture are shown in Fig. 4.4b. It consists of seven identical holes (in the plane of the fixture) of a diameter 13 mm. These holes are separated with an angular increment of 15°. The J-fixture contains a hole of diameter 13 mm in the thickness direction (as shown in Fig. 4.4b with the dotted lines) to connect the SECC specimen to the fixture using holes A and B. The out-of-plane loading angle ϕ is defined as the angle between the plane of the SECC specimen and the external loading direction (Fig. 4.4b). Hence, the magnitude of the mode III component can simply be adjusted by changing the angle ϕ.

The proposed specimen setup can be used for all possible combinations of mixed mode (I/II/III) by varying the in-plane loading angle α (which imparts mixed mode (I/II) loading) and out-of-plane loading angle ϕ (which imparts mode III loading component).

As shown in Fig. 4.4a, for $\alpha = 0°$ and $\phi \neq 0°$ the loading setup exerts mixed mode (I/III) loading onto the SECC specimen. In a similar way, different mode mixities (I/III) can be achieved in the specimen by choosing appropriate holes in the two identical plates of the J-fixture.

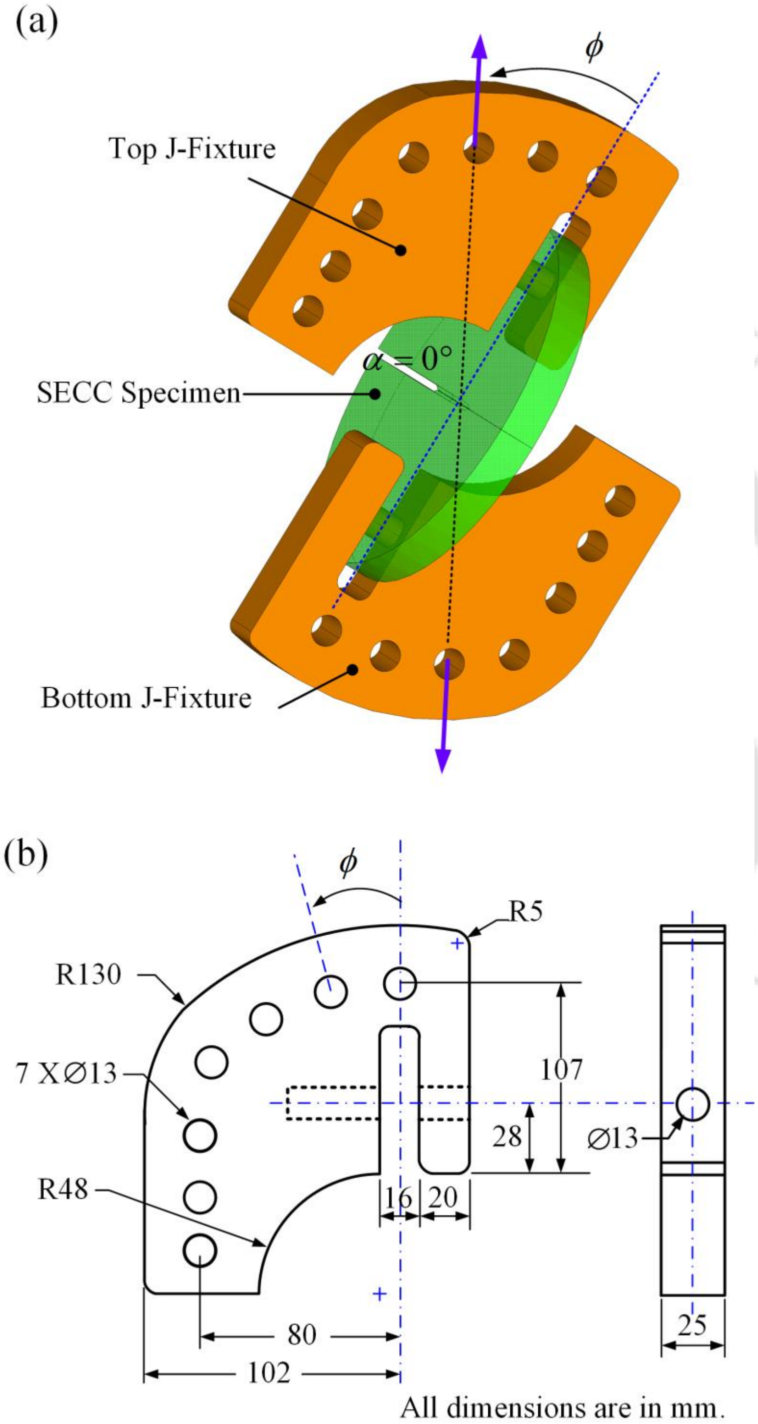

Fig. 4.4 (a) Mixed mode (I/III) loading configuration of the SECC specimen using J-fixture for $\alpha = 0°$ and $\phi \neq 0°$. (b) Geometric dimensions of the J-fixture; here, the hole in the thickness direction is used to hold the specimen with the fixture.

Fig. 4.5 shows seven different mixed mode (I/III) loading configurations of the loading setup. The loading angles $\alpha = 0°, \phi = 0°$ correspond to pure mode I, $\alpha = 0°, \phi = 90°$ corresponds to pure mode III, and $\alpha = 0°, \phi \neq 90°$ corresponds to a case of mixed mode (I/III) loading (Fig. 4.5). Similarly, a general case of mixed mode (I/II/III) loading can also be achieved by the proposed loading setup just by setting in-plane loading angle $\alpha \neq 0°$ and varying the ϕ from $0°$ to $90°$, as shown in Fig. 4.6.

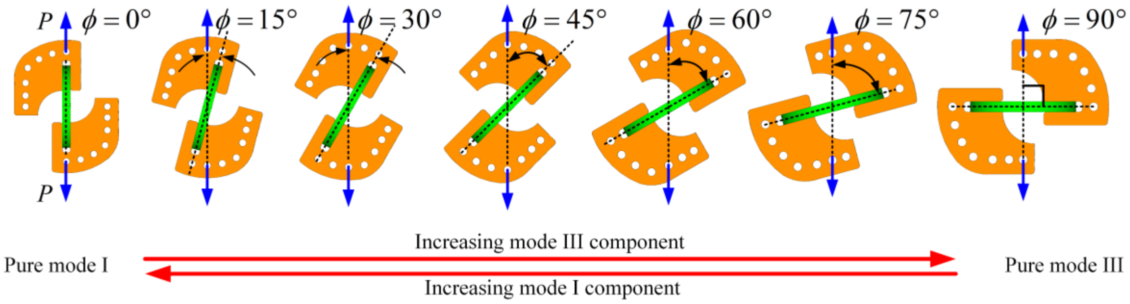

Fig. 4.5 Mixed mode (I/III) loading configuration of the proposed testing setup.

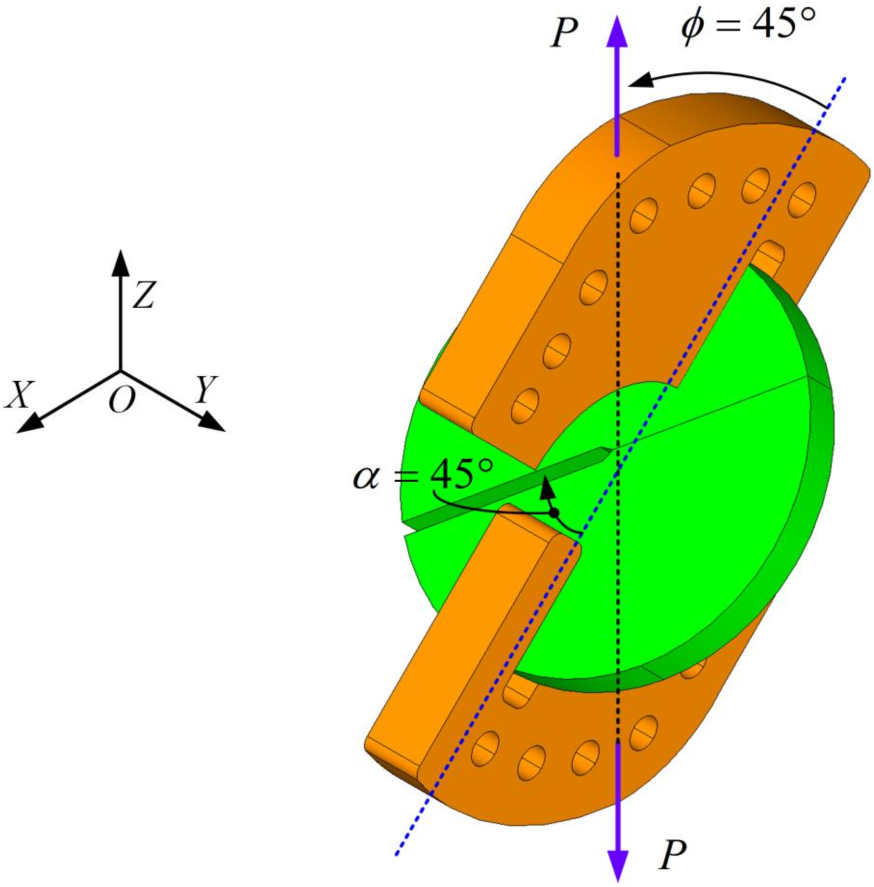

Fig. 4.6 Mixed mode (I/II/III) loading configuration of the proposed testing setup.

4.3 Deep groove clevis grips

A new set of deep groove clevis grips (having 90 mm groove depth) have been fabricated to accommodate the fatigue precracking configuration of the SECC specimen. Fig. 4.7 shows the dimensions of the clevis grip. These new grips can be used to test the SECC specimen up to 16 mm thickness. Other dimensions of the clevis grip shown in Fig. 4.7 are derived from standard one-inch clevis grips as per ASTM E399.

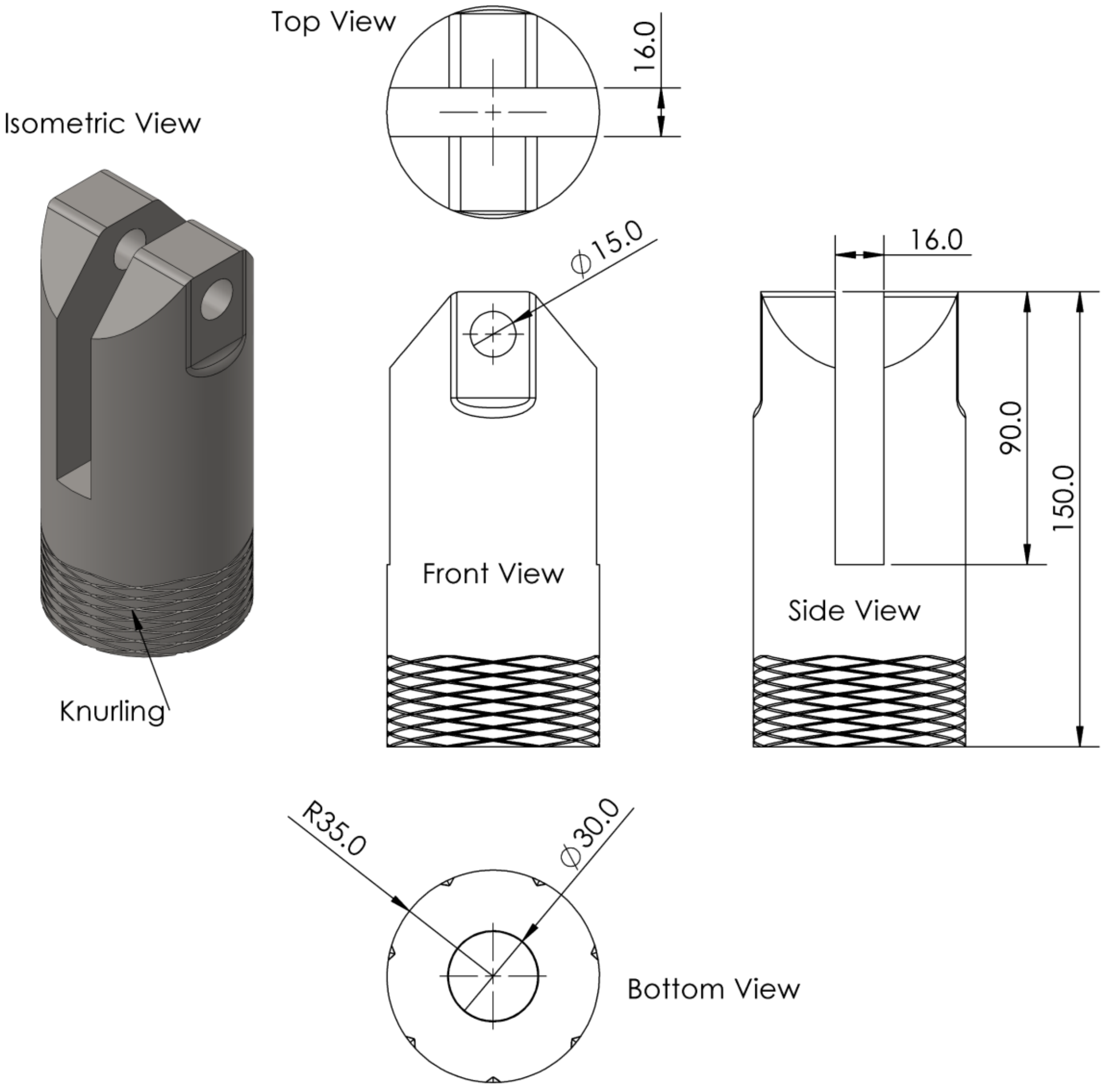

Fig. 4.7 Dimensions of the deep groove Clevis grip for the SECC specimen.

4.4 Compact tension (CT) specimen

The Paris material constants C and m of metallic materials used in the present investigation have been determined from the Mode I FCG experiments using the standard CT specimen. The planar dimensions of the CT specimen are shown in Fig. 4.8a, which are calculated for a 60 mm wide CT specimen as per ASTM E399. Fig. 4.8b shows the details of the starter notch and knife edge required for mounting the COD gauge.

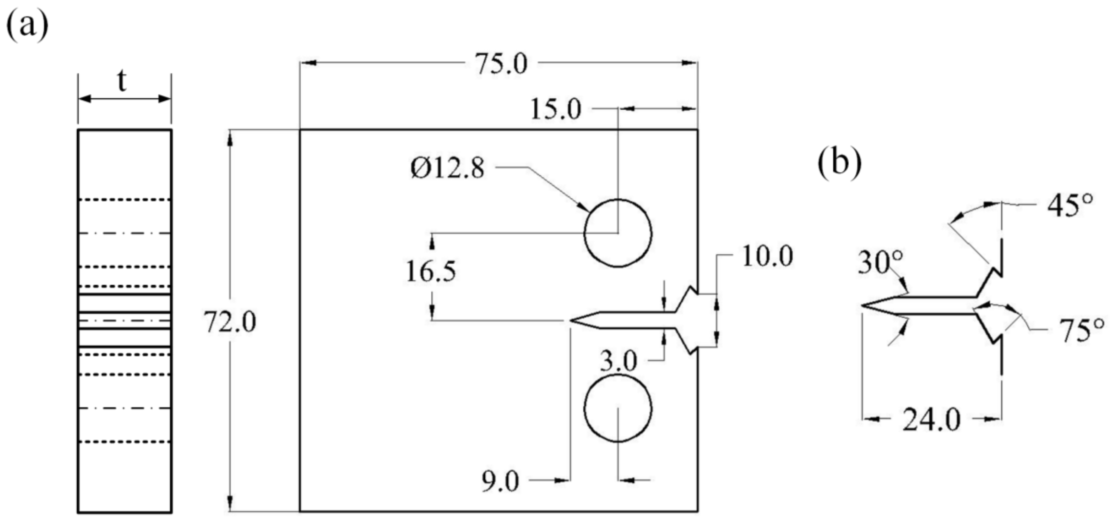

Fig. 4.8 (a) Dimensions of the CT specimen. (b) Dimensions of the starter notch.

4.5 Tensile test specimens

In the present experimental work, three different types of materials, viz., PMMA, AISI 304 steel, and Al 7075-T6 aluminum alloy, have been utilized for the fracture and fatigue experiments. The mechanical properties of these materials are required for finite element (FE) numerical simulations. Therefore, tension tests under quasi-static loading have been performed to determine the material properties. Fig. 4.9 shows the dimensions of the dog-bone-shaped specimen used for conducting the tensile tests. The mechanical properties of the PMMA sheets (having thicknesses of 6 mm, 10 mm, and 12 mm) are determined from the tensile tests in accordance with ASTM D638. And the mechanical properties of the AISI 304 steel and Al 7075-T6 alloy are determined from the tensile test conducted according to ASTM E8. For PMMA sheet material, tensile specimens of dimensions $L_{\text{full}} = 200$ mm, $w_{\text{gage}} = 12.5$ mm, and $w = 20$ mm have been used. And for Al 7075-T6 and AISI 304 steel plate, tensile specimens of dimensions $L_{\text{full}} = 250$ mm, $w_{\text{gage}} = 20$ mm,

$t = 15$ mm, and $w = 30$ have been employed. A biaxial extensometer (Epsilon make) of 25 mm gauge length has been used to measure the Poisson's ratio by measuring the strains in axial and transverse directions of all the coupon specimens. A displacement-controlled testing approach has been adopted for all the tensile tests.

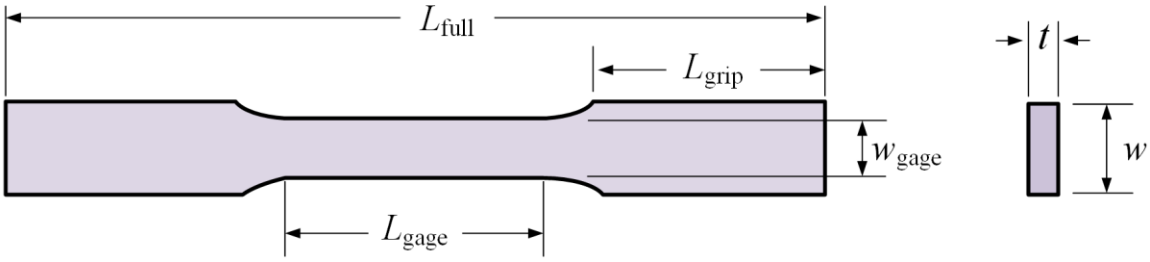

Fig. 4.9 Dimensions of the dog-bone-shaped specimen used for the tensile tests.

4.6 Details of fabrication of the specimens and fixtures

As explained earlier, in the present work, PMMA, AISI 304 steel, and Al 7075-T6 aluminum alloy have been utilized for the fracture and fatigue experiments. This section presents the fabrication procedure of the SECC specimens from brittle materials like PMMA and metallic materials like AISI 304 steel and Al 7075-T6 alloy. The fabrication details of associated fixtures, viz., deep groove clevis grips and J-fixture, have also been given.

4.6.1 Fabrication of PMMA specimens

Different steps involved in fabricating the SECC specimen from PMMA material are shown in Fig. 4.10. All the SECC specimens from PMMA have been fabricated using an LVD 4kW fast axial flow high power CO_2 LASER cutting machine. The laser cut loading holes have been further machined by reaming with an adjustable H4 reamer tool (Fig. 4.10) in order to arrive at perfect loading holes.

First, an initial notch (OS in Fig. 4.1a) of width 3 mm has been made for a length of 78 mm with the laser machine, and then a sharp pre-crack of length 2 mm (as shown in Fig. 4.1a) is created using a jewelry saw with a fine thickness wire of (8/0) grade. Finally, crack tips have been inspected under a Nikon Research Stereo Microscope fitted with a 1.0X objective lens at a magnification of 4.0X, and found the tip root radius is equal to 0.165 mm for all the specimens. Fig. 4.11 shows details of the measured notch OS, notch radius, and the sharp precrack created with the help of a jewelry saw.

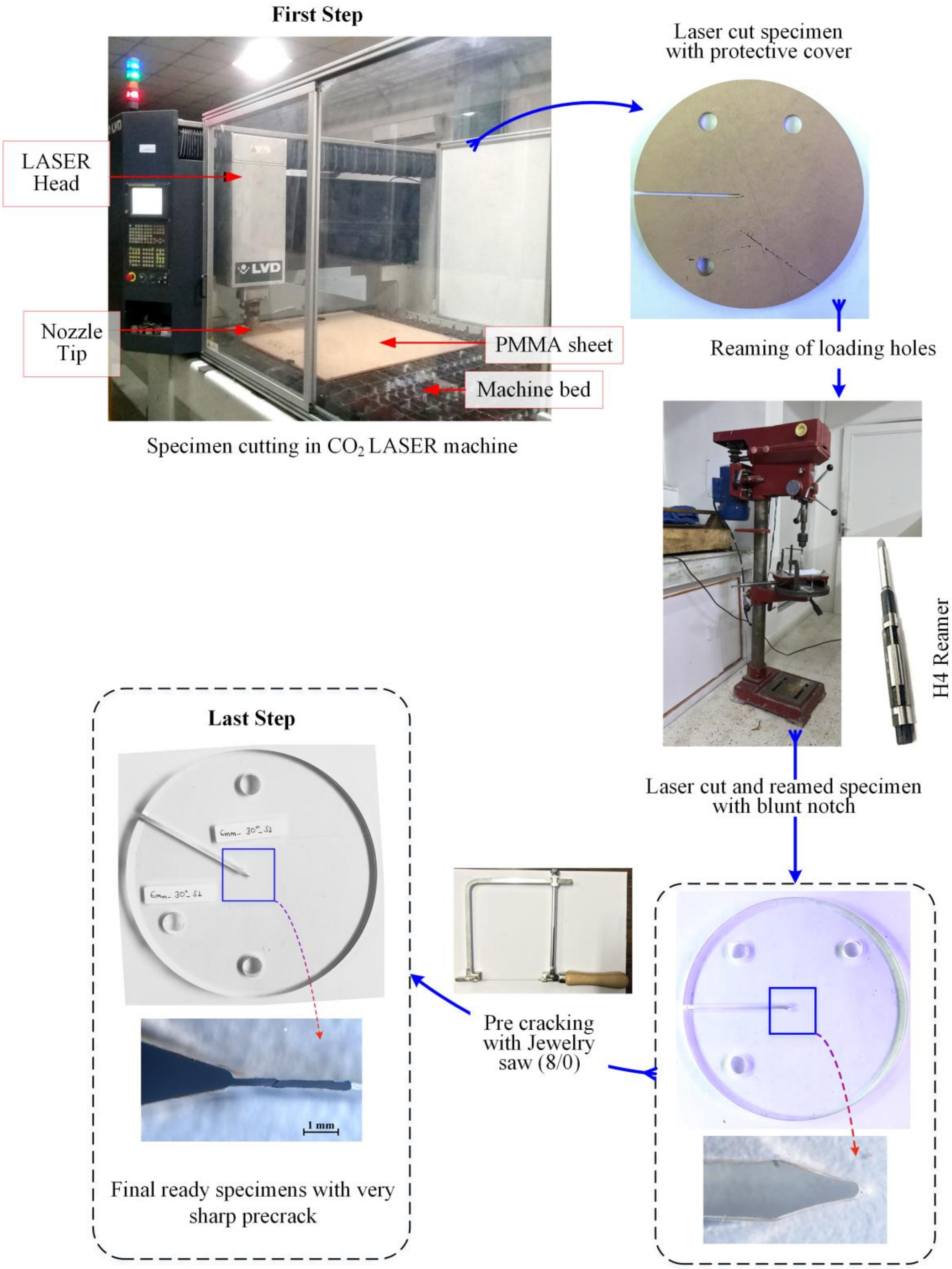

Fig. 4.10 Fabrication process of the SECC specimens using the PMMA material.

Fig. 4.12 shows typical pre-cracked SECC specimens having 6 mm thickness. The fabricated tensile specimen made of PMMA is also shown in Fig. 4.12g. Although not shown here, the SECC specimens made from 10 mm and 12 mm thick PMMA sheets have also been fabricated by following the same procedure as given in Fig. 4.10.

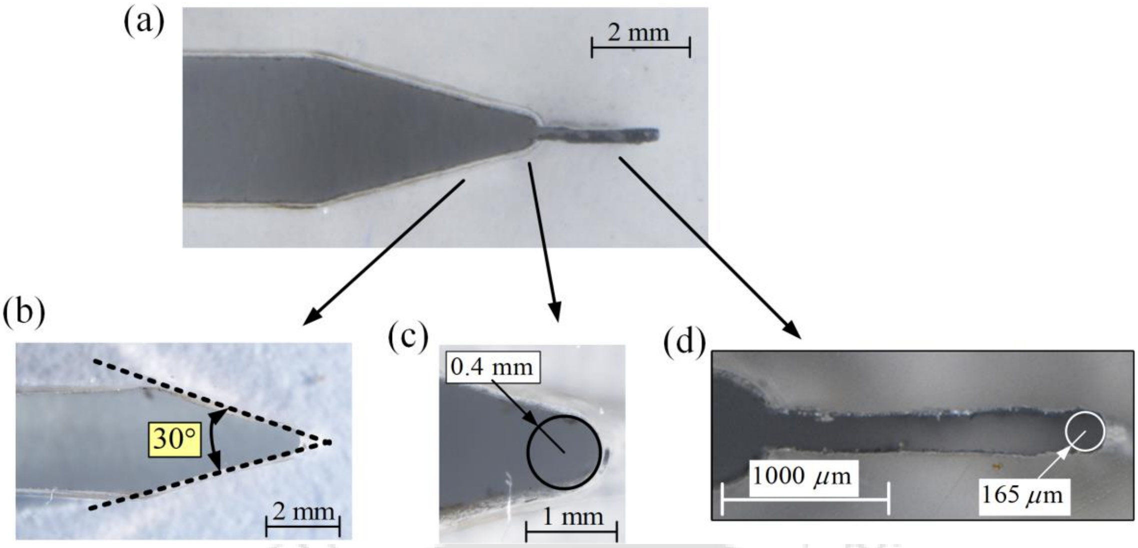

Fig. 4.11 (a) A close-up view showing the pre-crack at the laser cut notch tip. (b) The notch angle. (c) The notch tip root radius. (d) The length and root radius of the pre-crack.

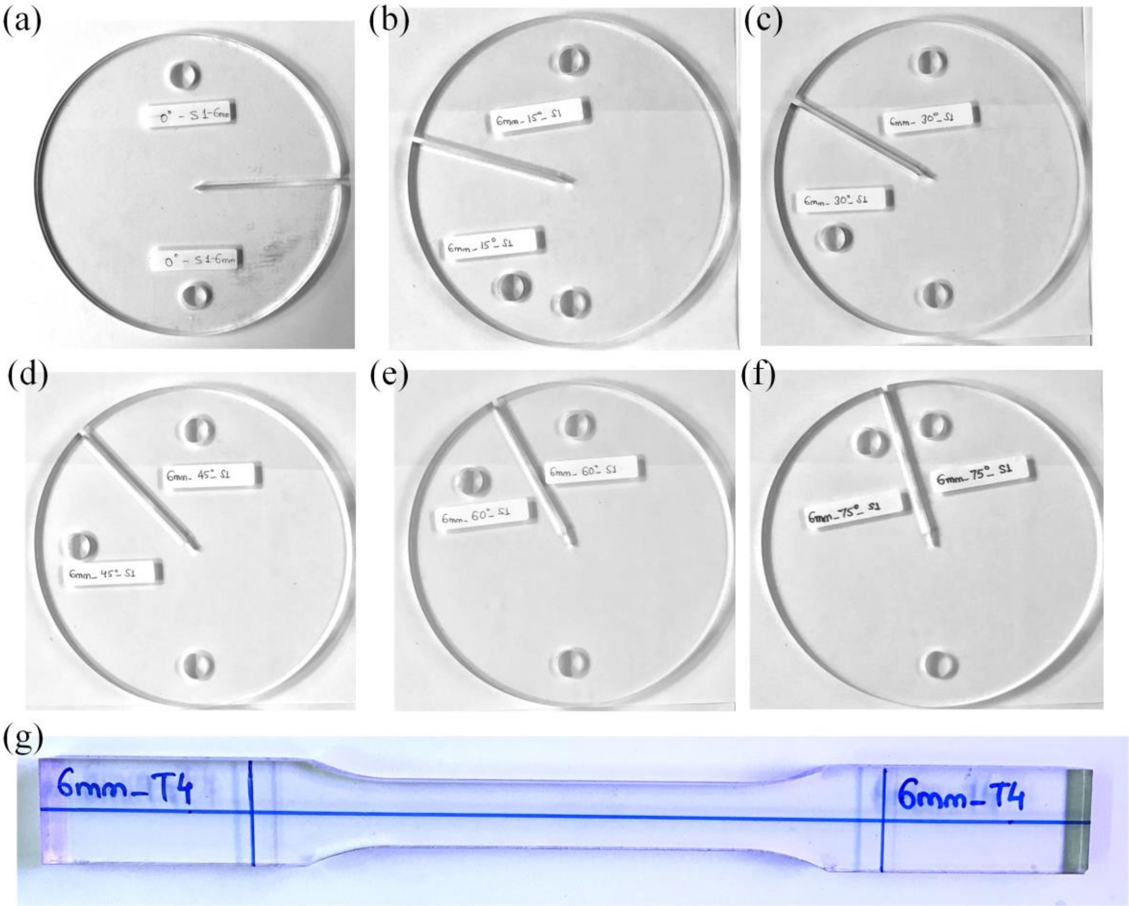

Fig. 4.12 The pre-cracked SECC specimens made from 6 mm thick PMMA sheet for different loading angles α: (a) 0°. (b) 15°. (c) 30°. (d) 45°. (e) 60°. (f) 75°. (g) Tensile specimen.

4.6.2 Fabrication of Al 7075-T6 alloy and AISI 304 steel specimens

All metallic specimens, i.e., tensile, CT, and SECC specimens, used in the present investigation have been fabricated in *L-T* orientation using a wire electro-discharge machining (wire-EDM) technique with a wire diameter of 0.25 mm from a 16 mm thick plate. Fig. 4.13 shows the orientation of the specimens with reference to the material's coordinate system. As per standard terminology (ASTM E1823-21), a specimen in *L-T* orientation has a crack plane normal to the longitudinal direction (L), and an incipient crack grows in the transverse direction (T). A very sharp initial notch in CT and SECC specimens has been cut using the wire-EDM process. The width and notch angle of the initial notch is kept at 3 mm and 30°, respectively (Fig. 4.8b). After all the machining operations, the surface of the SECC specimens has been mirror-polished to facilitate the optical measurement of the growing crack. Sandpaper of reducing grit sizes has been used to polish the surfaces. The polishing of the specimens is started with coarse grit sizes (100 and 120), and finally, for fine finishing, finer grit sizes are used.

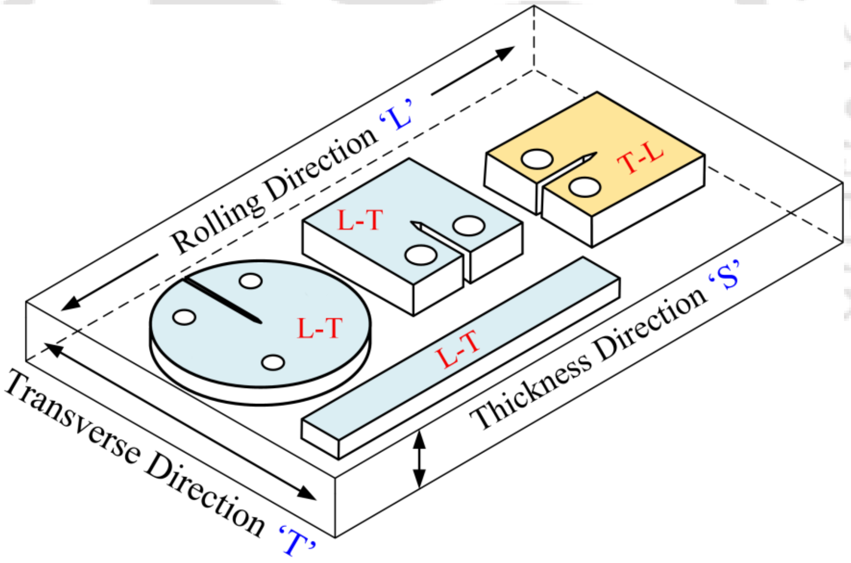

Fig. 4.13 Definition of the material coordinate system and orientation of the test specimens.

The mirror-polished surfaces of the SECC specimens made of AISI 304 steel have been achieved using 1000 and 1200 grit sizes. On the other hand, for the SECC specimens made of Al 7075-T6 alloy, the mirror-polished surfaces have been achieved using grit sizes of 1200 and 2000. Fig. 4.14a-c show the photographs of typical SECC specimens made of AISI steel, and Fig. 4.14d-f show photographs of the SECC specimens fabricated from Al 7075-T6 alloy.

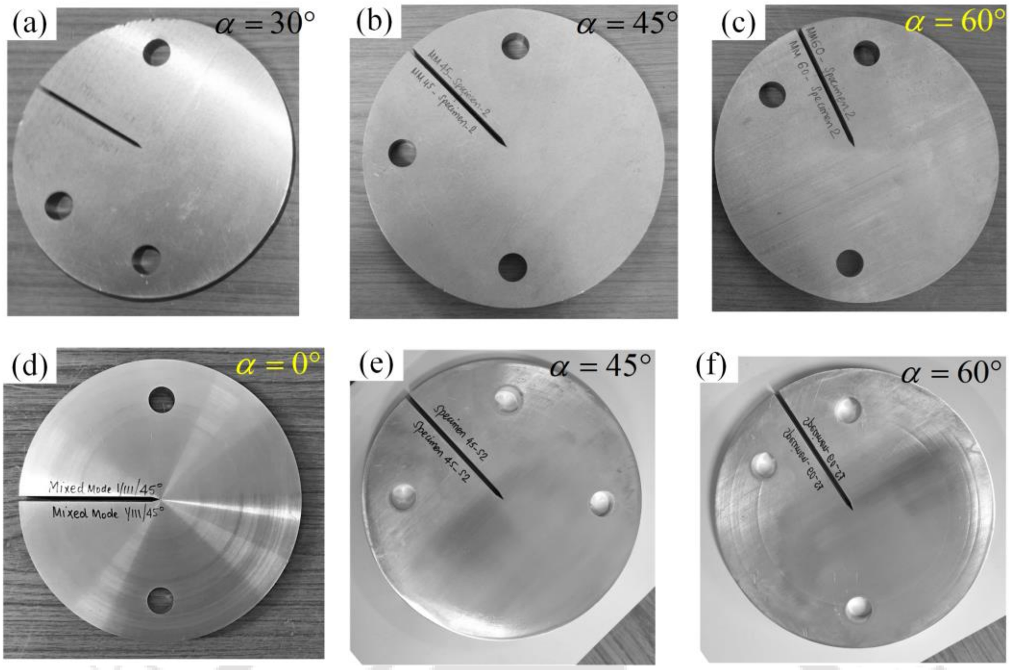

Fig. 4.14 (a)-(c) SECC specimens fabricated from AISI 304 steel. (d)-(f) SECC specimens fabricated from Al 7075-T6 alloy.

Fig. 4.15 shows the photograph of the tensile specimen made of Al 7075-T6 alloy, and Fig. 4.16 shows the photographs of the CT specimen made of AISI 304 steel and Al 7075-T6 alloy. In the present investigation, for each material, two CT specimens and two tensile specimens have been fabricated to observe the repeatability of the present experiments.

Fig. 4.15 Dog-bone-shaped tensile specimen fabricated using Al 7075-T6 alloy.

Fig. 4.16 CT specimens fabricated from AISI 304 steel (left) and Al 7075-T6 (right).

4.6.3 Fabrication of J-fixture and deep groove Clevis grips

The J-fixture, deep groove clevis grips, and loading pins have been fabricated from a high-strength steel (H13). The J-fixture (having dimensions given in Fig. 4.4b) has been fabricated from a 30 mm thick plate. On the other hand, new deep groove clevis grips and loading pins have been fabricated from 75 mm and 20 mm diameter cylindrical bars, respectively. The profile of the J-fixture and clevis grips have been cut using a wire-EDM technique, and CNC milling has been employed for drilling the holes at precise locations. The photograph of the fabricated J-fixture, deep grove clevis grips, and loading pins are shown in Fig. 4.17.

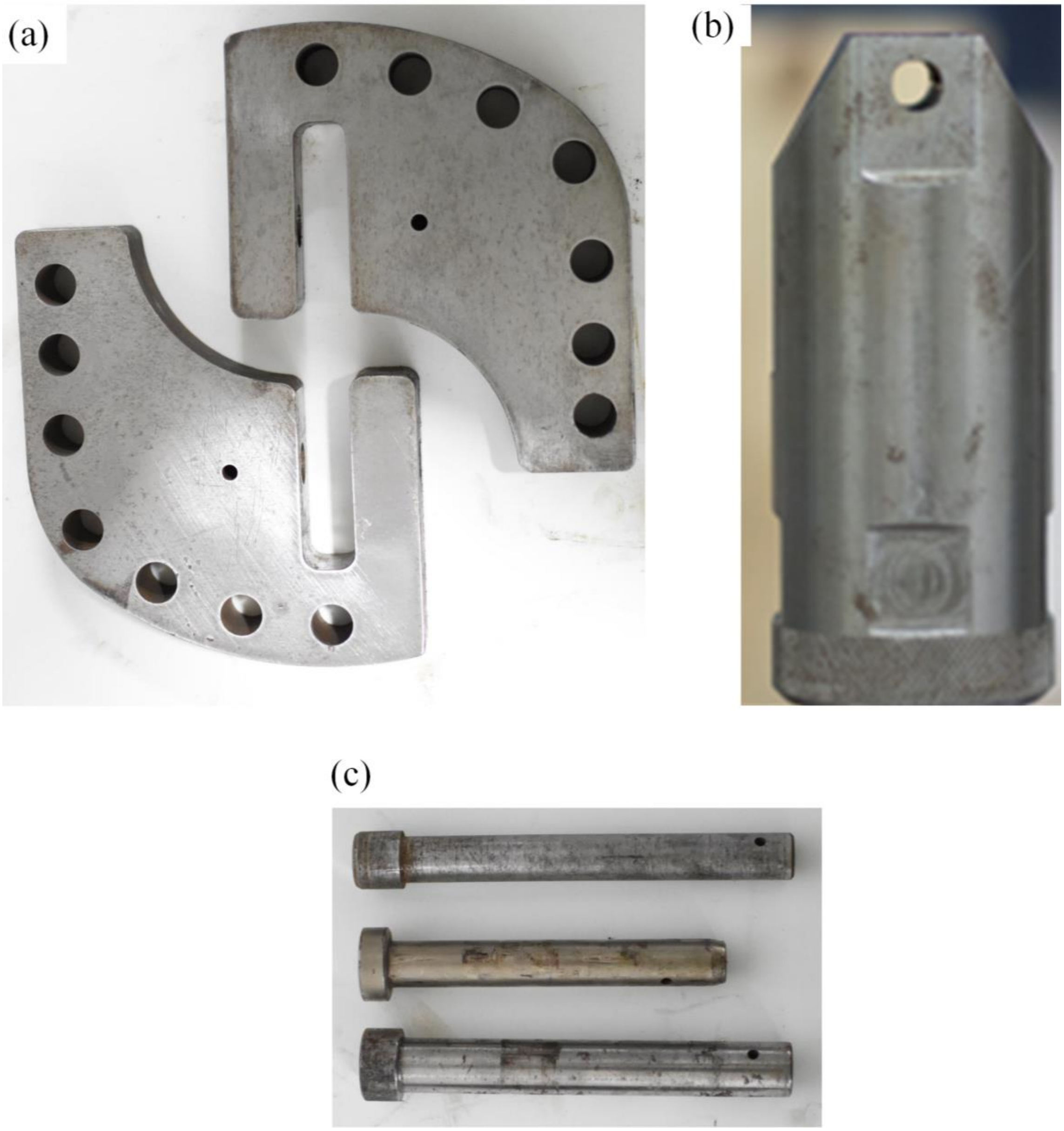

Fig. 4.17 Fabricated (a) J-fixture. (b) Deep grove Clevis grip. (c) Loading pins.

4.7 Details of the complete experimental setup

In the present work, a number of fracture and fatigue crack growth experiments have been performed, as given below:

- Mixed mode (I/II) fracture tests on the SECC specimens made of PMMA under quasi-static loading.
- Mixed mode (I/III) and (I/II/III) fracture tests on the SECC specimens made of PMMA under quasi-static loading.
- Mixed mode (I/II) FCG tests on the SECC specimen made of Al 7075-T6 alloy and AISI 304 steel under constant amplitude cyclic loading.
- Mode I FCG experiments using the CT specimen made of Al 7075-T6 alloy and AISI 304 steel under constant amplitude cyclic loading.
- Mixed mode (I/III) and (I/II/III) FCG tests on the SECC specimens made of Al 7075-T6 alloy under constant amplitude cyclic loading.

The details of these experimental setups for the above experiments have been given in this section. All the static and fatigue experiments in the present work have been conducted on a 250kN, BiSS ITW make, servo-hydraulic UTM.

4.7.1 Experimental setup for mixed mode (I/II) fracture studies on PMMA under quasi-static loading

Fig. 4.18a shows the complete loading setup used for the mixed mode (I/II) fracture experiments on PMMA under quasi-static loading. A load cell of 25kN capacity has been used to measure the actual load on the specimens. Fig. 4.18b shows a close-up view of the SECC specimen for $\alpha = 60°$ mounted on the UTM, and Fig. 4.18c shows the pure mode I, $(\alpha = 0°)$ loading configuration of the SECC specimen.

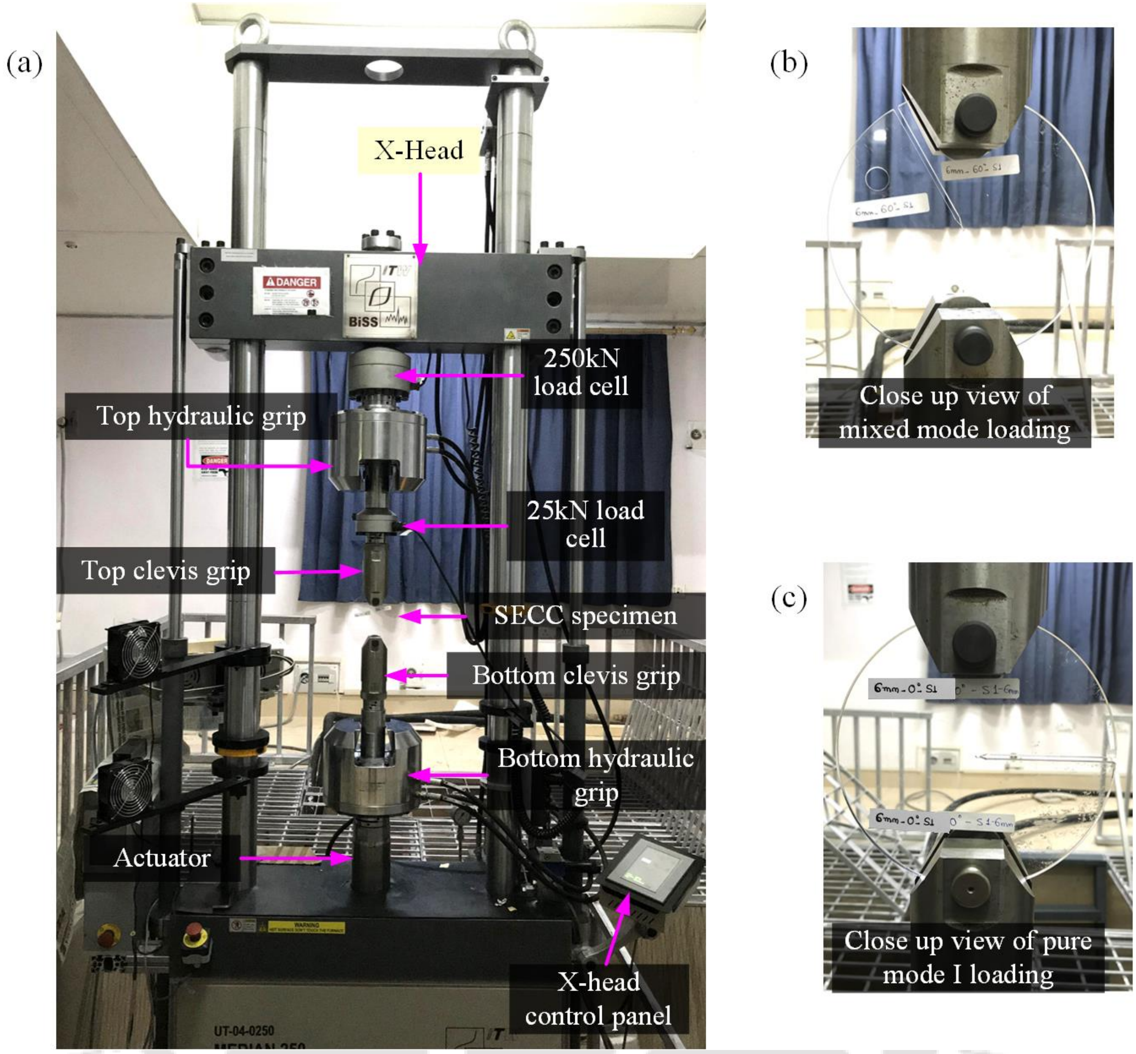

Fig. 4.18 (a) Complete loading setup used for the mixed mode (I/II) fracture tests. (b) Close up view of the mixed mode (I/II) loading for $\alpha = 60°$. (c) Pure mode I loading $\alpha = 0°$.

4.7.2 Experimental setup for mixed mode (I/III) and (I/II/III) fracture studies on PMMA under quasi-static loading

Fig. 4.19a and Fig. 4.19b show the complete experimental setup using SECC specimen that is used for conducting mixed mode (I/III) and (I/II/III) fracture tests on PMMA under quasi-static loading conditions, respectively. A load cell of 25kN capacity has been used to measure the actual load on the specimens. For mixed mode (I/III) fracture tests, the SECC specimen having in-plane loading angle $\alpha = 0°$ is used with the J-fixture, and the out-of-plane loading angle ϕ is varied to achieve the desired mixed mode (I/III) loading (Fig. 4.19a). On the other hand, for mixed mode (I/II/III) fracture tests, the SECC specimen having an in-plane loading angle $\alpha \neq 0°$ is used with the J-fixture, and the out-of-plane loading angle ϕ is varied to achieve desired mixed mode (I/II/III) loading (Fig. 4.19b).

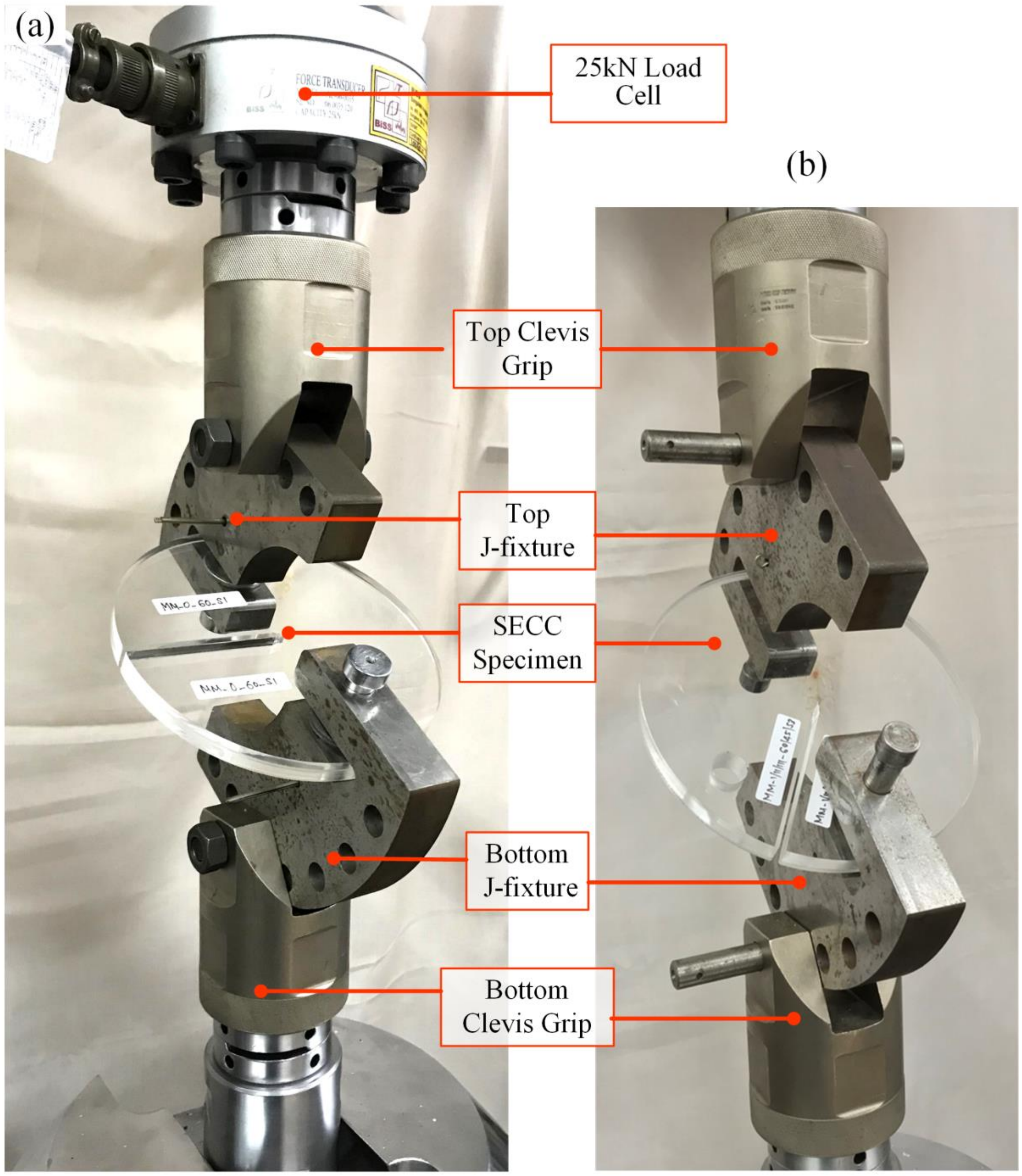

$\alpha = 0°, \phi = 60°$
Mixed mode (I/III)

$\alpha = 60°, \phi = 45°$
Mixed mode (I/II/III)

Fig. 4.19 (a)The mixed mode (I/III) loading setup for $\alpha = 0°, \phi = 60°$. (b) The mixed mode (I/II/III) loading setup for $\alpha = 60°, \phi = 45°$.

4.7.3 Experimental setup for mixed mode (I/II) FCG studies on Al 7075-T6 alloy and AISI 304 steel

Fig. 4.20a shows the complete experimental setup used for the mixed mode (I/II) FCG studies on Al 7075-T6 alloy and AISI 304 steel. The SECC specimen is attached to the

UTM using deep groove clevis grips. The mixed mode (I/II) FCG experiments using the SECC specimens have been conducted in two steps: first, all the SECC specimens have been precracked for a final nominal crack length of $a/D_o = 0.5$ (Fig. 4.21a-d). Then, the precracked SECC specimens have been oriented under the mixed mode configuration and the FCG tests are conducted (Fig. 4.21e-h).

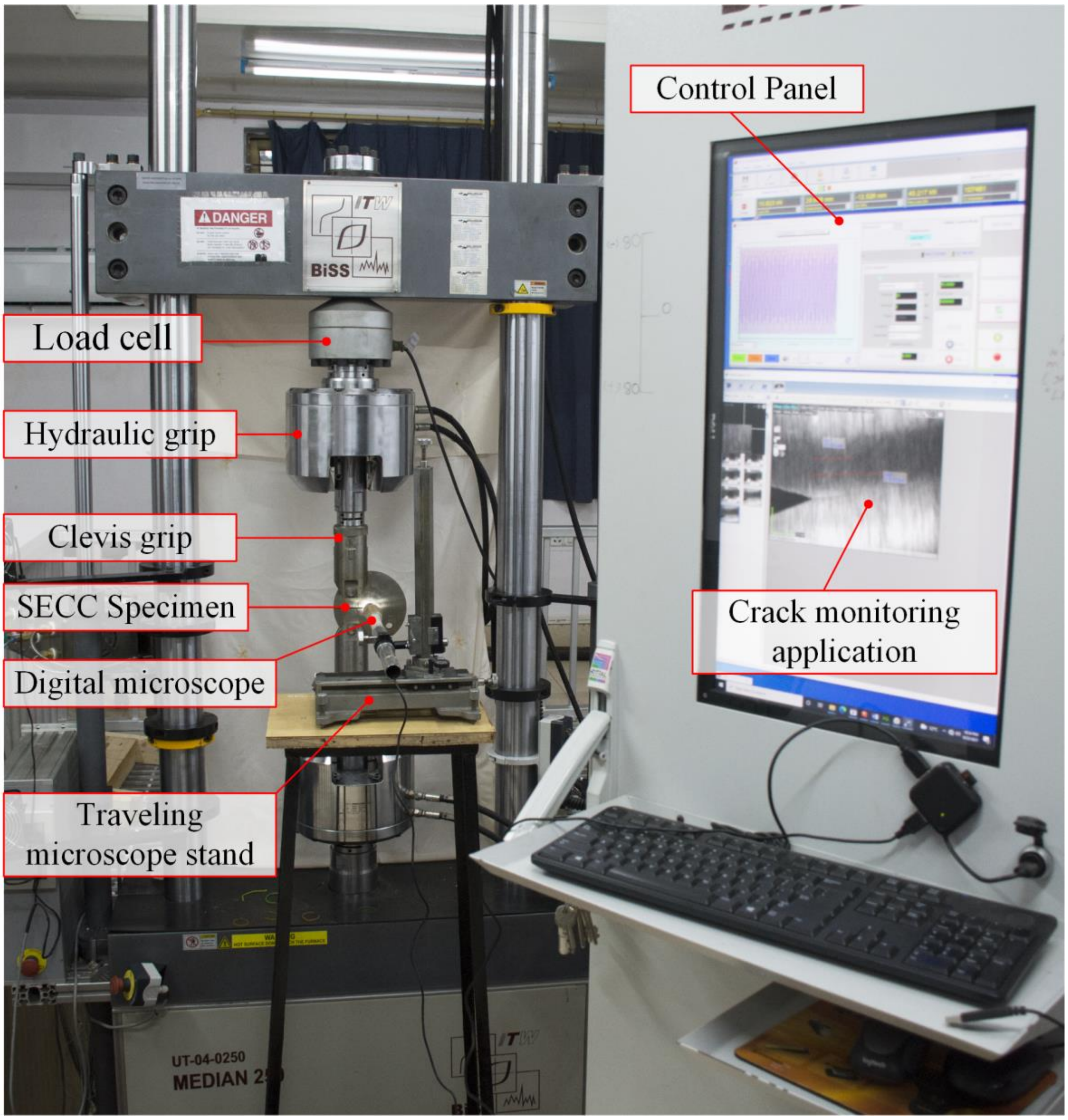

Fig. 4.20 Complete experimental setup used for the mixed mode (I/II) fatigue crack growth studies on Al 7075-T6 alloy and AISI 304 steel.

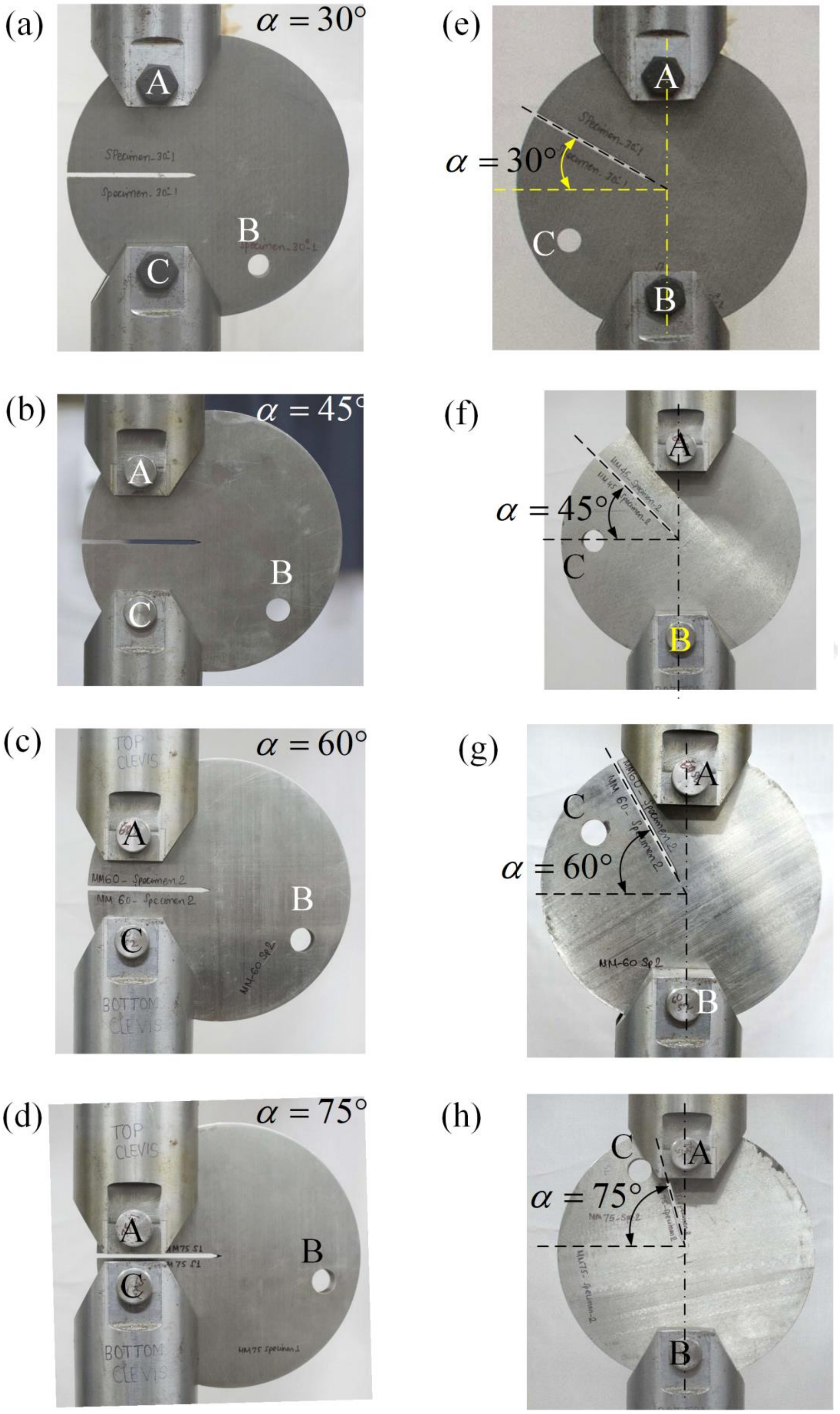

Fig. 4.21(a)-(d) Precrack orientation of the SECC specimen. (e)-(h) Mixed mode (I/II) orientation of the SECC specimen under four different loading angles.

4.7.4 Experimental setup for mixed mode (I/III) and (I/II/III) FCG studies on Al 7075-T6 alloy

Fig. 4.22a shows the experimental setup used for conducting the mixed mode (I/III) FCG studies using the SECC specimen (made of Al 7075-T6 alloy) and J-fixture. The specimen is attached with the J-fixture, and the complete loading assembly is connected with the UTM such that $\alpha = 0°$, $\phi = 45°$ (Fig. 4.22a). This arrangement, thus, induces mixed mode (I/III) fatigue loading to the specimen. Similarly, Fig. 4.22b shows the loading setup used for conducting the mixed mode (I/II/III) FCG studies on Al 7075-T6 alloy such that $\alpha = 45°, \phi = 45°$.

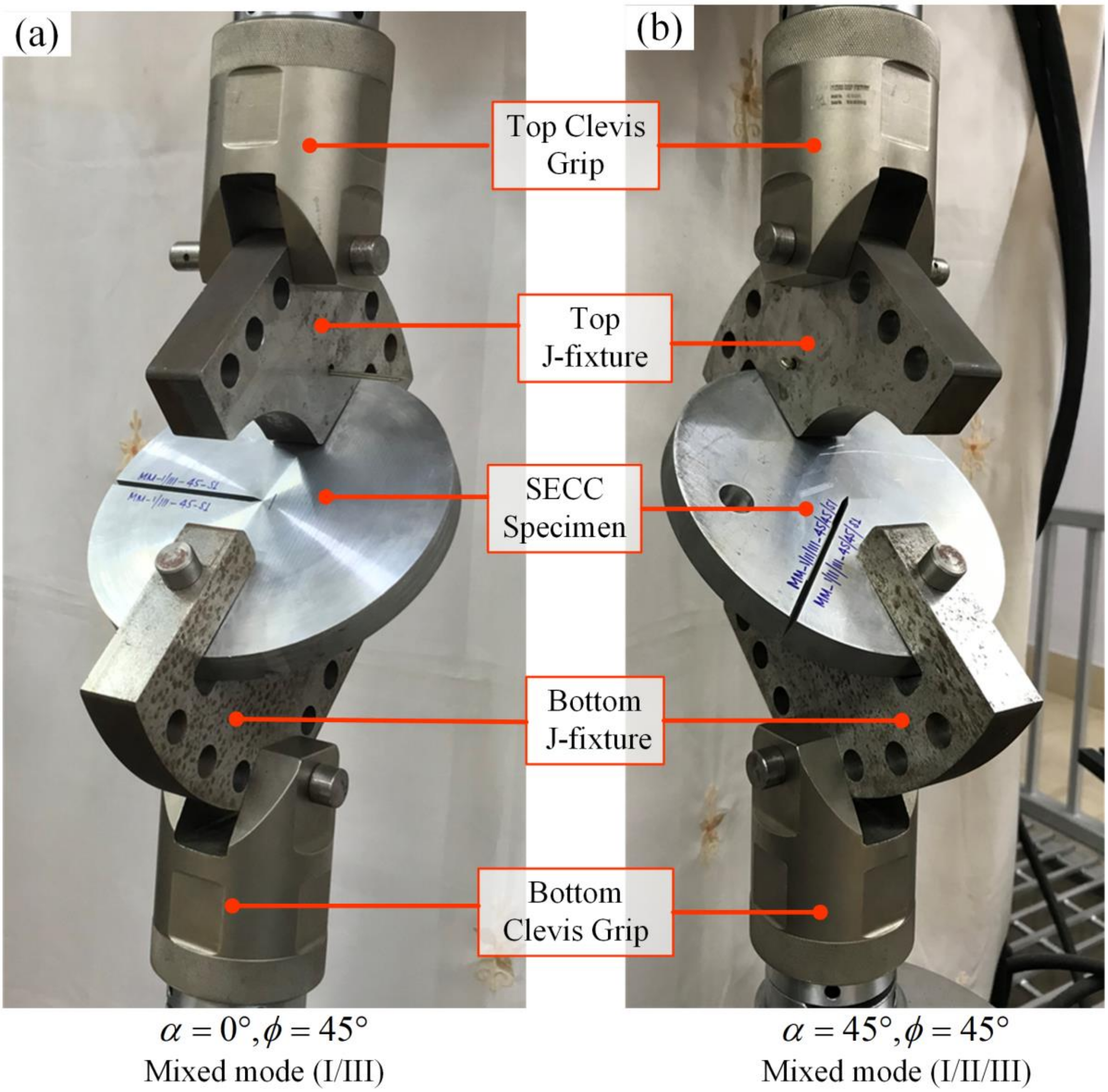

Fig. 4.22(a)The loading setup used for the mixed mode (I/III) FCG studies on Al 7075-T6 at an angle $\alpha = 0°, \phi = 45°$. (b) The loading setup used for the mixed mode (I/II/III) FCG studies at an angle $\alpha = 45°, \phi = 45°$.

4.7.5 Experimental setup for mode I FCG tests using CT specimen under constant amplitude cyclic loading

Fig. 4.23 shows the experimental setup for conducting the mode I FCG test using the CT specimen. The mode I FCG test on the CT specimen has been performed using the Variable Amplitude Fatigue Crack Propagation (VAFCP) module in-built into the testing machine. The instantaneous crack length in the CT specimen is measured using a clip gauge (or COD gauge). The CT specimens are connected to the top and bottom clevis grips using pins of diameter 12.7 mm as shown in Fig. 4.23. The COD gauge used in the present experiments is BiSS AC-07-0020, which has a 10 mm gauge length and +4 mm/ -1 mm travel range. The COD gauge is firmly mounted to the knife edges provided on the front face of the CT specimen (Fig. 4.23). The parallelism of both knife edges is checked to ensure that the COD gauge does not slip during the cyclic loading. This is ensured by moving the gauge along the knife edges and checking the gauge readings.

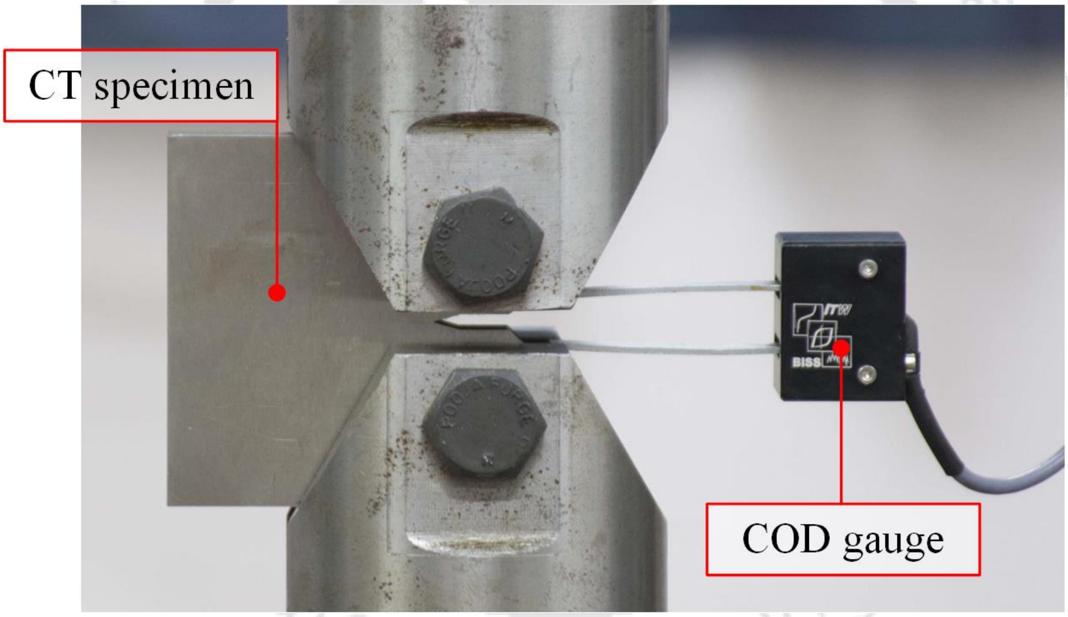

Fig. 4.23 Mode I FCG test set up for the CT specimen showing the COD gauge.

4.8 Procedure for measurement of crack kink angle θ_0

The crack kink angle (or fracture initiation angle) θ_0 of the fractured PMMA SECC specimens tested under the different mixed mode (I/II) loading conditions has been measured using the OPTOMECH make profile projector (Fig. 4.24a). First, the fractured specimen has been placed on the projector table, and the light is made to pass through it such that the magnified image of the specimen is projected on the projector screen. Then the crack kink angle has been measured using a digital measuring device attached to the profile projector. The tangent angle at the beginning of the crack propagation has been considered as the crack kink angle θ_0 as shown in Fig. 4.24b.

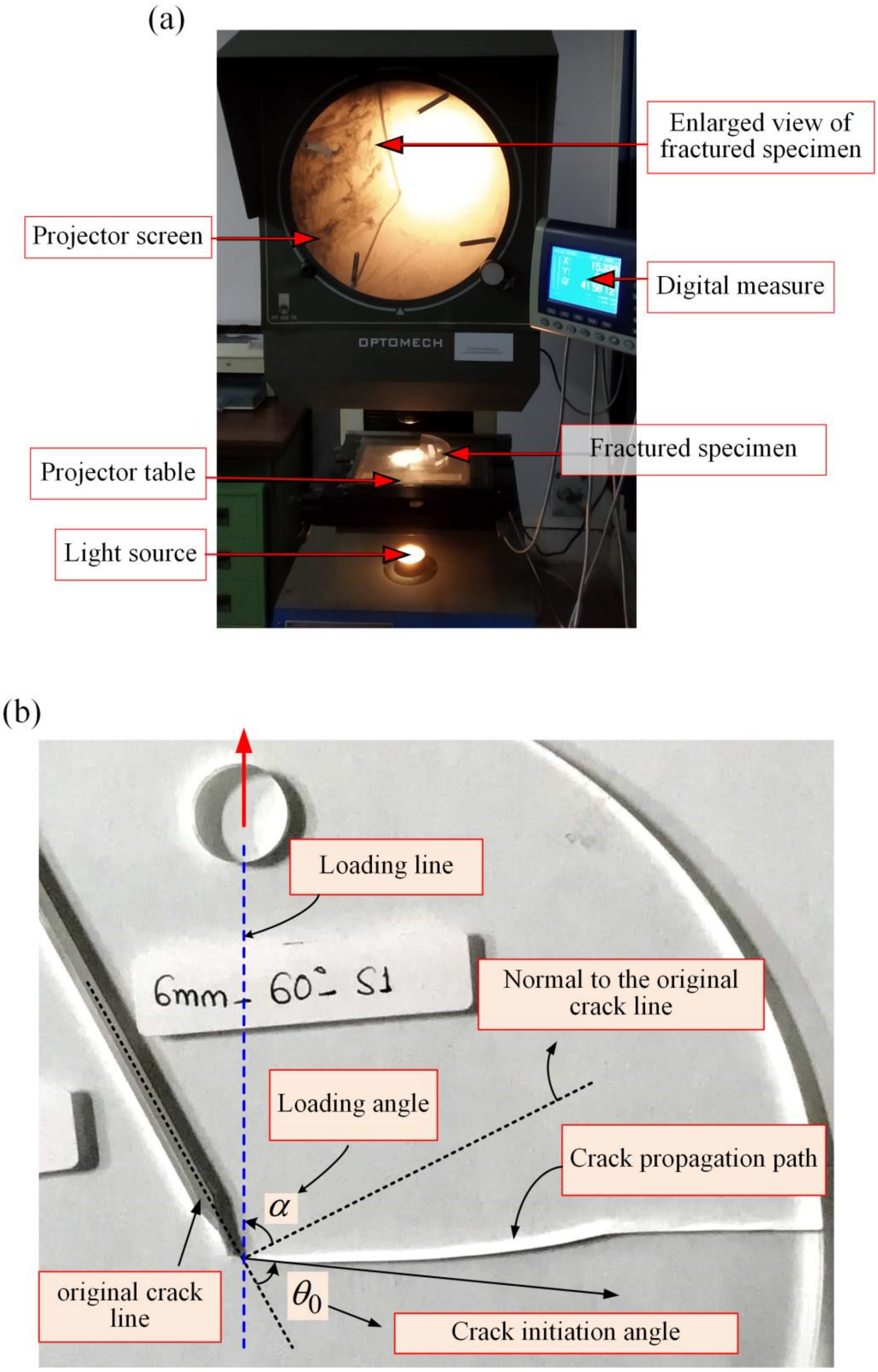

Fig. 4.24 (a) Profile projector used for measuring crack kink angle. (b) Measurement of the crack initiation angle θ_0 from the fractured specimen.

4.9 Procedure for measurement of crack twist angle ψ_0

Measurement of twist angle is a complex process. The complete procedure adopted for measuring the crack twist angle from the fractured PMMA SECC specimen under mixed mode (I/III) is shown in Fig. 4.25. To illustrate the adopted procedure, a photograph of the fractured specimen under $\phi = 75°$ is shown in Fig. 4.25a. Fig. 4.25b shows the enlarged view of the fractured surface showing the approximate location of section A-A at which the crack twist angle ψ_0 has been measured. A schematic view of the fractured specimen under mixed mode (I/III) is shown in Fig. 4.25c. The orientation of the newly developed fractured plane with respect to the initial crack plane is shown in Fig. 4.25c. Also, the viewing direction is normal to the assumed section plane A-A is indicated in Fig. 4.25c.

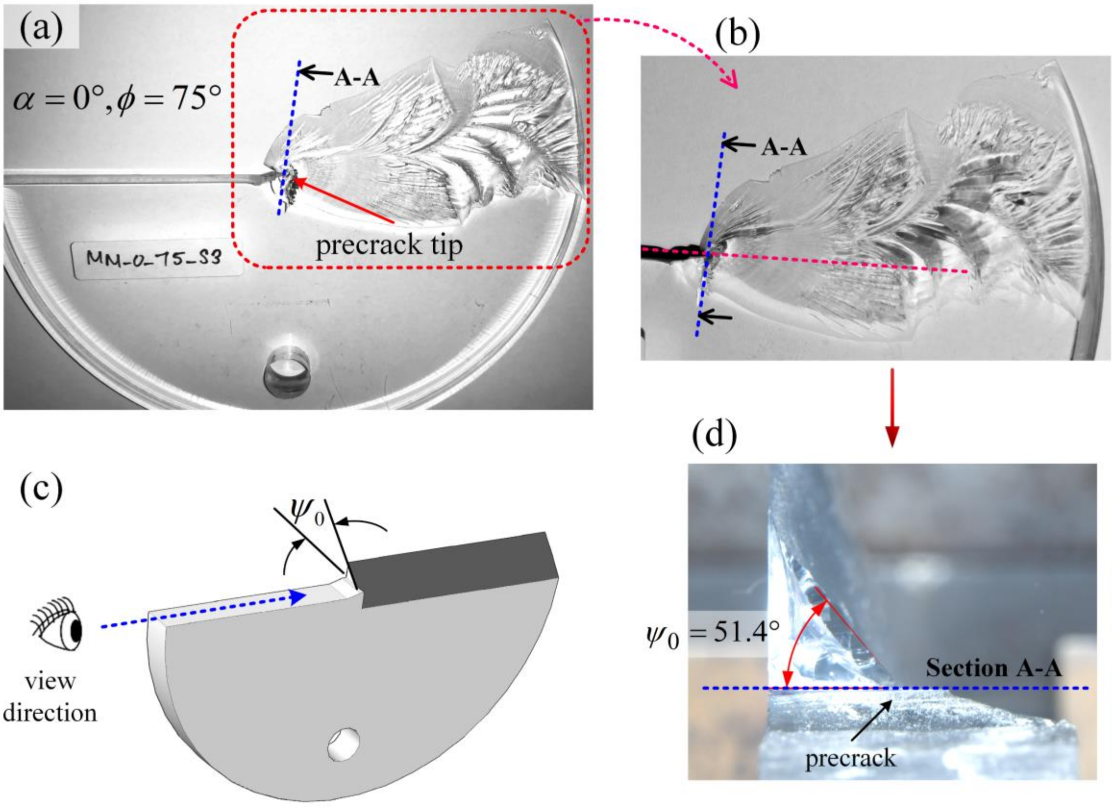

Fig. 4.25 (a) Photograph of the fractured specimen under mixed mode (I/III) loading. (b) close-up view of the fracture surface showing the position of the section plane A-A at which the crack twist angle is measured. (c) schematic diagram showing the orientation of the fracture surface and the viewing direction. (d) measured crack twist angle for the $\phi = 75°$.

Because of the transparent property of the PMMA fractured surfaces, the crack twist angle has been measured using a stereo microscope in the present work. Hence, the fractured

SECC specimen has been first positioned, as shown in Fig. 4.25c, such that the viewing direction is parallel to the initial crack plane. Then the precrack region has been focussed as shown in Fig. 4.25d. Finally, a reference line is drawn (dotted blue line in Fig. 4.25d) at the precrack in the thickness direction, and the orientation of the focussed fractured surface to this reference line has been measured as an approximate crack twist angle ψ_0. It is to be noted here that the selection of the location of section plane A-A (at which the fractured surface is focussed) is very important for measuring ψ_0. In the present analysis, utmost care has been taken to select the location of section plane A-A for different fractured specimens to minimize the measurement errors.

4.10 Pre-cracking procedure for metallic SECC specimens

Before conducting the actual mixed mode FCG tests, all the SECC specimens made of Al 7075-T6 alloy and AISI 304 steel have been fatigue precracked for a final nominal crack length of $a / D_o = 0.5$ that is equal to the length of the starter notch slot plus fatigue precrack Δa_p. The precrack is generated by loading the specimen using holes B and C (Fig. 4.26a), and applying a constant amplitude cyclic loading with maximum load of $P_{max} = 6$ kN for Al 7075-T6, and $P_{max} = 20$ kN for AISI 304 steel. Then, a load ratio $R = 0.1$ and frequency 10 Hz has been used. Initially, a marker line is drawn at a required distance from the notch tip (Fig. 4.26b), and then the length of precrack is monitored using the digital microscope. Once the precrack reaches this marker line, the precracking is stopped. In addition, all the specimens are subjected to a minimum 10^5 number of load cycles during precracking.

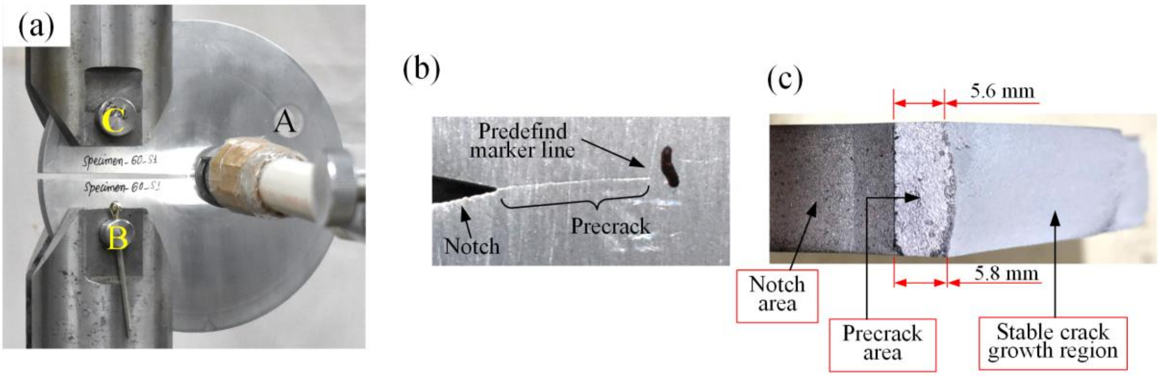

Fig. 4.26 (a) Precracking configuration of the SECC specimen. (b) Generated pre-crack at the notch tip. (c) Symmetric crack front at the end of pre-cracking step.

Fig. 4.26b shows the typical precrack obtained at the end of this step. It can be observed from Fig. 4.26c that crack front after the precracking is almost symmetric to the midplane of the specimen, and the difference between the crack sizes measured on front and back surface has been within the permissible range of 0.25×thickness of specimen (ASTM E647). The symmetric crack front affirms the symmetric load distribution in the thickness direction of the SECC specimen as well as the consistency and accuracy of the loading setup. Which also ensures the consistency of crack length measurement only on one surface of the specimen.

4.11 Determination of crack length during mixed mode (I/II) FCG tests

The measurement of the growing crack during the fatigue loading is one of the most tedious and time-consuming tasks of the present investigation. Due to the presence of the mode II component in the mixed mode (I/II) fatigue loading, clip gauges are found not suitable for crack growth measurements. Therefore, optical methods are commonly used to measure the crack lengths in such situations [28,29,227,228]. In the present work, a DinoLite Pro digital microscope (mounted on a traveling microscope stand) has been used to measure the crack lengths during the mixed mode FCG test (Fig. 4.27a). The crack length measurement procedure adopted by Sajith et al. [28,29] has been used in the present work. Initially, the magnified view of the crack tip is focused such that it is clearly visible. Subsequently, a highly accurate 5 mm scale has been used to calibrate the microscope at this specific magnification (Fig. 4.27c). Then, the crack tip images have been captured regularly at intervals of 5 seconds (Fig. 4.27c,d) using DinoCapture software, which is in-built with the microscope. Finally, crack growth has been measured by analyzing manually from these large numbers of captured images. In fact, the time interval for capturing the image further decreases as the crack approaches the final stages.

4.12 Fractography

Fractographic studies are essential to determine microscopic features like striations, secondary cracks, river line patterns, flat facets, etc. These features are the most typical attributes of fatigue fractures. It has been observed that different failure modes leave different features on the fractured surface, which aid in identifying the causes of failure. The field emission scanning electron microscope (FESEM) is an important tool for fractographic studies. In the present work, Zeiss Sigma 300 and Jeol JSM 7610 FESEM machines shown in Fig. 4.28 have been used for the fractographic studies.

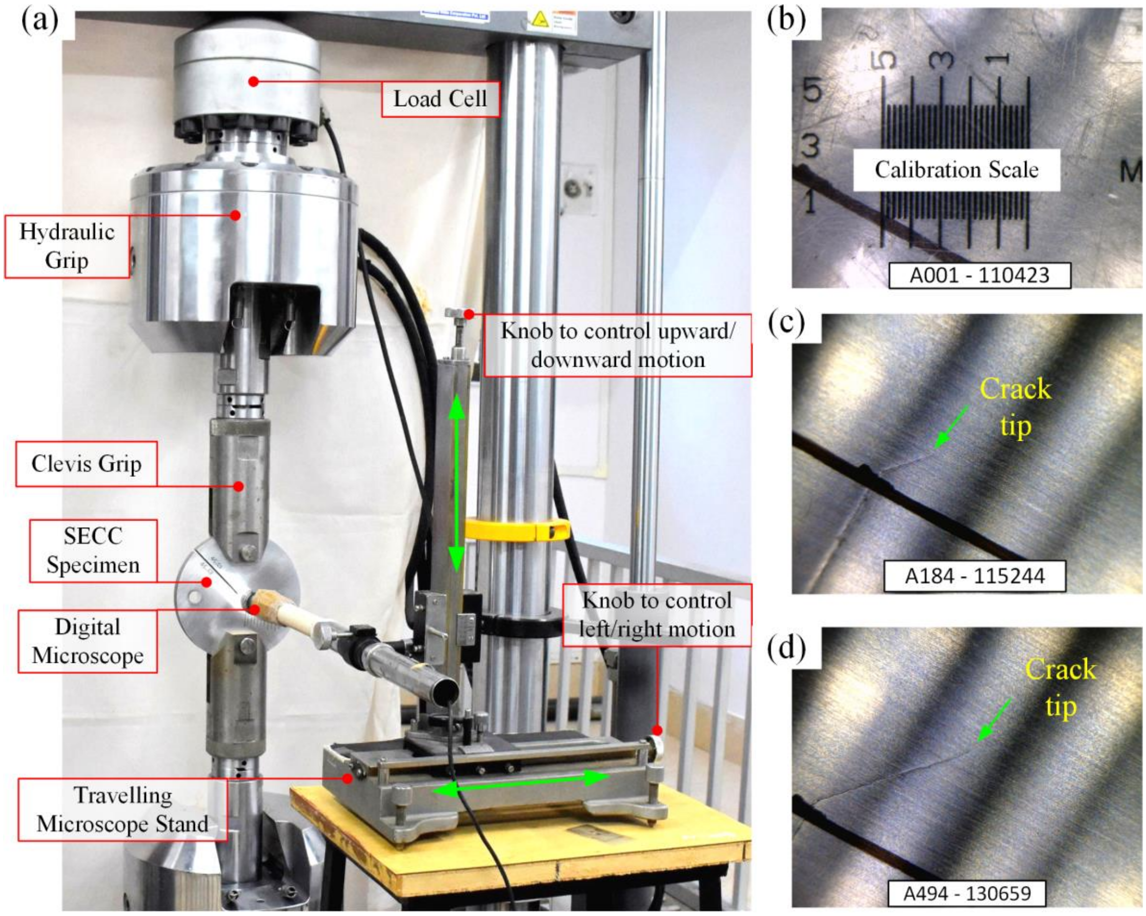

Fig. 4.27 (a) Experimental setup showing the crack growth measurement using DinoLitePro digital microscope. (b) Calibration of the microscope using a 5 mm calibration scale. (c,d) Typical captured images at different time intervals during the mixed mode FCG test.

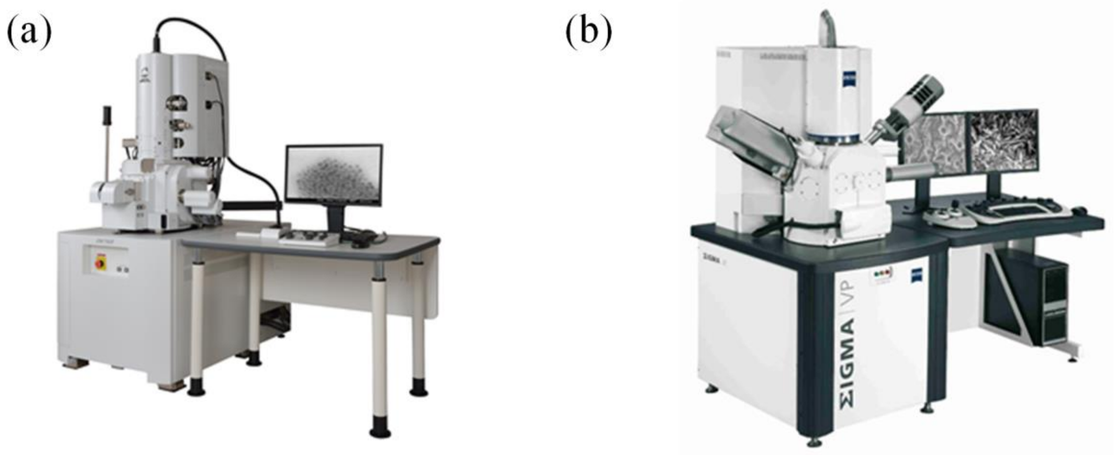

Fig. 4.28 FESEM machines used for the fractographic studies of present work: (a) Zeiss Sigma. (b) Jeol JSM 7610. (Image courtesy: Zeiss Germany, Jeol Japan).

4.13 Summary

This chapter described the design of the proposed SECC specimen, its associated J-fixture (loading device), and other specimens employed in the present study. The fabrication procedure of the SECC specimens from PMMA, Al 7075-T6 alloy, and AISI 304 steel has been described along with all other specimens in detail. Moreover, the details of the complete experimental setups employed for different tests have been provided. These setups have been used for conducting fracture and fatigue crack growth studies under different mixed mode (I/II), (I/III), and (I/II/III) loading conditions in the present research work. The subsequent chapters will discuss the results of experimental and numerical mixed mode fracture and FCG studies that have been performed using the proposed SECC specimen.

Chapter 5

Mixed mode (I/II) fracture studies

This chapter investigates the fracture behaviour under mixed mode (I/II) quasi-static loading using the proposed SECC specimen and compares the performance of the various fracture criteria in prediction of the mixed mode (I/II) fracture. This study also aimed at studying the efficacy of the proposed specimen in conducting such fracture studies. For this purpose, the proposed SECC specimen has been prepared using PMMA material. Two-dimensional finite element analyses have been performed to calculate the variation of SIFs ($K_{\mathrm{I}}, K_{\mathrm{II}}$) and $T-$stress as a function of the loading angles (α) and crack length ratio (a/D_o). Mixed mode (I/II) fracture experiments have been performed on a large number of SECC specimens made of 6 mm and 10 mm thick PMMA sheet material. The consistency of the experimental results has been compared with the widely used mixed mode (I/II) fracture criteria in terms of fracture toughness (or fracture locus), crack kink angle θ_0, and ratios of the critical loads.

5.1 Finite element analyses

All FE analyses of the SECC specimen for mixed mode (I/II) studies have been performed in the commercial software ANSYS®. The dimensions of the proposed SECC specimen given in Table 4.1 have been considered for the FE analyses: $D_o = 160$ mm, $D_i = 118$ mm, $d = 12.8$ mm, and different crack lengths. Young's modulus $E = 2950$ MPa and Poisson's ratio $\nu = 0.38$ have been used in all the FE analyses. These values have been obtained after tensile testing on the selected PMMA sheet material (subsection 5.2.1, Page 97).

5.1.1 Meshing and boundary conditions

Fig. 5.1 shows a typical mesh used for the FE analysis of the SECC specimen. The eight-noded-isoparametric quadratic plane elements have been employed to create the mesh. For modeling the inverse square root singularity near the crack tip, the quarter-point elements have been used in the first layer of elements around the crack tip in a typical spider web pattern. The rest of the geometry has been modeled with the regular eight-noded plane elements. Plane stress conditions have been assumed in all the finite element analyses. Convergence characteristics of the meshes have been studied so that results presented in this investigation are independent of the mesh density (see Appendix B.1).

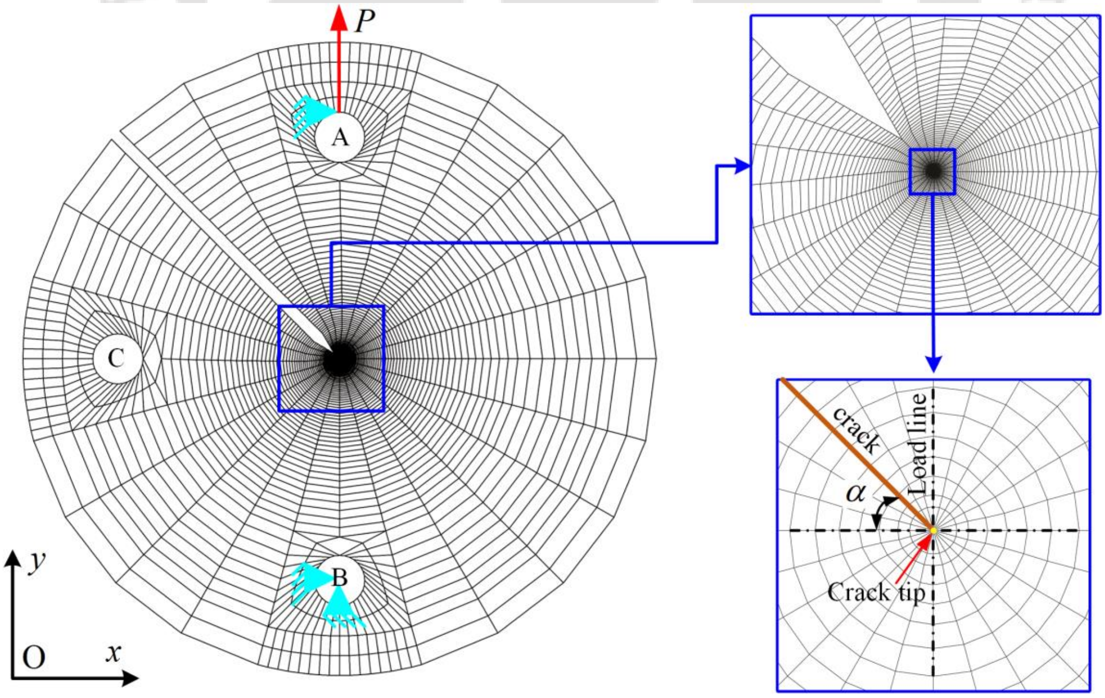

Fig. 5.1 A typical FE mesh of the SECC specimen showing the spider web mesh pattern near the crack tip.

A concentrated load of $P = 1000\,\text{N}$ has been applied at the top-hole A (Fig. 5.1). The periphery of the hole B has been constrained in the x and y directions. Also, the hole A has been constrained in x-direction as shown in Fig. 5.1.

5.1.2 Variation of stress intensity factors

The stress intensity factors (SIFs) and non-singular stress term called $T-$stress have been calculated using the interior collocation method proposed by Jogdand and Murthy [218] from the solutions obtained using ANSYS®. This method provides very accurate values in the computation of the above fracture parameters [229,230]. These parameters are important in testing the efficacy of the proposed SECC specimen. In the present analysis, the loading angle α has been varied from 0° to 80°, and the crack length ratio a/D_o has also been varied from 0.4 to 0.8. The mixed mode SIFs for the SECC specimen can be written as given in Eq. (5.1):

$$\begin{aligned} K_{\mathrm{I}} &= \frac{P}{D_o t}\sqrt{\frac{\pi a}{2}}\,Y_{\mathrm{I}}\left(\frac{a}{D_o},\alpha\right) \\ K_{\mathrm{II}} &= \frac{P}{D_o t}\sqrt{\frac{\pi a}{2}}\,Y_{\mathrm{II}}\left(\frac{a}{D_o},\alpha\right) \end{aligned} \tag{5.1}$$

where $Y_{\mathrm{I}}(a/D_o,\alpha)$ and $Y_{\mathrm{II}}(a/D_o,\alpha)$ are the dimensionless normalized SIFs or geometry factors for the mode I and mode II, respectively, P is the applied force, D_o and t are the diameter and thickness of the SECC specimen, respectively.

Fig. 5.2 shows variation of the normalized SIFs Y_{I} and Y_{II} for the different crack length ratios $0.4 \le a/D_o \le 0.8$ from the present finite element analyses. It can be seen from Fig. 5.2a that for a particular a/D_o, Y_{I} value monotonically decreases as expected. On the other hand, the value of Y_{II} is zero in the pure mode I (see Fig. 5.2b) for all the a/D_o ratios. It then increases with the mode mixity angle α, reaches to a maximum and decreases and converges to a particular value. As expected, both Y_{I} and Y_{II} increase with the increase in a/D_o ratio. Fig. 5.2c shows the variation of ratio $Y_{\mathrm{I}}/Y_{\mathrm{II}}$ for the different crack length ratios. As can be seen from Fig. 5.2c, with an increase of the mode II component, the ratio $Y_{\mathrm{I}}/Y_{\mathrm{II}}$ decreases monotonically and tends towards zero for all the crack length ratios. These results also demonstrate that the performance of the proposed SECC specimen is as expected.

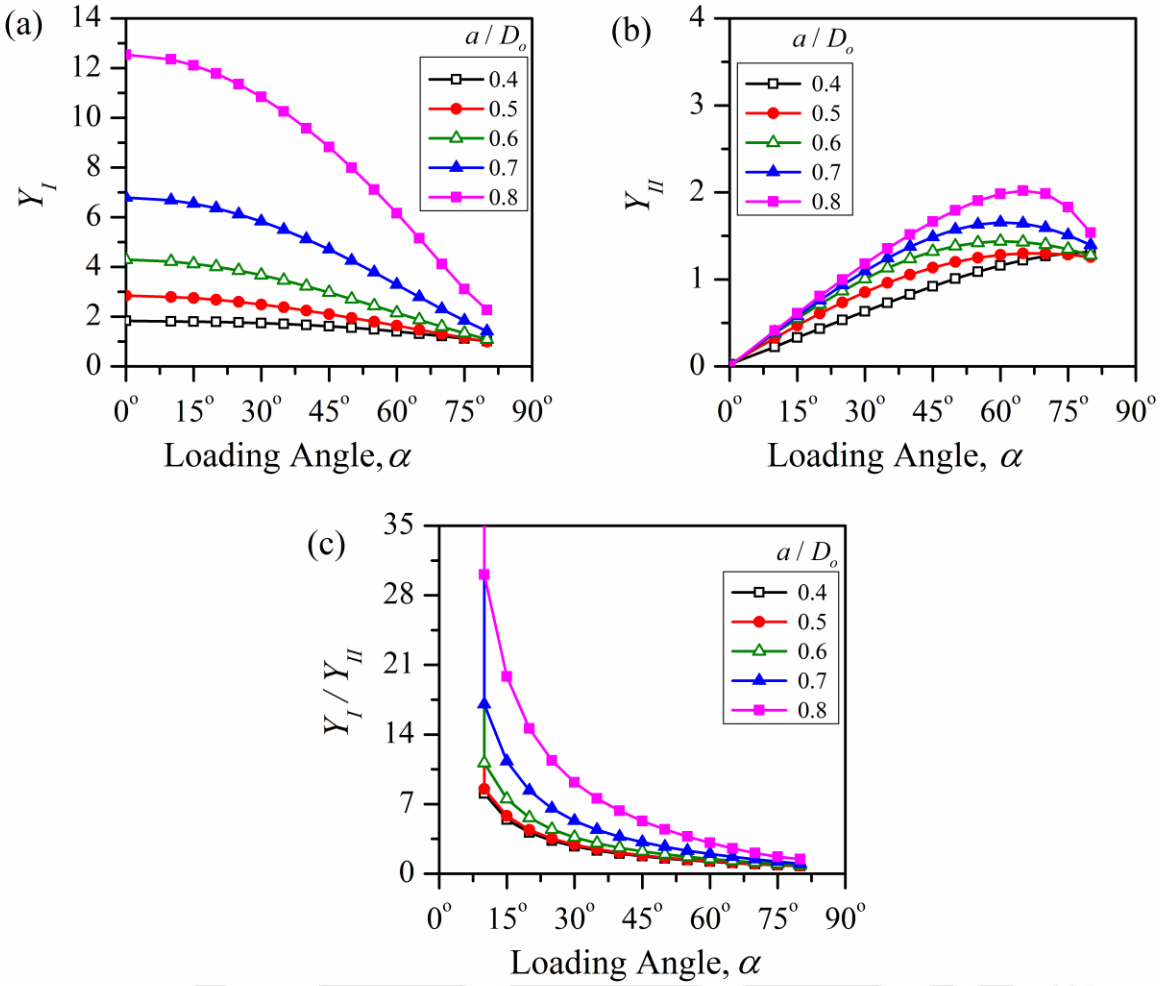

Fig. 5.2 Variation of dimensionless fracture parameters for different crack lengths $0.4 \le a/D_o \le 0.8$. (a) Variation of $Y_{\rm I}$. (b) Variation of $Y_{\rm II}$. (c) Variation of $Y_{\rm I}/Y_{\rm II}$.

5.1.3 Variation of von-Mises stress contours

Fig. 5.3 shows the von Mises stress contour plot for $a/D_o = 0.5$ for two mode mixities: the pure mode I $(K_{\rm II} = 0)$ and a typical mixed mode (I/II) loading where $K_{\rm II} \neq 0$. It can be noticed from Fig. 5.3 that in the case of pure mode I, the stress contour is symmetric with respect to the crack axis. However, in the mixed mode (I/II) loading, the contour is asymmetric with respect to the crack plane. It is well known that the von-Mises stress contour shows a symmetric pattern for pure mode I loading and becomes asymmetric in mixed mode (I/II) loading due to a lack of symmetry. The plotted von-Mises stress contours in Fig. 5.3 substantiate that the proposed specimen behaves as expected when it is loaded using the clevis pins. These results aid further to the results presented in Fig. 5.2, which focus on the SIFs to show the behavior of the specimen.

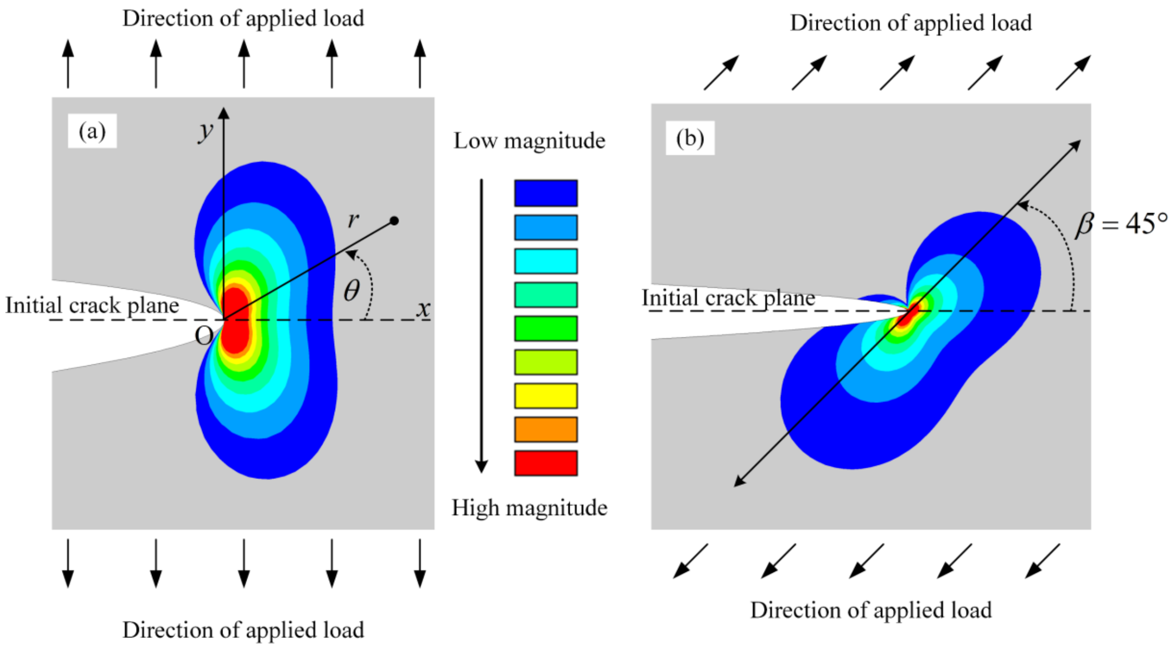

Fig. 5.3 Contours of the von Mises stress: (a) Pure mode I loading. (b) Mixed mode (I/II) loading.

5.1.4 Variation of *T*-stress

Next, $T-$stress analyses of the proposed SECC specimen configuration have been carried out for use in subsequent validation of the specimen. It is a non-singular stress term and unlike other stress terms it is independent of the radial distance from the crack tip. It is found that this stress has a profound effect on the mixed mode (I/II) fracture toughness and crack growth directions [25,50,87]. In general, it has been found that the fracture toughness increases due to the negative $T-$stress and decreases due to the positive $T-$stress value [25,50]. More specifically, the effect of $T-$stress in mixed mode loading is substantial only when the mode II loading is predominant and the magnitude of $T-$stress is significant [50,75,78]. It has also been demonstrated that the magnitude of $T-$stress improves the prediction of the crack initiation angle [75]. The sign and magnitude of this stress depend on the geometry and loading condition of the cracked specimen. Here, the dimensionless $T-$stress has been defined by Eq. (5.2).

$$T = \frac{P}{D_o t} T^*\left(\frac{a}{D_o}, \alpha\right) \tag{5.2}$$

where T^* is the dimensionless form of $T-$stress. Fig. 5.4 shows a variation of T^* for the various crack length ratios. It can be observed from Fig. 5.4 that T^* is negative for some loading angles of lower a/D_o ratios and always positive for all the loading angles for a/D_o ratios of 0.7 and 0.8.

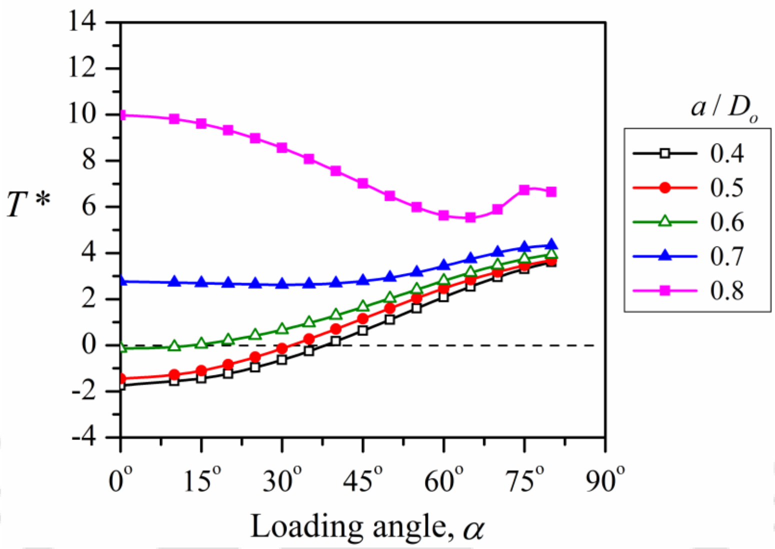

Fig. 5.4 Variation of the normalized T-stress for the various crack lengths and for the different loading angles.

5.2 Experimental analysis

The specimen preparation from PMMA sheet material and the experimental setup for conducting mixed mode (I/II) fracture tests have been explained in subsection 4.6.1 (Page 72) and subsection 4.7.1 (Page 78), respectively. All the fracture tests have been performed under a constant displacement rate of 0.1 mm/min.

A large number of mixed mode (I/II) fracture experiments have been conducted to study the applicability of the proposed SECC specimen and to study the various mixed mode fracture criteria. For this purpose, a total number of 44 specimens have been fabricated from locally available PMMA sheets. The dimensions given in Table 4.1 (Page 66) have been used for the fabrication of all the SECC specimens. Twenty-two (22) specimens have been fabricated from a 6 mm thick single sheet, and the rest 22 specimens have been manufactured from a 10 mm thick single sheet. For each loading angle $\alpha =$ 0°, 15°, 30°, 45°, 60°, and 75°, three to four specimens have been fabricated from each thickness for studying the repeatability of the experimental results. The crack length ratio $a/D_o = 0.5$ has been set in all the specimens. As the thicknesses are small compared to the crack length, it has been assumed that plane stress conditions prevail within the specimen. Although results have not been presented here for the sake brevity, the stress condition has been further verified with the help of 3D finite element analyses (Section 6.1.3, Page 113).

5.2.1 Material properties of PMMA

The material properties of the PMMA sheet have been measured from the tensile test as per ASTM D638-14. All the tensile tests have been conducted with a loading rate of 0.25 mm/min. Fig. 5.5 shows a typical stress-strain plot obtained from the tensile test. The elastic properties of both the thicknesses are found very close to each other, and average of these eight test samples is considered as the elastic properties of both thicknesses. Accordingly, Young’s modulus, Poisson’s ratio and ultimate strength of the PMMA sheets are given in Table 5.1. These experimentally obtained material properties have been used in all FE analyses of the work presented in this section.

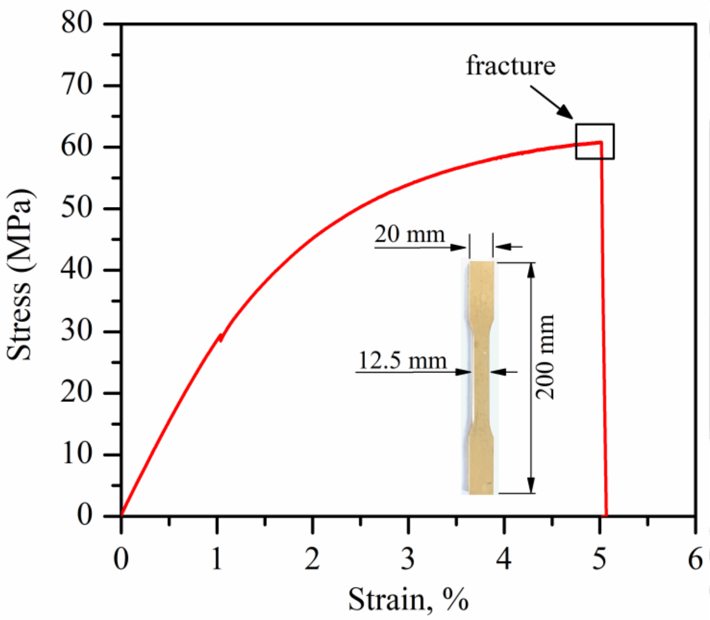

Fig. 5.5 Typical stress vs. strain plot obtained from the tensile tests of the PMMA material.

Table 5.1 Mechanical properties of the PMMA sheet material.

Property	Value
Young’s modulus E	2950 MPa
Poisson’s ratio, ν	0.38
Ultimate strength, σ_{ut}	57 MPa

5.2.2 Mixed mode (I/II) fracture tests

Next the mixed mode fracture tests have been conducted on all the 44 SECC test samples. Typical load-displacement plots for 6 mm and 10 mm thick SECC specimens during the mixed mode fracture tests are shown in Fig. 5.6. It can be observed from Fig. 5.6 that the load-displacement curves of both the types of specimens are linear up to the final fracture. All the specimens fractured suddenly after reaching the critical load showing a brittle fracture of the specimens. The critical loads (Fig. 5.6) have been obtained from the load-displacement plots and used them for calculating the critical SIFs.

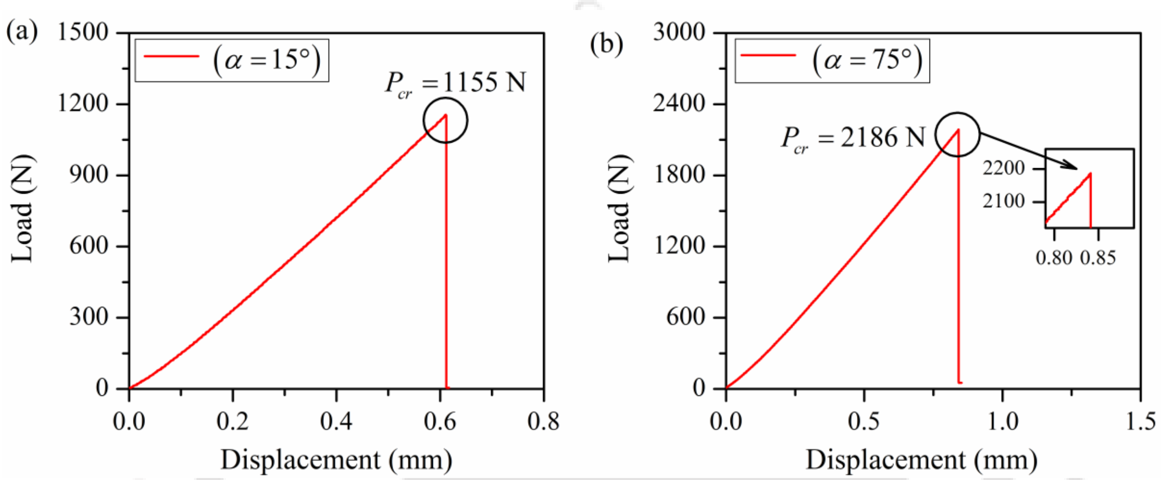

Fig. 5.6 Typical load-displacement plots. (a) Loading angle $\alpha = 15°$ for 6 mm thick SECC specimen. (b) Loading angle $\alpha = 75°$ for 10 mm thick SECC specimen.

The crack or fracture initiation angle θ_0 of the fractured SECC specimens under the different mode mixities has been measured using the profile projector, as explained in Section 4.8 (Page 84). The tangent angle at the beginning of the crack propagation has been considered as the crack kink angle θ_0. The experimental results of the critical loads and that of the kink angles have been then verified with the predicted values using previously described mixed mode (I/II) fracture criteria (Section 3.2, Page 42).

5.3 Experimental results and discussions

Details of each test with the loading angles α of each specimen tested, the measured crack initiation angles θ_0, measured fracture loads P_{cr}, and critical SIFs (K_{If} and K_{IIf}) are listed in Table 5.2 and Table 5.3 for 6 mm and 10 mm, respectively. These critical SIFs have been obtained using the FE analyses at the critical loads measured in the experiments. In these tables θ_0^{avg} represents the average fracture initiation angle of all the specimens of a given

α, similarly, P_{cr}^{avg} represent the average fracture loads. The fracture initiation angle θ_0 in Table 5.2 and Table 5.3 is averaged value measured from both faces of the each of the tested specimen. It can be noticed from Table 5.2 and Table 5.3 that the fracture initiation angle θ_0 corresponding to all the specimens tested for a given α and thickness is close to each other as expected.

Table 5.2 Experimental test results for 6 mm thick SECC specimens.

Specimen ID	α (°)	Crack length (mm)	θ_0 (°)	θ_0^{avg} (°)	P_{cr} (N)	P_{cr}^{avg} (N)	K_{If} $MPa\sqrt{m}$	K_{IIf} $MPa\sqrt{m}$
6mm_0_S1	0	80.11	0	0	1131	1129	1.77	0
6mm_0_S2		80.04	0		1171		1.80	0
6mm_0_S3		79.98	0		1084		1.70	0
6mm_15_S1	15	79.89	15.14	15.15	1155	1081	1.70	0.29
6mm_15_S2		80.26	15.21		1065		1.55	0.27
6mm_15_S3		80.36	15.12		1022		1.52	0.26
6mm_30_S1	30	80.16	29.59	29.88	1304	1193	1.73	0.59
6mm_30_S2		80.25	29.39		1091		1.44	0.49
6mm_30_S3		79.96	30.02		1192		1.60	0.55
6mm_30_S4		79.93	30.55		1184		1.62	0.55
6mm_45_S1	45	80.11	42.19	41.85	1003	1022	1.17	0.63
6mm_45_S2		80.33	41.05		1013		1.15	0.62
6mm_45_S3		80.21	42.15		0944		1.07	0.58
6mm_45_S4		79.92	42.03		1126		1.27	0.68
6mm_60_S1	60	80.03	51.22	51.1	1046	1088	0.93	0.73
6mm_60_S2		80.09	51.06		0906		0.81	0.64
6mm_60_S3		80.54	51.03		1094		0.97	0.76
6mm_60_S4		80.10	51.09		1306		1.17	0.91
6mm_75_S1	75	80.44	60.34	60.57	1324	1265	0.84	0.94
6mm_75_S2		80.32	61.26		1258		0.80	0.89
6mm_75_S3		79.94	61.12		1324		0.84	0.94
6mm_75_S4		79.26	59.58		1155		0.73	0.82

Table 5.3 Experimental test results for 10 mm thick SECC specimens.

Specimen ID	α (°)	Crack length (mm)	θ_0 (°)	θ_0^{avg} (°)	P_{cr} (N)	P_{cr}^{avg} (N)	K_{If} $MPa\sqrt{m}$	K_{IIf} $MPa\sqrt{m}$
10mm_0_S1	0	79.98	0	0	1658	1740	1.64	0
10mm_0_S2		80.16	0		1755		1.70	0
10mm_0_S3		79.84	0		1806		1.71	0
10mm_15_S1	15	80.12	14.55	15.05	1924	1721	1.76	0.30
10mm_15_S2		80.26	15.48		1763		1.59	0.27
10mm_15_S3		80.24	15.13		1477		1.33	0.23
10mm_30_S1	30	80.11	31.23	31.08	1359	1523	1.17	0.40
10mm_30_S2		79.86	30.37		1592		1.36	0.47
10mm_30_S3		80.34	31.02		1381		1.19	0.41
10mm_30_S4		79.96	30.10		1761		1.52	0.52
10mm_45_S1	45	80.12	41.16	41.03	1595	1463	1.17	0.63
10mm_45_S2		80.24	39.50		1424		1.04	0.56
10mm_45_S3		80.96	40.52		1414		1.03	0.56
10mm_45_S4		80.14	41.34		1419		1.04	0.56
10mm_60_S1	60	80.18	52.28	51.52	1904	1634	1.08	0.85
10mm_60_S2		80.32	51.09		1631		0.92	0.72
10mm_60_S3		80.02	52.33		1475		0.83	0.65
10mm_60_S4		80.96	50.40		1525		0.87	0.68
10mm_75_S1	75	80.86	58.28	60.24	2186	2005	0.87	0.98
10mm_75_S2		80.96	60.35		1810		0.72	0.81
10mm_75_S3		80.34	61.35		1988		0.79	0.89
10mm_75_S4		80.16	61.00		2034		0.81	0.91

Fractured specimens of 6 mm and 10 mm thickness have been shown in Fig. 5.7. Post-fracture analysis of the tested SECC specimens showed that a curvilinear crack growth not parallel to the crack axis has been observed in all the mixed mode (I/II) loading conditions.

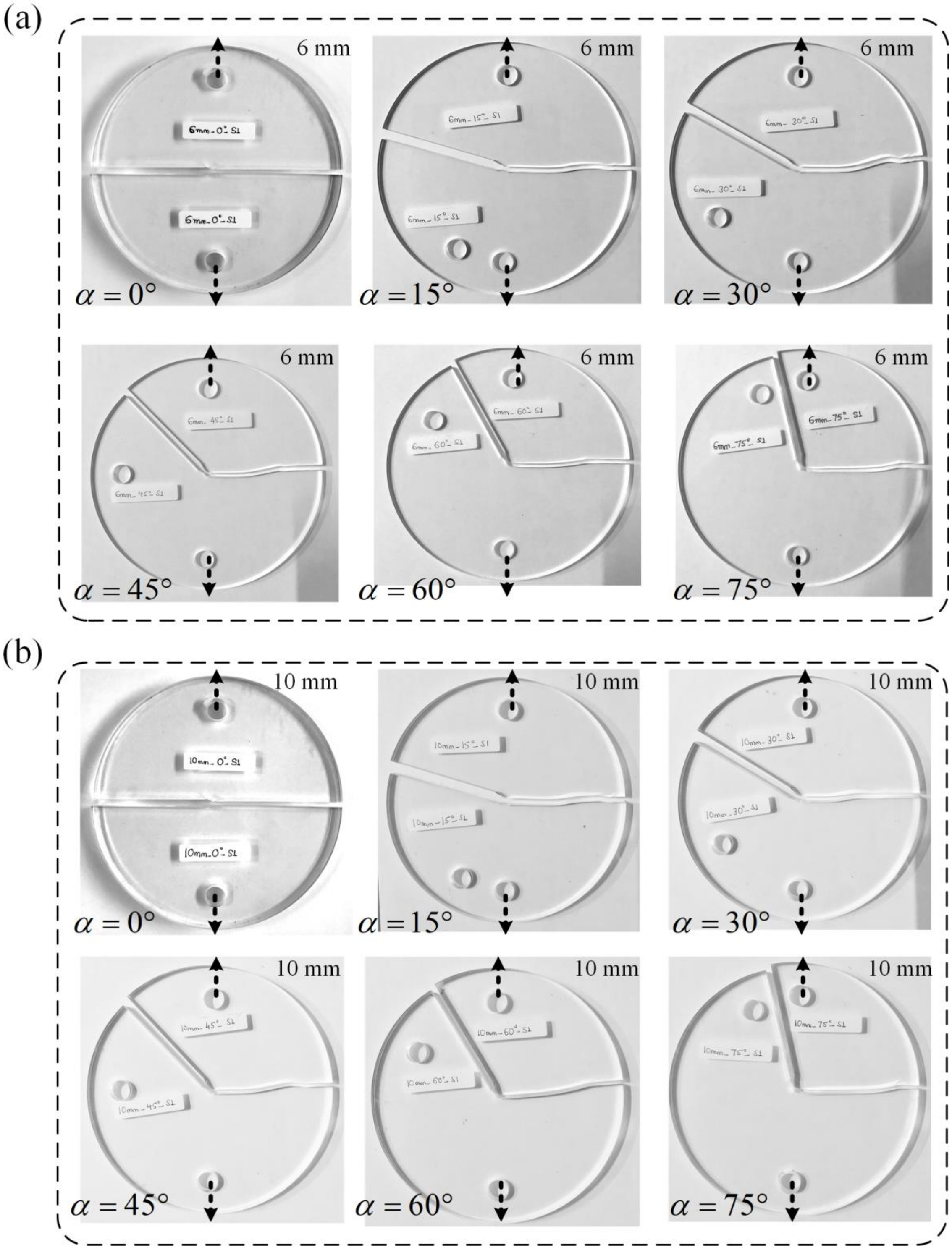

Fig. 5.7 Fractured SECC specimens at different mode mixity. (a) 6 mm thick specimens. (b) 10 mm thick specimens.

However, a self-similar crack propagation trajectory has been clearly noticed in the pure mode I, i.e., $\alpha = 0°$, tests as shown in Fig. 5.7. As expected, it is interesting to notice from Table 5.2 and Table 5.3 that the crack kink angles θ_0 for 6 mm and 10 mm thick specimens are nearly the same as expected. Furthermore, θ_0 also increases with increasing mode mixity, as also noticed by other researchers [25,78]. The variation of the average critical load $P_{\mathrm{cr}}^{\mathrm{avg}}$ per unit thickness with loading angle α is also nearly the same for both the 6 mm and 10 mm plates, as expected. As expected, due to the higher cross-sectional area, higher average critical loads can be noticed in 10 mm specimens than in 6 mm specimens. In both cases, the lowest critical load is observed for $\alpha = 45°$ and highest is observed for $\alpha = 75°$.

Average of the measured crack initiation angles θ_0^{avg} of 6 mm and 10 mm thick specimens have been compared as shown in Fig. 5.8 with predictions made by the selected mixed mode (I/II) crack growth criteria.

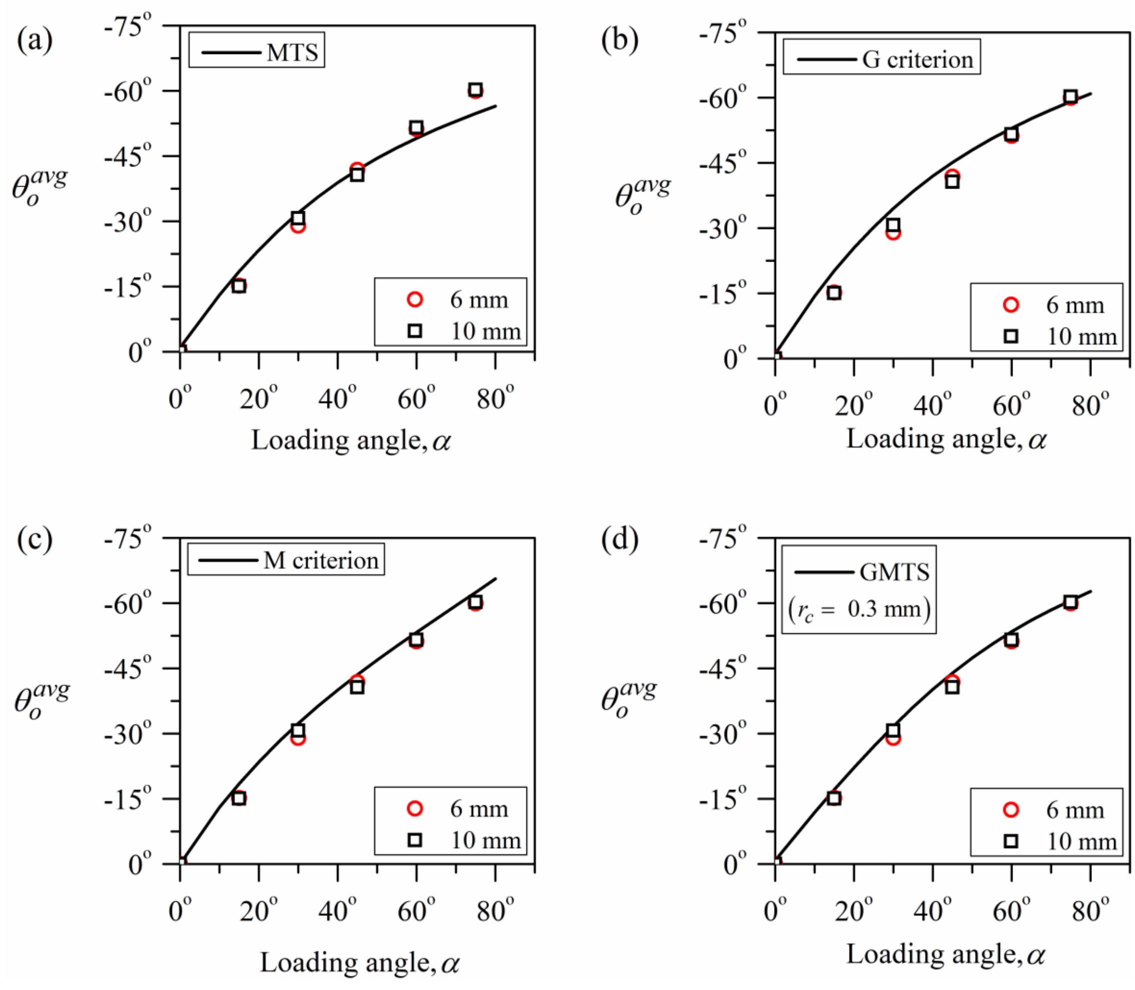

Fig. 5.8 The crack initiation angles for 6 mm and 10 mm thick SECC specimens and comparison of the experimental results with the theoretical criteria. (a) MTS. (b) G-criterion. (c) M-criterion. (d) GMTS-criterion.

It can be seen from Fig. 5.8a-d that the experimental results of both the 6 mm and 10 mm thick specimens have been in very good agreement with the theoretical predictions of the MTS, GMTS (with $r_c = 0.3$ mm), M and G-criteria for almost all the loading angles considered here. The effect of $T-$stress can be clearly seen when GMTS (Fig. 5.8d) is compared with the classical MTS criteria (Fig. 5.8a), specifically when mode II is predominant. As mentioned in subsection 3.2.5 (Page 46), ASED criterion is available only for the prediction of the fracture load rather than the kink angle and therefore has not been presented in Fig. 5.8.

Next, the mixed mode (I/II) fracture results have been presented in the form of the fracture limit or fracture toughness curves or fracture locus by plotting the normalized $K_{\mathrm{II}} / K_{\mathrm{Ic}}$ versus $K_{\mathrm{I}} / K_{\mathrm{Ic}}$. The expressions presented in subsection 3.2 (Page 42) have been employed here in obtaining the fracture limit curves of the selected mixed mode (I/II) fracture criteria. For this purpose, the mode I fracture toughness K_{Ic} is also needed and has been obtained from the experimental results corresponding to $\alpha = 0°$. The average K_{Ic} of 6 mm and 10 mm thick specimens has been found to be equal to $K_{\mathrm{Ic}} = 1.77\,\mathrm{MPa\,m^{1/2}}$ and $K_{\mathrm{Ic}} = 1.72\,\mathrm{MPa\,m^{1/2}}$, respectively. These values are in the range of $1.0-2.0\ \mathrm{MPa}\sqrt{\mathrm{m}}$ reported in the literature by other researchers also [25,78]. Thus, for both the thickness, the value of K_{Ic} is nearly the same as expected.

Fig. 5.9 shows comparison of the present experimental results of all 44 specimens (Table 5.2 and Table 5.3) with the predicted fracture limit or toughness curves obtained using the selected mixed mode (I/II) fracture criteria. As stated earlier in subsection 3.2.4 (Page 45), the $M-$criterion is available only for the prediction of the crack kink angle rather than the critical loads and therefore has not been presented in Fig. 5.9.

An important aspect of the static mixed mode (I/II) facture experiments is the presence of significant scatter in the experimental results. Such intrinsic behavior in the data has been reported by many researchers [19,21,25,80,94,231,232]. In order to unveil more conclusive results, Fig. 5.10 shows the comparison of the averaged experimental results of 6 mm and 10 mm thick specimens with the predicted fracture toughness curves. For this purpose, the average experimental critical load $P_{\mathrm{cr}}^{\mathrm{avg}}$ given in Table 5.2 and Table 5.3 has been employed for the calculation of $K_{\mathrm{I}} / K_{\mathrm{Ic}}$ and $K_{\mathrm{II}} / K_{\mathrm{Ic}}$ values.

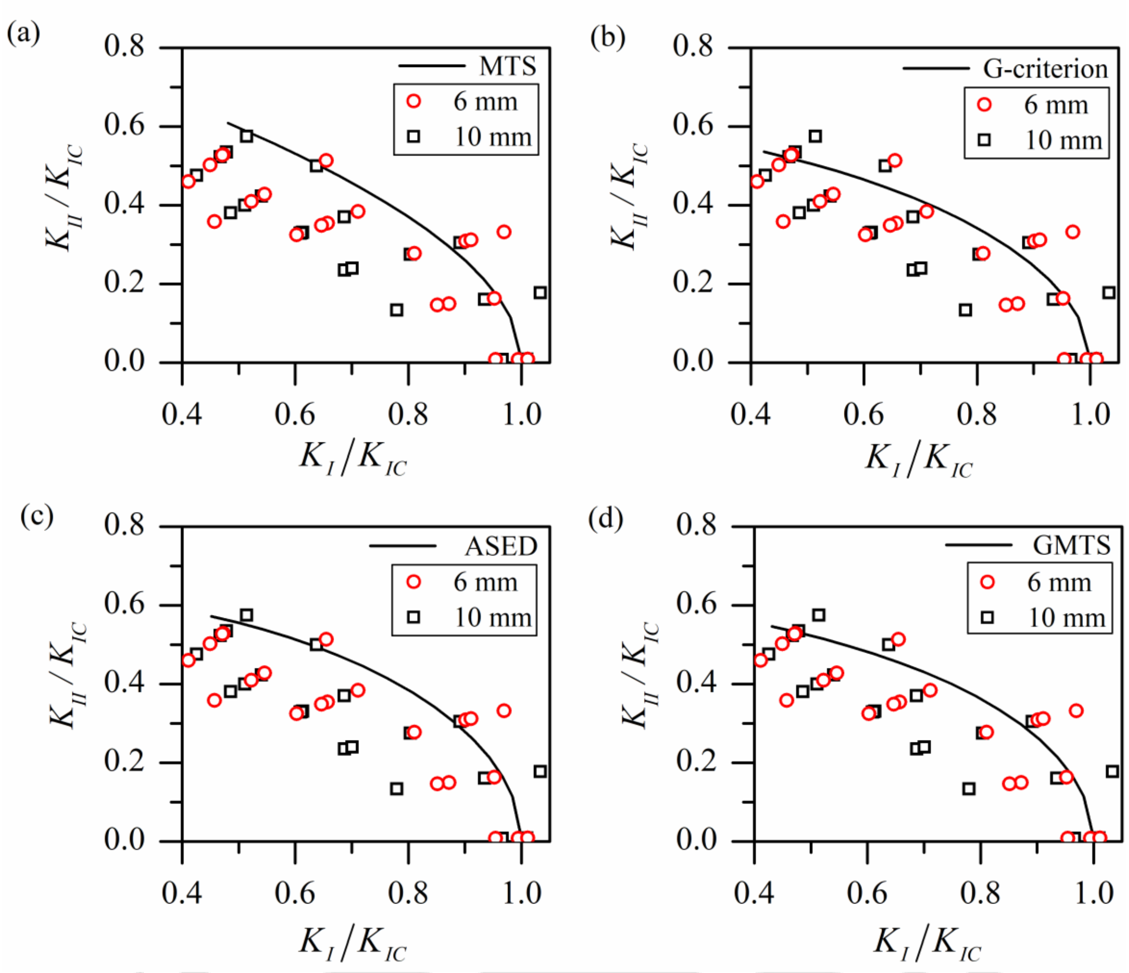

Fig. 5.9 Experimental results of 6 mm and 10 mm thick SECC specimens along with the fracture limit curves. (a) MTS criterion. (b) G- criterion. (c) ASED. (d) GMTS criterion.

It can be clearly seen from Fig. 5.10 that, despite the natural scatter in the experimental results, the averaged experimental results of 6 mm thick and 10 mm thick specimens are in very good agreement with predictions made by the $G-$criterion, ASED-criterion, GMTS-criterion ($r_c = 0.3$ mm) for the entire range of mode mixity considered here. The MTS criterion has deviated a little far from the experimental data, especially at higher mode mixities. At lower mode mixities all criteria have exhibited similar predictions.

The effect of $T-$stress can be clearly seen when the GMTS (Fig. 5.10d) results have been compared with the classical MTS criteria (Fig. 5.10a). It should be noted that the effect of $T-$stress is more prominent when mode II is predominant [25,50]. It is also interesting to notice from results in Fig. 5.10 that there is very good agreement of the experimental results with both the energy-based methods, i.e., $G-$criterion, and the ASED-criterion. In summary, the experimental results of the present proposed specimen are in very good agreement with the predictions made by the three widely used mixed mode (I/II) fracture criteria.

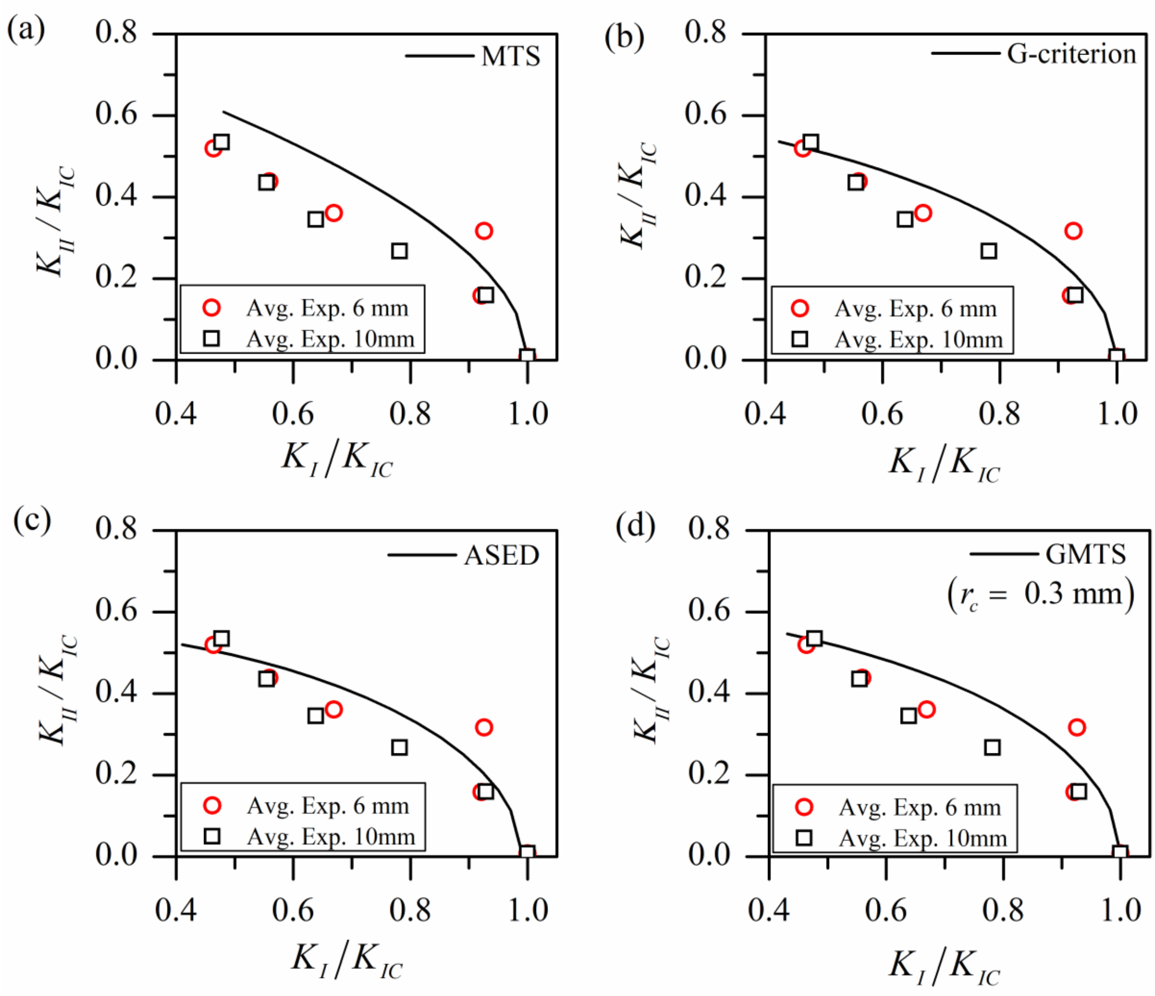

Fig. 5.10 The average experimental results of 6 mm and 10 mm thick SECC specimens along with fracture limit curves. (a) MTS. (b) G-criterion. (c) ASED. (d) GMTS criterion.

The maximum error between experimental loads and theoretical estimation of the MTS, ASED, G and GMTS criterion for 6 mm thick specimens are 37%, 36%, 27%, and 30%, respectively. Similarly, for 10 mm thick specimens, the maximum error for the MTS, ASED, G and GMTS estimations are 27%, 26%, 22%, and 24%, respectively. These errors have been mainly due to one of the four specimens tested. The remaining three specimens have exhibited a maximum error less than 24 %.

5.4 Summary

In this chapter, the suitability of the proposed SECC specimen and the performance of various mixed mode fracture criteria has been investigated by conducting extensive numerical and experimental studies on PMMA. The FE method has been adopted to calculate the SIFs and $T-$stress as a function of the loading angle and crack length ratio. A large number of the SECC specimens made of 6 mm and 10 mm thick PMMA material have been tested under different mixed mode (I/II) loading conditions, and the resultant loads and crack initiation angles have been verified by existing mixed mode (I/II) fracture criteria. The results of the present investigation using a large number of FE analyses and static fracture experiments on the PMMA specimens clearly show that crack initiation angles and fracture toughness of PMMA agree well with the widely used existing mixed mode (I/II) fracure criteria and the proposed SECC specimen can be recommended for conducting the mixed mode (I/II) fracture tests.

Chapter 6

Mixed mode (I/III) fracture studies

This chapter investigates the fracture behaviour under mixed mode (I/III) quasi-static loading using the proposed SECC specimen along with the J-fixure loading device and compares the performance of the various fracture criteria in prediction of the mixed mode (I/III) fracture. This study also aimed at studying the efficacy of the proposed specimen setup in conducting such fracture studies. For this purpose, the proposed SECC specimens have been prepared using PMMA material. Also, the efficacy of the proposed loading setup to perform mixed mode (I/III) fracture studies has also been examined by three-dimensional finite element analyses in this chapter. Furthermore, a large number of mixed mode (I/III) experiments have been performed on the SECC specimens made of 12 mm thick PMMA sheet material. Detailed analyses of the fractured surfaces have been carried out, and the experimental results are compared with the available mixed mode (I/III) fracture criteria in terms of crack twist angle ψ_0 and fracture locus.

6.1 Finite element analyses

This section presents detailed 3D FE analyses of the proposed specimen setup using ANSYS® APDL software to understand its characteristics and performance while loading under the mixed mode (I/III). First, details about the finite element mesh and the boundary conditions used have been presented in subsection 6.1.1. Subsection 6.1.2 focuses on the determination of the mixed mode SIFs and their variation across the thickness to understand the behavior of the setup under mixed mode (I/III) loading. Detailed 3D von-Mises stress analyses at every point of the test setup under mixed mode (I/III) loading have been presented in subsection 6.1.4 to identify the potential sites of failure in the setup.

To achieve these goals, the dimensions of the SECC specimen given in Table 4.1 (Page 66) have been employed. The dimensions of the proposed J-fixture provided in Fig. 4.4b (Page 68) have been used to create the FE model in ANSYS®. PMMA has been used as the SECC specimen material. Material properties of PMMA given in Table 5.1 (Page 97), Young's modulus $E = 2950$ MPa, Poisson's ratio $\nu = 0.38$, and ultimate strength σ_{ut} = 57 MPa, have been used in all FE analyses of this section. These material properties have been obtained from tensile testing of 12 mm thick PMMA sheet material. Material properties of H13 (high-strength steel) have been employed for the J-fixture.

6.1.1 Finite element discretization and boundary conditions

The 3D FE model of the proposed mixed mode test setup is shown in Fig. 6.1a. 10-noded tetrahedron structural solid elements, termed as SOLID187 element in ANSYS® (subsection 3.5.3, Page 57), have been used to model the J-fixture, and 20-noded structural quadratic brick elements (SOLID186) have been used to mesh the SECC specimen, respectively. Fig. 6.1b shows the FE mesh of the SECC specimen. As shown in Fig. 6.1c, the square root singularity near the crack front has been modeled using the collapsed quarter-point wedge elements. The first layer of elements around the crack front consists of 32 wedge elements in the circumferential direction, and 10 such layers have been placed in the thickness direction of the SECC specimen. The rest of the geometry has been meshed with the regular 20-noded brick elements. The minimum size of the above wedge elements is 0.05 mm near the crack front, and nearly 75,000 elements have been used to model the SECC specimen (Fig. 6.1b).

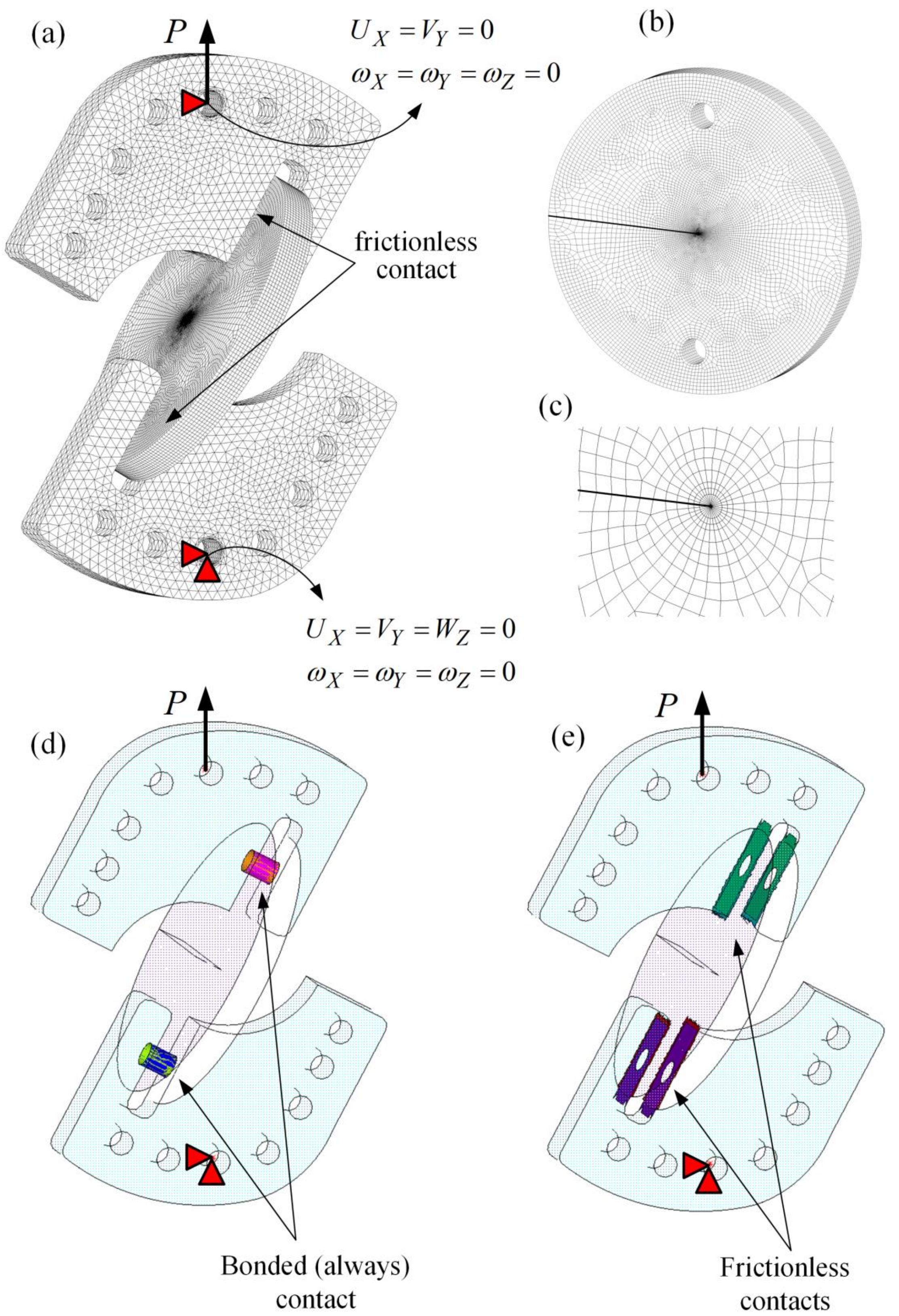

Fig. 6.1 (a) Three-dimensional FE mesh and applied boundary conditions of the test assembly. (b) FE mesh of the SECC specimen. (c) Mesh pattern near the crack front; the first row of elements are quarter-point wedge elements. (d) Bonded contact boundary conditions at the pin joints. (e) Frictionless contact boundary conditions between the SECC specimen and the J-fixture.

Fig. 6.1a shows the boundary conditions used in the present FE analyses. A reference load $P = 1000\ \text{N}$ has been applied to a suitable hole (depending on the required mode mixity) of the top plate of the J-fixture (to induce mode III component). All degrees of freedom (displacements U_i and rotations ω_i) of the corresponding bottom hole have been constrained as shown in Fig. 6.1a. The top hole has been constrained to move only in the load direction by applying boundary conditions, as shown in Fig. 6.1a. The contact between the outer surface of pins and the inner surface of holes of the SECC specimen (used to connect the SECC specimen with the J-fixture) have been modeled as “bonded contact pairs” (Fig. 6.1d) in ANSYS®. On the other hand, “standard frictionless contacts pairs” option has been used to define (in ANSYS® APDL) the contact between the surfaces of the SECC specimen and the surfaces of the top and bottom plates of the J-fixture (Fig. 6.1e).

6.1.2 Computation of the mixed mode SIFs

In the context of LEFM, mixed mode SIFs play an essential role in accurately assessing the efficacy of the proposed test configuration. Interaction integral method (explained in subsection 3.6.2, Page 60) has been employed in the present FE analyses as it has been widely used to compute the mixed mode SIFs [33,140,233], specifically when $K_{\text{I}}, K_{\text{II}}$ and K_{III} are required. Although not presented here, a detailed mesh convergence and verification study have been performed using the computed values of the SIFs, and the results presented in this section are independent of the mesh density (see Appendix B.2). The SECC specimen has been numerically analyzed under different mixed mode (I/III) loading configurations. For this purpose, the in-plane loading angle α has been kept equal to zero, and the out-of-plane loading angle ϕ has been varied from 0° to 90° with an increment of 15°. Normalized SIFs, as given in Eq. (6.1), have been used to present the numerical results.

$$Y_i = \frac{K_i D_o t}{P\sqrt{\pi a}}, \quad i = \text{I}, \text{II}, \text{III} \tag{6.1}$$

where Y_i is the dimensionless geometric factor or normalized SIF, D_o is the specimen diameter, t is the specimen’s thickness, P is the applied load, and a is the crack length. Finite element solutions of the normalized mixed mode SIFs $Y_{\text{I}}, Y_{\text{II}}$ and Y_{III} along the crack front for the case of $\alpha = 0°$ and $\phi = 0°, 15°, 30°, 45°, 60°, 75°$, and 90° have been presented in Fig. 6.2a-g. As shown in Fig. 6.2h, the position of a point along the crack front has been represented by the normalized values of z/t, and the origin of the coordinate system is at the center of the crack front. Here, $2z/t=0$ corresponds to the midpoint of the crack front. $2z/t=-1.0$ and $2z/t=1.0$ correspond to the leading and trailing edges of the crack front, respectively (Fig. 6.2h).

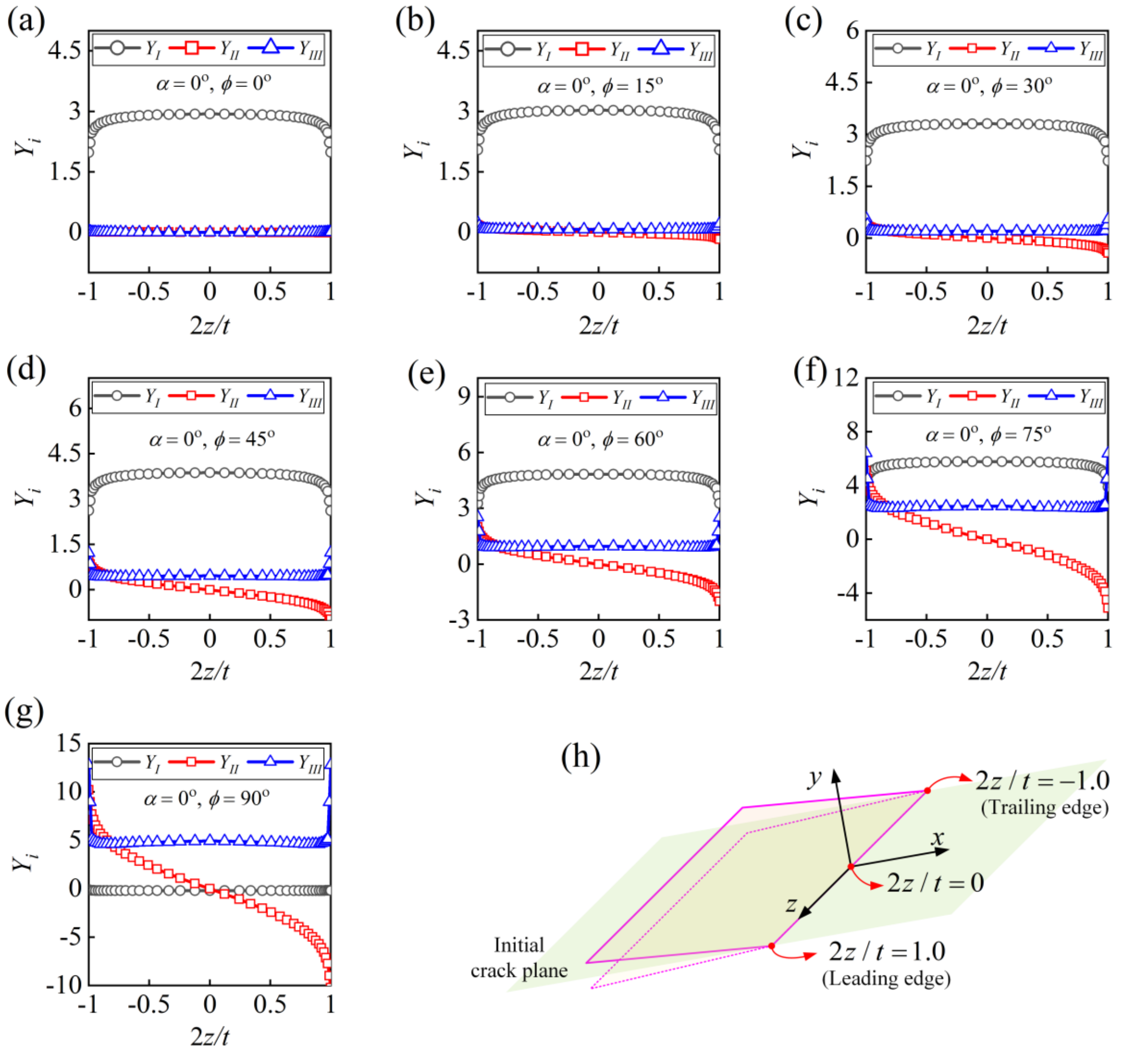

Fig. 6.2 The variation of geometric factors Y_i along the crack front of the SECC specimen for the following mixed mode (I/III) loading configurations: (a) $\phi=0°$. (b) $\phi=15°$. (c) $\phi=30°$. (d) $\phi=45°$. (e) $\phi=60°$. (f) $\phi=75°$. (g) $\phi=90°$. (h) Normalized positions along the crack front.

Fig. 6.2a shows the variation of $Y_{\text{I}}, Y_{\text{II}}$ and Y_{III} for the case of pure mode I $(\alpha=0°, \phi=0°)$. It can be observed from Fig. 6.2a that as expected $Y_{\text{II}}=Y_{\text{III}}=0$ along the complete crack front and the variation of Y_{I} is symmetric to the midpoint of the crack front and nearly uniform. It can also be observed that Y_{I} decreases near the leading and trailing edge of the crack front, which are free surfaces (Fig. 6.2a). This trend of Y_{I} is consistent with the reported observations [33]. Furthermore, Fig. 6.2b-g show that while the Y_{I} and Y_{III} remain nearly uniform along the crack front under mixed mode (I/III) loading, the in-plane mode II SIF $Y_{\mathrm{II}} = 0$ at the midpoint for all the loading configurations and varies antisymmetric to the midpoint of the crack front with maximum values at both the free surfaces.

It has been well established that the in-plane shearing (mode II) and out-of-plane shearing (mode III) are coupled due to Poisson's ratio effect and boundary conditions in the mixed mode problems [33,234–237]. This means that mode II or mode III loading of an elastic body with through-the-thickness crack also generates coupled three-dimensional mode II and mode III singular stress fields [33]. Thus, whilst only out-of-plane load has been applied on the SECC specimen (Fig. 6.1a), Y_{II} component presents near the free surfaces (also known as corner points) and increases with an increase in mode III component loading (Fig. 6.2b-g). These higher SIFs near free surfaces enhance the probability of crack initiation from these edges [238]. All these observations of the present results are consistent with the previous findings by various scholars [33,238,239].

A simple measure of stress singularity under mixed mode loading can be found using the effective SIF K_{eff} which is defined as Eq. (6.2) [33]

$$K_{\mathrm{eff}} = \sqrt{K_{\mathrm{I}}^2 + K_{\mathrm{II}}^2 + K_{\mathrm{III}}^2} \tag{6.2}$$

In order to present more clearly the mixed mode (I/III) loading conditions produced by the present specimen setup, a plot of K_i / K_{eff} computed at the midpoint of the crack front is shown in Fig. 6.3a for different out-of-plane loading angles ϕ. It can be seen from Fig. 6.3a that $K_{\mathrm{II}} / K_{\mathrm{eff}} = 0$ for $0° \leq \phi \leq 90°$ which confirms that the midsection of the SECC specimen is under mixed mode (I/III) loading conditions for $\alpha = 0°$.

In mixed mode problems, mode mixity parameters are a convenient way of representing the dominance of individual modes. One of the widely used mode mixity parameters for different mixed mode conditions are given by Eq. (6.3)

$$M_{12}^e = \frac{2}{\pi}\tan^{-1}\left(\frac{K_{\mathrm{I}}}{K_{\mathrm{II}}}\right); \quad M_{13}^e = \frac{2}{\pi}\tan^{-1}\left(\frac{K_{\mathrm{I}}}{K_{\mathrm{III}}}\right); \quad M_{23}^e = \frac{2}{\pi}\tan^{-1}\left(\frac{K_{\mathrm{II}}}{K_{\mathrm{III}}}\right) \tag{6.3}$$

where M_{12}^{e}, M_{13}^{e} and M_{23}^{e} are the mode mixity parameters. In the above equation, K_i values have been calculated at the midpoint of the crack front. $M_{12}^{e}=1$ and $M_{13}^{e}=1$ represent the case of pure mode I. Similarly, $M_{13}^{e}=0$ and $M_{23}^{e}=0$ represent the case of pure mode III. Fig. 6.3b shows the variation of mode mixity parameters M^{e} for various mixed mode (I/III) loading angles ϕ. The results presented in Fig. 6.3b once again confirm that the proposed specimen setup produces mixed mode (I/III) loading conditions. Thus, the results of the present section affirm that the combination of the SECC specimen and the new J-fixture is capable of producing pure mode I, pure mode III, and mixed mode (I/III) loading conditions.

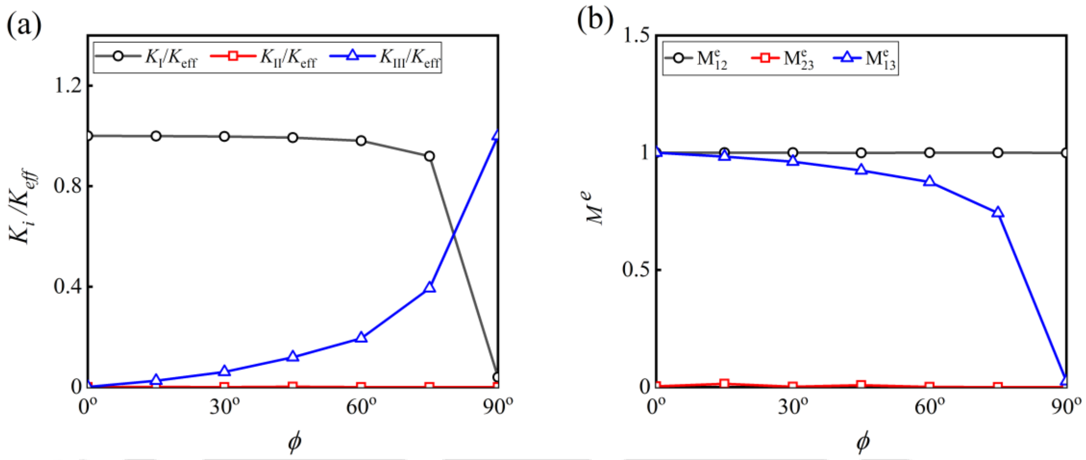

Fig. 6.3 (a) Variation of K_i/K_{eff}. (b) Variation of mode mixity parameters M_{12}^{e}, M_{13}^{e} and M_{23}^{e} at the midpoint $2z/t=0$ of the crack front for varying out-of-plane loading angle ϕ.

6.1.3 Stress analysis of the mixed mode (I/II) test configuration

As the proposed setup can also be used for the mixed mode (I/II) studies, therefore, a detailed 3D stress analyses of the SECC specimen have also been performed here to determine the stress distribution under different in-plane loading angle α. Such analysis is the prerequisite to assure the possibility to achieve mixed mode (I/II) fracture. The amount of the load and the different configuration of the specimen results in different stress distribution around the crack tip. Fig. 6.4 shows the 3D von Mises stress distribution on the SECC specimen for $a/D_o=0.5$ subjected to different mixed mode (I/II) loading. As explained in Section 4.2 (Page 67), by keeping the out-of-plane loading angle $\phi=0°$ and varying the in-plane loading angle $\alpha\ (=90°-\beta)$, the SECC specimen can achieve desired mixed mode (I/II) loading configuration. For ease of presentation, β has been used instead of α in Fig. 6.4a-g. The direction of the applied load has been shown with arrow marks in each figure. The stress distribution of the mode I configuration ($\alpha = 0°$) has been shown in Fig. 6.4a. And Fig. 6.4b-g show the stress contours at different mixed mode (I/II) loading angle $\alpha = 15°$, 30°, 45°, 60°, and 75°, respectively. Fig. 6.4c shows the 3D von Mises stress distribution of the complete loading assembly for $\phi = 0°, \alpha = 30°$. It can be observed from Fig. 6.4 that the shape of the stress contours resembles a dumbbell. For the case of pure mode I, i.e., $\phi = 0°, \alpha = 0°$, the stress contours are symmetric with respect to the crack plane. However, for the mixed mode (I/II) $\phi = 0°, \alpha \neq 0°$, stress contours are asymmetric with respect to the crack plane. Thus, it is clear from these results that the SECC specimen is capable of inducing desired mixed mode (I/II) case by changing the loading angle α.

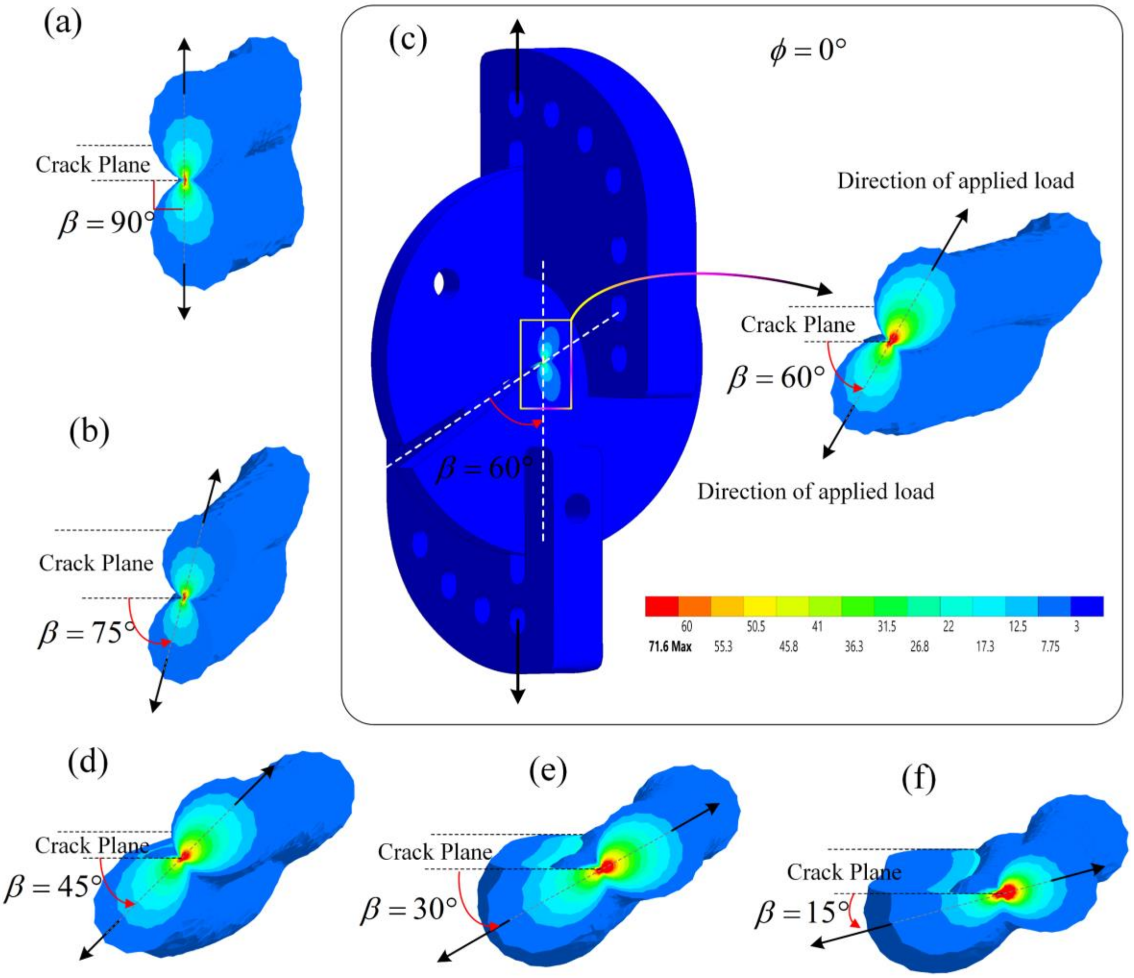

Fig. 6.4 Von mises stress contours at the crack front of the SECC specimen for the case of different mixed mode (I/II) loading angles. (a) pure mode I, $\alpha = 90° - \beta = 0°$. (b) $\alpha = 15°$. (c) $\alpha = 30°$. (d) $\alpha = 45°$. (e) $\alpha = 60°$. (f) $\alpha = 75°$.

6.1.4 Stress analysis of the mixed mode (I/III) test configuration

The von Mises stress contour plots of the complete loading assembly for different mixed mode (I/III) configurations are shown in Fig. 6.5. As expected, it is evident from Fig. 6.5 that the stresses are relatively high near the pin holes joining the J-fixture with the clevis grips. This trend can be seen with all the mixed mode loading configurations (Fig. 6.5). An exploded view of the testing assembly for $\phi = 30°$ is shown in Fig. 6.6 to investigate the stress distribution in the pins joining the SECC specimen with the J-fixture.

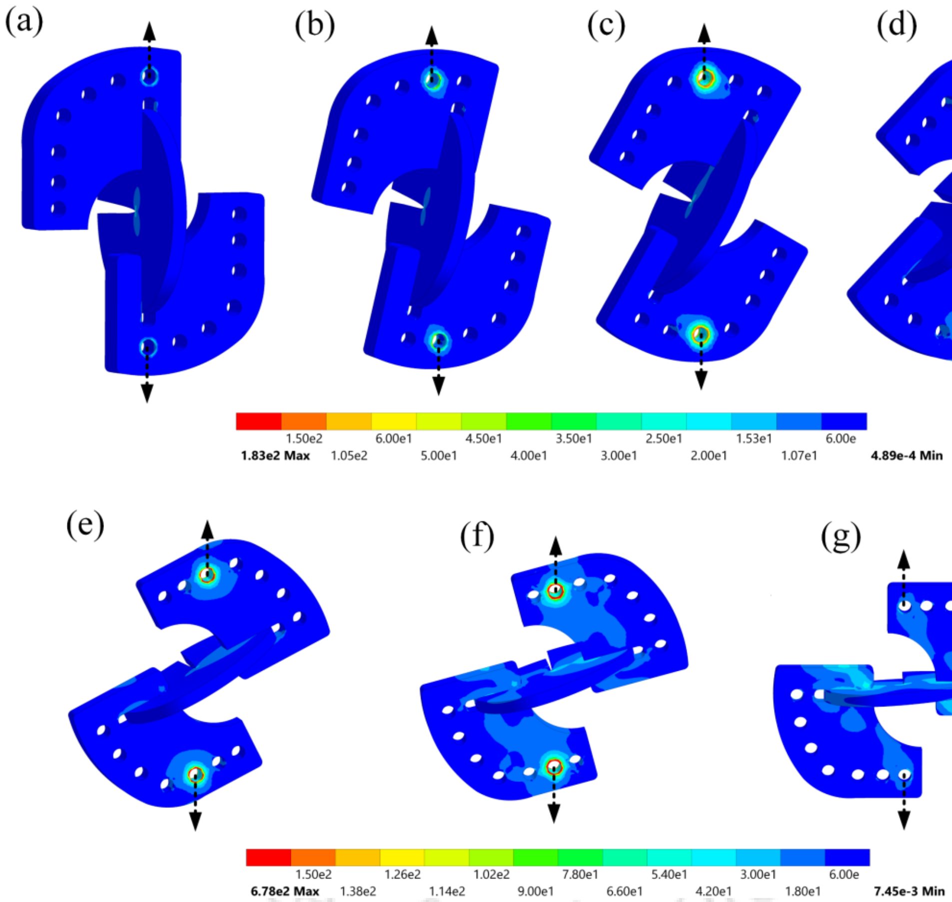

Fig. 6.5 von Mises contours of the loading assembly for different out-of-plane loading angles (a) $\phi = 0°$. (b) $\phi = 15°$. (c) $\phi = 30°$. (d) $\phi = 45°$. (e) $\phi = 60°$. (f) $\phi = 75°$. (g) $\phi = 90°$.

The von Mises stress distribution on the pin is shown in Fig. 6.6b. The contact pressure on the pins joining the SECC specimen with the J-fixture is shown in Fig. 6.6d, which shows that considerable shear stresses may occur in the pins under dominant mode III loading conditions.

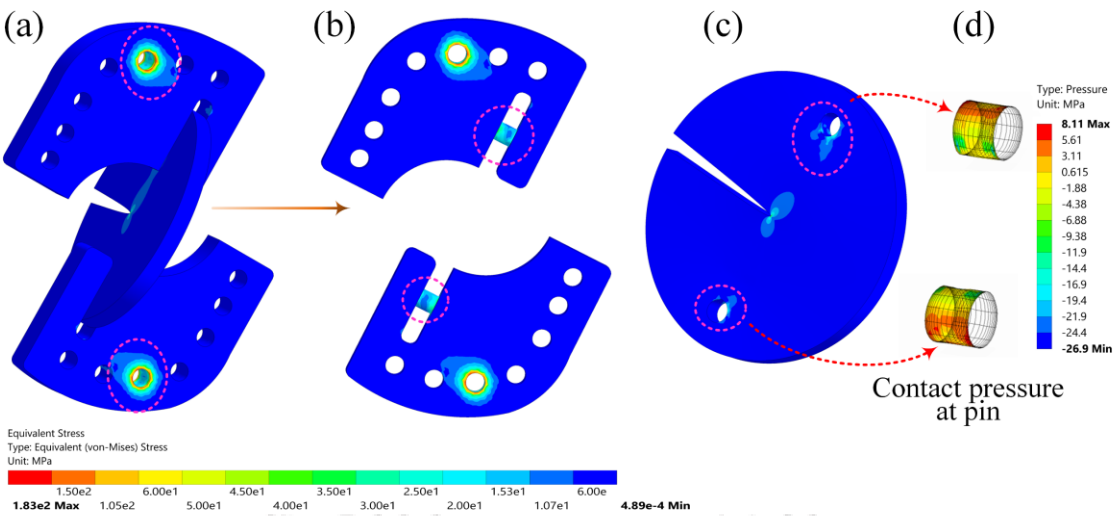

Fig. 6.6 Exploded view of the loading assembly showing the von Mises stress contours for $\alpha = 0°, \phi = 30°$ loading case. (a) Complete testing setup. (b) J-fixture. (c) SECC specimen. (d) contact pressure distribution on loading pins joining the SECC specimen with the J-fixture.

It is clear from the aforementioned FE stress analyses that a complete range of mixed modes (I/II), (I/III), and (I/II/III) can be tested using the proposed testing assembly consisting of SECC specimen and J-fixture.

6.2 Mixed mode (I/III) fracture experiments

A large number of mixed mode (I/III) fracture experiments have been conducted to study the suitability of the proposed SECC specimen. To perform a complete range of mixed mode (I/III) fracture tests, a total of 21 SECC specimens have been prepared from a 12 mm thick PMMA sheet for $\alpha = 0°$ by using the fabrication method explained in subsection 4.6.1 (Page 72). The dimensions of the SECC specimen given in Table 4.1 (Page 66) has been used for fabrication. A crack length ratio $a/D_o = 0.5$ has been set in all the specimens. For each loading angle $\phi = 0°$, 15°, 30°, 45°, 60°, 75° and 90°, three specimens have been tested to ensure the repeatability of the experimental results. The experimental setup given in subsection 4.7.2 (Page 79) have been used for conducting mixed mode (I/III) fracture tests under quasi-static loading conditions. All fracture tests have been performed under a constant displacement rate of 1 mm/min. The average mechanical properties of the PMMA material using four tensile coupons have been found to be equal to $E = 2950$ MPa, $\nu = 0.38$ and $\sigma_t = 57$ MPa. Where σ_t is the ultimate tensile strength. These average values of the elastic properties have been used in all the experimental and numerical analyses of the present chapter.

A typical load-displacement plot of the SECC specimen loaded under pure mode I and pure mode III are shown in Fig. 6.7. It can be observed from Fig. 6.7 that the load-displacement curves are linear up to the final fracture. All the specimens fractured suddenly after reaching the critical load showing a brittle fracture. The maximum load in the load-displacement curve has been considered as the critical load, and this load is used to calculate the critical mixed mode SIFs ($K_{\mathrm{If}}, K_{\mathrm{IIIf}}$) using FE analyses.

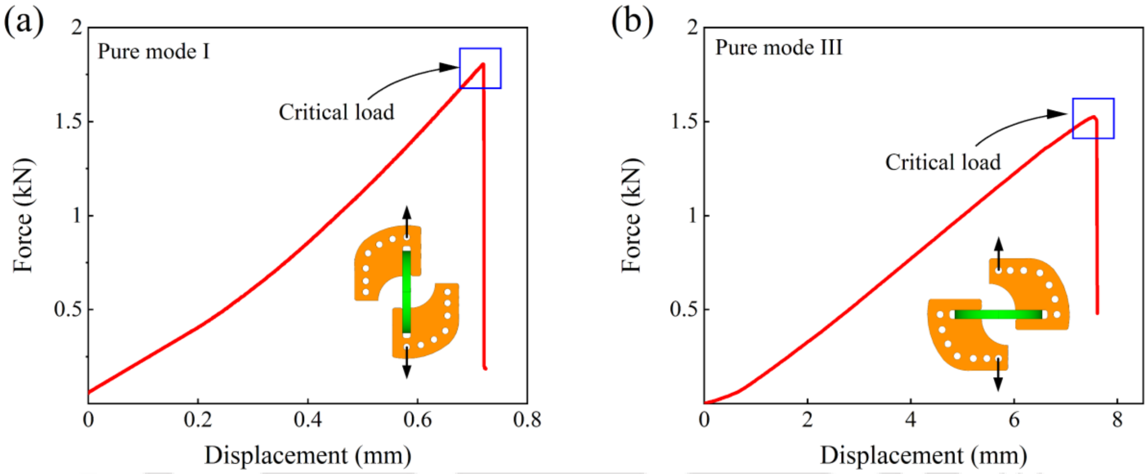

Fig. 6.7 Load-displacement curve obtained from (a) pure mode I and (b) pure mode III testings. In all these plots, the load versus displacement is linear until failure.

6.3 Experimental results and discussions

Experimental results, i.e., measured critical loads P_{cr}, critical mixed mode SIFs K_{If} and K_{IIIf}, and the measured crack twist angle ψ_0 of all the mixed mode (I/III) fracture tests are given in Table 6.1. The crack twist angle ψ_0 has been measured by following the procedure given in Section 4.9 (Page 86). Table 6.1 also shows the results of repeated tests conducted for each mode mixity i.e., three specimens for each mode mixity. The critical SIFs reported in Table 6.1 correspond to the midpoint of the crack front or the midpoint of the thickness of the SECC specimen.

From Table 6.1, the averaged mode I and mode III fracture toughness of PMMA have been found to be equal to $K_{\mathrm{Ic}} = 44.62\ \mathrm{MPa}\sqrt{\mathrm{mm}}$ and $K_{\mathrm{IIIc}} = 65.25\ \mathrm{MPa}\sqrt{\mathrm{mm}}$, respectively. These values are in good agreement with the reported values of the PMMA in the literature [33,76,144,240]. It is worth noting here that approximately 1.46 times higher mode III fracture toughness than that of the mode I value has also been observed by other researchers [32,33,241]. This difference has been attributed to the size of the inelastic deformation at the crack tip [33,140,242], which is demonstrated in next subsection 6.3.1.

Table 6.1 Experimental results for the 12 mm thick SECC specimen under various mixed mode (I/III) loading configurations.

Specimen ID	$\phi°$	P_{cr} (N)	$K_{\text{If}}\left(\text{MPa}\sqrt{\text{mm}}\right)$	$K_{\text{IIIf}}\left(\text{MPa}\sqrt{\text{mm}}\right)$	ψ_o (°)
MM_0_0_S1	0	1806	43.80	0.00	0
MM_0_0_S2	0	1874	45.45	0.00	0
MM_0_0_S3	0	1840	44.62	0.00	0
MM_0_15_S1	15	2092	52.34	1.34	21.4
MM_0_15_S2	15	1858	46.49	1.19	19.1
MM_0_15_S3	15	2009	50.26	1.29	18.7
MM_0_30_S1	30	1861	50.90	3.09	27.2
MM_0_30_S2	30	2073	56.70	3.44	26.3
MM_0_30_S3	30	2000	54.70	3.32	26.8
MM_0_45_S1	45	1753	56.08	6.70	39.3
MM_0_45_S2	45	1930	61.74	7.38	35.5
MM_0_45_S3	45	1834	58.67	7.01	34.7
MM_0_60_S1	60	1530	61.15	12.14	44.6
MM_0_60_S2	60	1678	67.07	13.32	42.2
MM_0_60_S3	60	1591	63.59	12.63	40.1
MM_0_75_S1	75	1676	80.12	34.28	50.1
MM_0_75_S2	75	1898	90.74	38.82	47.5
MM_0_75_S3	75	1869	89.35	38.23	51.4
MM_0_90_S1	90	1530	0.00	62.60	50.3
MM_0_90_S2	90	1646	0.00	67.34	50.1
MM_0_90_S3	90	1609	0.00	65.83	49.8

It is also interesting to notice from Table 6.1 that $K_{\mathrm{If}} > K_{\mathrm{Ic}}$ for the tested SECC specimen under mixed mode (I/III) loading. Such an observation has also been reported by other researchers [23,32,33,135,243]. Razavi and Berto [33] and Zeinedini [32] opined that this behavior is due to high inelastic deformation near the crack front. However, Yishu [243] concluded $K_{\mathrm{If}} > K_{\mathrm{Ic}}$ due to the coupling effect of K_{III} on the K_{I} under mixed mode (I/III) loading.

6.3.1 Plastic zone size under mixed mode (I/III) loading

Another possible reason for $K_{\mathrm{IIIc}} > K_{\mathrm{Ic}}$ can be attributed to the higher fracture energy under mode III loading. As can be seen from Fig. 6.7 that the area under the load-displacement curve for the case of mode III loading (Fig. 6.7b) is higher compared to the case of mode I loading (Fig. 6.7a). It is well known that the area under the load-displacement curve gives the total energy required for fracture. For the case of mode III loading (Fig. 6.7b), most of this fracture energy possibly be dissipated in the plastic deformations and creation of new multiple cracks at the precrack front [33]. Also, higher fracture energy indicates the presence of a larger plastic zone size. Therefore, using 3D FE analyses, the plastic zone size for different mixed mode (I/III) loading has also been calculated in this section by considering the average experimental load from Table 6.1. The measured tensile strength $\sigma_t = 57\ \mathrm{MPa}$ has been considered for this analysis. The plastic zone shape and size for the SECC specimen are shown in Fig. 6.8.

According to Fig. 6.8, as the loading angle ϕ increases from 0° to 90°, i.e., the mode III component increases, the plastic zone size increases. The plastic zone size for the pure mode I has been observed on the scale of micrometer (Fig. 6.8a). On the other hand, the plastic zone size for the pure mode III loading has been observed on the millimeter scale (Fig. 6.8g). And for the mixed mode (I/III) loading, the scale of the plastic zone varies from 0.1 mm to 3 mm (Fig. 6.8b-f). Thus, the plastic zone size under pure mode III loading is considerably larger than pure mode I loading. It has been well-established in fracture mechanics that a larger plastic zone dissipates more energy and increases the fracture toughness of the material [33,140,242]. This observation can be related to the load-displacement pattern for mixed mode (I/III) loading of PMMA using the SECC specimen (Fig. 6.7). As a consequence of these effects, it can be concluded that $K_{\mathrm{IIIc}} > K_{\mathrm{Ic}}$.

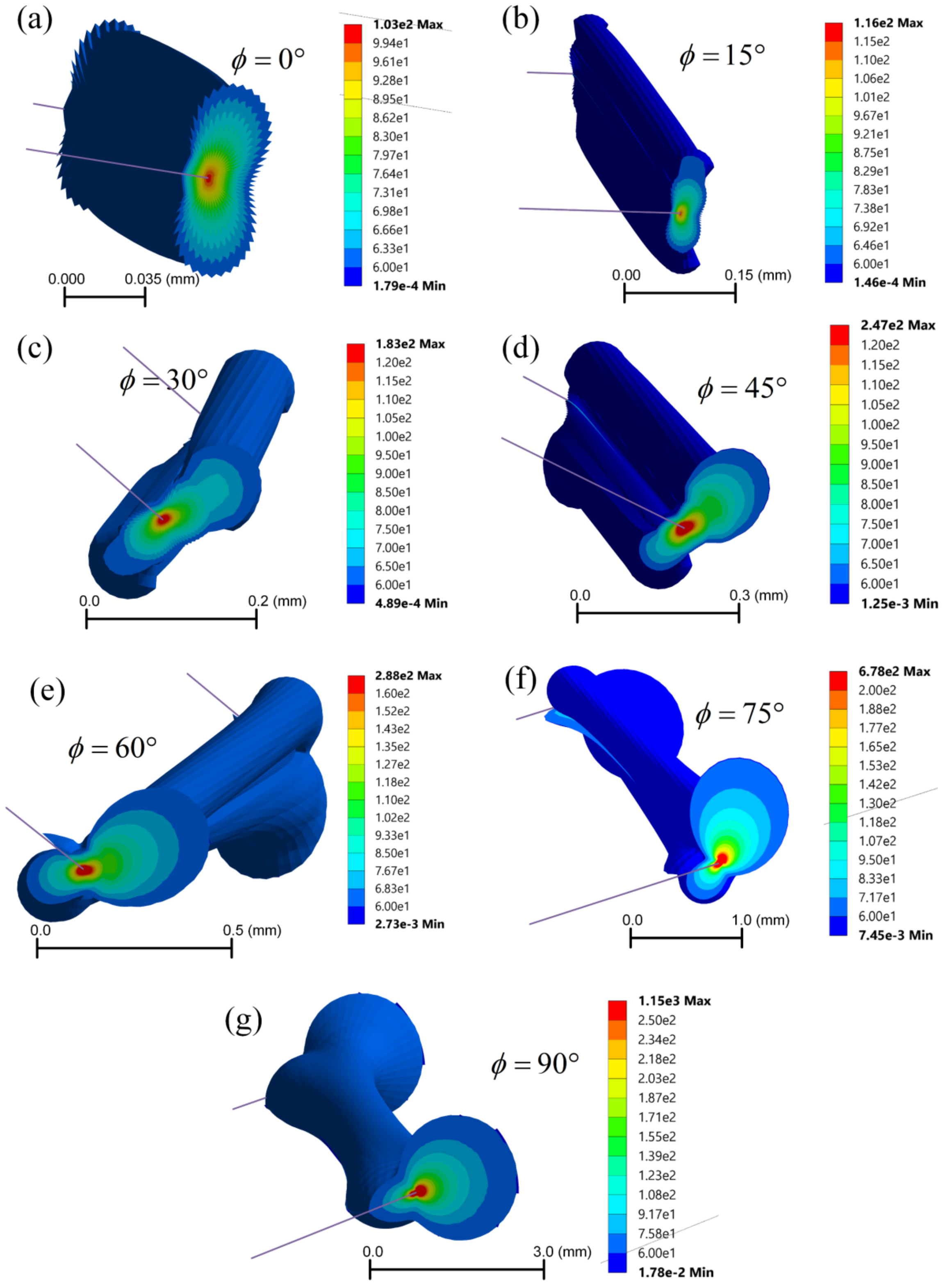

Fig. 6.8 Three-dimensional shape and size of the plastic zone around the crack front under (a) mode I $\phi = 0°$. (b)-(f) various mixed mode (I/III), and (g) mode III $\phi = 90°$ loading.

6.3.2 Study of fractured surfaces

The fractured specimens under various mixed mode (I/III) loading are shown in Fig. 6.9, and it shows that mode III loading has a considerable effect on fracture behavior. While the fractured surface is smooth under the pure mode I loading (see Fig. 6.9a); however, the roughness of the fractured surface increases with the increase of the mode III component (Fig. 6.9b-g). Although a comprehensive investigation on features of the fracture surface is not the subject of the present study, for completeness, a widely believed qualitative description of the fractured surfaces (Fig. 6.9) has been discussed here. Fig. 6.10 shows the fractured surfaces shaved out from the post-fractured specimens shown in Fig. 6.9 using a saw.

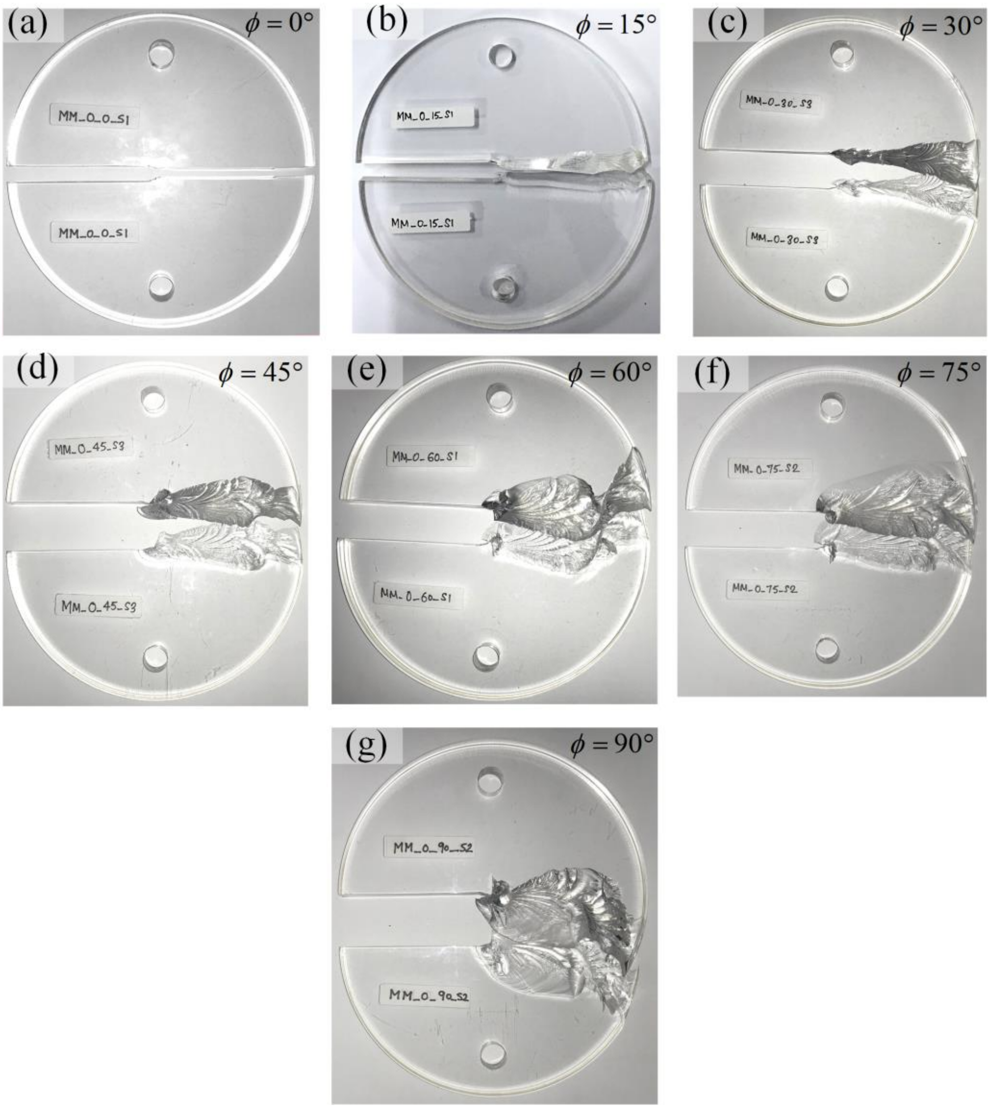

Fig. 6.9 Fractured specimens under various mixed mode (I/III) loading conditions. The area of the fracture surface becomes larger and the roughness increases with the increase in out-of-plane loading angle ϕ .

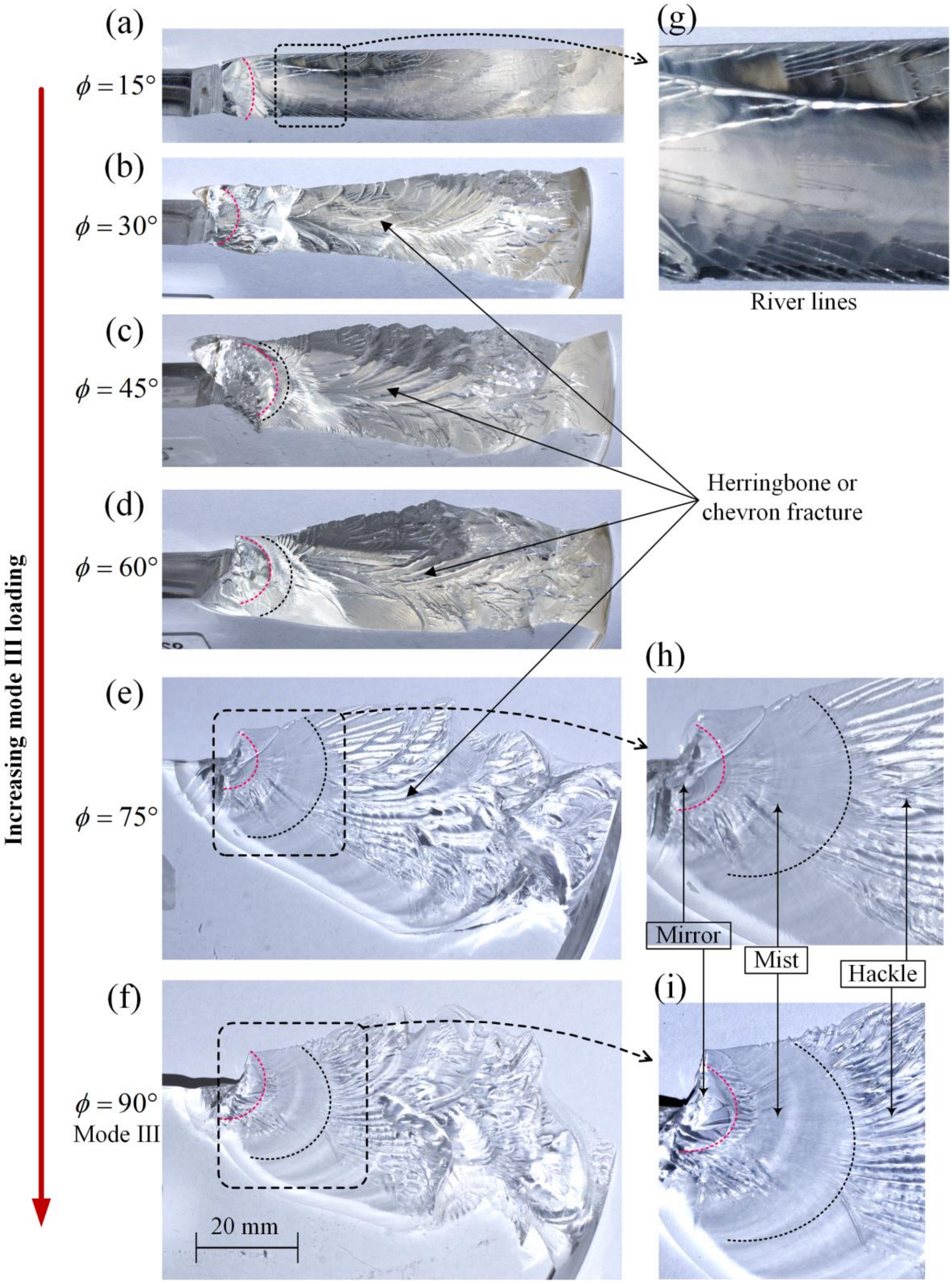

Fig. 6.10 (a)-(f) Fracture surfaces showing various features and fracture mechanisms under mixed mode (I/III) loading. The fracture propagation direction is from left to right. The Herringbone features are present in all the fracture surfaces near the final rapid fracture. Fracture surface showing the (g) river line pattern and (h), (i) mirror, mist, and hackle regions. The fracture propagation is generally discontinuous and consists of multitudes of separately initiated crack fronts.

It has been well established that a crack front under mixed mode (I/III) loading fragments into multiple daughter cracks and as a result, river line type features appear on the fractured surface (Fig. 6.10g) [5,99,106,244–248]. Conversely, crack growth under mixed mode (I/III) involves the fragmentation of the crack front into echelon cracks and the formation of a peculiar river line pattern due to the advance of these echelon cracks. Similar crack fragmentation and river line features can also be observed in Fig. 6.10g. It can be seen from Fig. 6.10a-f that multiple disconnected cracks initiate the fracture, and the crack propagation is accompanied by the merger of these multiple cracks at different scales. The initial straight crack front evolves into a semi-elliptical crack front before the final fracture giving rise to the mirror, mist, and hackle regions (Fig. 6.10c-f). As can be seen from Fig. 6.10a that even a small contribution of mode III leads to the fragmentation of the crack front instantly [105,106], which increases the roughness of the fracture surfaces.

Furthermore, the area of the fractured surface increases with the increase in mode III loading, and the maximum being under the pure mode III loading. This observation is in accordance with the numerical results presented in Fig. 6.3b. Thus, the present features of the fractured surfaces (Fig. 6.9 and Fig. 6.10) of the SECC specimen made using PMMA under mixed mode (I/III) agree well with the previous findings [5,98,106,244,249].

6.3.3 Comparison of crack twist angle and mixed mode fracture locus curves

As discussed in Section 4.9 (Page 86), the measurement of crack twist angle ψ_0 is a complicated process. Most often, difficulties in accurately measuring twist angle arise due to crack segmentation and the inability to locate the crack initiation point clearly at the crack front. These challenges introduce possible errors in measuring the twist angle ψ_0. Further, as the propagating crack tilts and twists continuously, the twist angle at the measurement point can be different at the crack tip. Deviation of the experimentally measured twist angle ψ_0 with the theoretical prediction is usually attributed to the error in the twist angle measurement from the fractured surfaces [33,140].

Since the fracture surface is not in one plane and continuously changes its’ curvature, multiple measurements near the incipient crack have been taken from both parts of the fractured specimen. The average measured twist angle from both parts for the fracture SECC specimen is given in Table 6.1 for all the tests conducted. The experimentally measured crack twist angles ψ_0 have been compared with the theoretical predictions of the selected mixed mode (I/III) fracture criteria, as shown in Fig. 6.11a. As stated in Section 3.3 (Page 47) three fracture criteria, viz., Richard's, MPS and MMPS criterion have been considered for comparison purpose.

The relative difference between the theoretical and experimental results are calculated by taking their ratios $\Delta = \psi_0^{\exp} / \psi_0^{\text{predict}}$. Fig. 6.11b plots the Δ against the mixity parameter M_{13}^e. As can be seen from Fig. 6.11b, with the decrease in M_{13}^e, the value of Δ for all fracture criteria decreases. Moreover Δ of the MMPS criterion is smaller than Δ of the Richard and MPS criteria. It can be noticed from Fig. 6.11 that the present experimental results agree reasonably well with the theoretical predictions made by the MMPS criterion.

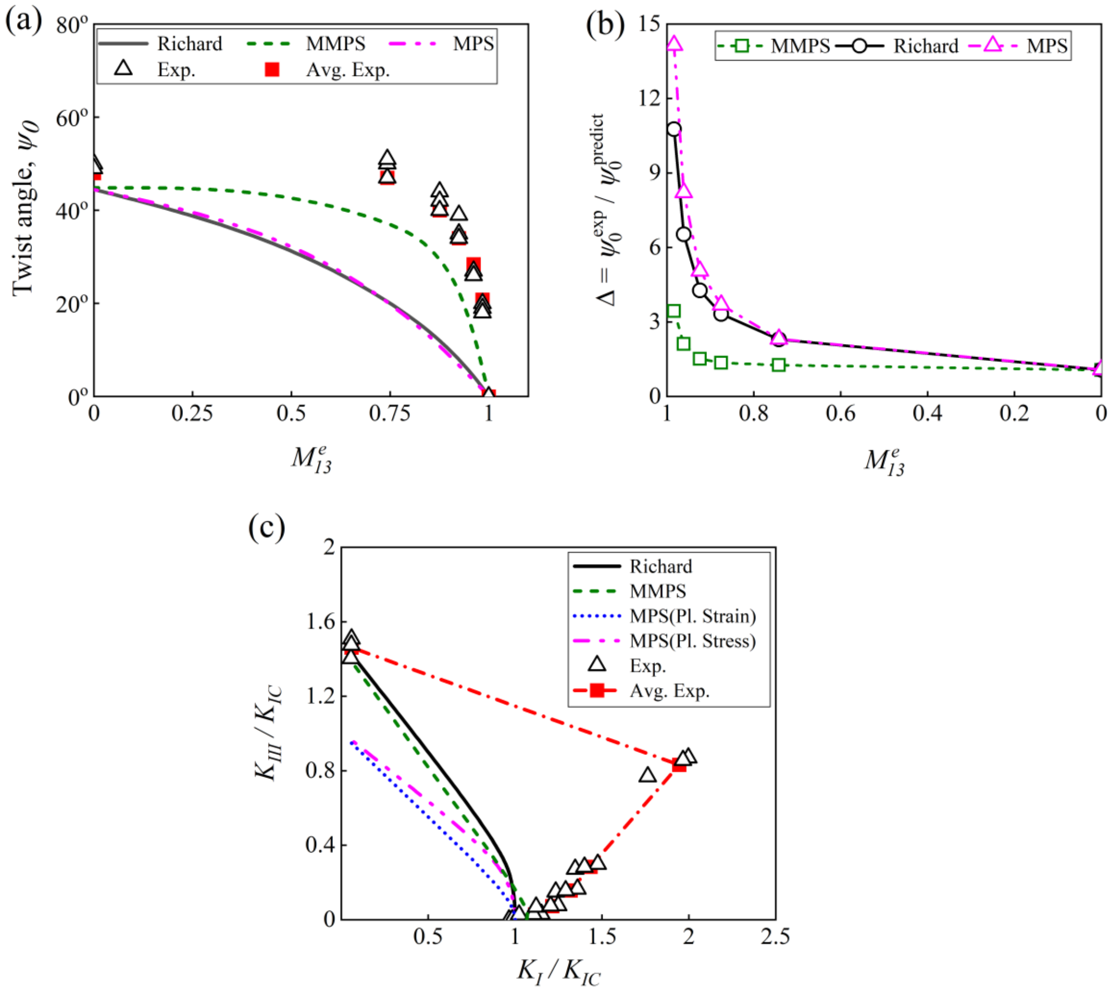

Fig. 6.11 (a) Comparison of predicted crack twist angle ψ_o with the experimental crack twist angle under mixed mode (I/III) loading. (b) Variation of the ratio of experimental twist angle $\psi_0^{\exp}$ and predicted twist angle ψ_0^{predict} to show the relative effectiveness of different mixed mode fracture criteria. (c) Fracture envelope predicted by different fracture criteria and experimental results under mixed mode (I/III) loading.

The mixed mode (I/III) fracture results are more often presented as a fracture locus or fracture toughness or fracture limit curves by plotting the $K_{\mathrm{I}} / K_{\mathrm{Ic}}$ versus $K_{\mathrm{III}} / K_{\mathrm{Ic}}$. These plots provide a comparison of the theoretical predictions with the experimental results. Fig. 6.11c shows a comparison of the present experimental results of all 21 specimens (Table 6.1) with the predicted fracture limit or toughness curves obtained using the selected mixed mode (I/III) fracture criteria described in Section 3.3 (Page 47). The theoretical plots of fracture locus have been obtained using the expressions developed in Section 3.3.

It can be noticed from Fig. 6.11c that there is a relatively good agreement between the experimental results and the predictions made by the Richard and MMPS criteria for the cases of dominant mode I component in the mixed mode (I/III) loading conditions. On the other hand, a considerable discrepancy between the predicted and the experimental values can be noticed for the cases where the mode III components are dominant. One possible reason for such a significant spread may be due to absence of the crack fragmentation effect during the mixed mode (I/III) in the selected fracture criteria [19]. Furthermore, except for the cases of pure mode I and pure mode III, the value of $K_{\mathrm{If}} / K_{\mathrm{Ic}}$ is greater than 1.0. These results are consistent with the earlier findings by researchers [32,33,243] in the mixed mode (I/III) fracture experiments.

Table 6.2 shows the predicted values of $K_{\mathrm{IIIc}} / K_{\mathrm{Ic}}$ by the selected fracture criteria. Results presented in Fig. 6.11c and Table 6.2, show that the MMPS and Richard criteria agree reasonably well with the present experimental results for the pure mode III and K_{IIIc} has been accurately predicted by both the MMPS and Richards criteria.

Table 6.2 Predictions of the $K_{\mathrm{IIIc}} / K_{\mathrm{Ic}}$ by various mixed mode (I/III) fracture criteria

Criterion	$K_{\mathrm{IIIc}} / K_{\mathrm{Ic}}$
MPS	1.0
MMPS	1.4
Richard	1.43
Present experiments	1.46

6.4 Summary

This chapter presents detailed analyses to study the effectiveness of the proposed setup (SECC specimen + J-fixture) in conducting static mixed mode (I/III) fracture tests using conventional UTM machines, and to study various fracture criteria available for mixed mode (I/III) loading conditions. It has been found that the proposed loading setup facilitate a simple geometry of the cracked test specimen, and the new J-fixture provides a straightforward provision to apply out-of-plane load to the SECC specimen using any uniaxial testing machine. 3D FE analyses of the entire setup clearly demonstrate that when a uniaxial load is applied, the test setup produces desired mixed mode combinations without producing undesirable modes. This analysis revealed that the mode I and mode III SIFs' distribution along the thickness of the SECC specimen are symmetric with respect to the midpoint of the crack front. A total of 21 static mixed mode (I/III) fracture experiments have been conducted using the proposed setup with the specimen made of PMMA material. Three repeated tests have been conducted for each category of the test sample. The measured critical loads, critical SIFs and twist angles have been compared with the predictions made using widely used mixed mode (I/III) fracture criteria. These experimental results are in good agreement with the existing 3D mixed mode (I/III) criteria and the published results.

Further detailed analyses of the fractured surfaces revealed that the inclusion of the mode III component has a considerable effect on the features of fractured surfaces. Under the pure mode I loading, the crack propagates in a self-similar manner and the resulting fracture surfaces have been found to be smooth and flat. On the other hand, an initial straight crack fragments into multiple daughter cracks and further evolves into a semi-elliptical or parabolic shape, giving rise to the riverline pattern and herringbone fracture features when the mode III component is added to the specimen. As a consequence, the fracture surfaces under mixed mode (I/III) loading are very rough which increases with the increase in mode III component of loading.

Chapter 7

Mixed mode (I/II) fatigue crack growth studies on Al 7075-T6

This chapter deals with possibility of conducting the mixed mode (I/II) fatigue crack growth experiments in metals using the proposed SECC specimen. For this purpose, Al 7075-T6 alloy has been considered as the specimen material as it is widely used in the aerospace applications. Apart from this some issues of mixed mode (I/II) FCG as mentioned in Chapter 2 (Section 2.7) have also been studied using the proposed specimen. First, the results obtained from mode I and mixed mode (I/II) FCG analysis have been presented. The FE mixed mode (I/II) FCG simulations have been performed along the actual crack path to calculate the variation of fracture parameters, i.e., $K_{\mathrm{I}}, K_{\mathrm{II}}$ and $T-$stress. With the help of original experimental results, the usefulness of GMTS-based ΔK_{eq} model has been tested for the first time for mixed mode FCGR correlation and prediction of the fatigue life. Furthermore, the effect of the use of three different Paris constants, i.e., the modified Paris constant (C^*, m^*) as proposed by Ma et al. [162], conventional mode I (C, m), and mixed mode Paris constants ($C_{\mathrm{eq}}, m_{\mathrm{eq}}$) on the predicted fatigue life by various ΔK_{eq} models (including the GMTS based model) have been discussed. Moreover, the competence of the existing ΔK_{eq} models in combination with the above different Paris constants has also been investigated. Along with this, the suitability of the proposed SECC specimen in conducting the mixed mode (I/II) FCG studies has been demonstrated. Finally, the results of the fractographic studies have been presented to aid in further understanding mixed mode fatigue crack propagation in Al 7075-T6 alloy.

7.1 Experimental procedure

In this chapter, the SECC specimens made of Al 7075-T6 alloy have been used for the mixed mode (I/II) FCG studies. Due to its desirable fatigue strength, fracture toughness, and excellent corrosion resistance [250], this aluminium alloy is widely employed in components of civil aircraft, including wings and fuselage [251,252] which are subjected to complex multiaxial loading conditions.

The specimens used in the present work have been fabricated using the procedure given in subsection 4.6.2 (Page 75). All fatigue experiments have been performed using a BiSS ITW make, 250 kN servo-hydraulic UTM. The complete experimental setup given in Fig. 4.20 (Page 81) has been used for the present investigation. Mode I and mixed mode FCG tests have been carried out under constant amplitude tension-tension cyclic loading using a sinusoidal waveform with a load ratio $R = 0.1$ and frequency of 10 Hz. The mixed mode (I/II) FCG experiments using the SECC specimens have been conducted in two steps: first, all the SECC specimens have been precracked under mode I loading configuration as explained in section 4.10 (Page 87), and then in second step, the precracked SECC specimens have been oriented under the mixed mode configuration shown in Fig. 4.21 (Page 82), and the actual fatigue test is conducted. The recommendations of the ASTM E647 standards have been followed for both the pure-mode I and mixed mode (I/II) FCG investigations.

During the mixed mode FCG tests, the SECC specimen has been subjected to a maximum cyclic load $P_{\max} = 10$ kN, and the crack growth has been observed until the final fracture. The FCG tests have been performed under three loading angles $\alpha = 30°$, 45° and 60°, and two or three SECC specimens for each of these loading angles have been tested to understand the reproducibility of the results. Mode I FCG tests on the two identical CT specimens have been performed with a maximum cyclic load of $P_{\max} = 6$ kN. The instantaneous crack length in the CT specimen has been measured using a clip gauge (subsection 4.7.5, Page 84). A frequency of 10 Hz has been maintained in the above tests.

The optical method as explained in Section 4.11 (Page 88) has been adopted for measuring the crack length during the mixed mode (I/II) FCG tests. A large number of images of the crack tip have been captured during the mixed mode (I/II) FCG tests for every 5 second interval (Fig. 4.27c,d, Page 89). And the final crack lengths are measured from these captured images (large in number) using DinoCapture software. Due to the tedious image processing involved in measuring fatigue crack growth using the above methods, availability of number of (N,a) data points are very less as compared with the mode I crack length measurements using a clip gauge. For obtaining the da/dN versus ΔK plot in mixed mode (I/II) loading, a best-fit curve to the (N,a) data is commonly made [28,29]. In the present investigation, a five-parameter double-exponential expression Eq. (7.1) has been employed to best-fit the measured (N,a) data for the mixed mode (I/II) loading conditions. This equation is very similar to the one proposed by Sajith et al. [28,29].

$$a_i = C_1 e^{pN_i} + C_2 e^{qN_i} + (a_0 + k) \tag{7.1}$$

where a_0 is the precrack length and C_1, C_2, p, q, k are unknown parameters.

7.2 Tensile tests and mode I FCG results

7.2.1 Tensile test results

The mechanical properties of Al 7075-T6 alloy have been obtained from the tensile tests (as per ASTM E8) on three specimens, and the average values of these properties are given in Table 7.1. The material properties are not a prerequisite for the FCG experiments; however, they are necessary for the numerical simulation of the FCG.

Table 7.1 Mechanical properties of Al 7075-T6 alloy obtained from the tensile test.

Yield strength (MPa)	Ultimate strength (MPa)	% Elongation	Young's modulus (GPa)	Poisson's ratio
503	576	12	70	0.3

7.2.2 Mode I FCG results

Mode I FCG tests on two identical CT specimens have been performed using the variable amplitude fatigue crack propagation (VAFCP) module in-built into the BiSS 250 kN testing machine with a maximum cyclic load $P_{\max} = 6$ kN, load ratio $R = 0.1$ and frequency 10 Hz. The FCG tests on the CT specimens have been started with initial notch length 9 mm, and continued until final fracture of the specimens. Using the data acquisition system, FCG is recorded at every 0.01 mm crack increment.

Table 7.2 shows the results of the mode I FCG tests conducted on the two identical CT specimens (to understand the repeatability) made of Al 7075-T6 alloy. Both the CT specimens were fractured unstably after attaining a critical crack length of $a_c \approx 41$ mm, and the approximate fracture toughness value of the alloy is found to be equal to $39.7\,\mathrm{MPa}\sqrt{\mathrm{m}}$. This value corresponds to the maximum mode I SIF $K_{\max}$ at the point of unstable fracture. For a constant-amplitude FCG test (or $K-$increasing test), the fracture toughness of a material can be calculated by putting the maximum cyclic load $P_{\max}$ and the critical crack length a_{c} (at which unstable crack growth occurs) into Eq. (7.2). Other parameters like B and W are the thickness and width of the CT specimen, respectively. The width W is defined as the distance between the load line (or center of the loading holes) and the backface of the CT specimen (see Fig. 4.3a, Page 67).

Table 7.2 Results of the mode I FCG test using the CT specimen.

Specimen ID	Initial Notch length	$P_{\max}$ (kN)	R	a_{c} (mm)	Cycles to fracture N_{f}
CT-1	9 mm	6	0.1	41.2	3.4
CT-2	9 mm	6	0.1	40.8	3.3

Fig. 7.1a shows the crack length (a) versus the number of cycles (N) curve obtained from the mode I FCG experiments for both the CT specimens. The point of final unstable fracture of specimens is marked as a star symbol in Fig. 7.1a. The da/dN versus ΔK curve obtained using both CT specimens is shown in Fig. 7.1b. These plots have been made using the seven-point incremental polynomial method [253]. ΔK for the CT specimen at each crack length is obtained from the SIF calibration equation given in ASTM 647 Eq. (7.2).

$$\Delta K_I = \frac{\Delta P}{B\sqrt{W}} \frac{(2+\eta)}{(1-\eta)^{3/2}}\left(0.886+4.64\eta-13.32\eta^2+14.72\eta^3-5.6\eta^4\right); \text{for}\, \eta \geq 0.2 \qquad (7.2)$$

It can be noticed from the results presented in Fig. 7.1 that nearly identical crack growth can be seen in both CT specimens. These results show a very good reproducibility of the present FCG experiments. Table 7.3 shows the Paris' material constants C and m of Al 7075-T6 alloy under mode I fatigue loading. These values have been obtained by fitting a single straight line to the data of both the specimens as shown in Fig. 7.1b. These values are of the same order as reported in the previous studies on Al 7075-T6 alloy [45,254].

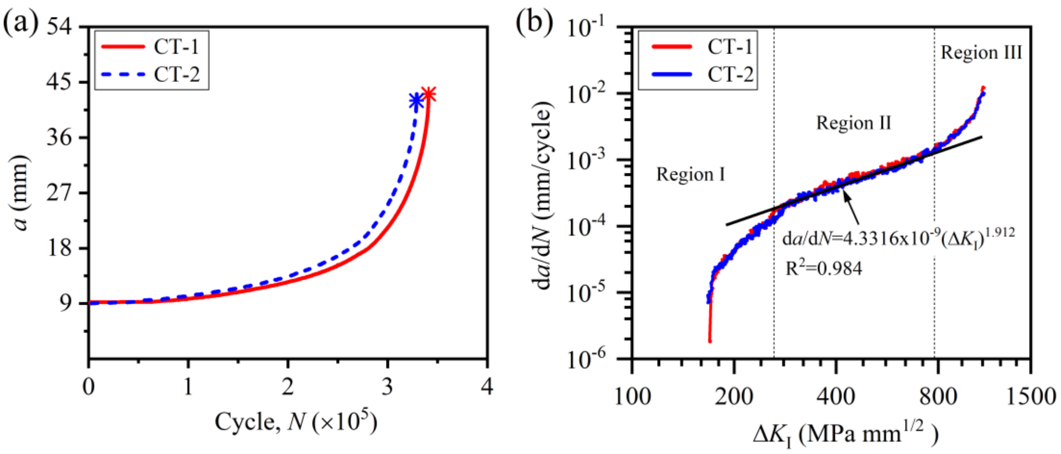

Fig. 7.1 Fatigue crack growth curves obtained from the mode I FCG test using CT specimen (a) $a-N$ curves. (b) $da/dN-\Delta K$ curve in log-log scale.

Table 7.3 Paris material constants for AL 7075-T6 obtained from mode I fatigue tests.

Material	C (mm/cycle)/(MPa$\sqrt{\text{mm}}$)^m	m
Al 7075-T6	4.3316×10^{-9}	1.912

7.3 Mixed mode (I/II) experimental FCG results

7.3.1 Crack growth direction and fatigue life results

The fatigue life curves of Al 7075-T6 tested under different loading angles, i.e., $\alpha = 30°$, 45° and 60° using two identical SECC specimens for each loading angle have been shown in Fig. 7.2a-c, respectively. As explained in Section 7.1, the length of the growing crack under mixed mode (I/II) loading has been calculated by analyzing a very large number of images produced by the digital microscope (approximately 2500 to more than 10000) and recording the number of load cycles for each image. It can be noticed from Fig. 7.2a-c that, $a-N$ plots for each loading angle show a high degree of repeatablity. The $a-N$ plots of at least two specimens for all the three loading angles, viz., $\alpha = 30°$, 45°, and 60° are nearly identical. For a specific loading angle α, the small variation among the $a-N$ plots from different specimens can be attributed to the different precrack lengths for each specimens (Table 7.4), and due to the inherent nature of fatigue loading and image processing. It is to be noted here that the precrack lengths do not have any effect on the calculation of FCGR in the Paris region which is evident from the da/dN versus ΔK_{eq} plots given in subsection 7.3.2 (Page 135). It can be observed from Fig. 7.2 that with an increase in the loading angle α, the number of cycles N_f to reach the final fracture increases for a given P_{max} and load ratio R. The complete experimental results of the mixed mode (I/II) FCG tests are shown in Table 7.4. The results presented in Table 7.4 once again affirm the very good reproducibility achieved in the present experiments.

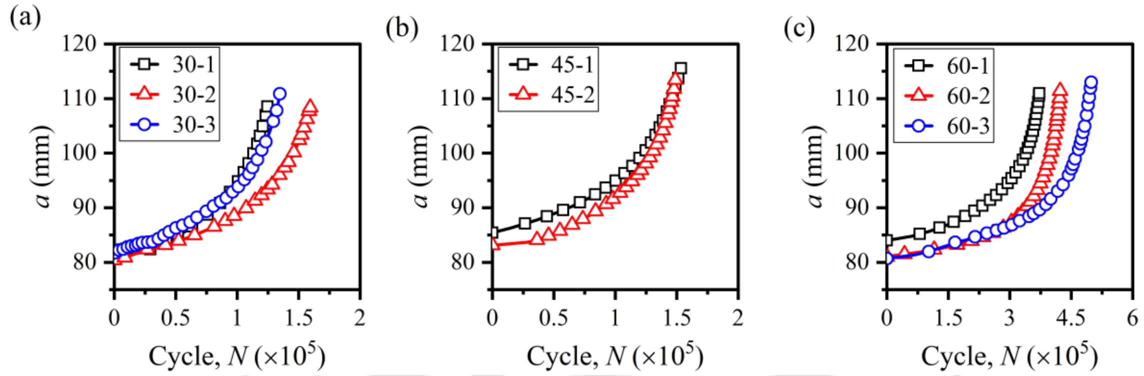

Fig. 7.2 Fatigue life ($a-N$) curve obtained from mixed mode (I/II) FCG experiments using the SECC specimens loaded at: (a) $\alpha = 30°$, (b) $\alpha = 45°$, (c) $\alpha = 60°$.

As can be noticed from Table 7.4, the average fatigue life, N_f of the SECC specimen when $\alpha = 45°$ is approximately 10% higher than the average fatigue life of $\alpha = 30°$. Similarly, for $\alpha = 60°$ the fatigue life N_f is about 2.8 times higher than that of the specimen loaded at $\alpha = 45°$.

Table 7.4 Results of mixed mode (I/II) FCG experiments using the SECC specimen.

Specimen ID	$\alpha(°)$	P_{max} (kN)	Initial crack length (Notch length + Δa_p) (mm)	N_f ($\times 10^5$)	First kink angle θ_0 (°)
30-1	30	10	80.4	1.34	32.7
30-2			80.9	1.70	33.0
30-3			81.7	1.39	31.5
45-1	45	10	85.4	1.60	42.2
45-2			83.1	1.57	40.5
60-1	60	10	84.2	3.80	53.0
60-2			81.1	4.25	52.0
60-3			80.7	5.12	51.8

A careful observation of Fig. 7.2 reveals that as the loading angle α increases, $a-N$ curves become flatter near the crack initiation region, which shows that the resistance to the crack initiation increases with an increase in the loading angle. Similar observations have also been reported by Tamilselvan et al. [45] for the CTS specimen. Furthermore, the magnitude of N_f clearly indicates that all the specimens have been loaded under high cycle fatigue. Fig. 7.3 shows the fractured SECC specimens under different loading angles. The starting crack kink angle θ_0 has been measured from both sides of the two fractured parts of each specimen, and an average of these four measured angles for each specimen has been given in Table 7.4. The difference between the measured angle from both sides of the broken specimen is found to be less than ±3°, and the difference of measured kink angle from two different specimens (for the same loading angle) is not more than the ±2°.

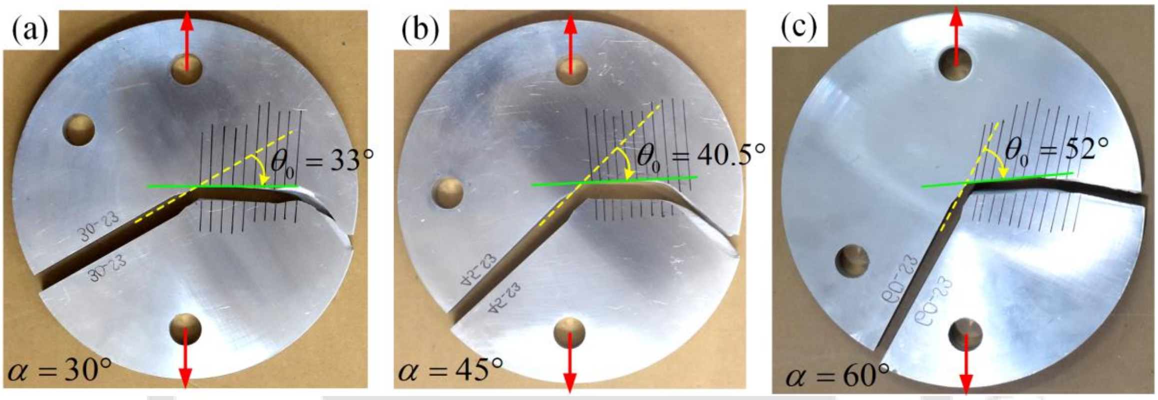

Fig. 7.3 Fractured SECC specimens showing the actual crack path under different loading angles: (a) $\alpha = 30°$, (b) $\alpha = 45°$, (c) $\alpha = 60°$.

In the present analysis, to minimize measurement errors, utmost care has been taken to correctly align the intersection point of the yellow and green lines at the precrack tip as shown in Fig. 7.3. The position of the intersection point is critical for accurate measurements of the first crack kink angle θ_0.

Fig. 7.4a shows the comparison of the experimental crack kink angle θ_0 with the theoretical predictions of the MTS and GMTS criteria. It can be noticed from Fig. 7.4a that the GMTS criterion (using $r_c = 0.8$ mm) accurately predicts crack kink angles θ_0 closer to the experimental results for all the three loading angles. On the other hand, the MTS criterion fails to predict the θ_0 close to the experimental results for the higher loading angles $\alpha > 45°$. The better predictability of the GMTS criterion than the MTS criterion under mode II dominated mode mixities has also been reported by previous studies [76,78]. Similar observation can also be noticed in case of mixed mode (I/II) fracture tests (Section 5.3, Fig. 5.8, Page 102).

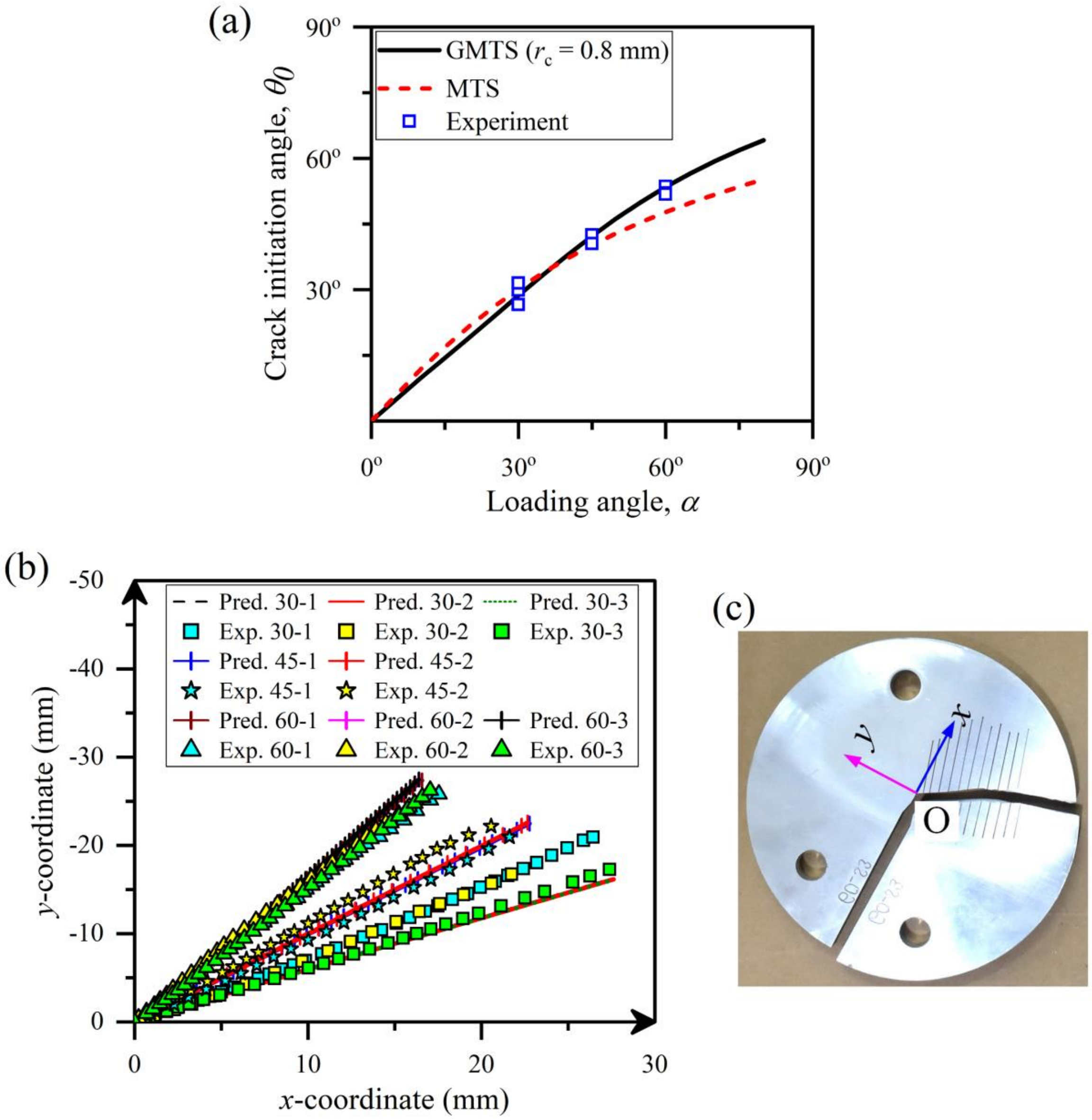

Fig. 7.4 (a) Comparison of experimental crack kink angle θ_0 with the theoretical predictions of the MTS and GMTS criteria. (b) Actual crack paths measured from the fractured SECC specimens under three different loading angles. (c) Position of the local coordinate system at the pre-crack tip of fractured specimen that is used for measuring actual crack path.

Since the prediction of the residual fatigue life is considerably affected by the accuracy of the predicted crack path, the GMTS criterion has been used to calculate the complete crack path in the following FCG simulations for calculating the fatigue life in the present chapter. Fig. 7.4b shows the measured crack paths (on the fractured specimens in Fig. 7.3) from the pre-crack-tip until the unstable fracture of all the specimens tested. For each loading angle, the actual crack path shown in Fig. 7.4b is measured on the basis of a local cartesian coordinate system at the pre-crack-tip of fracture SECC specimen, as shown in Fig. 7.4c. The predicted crack paths using the GMTS criterion for different loading angle have also been plotted in Fig. 7.4b. As can be noticed from Fig. 7.4b that with an increase in loading angle α, both the kink angle θ_0 and deviation from the plane of the initial crack increase. Similar results can also be noticed in the case of static mixed mode (I/II) fracture tests (Section 5.3, Fig. 5.7, Page 101). Furthermore, comparing the results in Fig. 7.3 and Fig. 7.4b shows that the crack grows practically straight and perpendicular to the direction of the applied loading, as expected. These actual crack paths are useful in the finite element FCG simulations presented in the next section. Plotting of da/dN versus ΔK plots has been postponed to subsection 7.3.2 (Page 135) as they require FE analyses to calculate the variation of SIFs along the actual crack path.

7.3.2 FCGR curves for different $\Delta K_{\mathbf{eq}}$ models under mixed mode loading

In mixed mode (I/II) fatigue loading, a FCGR curve is plotted between the crack growth rate da/dN and ΔK_{eq}. In order to accurately depict the FCGR curves using the experimental data, firstly, accurate FE computation of the mixed mode SIFs K_{I}, K_{II} and $T-$stress along the measured crack trajectory (Fig. 7.4b) is required. To this end, FE simulation of FCG in the SECC specimen has been done in the commercial software ANSYS®. Plane stress conditions have been assumed in all analyses. The material properties of Al 7075-T6 given in Table 7.1 have been used in the FE analyses. Eight noded (Q8) isoparametric quadrilateral elements have been employed to discretize the specimens. Quarter point elements have been used at the crack tip in a spider-web pattern by collapsing the Q8 elements. An interior collocation method proposed by Jogdand and Murthy [218] (subsection 3.6.1, Page 58) has been used to calculate the SIFs and $T-$stress.

The dimensions of the SECC specimen, given in Table 4.1 (Page 66), have been used to generate the FE model. Before conducting the simulations, a mesh convergence and verification study has been carried out (see Appendix B.3, Page 185). Based on this study, mesh density for further FE analysis is selected. Fig. 7.5a shows a typical FE mesh along with the boundary conditions. The load $\Delta P = (P_{\max} - P_{\min})$ employed in the experiments has been applied at the top-hole A (Fig. 7.5a), and the bottom hole B has been constrained in all directions. Additionally, top hole A is constrained to move in the vertical direction only (Fig. 7.5a). Fig. 7.5a also shows mesh near the crack tip. Fig. 7.5b and Fig. 7.5c show FCG simulation of the SECC specimen for the loading angle $\alpha = 30°$ at the 6th step and final step before the unstable fracture. These figures also depict mesh near the growing crack tip. A total of 60 FE simulation steps have been analyzed to reach the critical crack length a_c. Similar order of FE simulations has been made for other loading angle α. At each step, the mixed mode SIFs (K_{I}, K_{II}) and $T-$stress have been computed using the interior collocation technique [218] (explained in subsection 3.6.1, Page 58).

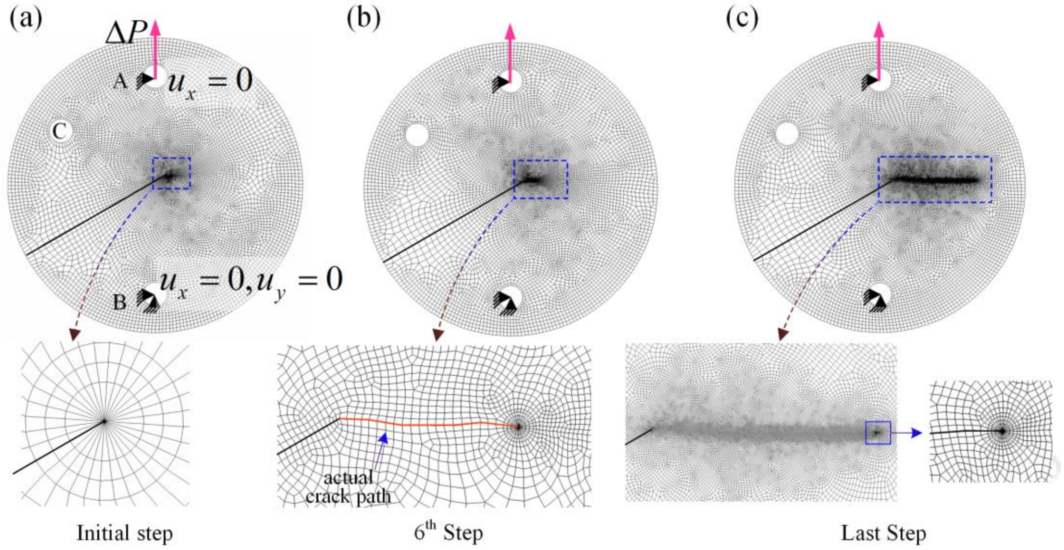

Fig. 7.5 FE meshes of the SECC specimen at different steps along the actual crack path for loading angle $\alpha = 30°$. Mesh at (a) initial step, (b) 6th step ($a \approx 84$ mm), (c) last step just before the unstable fracture.

After best-fitting the $a-N$ experimental data with Eq. (7.1), da/dN has been obtained from the best-fit at the crack lengths where K_{I}, K_{II} and $T-$stress have been computed. After computation of the K_{I}, K_{II} and $T-$stress along the crack trajectory (Fig. 7.4b), ΔK_{eq} has been computed for different models given in Table 3.1 (Page 52). Fig. 7.6 show the FCGR curves (obtained using the SECC specimen) plotted against the selected ΔK_{eq} models. Each plot in Fig. 7.6 has been appended with the mode I FCGR curve (obtained using the CT specimen) for comparison purposes. As can be observed from Fig. 7.6a-h, all selected ΔK_{eq} models exhibit a similar correlation pattern, and the FCGR is higher in mixed mode (I/II) than in mode I. This observation aligns with the previous studies [1,45,162,189]. It is interesting to notice that although the final crack growth is nearly perpendicular to the loading axis, but the crack growth rates are higher in mixed mode fatigue loading than the mode I loading. Furthermore, the FCGR for a specific ΔK_{eq}

decreases with the increase in loading angle α (Fig. 7.6). Similar trend has also been noticed in Fig. 7.2. To further explore the correlation behavior of various ΔK_{eq} models, the FCGR for each tested SECC specimen has been replotted in Fig. 7.7.

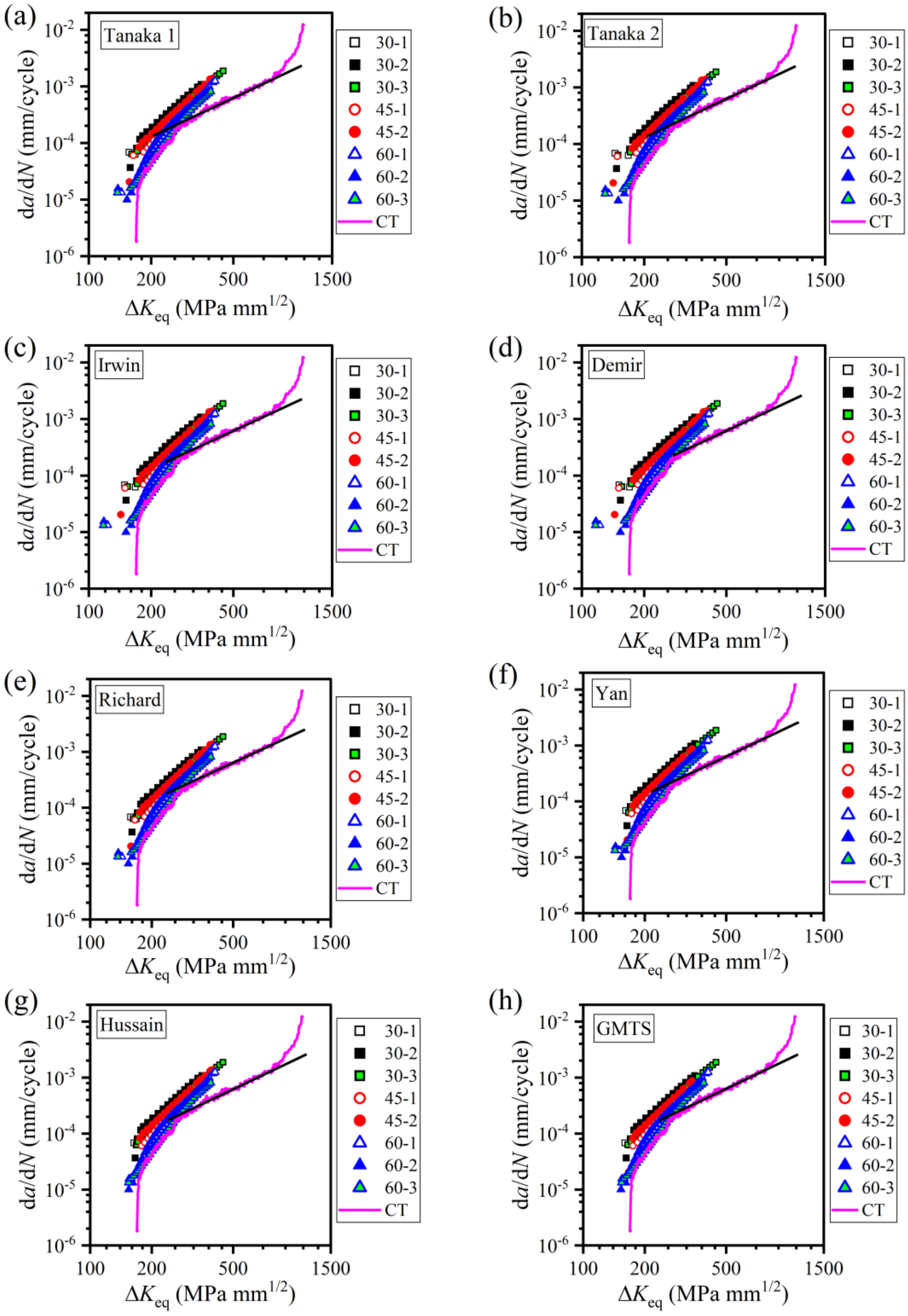

Fig. 7.6 FCGR at different loading angles as a function of various ΔK_{eq} models: (a) Tanaka 1. (b) Tanaka 2. (c) Irwin. (d) Demir. (e) Richard. (f) Yan. (g) Hussain. (h) GMTS model.

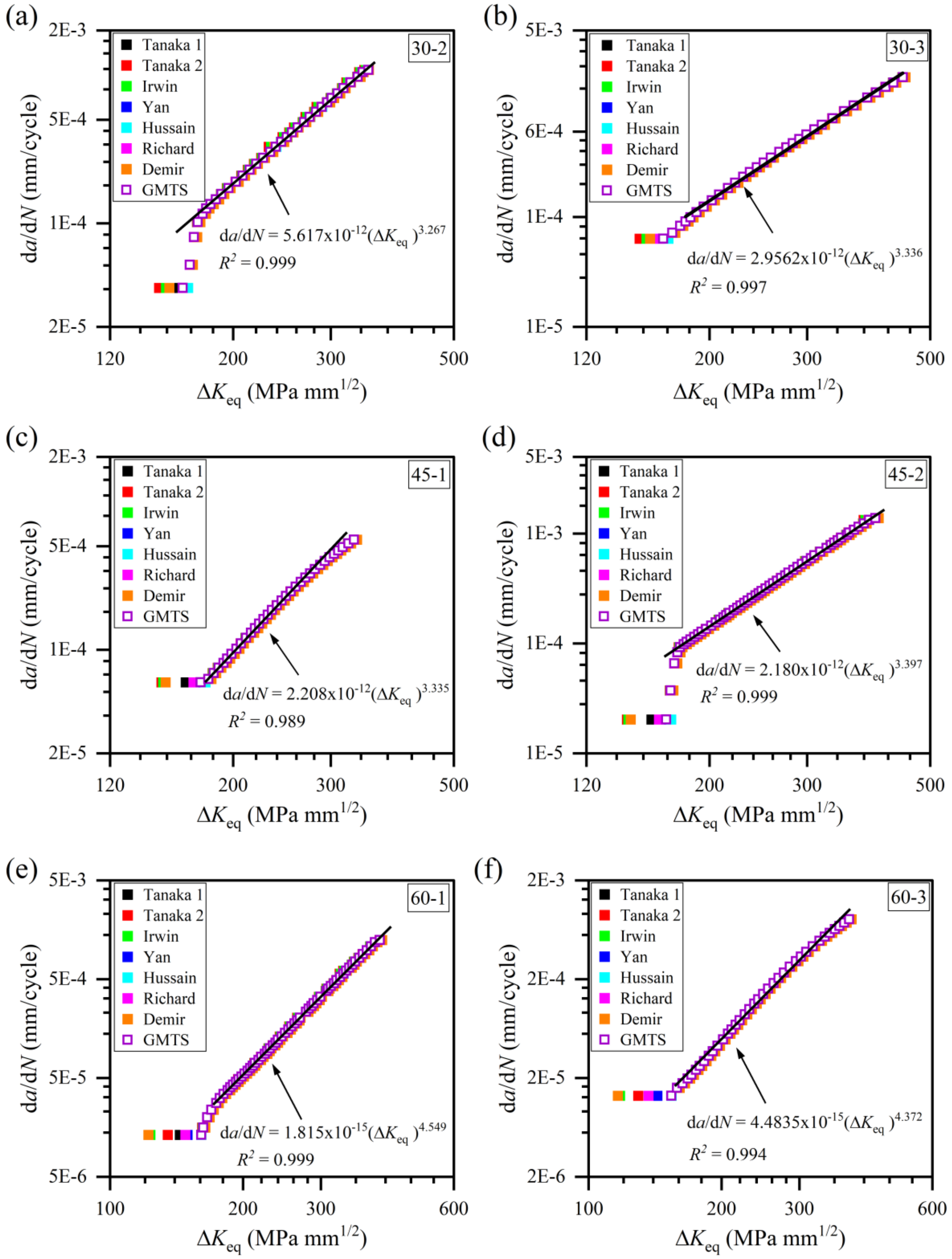

Fig. 7.7 FCGR as a function of selected ΔK_{eq} models at different loading angles: (a) $\alpha = 30°$, specimen 2, (b) $\alpha = 30°$, specimen 3, (c) $\alpha = 45°$, specimen 1, (d) $\alpha = 45°$, specimen 2, (e) $\alpha = 60°$, specimen 1, (f) $\alpha = 60°$, specimen 3.

It can be observed from Fig. 7.7, except for the initial points, the FCGR correlation of all the ΔK_{eq} models almost overlap with each other. For the initial crack orientations, different models predict different ΔK_{eq} values, but with further crack growth, the correlation of all the selected models almost coincide with each other. Similar observations have also been reported by Fageehi and Alshoaibi [255]. The results of Fig. 7.7 apparently suggest that any ΔK_{eq} model can be used for fatigue life prediction. However, the predicted plots of $a-N$ using these models provides a better picture on the performance due to the influence of the Paris constants.

To obtain the mixed mode Paris material constants C_{eq} and m_{eq}, a linear curve has been fitted to each plot (shown in Fig. 7.7) in the Paris region. Table 7.5 summarizes the Paris material constants C_{eq} and m_{eq} for each specimen corresponding to the different loading angles. This table also presents the mode I, C and m values for comparison purposes. As can be seen from Table 7.5, the mixed mode Paris constants obtained from different loading angles α significantly differ from the mode I Paris constants C and m. As expected, Table 7.5 clearly shows that mixed mode FCGR are higher than the mode I value. Further m_{eq} increases with increase in α.

Table 7.5 Paris constants for Al 7075-T6 in the mixed mode (I/II) loading.

Specimen ID	Loading angle, $\alpha(°)$	C_{eq} $((\mathrm{mm/cycle})/(\mathrm{MPa}\sqrt{\mathrm{mm}})^{m})$	m_{eq}
30-1	30	9.005×10^{-13}	3.556
30-2	30	5.617×10^{-12}	3.267
30-3	30	2.956×10^{-12}	3.336
45-1	45	2.208×10^{-12}	3.335
45-2	45	2.180×10^{-12}	3.397
60-1	60	1.815×10^{-15}	4.549
60-2	60	3.208×10^{-13}	3.675
60-3	60	4.484×10^{-15}	4.372
CT	Mode I	4.3316×10^{-9}	1.912

7.4 Results and discussion of fatigue life prediction

As stated earlier, the current practice of numerical prediction of the fatigue life in mixed mode (I/II) loading conditions is to employ the modified Paris law (Eq. (2.2)) with a selected ΔK_{eq} model and mode I Paris constants designated here as C_{I} and m_{I}

[1,28,29,37,40,42–45]. Ma et al. [162] assumed that the parameter C_{I} in the Paris law is related to the mixed mode ratio M^{e} by the relation given in Eq. (7.3)

$$C^{*}=C_{\mathrm{I}}\left[1+\gamma\left(M^{\mathrm{e}}-1\right)^{2}\right] \tag{7.3}$$

where M^{e} is the mode mixity parameter given as $M^{\mathrm{e}}=\frac{2}{\pi}\tan^{-1}\left|K_{\mathrm{I}}/K_{\mathrm{II}}\right|$. For $\gamma=3$, Ma et al. [162] found a very good agreement with their experimental results. According to Ma et al. [162], although C^{*} is different from C_{I} but $m^{*}=m_{\mathrm{I}}$. As stated earlier, numerical fatigue life predictions using the $C_{\mathrm{eq}}, m_{\mathrm{eq}}$ and C^{*}, m^{*} in the modified Paris law Eq. (2.2) has been scarcely investigated.

Therefore, this section presents a detailed study on the use of the three different Paris constants in predicting mixed mode fatigue life. For this purpose, FE based incremental crack tip extension approach explained in subsection 3.4.3 (Page 53) has been adopted. The GMTS criterion (Eq. (3.5)) has been used to calculate the direction of the crack path. And a crack increment length of $\Delta a=0.5$ mm has been used. The residual fatigue life has been calculated through FE simulations using three different approaches: (a) using C_{I} and m_{I} values of Al 7075-T6 alloy obtained from mode I FCG test (Table 7.3), (b) using C_{eq} and m_{eq} values corresponding to each loading angle α as given in Table 7.5, and (c) using C^{*} and $m^{*}=m_{\mathrm{I}}$ as proposed by Ma et al. [162].

Fig. 7.8 compares the experimental life with the predicted life using the above three approaches for the first specimen of all three loading angles α. Here, C_{eq} and m_{eq} values corresponding to the first specimen in Table 7.5 have been employed in the simulations. Nearly 60 numbers of FE simulations of mixed mode crack growth have been carried out until the initial crack reaches a length of 32 mm with an increment of $\Delta a=0.5$ mm in each simulation. The top, middle and bottom rows in Fig. 7.8 show the results for $\alpha=30°$, $\alpha=45°$ and $\alpha=60°$, respectively. Fig. 7.8a-c show the comparison of the predicted life using $C_{\mathrm{I}}, m_{\mathrm{I}}$. While, Fig. 7.8d-f show the predicted life with mixed mode Paris constants $C_{\mathrm{eq}}, m_{\mathrm{eq}}$ in Eq. (2.2). While Fig. 7.8g-i show the predicted life using C^{*}, m^{*}. It is interesting to observe from Fig. 7.8 that the fatigue life predicted by all ΔK_{eq} models for the given Paris' constants is very close to each other, and no significant difference exists. This observation is in line with the results shown in Fig. 7.7. However, there is noticeable change in the predicted life by various ΔK_{eq} models while using $C_{\mathrm{eq}}, m_{\mathrm{eq}}$ (Fig. 7.8d-f) as compared with predictions made using the other Paris' constants. It can be observed from Fig. 7.8 that for all the loading angles α, among the three types of Paris constants considered, the predicted life using mixed mode Paris constants ($C_{\mathrm{eq}}, m_{\mathrm{eq}}$), on overall, is closer to the experimental results for the complete crack path. A significant deviation for $\alpha = 60°$ can be noticed in the first and last column plots of Fig. 7.8.

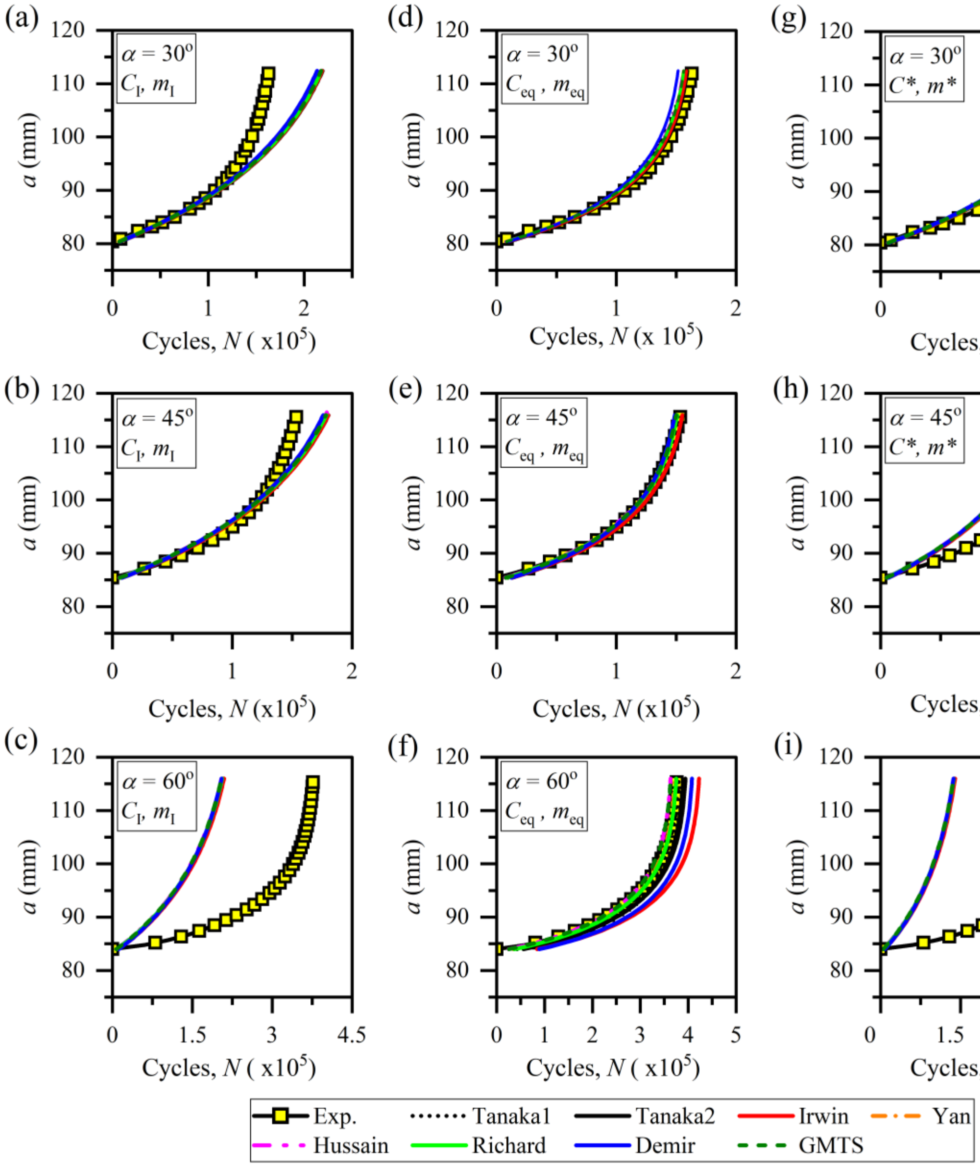

Fig. 7.8 Results for the first specimens. Predicted fatigue life using C_{I} and m_{I} for: (a) $\alpha = 30°$, (b) $\alpha = 45°$, (c) $\alpha = 60°$. Predicted fatigue life using C_{eq} and m_{eq} for: (d) $\alpha = 30°$, (e) $\alpha = 45°$, (f) $\alpha = 60°$. Predicted fatigue life using C^* and m^* for: (g) $\alpha = 30°$, (h) $\alpha = 45°$, (i) $\alpha = 60°$.

On the other hand, the predicted life using mode I Paris constants ($C_\mathrm{I}, m_\mathrm{I}$) shown in Fig. 7.8a-c, and modified Paris constants (C^*, m^*) shown in Fig. 7.8g-i do not follow any definite trend. For loading angles $\alpha = 30°$ and $45°$ the predicted life using ($C_\mathrm{I}, m_\mathrm{I}$) is close to the experimental results for a small initial crack path. And at higher mode mixity, i.e., for loading angle $\alpha = 60°$, highly conservative fatigue life is predicted using $C_\mathrm{I}, m_\mathrm{I}$. A similar trend can also be observed from Fig. 7.8g-i for the predicted fatigue life using C^*, m^*.

Furthermore, the predictability of selected ΔK_eq models for different loading angles is assessed by calculating the performance index Ω, which is the ratio of predicted life to the experimental life using Eq. (7.4).

$$\Omega = \frac{\text{Predicted life}}{\text{Experimental life}} \tag{7.4}$$

The parameter $\Omega < 1$, $\Omega = 1$ and $\Omega > 1$ represent the conservative, consistent, and overpredicted fatigue life. The plots of the performance index of different ΔK_eq models when used with mixed mode Paris constants ($C_\mathrm{eq}, m_\mathrm{eq}$) are shown in Fig. 7.9. It can be seen from Fig. 7.9 that all ΔK_eq models show a significant deviation during the initial period of the crack growth and afterwards predict the fatigue life close to the experimental values.

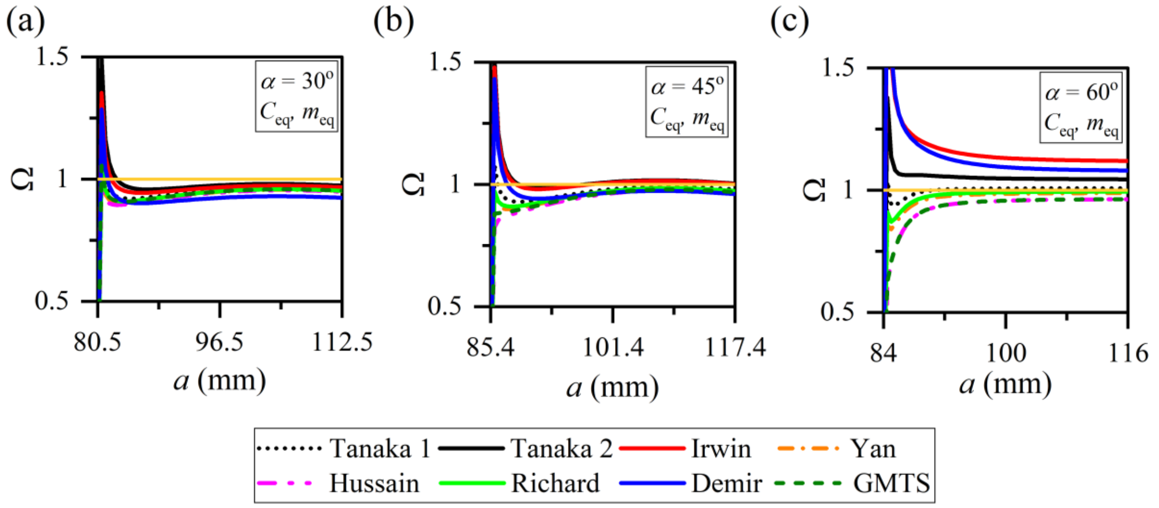

Fig. 7.9 The performance index of different ΔK_eq models for predicting fatigue life using $C_\mathrm{eq}, m_\mathrm{eq}$ for: (a) $\alpha = 30°$. (b) $\alpha = 45°$. (c) $\alpha = 60°$.

More specifically Tanaka 1 and Richard models predict the fatigue life consistently close to the experimental values for all loading angles considered. On the other hand, Sajith et al. [29] reported the best performance of Irwin's ΔK_{eq} model for Al 6061 and Steel 316. Thus, it is evident that the performance of a ΔK_{eq} model strongly depends on the material of the specimen. However, the fatigue life prediction using the GMTS ΔK_{eq} model is found to be the most conservative for all three loading angles.

Importantly and interestingly, the results presented in Fig. 7.8d-f and Fig. 7.9a-c clearly show that when the fatigue life is computed using the mixed mode Paris constants $(C_{\text{eq}}, m_{\text{eq}})$, the predictions are very superior and close to experimental data for all the loading angles considered here. More importantly, the results clearly show that the Paris constants have more effect on the predicted fatigue life than the ΔK_{eq} models. Thus, the results of the present investigation clearly demonstrate that the proposed SECC specimen is the simple and most convenient specimen for conducting mixed mode (I/II) fatigue studies. Further, results also indicate that accurate numerical prediction of the mixed mode fatigue life can be achieved in engineering sense, if mixed mode Paris constant $(C_{\text{eq}}, m_{\text{eq}})$ are employed with any ΔK_{eq} models, in particular, Tanaka 1 and Richard model. Furthermore, the crack kink angle prediction of the GMTS model is superior to that of the MTS criterion (Fig. 7.4a) for any loading angle.

It should be noted that C_{I} and m_{I} remain the same irrespective of all the mixed mode specimens, as they have been obtained using the CT specimen, and $C*$ and $m*$ remain same irrespective of the specimen ID (Table 7.5) for a given loading angle α. Thus, plots such as Fig. 7.8(d)-(f) (corresponding to C_{eq} and m_{eq} values) can be expected to be different for different specimens of a given loading angle α. In line with this observation, Fig. 7.10 compares the experimental life with the predicted life for the third specimen of $\alpha = 30°$ and $60°$ (i.e., specimen IDs 30-3 and 60-3 in Table 7.5) for different values of the Paris' constants. It is interesting to notice that there have been no significant changes in the pattern of the results in Fig. 7.8 and Fig. 7.10. As a consequence, the above observations made with reference to Fig. 7.8 remain valid for other mixed mode specimens in Table 7.5. Although not shown here, indeed similar results have also been obtained for the other specimens of all the loading angles.

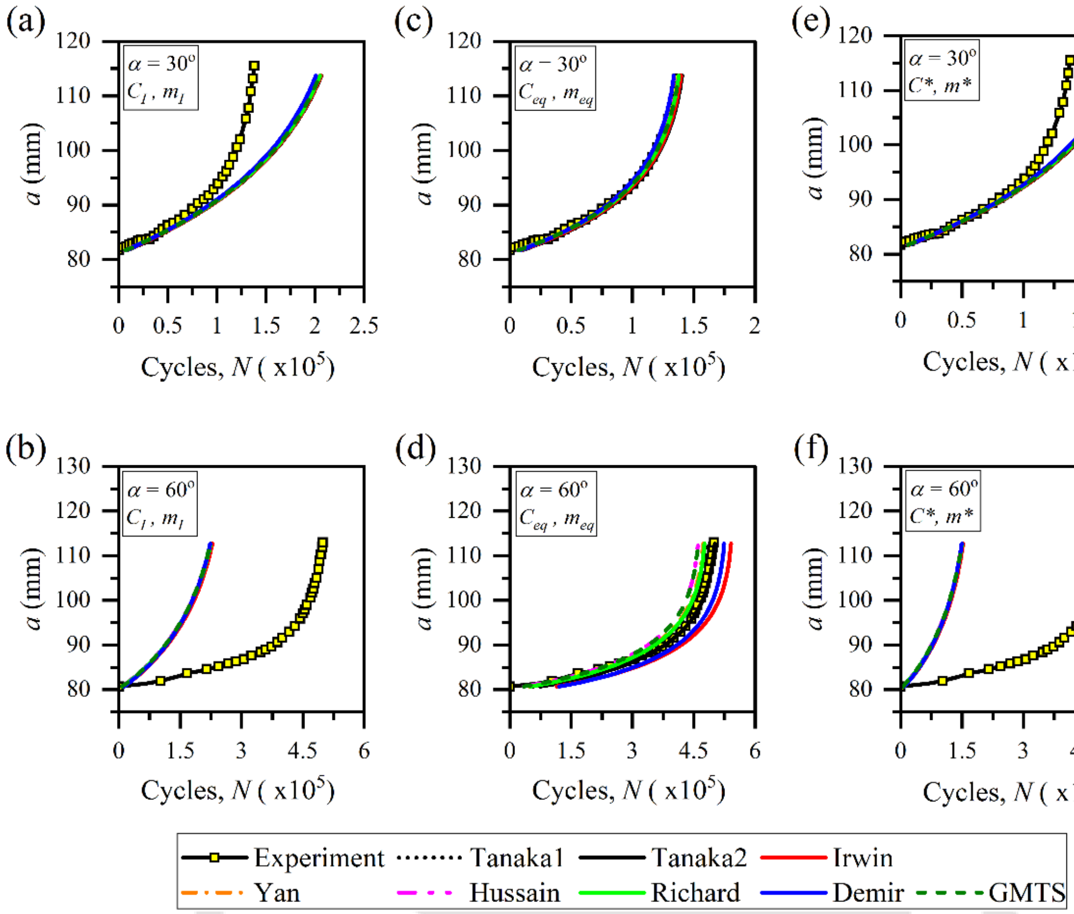

Fig. 7.10 Results for the third specimens. Predicted fatigue life using C_I and m_I for: (a) $\alpha = 30°$, (b) $\alpha = 60°$. Predicted fatigue life using C_eq and m_eq for: (c) $\alpha = 30°$, (d) $\alpha = 60°$. Predicted fatigue life using $C*$ and $m*$ for: (e) $\alpha = 30°$, (f) $\alpha = 60°$.

7.5 Fractographic studies

The fractured surfaces of the tested SECC specimens have been observed under a Zeiss Sigma field emission scanning electron microscope (FESEM), and different features of fractured surfaces have been investigated, viz., striations, secondary cracks, river line patterns, and microcracks. These observable microscopic features are the most typical attributes of cyclic effects on the fatigue fracture mode [256]. SEM images of fracture surfaces of the CT and SECC specimen have been shown in Fig. 7.11. A red color arrow mark at the top-right corner of each image shows the crack growth direction. Fig. 7.11a and Fig. 7.11b show the SEM images of the fracture surface at the crack initiation region of the CT specimen under mode I loading. It can be observed from Fig. 7.11a and Fig. 7.11b that the fracture initiates on multiple parallel cleavage planes forming a river pattern, suggesting the brittle nature of fracture [256,257].

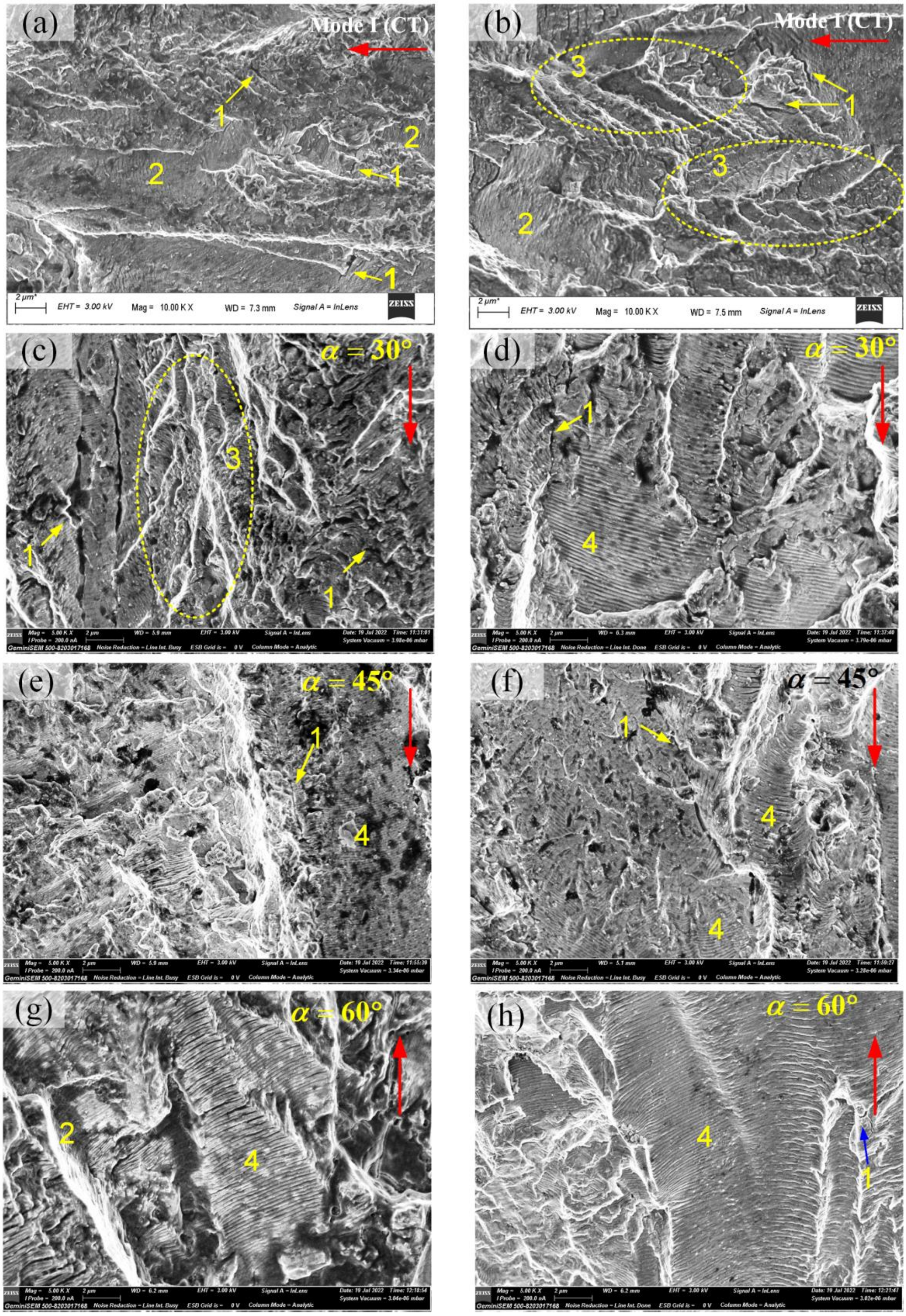

Fig. 7.11 Fracture surfaces of the CT and SECC specimens tested under mode I and mixed mode (I/II) at crack length (a) $a \approx 11.2$ mm (mode I) (b) at $a \approx 13.8$ mm (mode I) (c) $a \approx 87.6$ mm, $\alpha = 30°$, (d) $a \approx 91.4$ mm, $\alpha = 30°$ (e) $a \approx 95.8$ mm, $\alpha = 45°$ (f) $a \approx 97.1$

mm, $\alpha = 45°$, (g) $a \approx 88.4$ mm, $\alpha = 60°$ and (h) $a \approx 93.5$ mm, $\alpha = 60°$. Fracture features are marked as: 1-secondary cracks, 2- cleavage steps, 3-river pattern, 4- striation marks.

Among all the characteristic features, cleavage steps, secondary cracks, and river patterns are most frequently observed and are spread across the entire region (Fig. 7.11a,b). Singh et al. [257] have opined that the interaction of inclusions/hard particles with the propagating striations may be the reason for the generation of secondary cracks (Fig. 7.11a-f). The SEM images of the fractured surface of the SECC specimens tested under different loading angles, i.e., $\alpha = 30°$, 45°, and 60° are shown in Fig. 7.11c-h. Peculiar features of fatigue fracture, like the striation marks, can be seen clearly in Fig. 7.11d-h. These morphological features are characteristic of the stable crack growth process in stage II of fatigue [257]. These observations agree with the result of the macroscopic crack growth.

7.6 Summary

The present work focuses primarily on studying the effect of different Paris constants on the prediction of mixed mode (I/II) fatigue life using the equivalent stress intensity factor models. The efficacy of a new equivalent stress intensity factor model ΔK_{eq} based on the GMTS criterion hass also been examined for the mixed mode (I/II) FCG studies. Furthermore, the effectiveness of the proposed SECC specimen in conducting mixed mode (I/II) FCG tests on metallic materials has also been investigated. For this purpose, a series of mixed mode (I/II) FCG experiments using the SECC specimen made of high-strength Al 7075-T6 alloy have been conducted. The experimental data have been analyzed with the help of finite element mixed mode FCG simulations. The experimental data have then been used to investigate the performance of different ΔK_{eq} models in predicting fatigue life using different Paris constants. Finally, fractography of fracture surfaces under mixed mode fatigue loading are performed. Fractographic studies reveal that the stable crack growth region is dominated by the striations marks for all the mode mixity loading angles.

Chapter 8

Mixed mode (I/II) fatigue crack growth studies on AISI 304 steel

In the previous chapter, certain very important conclusions have been obtained on the mixed mode (I/II) fatigue crack growth phenomenon. These are with reference to the rate of crack growth with change in mode mixity, the influence of the Paris' constants on the predicted mixed mode fatigue life, the efficacy of the proposed specimen, and relative influence of ΔK_{eq} along with the Paris' constants, etc. These observations have been made using the Al 7075-T6 alloy. It is important to see whether or not the observations made in the previous chapter remain valid for other metals. Thus, the thrust of this chapter is the same as that of the previous chapter, but with AISI 304 steel as the material of the proposed SECC specimen. First, the results obtained from mode I and mixed mode (I/II) FCG analysis are presented. Then, the FE mixed mode (I/II) FCG simulations have been performed along the actual crack path to calculate the variation of fracture parameters, i.e., $K_{\mathrm{I}}, K_{\mathrm{II}}$ and $T-$stress. Similar to the previous chapter, the effect of the use of three different Paris constants, i.e., the modified Paris constant (C^*, m^*), conventional mode I (C, m), and mixed mode Paris constants ($C_{\mathrm{eq}}, m_{\mathrm{eq}}$) on the predicted fatigue life by various ΔK_{eq} models (including the GMTS based model) have been discussed in context of steel. The fractographic studies have been presented to aid in further understanding mixed mode fatigue crack propagation in AISI 304 steel.

8.1 Experimental procedure

In the present work, the SECC specimens made of AISI steel have been used for the mixed mode (I/II) FCG studies. Due to its excellent mechanical strength and corrosion resistance, AISI 304 steel has been widely utilized in many advanced engineering applications, including nuclear reactors, marine environments, pressure vessels, and additively manufactured materials [258–260].

The specimens used in the present work have been fabricated using the procedure given in subsection 4.6.2 (Page 75). The complete experimental setup given in Fig. 4.20 (Page 81) has been used for the present investigation. All fatigue experiments have been performed using a BiSS ITW make, 250 kN servo-hydraulic UTM. Mode I and mixed mode FCG tests have been carried out under constant amplitude tension-tension cyclic loading using a sinusoidal waveform with a load ratio $R = 0.1$ and frequency of 10 Hz. The SECC specimens under $\alpha = 30^\circ$, 45° and 60° have been subjected to $P_{\max} = 30$ kN, and the specimen under $\alpha = 75^\circ$ has been subjected to $P_{\max} = 40$ kN. Mode I FCG tests on two identical CT specimens have been performed with a maximum cyclic load of $P_{\max} = 20$ kN. The instantaneous crack length in the CT specimen has been measured using a clip gauge (subsection 4.7.5, Page 84).The recommendations of the ASTM E647 standards have been followed for both the pure-mode I and mixed mode (I/II) FCG investigations. The optical method as explained in Section 4.11 (Page 88) has been adopted for measuring the crack length during mixed mode (I/II) FCG testing. And a five-parameter double-exponential expression (given in Eq. (7.1)) has been employed to best-fit the measured (N, a) data.

8.2 Mode I FCG and Tensile test results

8.2.1 Mode I FCG Results

The results of the mode I FCG tests conducted on two identical CT specimens made of AISI 304 steel are given in Table 8.1. As can be observed from Table 8.1, after reaching around 2.8×10^5 number of loading cycles, both the CT specimens fractured unstably at an approximate critical crack length of $a_c \approx 40$ mm. The average fracture toughness of the tested AISI 304 steel is determined to be equal to $K_C = 99.8\,\text{MPa}\sqrt{\text{m}}$. This value corresponds to the maximum mode I SIF $K_{\max}$ of the tested CT specimen at the point of unstable fracture. For a constant-amplitude FCG test (or $K-$increasing test), the fracture toughness of the tested material can be calculated by putting the maximum cyclic load $P_{\max}$ and the critical crack length a_c (at which unstable crack growth occurs) into Eq. (7.2).

Table 8.1 Results of the mode I FCG test obtained using the CT specimen.

Specimen ID	Initial Notch length	$P_{\max}$ (kN)	Specimen's thickness	Final crack length a_c	Cycles to fracture N_f ($\times 10^5$)
CT-1	9 mm	20	15.4 mm	40.6 mm	2.85
CT-2	9 mm	20	15.1 mm	40.7 mm	2.79

Fig. 8.1a shows the fatigue life curve (or $a-N$ curve) obtained from the mode I FCG experiments on two CT specimens. It can be seen from Fig. 8.1a that the crack under fatigue loading grows exponentially. Finally, as the crack length approaches the critical crack length a_c, the CT specimen fractures suddenly.

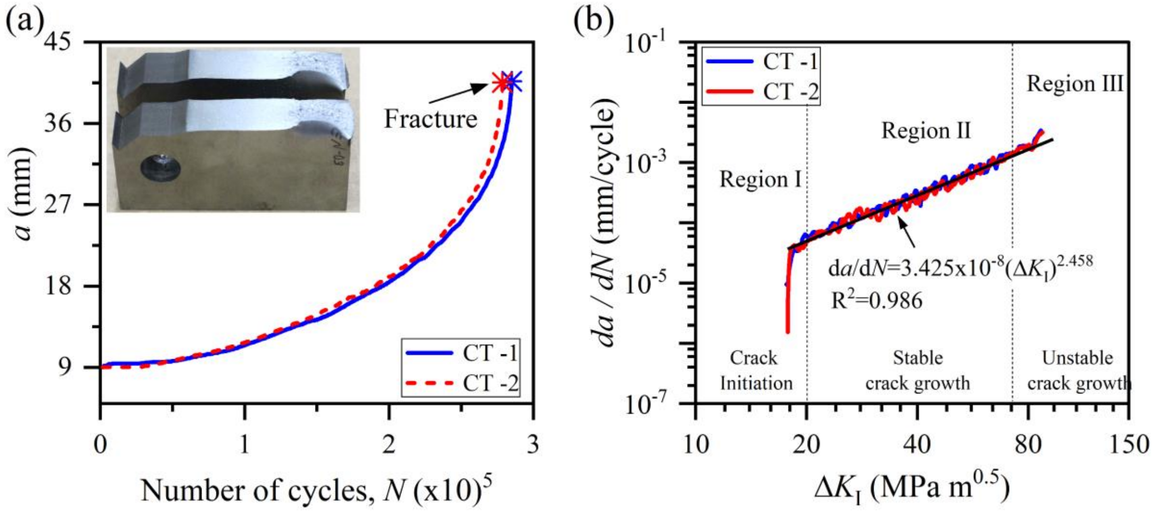

Fig. 8.1 Fatigue crack growth curves obtained from the mode I FCG test using CT specimen (a) $a-N$ curves. (b) $da/dN-\Delta K$ curve in log-log scale.

The FCGR da/dN versus ΔK_{I} plots in a log-log scale of both the CT specimens have been shown in Fig. 8.1b. The FCGR for the CT specimen has been calculated from the $a-N$ plot (Fig. 8.1a) using the seven-point incremental polynomial method [253]. And ΔK_{I} values for the CT specimen at each crack length have been determined using the SIF calibration equation Eq. (7.2) as given in ASTM 647. As shown in Fig. 8.1, mode I fatigue tests show very good reproducibility. The mode I Paris material constants (C, m) for AISI 304 steel have been calculated by fitting a single straight line in Region II of the da/dN

versus ΔK_{I} plot (Fig. 8.1b) for both the CT specimens. The calculated mode I Paris constants are given in Table 8.2. These values of mode I Paris constants (C, m) for AISI 304 steel are of the same order as reported in the previous studies [204,261].

Table 8.2 Paris material constants for AISI 304 steel obtained from mode I fatigue tests.

Material	C ((mm/cycle)/(MPa$\sqrt{\mathbf{m}}$)^m)	m
AISI 304	3.425×10^{-8}	2.458

8.2.2 Tensile tests results

The mechanical properties of AISI 304 steel have been obtained from the tensile tests (as per ASTM E8) on three specimens, and the average results are presented in Table 8.3. These material properties will be used for the numerical simulation of the FCG.

Table 8.3 Mechanical properties of AISI 304 steel obtained from the tensile test.

Yield strength (MPa)	**Ultimate strength (MPa)**	**% Elongation**	% Reduction in area	**Young's modulus E (GPa)**	**Poisson's ratio ν**
273	686	28	68	200	0.3

8.3 Mixed mode (I/II) experimental FCG results

8.3.1 Crack growth direction and fatigue life results

The complete results of mixed mode (I/II) FCG studies on AISI 304 steel using the SECC specimens are given in Table 8.4. Except for $\alpha = 30°$, two identical SECC specimens have been tested for each loading angle for repeatability. It can be observed from Table 8.4 that the fatigue life of the AISI 304 steel increases with the increase in the loading angle for a given $P_{\max}$, and stress ratio R. As explained in Section 8.1, $P_{\max}$ is different for the specimen with $\alpha = 75°$. As a result, N_{f} is different from other loading angles. The average fatigue life N_{f} of the SECC specimen tested under $\alpha = 45°$ is approximately 50% higher than the average fatigue life for $\alpha = 30°$. Similarly, the average fatigue life N_{f} of the SECC specimen tested under $\alpha = 60°$ is approximately 50% higher than the average fatigue life at $\alpha = 45°$. Similar to the AL 7075-T6 alloy, this increase in the experimentally observed fatigue life of AISI 304 steel with the increase in loading angle α can be attributed to the fact that, in the SECC specimen, the mode II loading component increases with the increase in loading angle α (subsection 5.1.2, Page 93), which lead to a higher resistance to the crack kinking, and also possibly due to the friction between the crack surfaces during the mode II deformation.

Table 8.4 Results of mixed mode (I/II) FCG experiments using the SECC specimen.

Specimen ID	$\alpha\,(^\circ)$	$P_{\max}$ (kN)	Specimen's Thickness (mm)	Notch + Δa_{p} (mm)	N_{f} ($\times 10^5$)	$\theta_0\,(^\circ)$
30-1	30	30	14.7	89.4	3.24	28.5
45-1	45	45	14.4	87.4	4.81	40.5
45-2	45		14.9	88.9	4.74	
60-1	60	30	14.9	88.9	7.31	50
60-2	60		15.2	89.9	7.29	
75-1	75	40	15.0	89.2	4.72	60
75-2	75		15.0	91.9	4.55	

Fig. 8.2 shows the fatigue life (or $a-N$) curves of the AISI 304 steel tested under four different loading angles, i.e., $\alpha = 30^\circ$, 45°, 60°, and 75°. A best-fit curve (Eq. (7.1) has also been fitted to the experimental $a-N$ data for each loading angle (Fig. 8.2). As can be observed from Fig. 8.2, considering the nature of variability in the fatigue experiments, the present experimental setup and testing procedure have achieved excellent reproducibility. A careful observation of Fig. 8.2 reveals that as the loading angle α increases, the $a-N$ curves exhibit flatter behavior in the early stages of the crack growth, suggesting increased resistance to the crack growth. However, once the crack kinks from the precrack, subsequent propagation occurs rapidly. This observation is consistent with the findings reported in previous studies by Tamilselvan et al. [45], and also in line with the finding obtained using the Al 7075-T6 alloy in the previous chapter. Furthermore, the magnitude of the number of cycles N_{f} taken before the final fracture indicates that all specimens have been subjected to high cycle fatigue loading conditions.

Fig. 8.3 shows the fractured SECC specimens at four different loading angles. The initial crack kink angle θ_0 has been measured from both sides of the two parts of each fractured specimen. The average value of the four measured angles for each specimen is given in Table 8.4. The variation between the measured angle from both sides of the fractured specimens has been found to be in tolerance of $\pm 3^\circ$. Similarly, the difference in the measured kink angles between the two SECC specimens for each loading angle has been observed to be below ±2°. It can be noticed from Fig. 8.3 that as in case Al 7075-T6, the final crack growth is practically perpendicular to the applied loading axis.

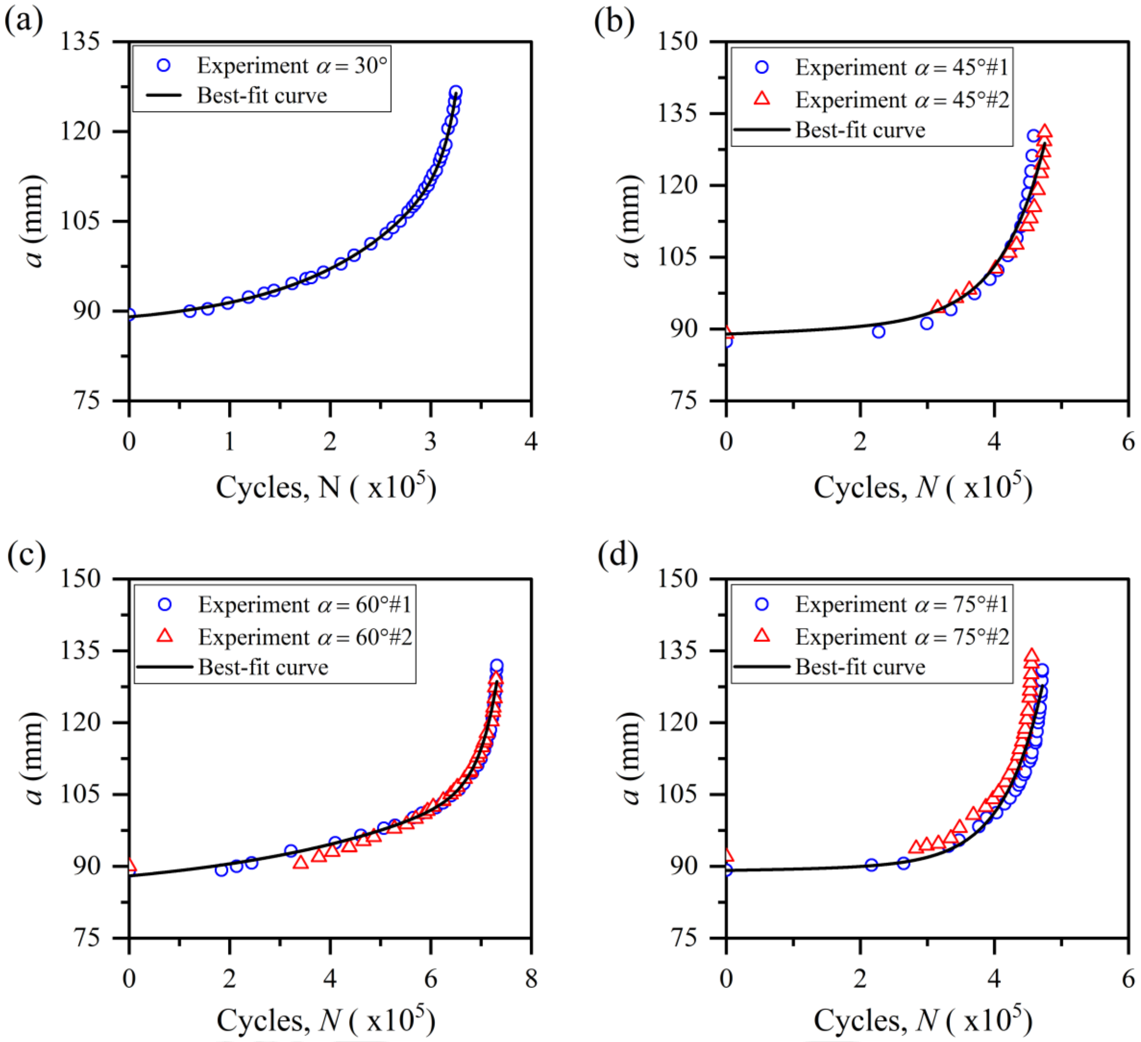

Fig. 8.2 Experimental data and the fitted best-fit curve for: (a) $\alpha = 30°$. (b) $\alpha = 45°$. (c) $\alpha = 60°$. (d) $\alpha = 75°$.

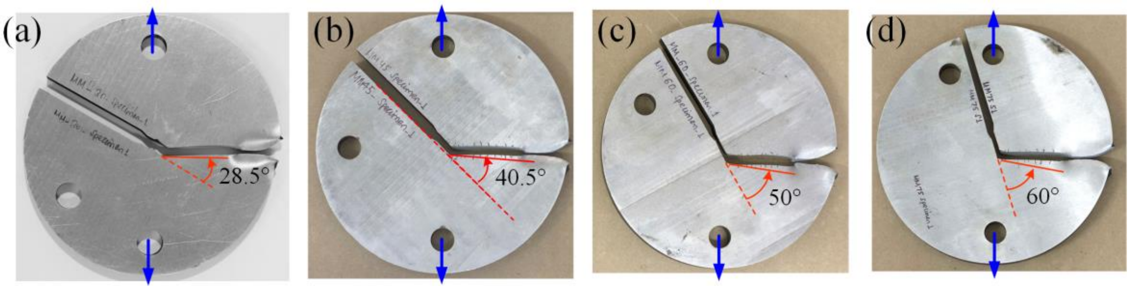

Fig. 8.3 Fractured SECC specimens, showing the actual crack path for: (a) $\alpha = 30°$. (b) $\alpha = 45°$. (c) $\alpha = 60°$. (d) $\alpha = 75°$.

Fig. 8.4a shows the comparison of the experimentally observed initial crack kink angles θ_0 with the theoretical predictions of the MTS and GMTS criteria. It can be observed from Fig. 8.4a, the GMTS criterion (using $r_c = 0.5$ mm) accurately predicts initial crack kink angle θ_0 very close to the experimental value for all the loading angles. In contrast, the MTS criterion can only predict the crack kink angles θ_0 close to the experimental results, particularly for lower mode mixities. It is interesting to notice that similar trends have also been observed for the case of Al 7075 T6 material (see Fig. 7.4, Page 134). Since the accurate prediction of fatigue life depends significantly on the predicted crack path, in the present work, the GMTS criterion has been employed to predict the complete crack path in numerical simulations. Fig. 8.4b shows the actual crack paths under mixed mode fatigue loading. These paths are measured from the pre-crack tip to the point of final unstable fracture for the SECC specimens shown in Fig. 8.3. It is evident from Fig. 8.4b that as the loading angle α increases, both the kink angle θ_0 and deviation from the plane of the initial crack also increase. Furthermore, the straight line trend of plots in Fig. 8.4b and fractured surfaces in Fig. 8.3 clearly indicate that crack grows practically straight and perpendicular to the direction of the applied loading as in case of Al 7075 T6 alloy (see Fig. 7.4b).

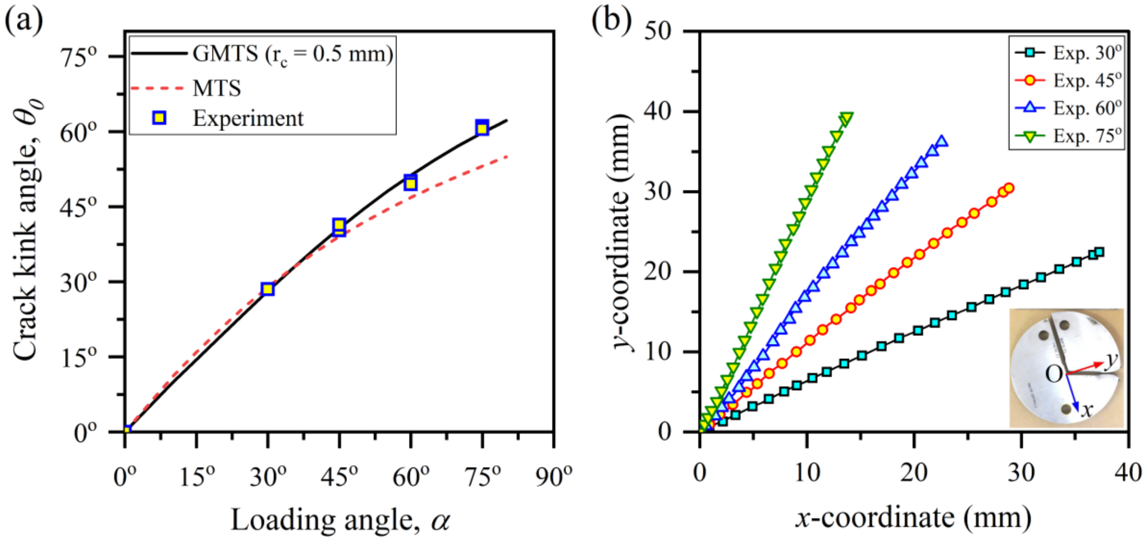

Fig. 8.4 (a) Comparison of experimental crack kink angle θ_0 with the theoretical predictions of MTS and GMTS criteria. (b) Actual crack paths measured from the fractured SECC specimens under four different loading angles.

These actual crack paths shown in Fig. 8.4b have been used for the finite element FCG simulations. The FE analyses as explained in previous chapter (subsection 7.3.2, Page 135) has also been performed for the AISI steel to calculate the variation $K_{\mathrm{I}}, K_{\mathrm{II}}$), and $T-$stress along the actual crack path.

8.3.2 FCGR curves for different ΔK_{eq} models under mixed mode loading

After obtaining SIFs and $T-$stress at the successive positions of the crack tip along the actual crack path (Fig. 8.4b) using FE analyses, these values have then been used to calculate the different ΔK_{eq} models given in Table 3.1 (Page 52). Plane stress conditions have been assumed in all FE analyses. The material properties of steel given in Table 8.3 have been used in the FE analyses. The procedure explained in the previous chapter for AL 7075 T6 alloy has been used here. FE simulations similar to that shown in Fig. 7.5 (Page 136) have been performed until the critical crack length. The mixed mode FCGR da/dN (corresponding to the simulated crack length) has been derived from the first derivative of the best-fit curve (Eq. (7.1)). Finally, the mixed mode FCGR data obtained from the SECC specimen have been plotted against selected ΔK_{eq} models in a log-log scale as shown in Fig. 8.5. The mode I FCGR data (obtained from the CT specimen) is also appended in each plot of Fig. 8.5 for comparison purpose. As can be observed from Fig. 8.5, all selected ΔK_{eq} models exhibit the same correlation pattern. The mixed mode FCGR curves from different loading angles fall on a narrow band in the Paris region close to the mode I FCGR curve, but not the coincident. In contrast to Al 7075-T6 alloy, the crack growth rates of this steel are of the same order as that of the mode I, specifically in the Paris' regime.

To further investigate how different ΔK_{eq} models correlates mixed mode FCGR, the FCGR for each loading angle has been replotted separately in Fig. 8.6. Fig. 8.6 illustrates that, except for the initial crack-tip positions, the selected ΔK_{eq} models exhibit similar FCGR correlations. The results shown in Fig. 8.6 indicate that any ΔK_{eq} model can potentially be used for predicting fatigue life. These observations are similar to the results of Al 7075-T6 (Fig. 7.7). Moreover, similar observations have also been reported in Ref. [255,262]. Nevertheless, the predicted fatigue life plots (or $a-N$ plots) give a clearer understanding of the effect of Paris constants using these ΔK_{eq} models.

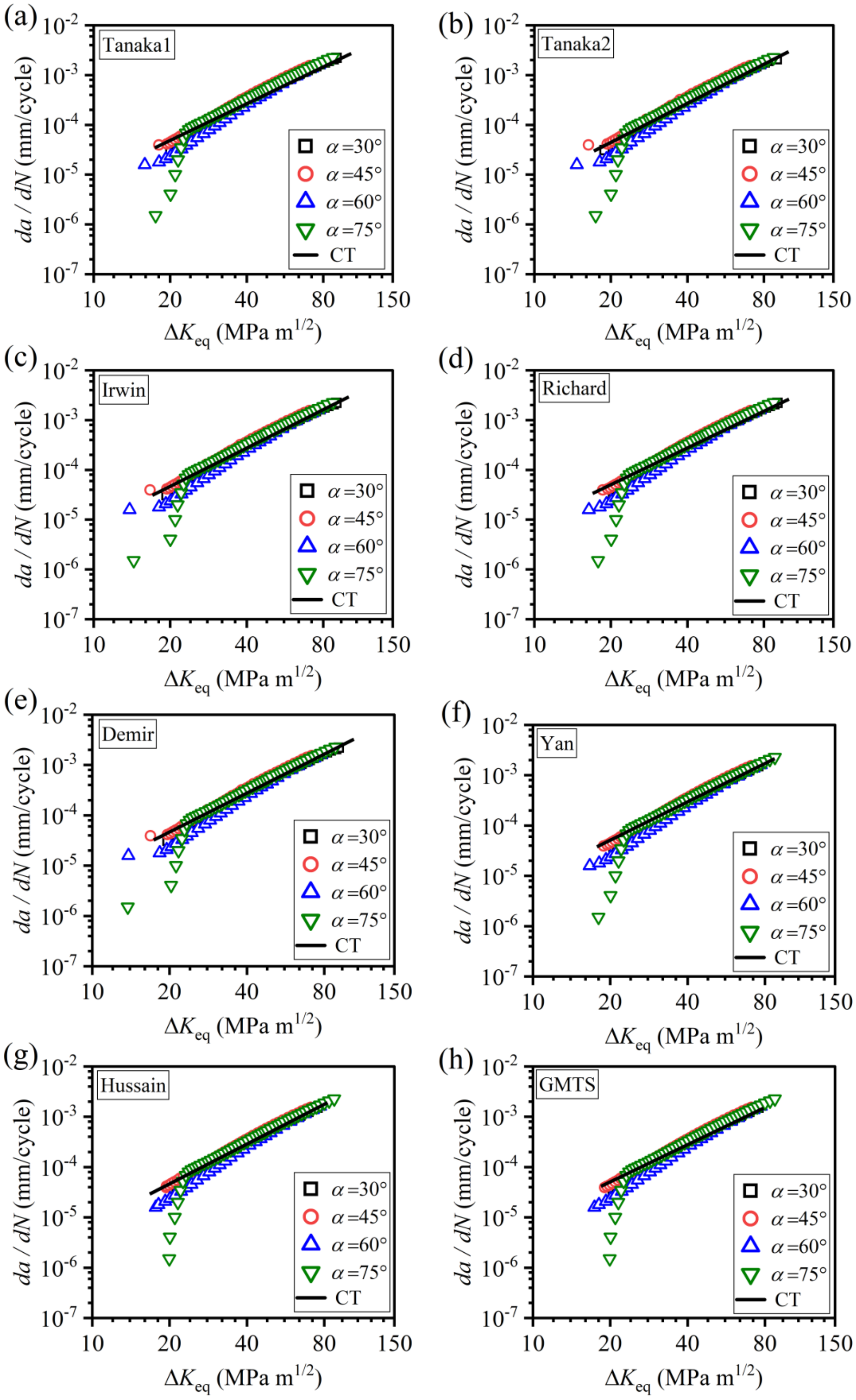

Fig. 8.5 FCGR at different loading angles as a function of various ΔK_{eq} models: (a) Tanaka 1. (b) Tanaka 2. (c) Irwin. (d) Richard. (e) Demir. (f) Yan. (g) Hussain. (h) GMTS model.

To determine the mixed mode Paris constants (C_{eq}, m_{eq}) for each ΔK_{eq} model and loading angle α, a linear best-fit curve is fitted in the Paris region of Fig. 8.6. Table 8.5 presents the calculated mixed mode Paris constants for each ΔK_{eq} model at four different loading angles, i.e., $\alpha = 30°$, 45°, 60° and 75°. As can be seen from Table 8.5, the mixed mode Paris constants (C_{eq}, m_{eq}) obtained from different ΔK_{eq} model are close to each other for a given loading angle.

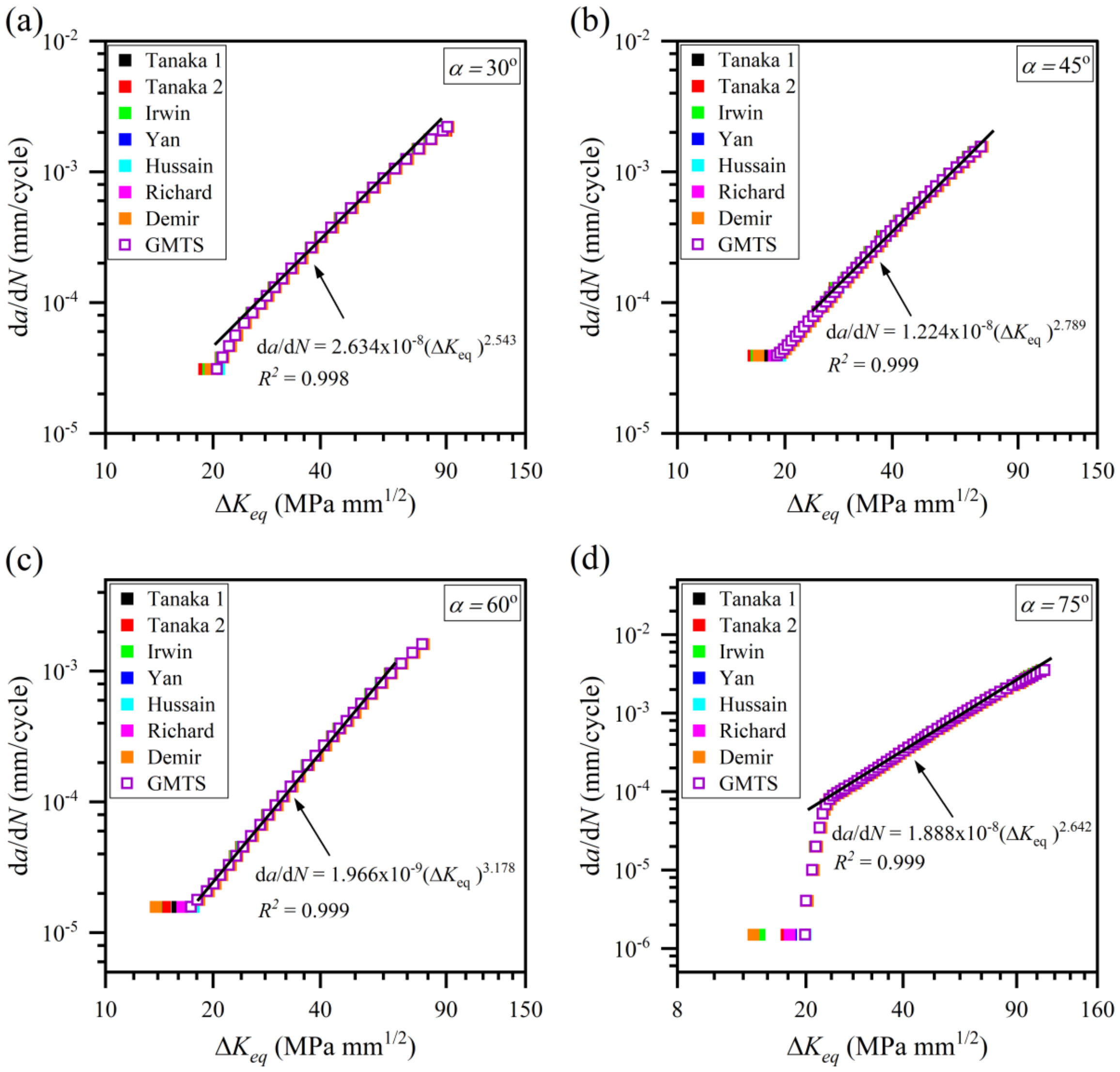

Fig. 8.6 FCGR as a function of selected ΔK_{eq} models at different loading angles: a) $\alpha = 30°$. (b) $\alpha = 45°$. (c) $\alpha = 60°$. (d) $\alpha = 75°$.

Moreover, the C_{eq} parameter for each loading angle is significantly different than the mode I C parameter. On the contrary, the mixed mode m_{eq} parameter for each loading angle is close to the mode I m parameter. A similar trend has also been observed for Al 7075-T6 alloy in previous chapter and reported by Ma et al. [162]. In Section 8.4, the average values of C_{eq} and m_{eq} obtained for each loading angle α (Table 8.5) have been used to calculate the predicted fatigue life.

Table 8.5 The mixed mode Paris constants C_{eq} and m_{eq} for each ΔK_{eq} model.

ΔK_{eq} Model	$\alpha = 30°$		$\alpha = 45°$		$\alpha = 60°$		$\alpha = 75°$	
	C_{eq} ($\times 10^{-8}$)	m_{eq}	C_{eq} ($\times 10^{-8}$)	m_{eq}	C_{eq} ($\times 10^{-9}$)	m_{eq}	C_{eq} ($\times 10^{-8}$)	m_{eq}
Tanaka_1	2.641	2.543	1.218	2.791	1.980	3.178	1.901	2.642
Tanaka_2	2.641	2.545	1.345	2.769	2.091	3.165	1.901	2.643
Irwin	2.641	2.544	1.255	2.785	2.035	3.172	1.901	2.642
Yan	2.639	2.542	1.186	2.797	1.934	3.183	1.901	2.641
Hussain	2.643	2.542	1.182	2.797	1.925	3.184	1.903	2.641
Richard	2.642	2.542	1.197	2.795	1.949	3.181	1.901	2.641
Demir	2.558	2.544	1.209	2.786	1.872	3.183	1.782	2.651
GMTS	2.663	2.540	1.198	2.794	1.942	3.182	1.913	2.639
Average	**2.634**	**2.543**	**1.224**	**2.789**	**1.966**	**3.178**	**1.888**	**2.642**

Note: Unit of C and C_{eq} for AISI steel is taken as $((\text{mm/cycle})/(\text{MPa}\sqrt{\text{m}})^{\text{m}})$ in this chapter.

8.4 Results and discussion of fatigue life prediction

This section provides a comprehensive investigation on utilizing the three different types of Paris constants to predict fatigue life under mixed mode (I/II) loading conditions, viz., (a) using C and m values of AISI 304 steel obtained from the mode I FCG tests on CT specimen, (b) using average C_{eq} and m_{eq} values associated with each loading angle α given in Table 8.5), and (c) using $C*$ and $m* = m$ as proposed by Ma et al. [162]. For this purpose, the incremental crack tip extension approach as explained in subsection 3.4.3 (Page 53) has been employed in FCG simulations. The direction of the crack path has been determined using the GMTS criterion Eq. (3.5), while a crack increment length of $\Delta a = 1$ mm has been utilized. Nearly 40 FE simulations of mixed mode crack growth have been carried out until the initial crack reaches a length of 42 mm from the pre-crack-tip.

Fig. 8.7 shows a comparison between the experimental life and the predicted life utilizing the three distinct approaches for four different loading angles. In Fig. 8.7, the predicted fatigue life plots have been shifted such that the initial crack identified during the mixed mode FCG experiment has been utilized as the starting point for cycle counting [263]. As per Amato et al. [263], this shift in numerical cycle count ensures that both experimental and simulated data have a consistent reference point for comparing fatigue life. It has been observed that, depending upon the loading angle α, a significant portion of the early fatigue life of AISI 304 steel is spent without any visible crack growth (see Fig. 8.2). When compared to AISI 304 steel, visible crack propagation appeared in the Al 7075-T6 alloy as soon as the loading started. On the other hand, for AISI 304 steel, a visible crack kinking from the pre-crack-tip appeared only after a significant number of loading cycles (nearly 10^5 to 2×10^5 cycles). As a result, this shift in numerical cycle count is essential for consistent comparison and to compensate for ultra-slow crack growth during initial phase of crack propagation especially for ductile materials like AISI 304 steel [263].

Fig. 8.7 shows the comparison between the predicted and experimental fatigue life. The results for loading angles $\alpha = 30°$, 45°, 60°, and 75° are shown in the first, second, third, and fourth rows, respectively, in Fig. 8.7. Fig. 8.7a-d show the predicted life using mode I Paris constants C, m. While, Fig. 8.7e-h show the predicted life using mixed mode Paris constants $C_{\text{eq}}, m_{\text{eq}}$. And Fig. 8.7i-l show the predicted life using modified Paris constants C^*, m^*. It is worth noting that, according to Fig. 8.7, the predicted fatigue life by the ΔK_{eq} models are very close to each other, with no significant differences for the given Paris' constant. These observations are in line with the results shown in Fig. 8.6. Again, one can notice that a significant deviation between the predicted and experimental results in first and last column plots of Fig. 8.7. The overall prediction of the fatigue life using various ΔK_{eq} models for a given Paris' constants remain same as that observed in case of Al 7075-T6 alloy. Interestingly once again, when compared to the other pair of Paris' constants, the predicted life using mixed mode Paris constants ($C_{\text{eq}}, m_{\text{eq}}$) is obtained closer to the experimental results for all the loading angles. Fig. 8.7a,b show that the predicted life using mode I Paris constants (C, m) is close to the experimental results only for lower loading angles $\alpha = 30°$ and 45°. On the other hand, for higher loading angles, i.e., $\alpha = 60°$ and 75°, highly conservative fatigue life is obtained using mode I Paris constants (C, m). As far as predicted life using modified Paris constants (C^*, m^*) is concerned, the predicted life exhibits a highly conservative trend for all the loading angles (Fig. 8.7i-l). However, similar to the case of Al 7075-T6 alloy, the predictions using C_{eq} and m_{eq} are closer to the experimental results for all the selected ΔK_{eq} models. Further results in Fig. 8.7 once again undoubtedly substantiate that the effect of Paris' constants is more pronounced than the selection of a particular ΔK_{eq} model.

In order to obtain an explicit demonstration of the performance of various models, the predictability of selected ΔK_{eq} models for different loading angles has been assessed by calculating the performance index Ω, which is the ratio of predicted life to experimental life using Eq. (7.4). The value of parameter $\Omega < 1$, $\Omega = 1$, and $\Omega > 1$ represent the conservative, consistent, and overpredicted fatigue life. The plots of the performance index of selected ΔK_{eq} models when used with $C_{\text{eq}}, m_{\text{eq}}$ are shown in Fig. 8.8. It can be seen from Fig. 8.8 that all ΔK_{eq} models show a significant deviation for a few steps in the initial crack growth period and afterwards predict the fatigue life close to the experimental values. More specifically, for loading angles $\alpha = 30°$ and 45°, Tanaka 2 and Irwin models predict the fatigue life consistently close to the experimental values. And for higher loading angles, i.e., $\alpha = 60°$ and 75°, the Demir model predicts the fatigue life close to the experimental life. As can be seen from Fig. 8.8d, for $\alpha = 75°$, the predictions made by the Demir model are as close as those of Irwin model.

Overall, the Irwin model with C_{eq} and m_{eq} consistently provides predictions closer to the experimental values, though for all practical purposes, any model can be considered for reasonably accurate values using C_{eq} and m_{eq} as depicted in Fig. 8.7. These results are consistent with the findings of Sajith et al. [28]. However, the fatigue life prediction using the GMTS-based ΔK_{eq} model is found to be the most conservative for all four loading angles. The results of the present chapter also indicate that the proposed SECC specimen can be successfully employed for mixed mode (I/II) FCG studies of metals.

Thus, the results of the present investigation clearly demonstrate that the proposed SECC specimen is the simple and most convenient specimen for conducting mixed mode (I/II) FCG studies. Further, results also indicate that accurate numerical prediction of the mixed mode fatigue life can be achieved if mixed mode Paris constant $(C_{\text{eq}}, m_{\text{eq}})$ are employed with ΔK_{eq} models in particular Tanaka 2 and Irwin model.

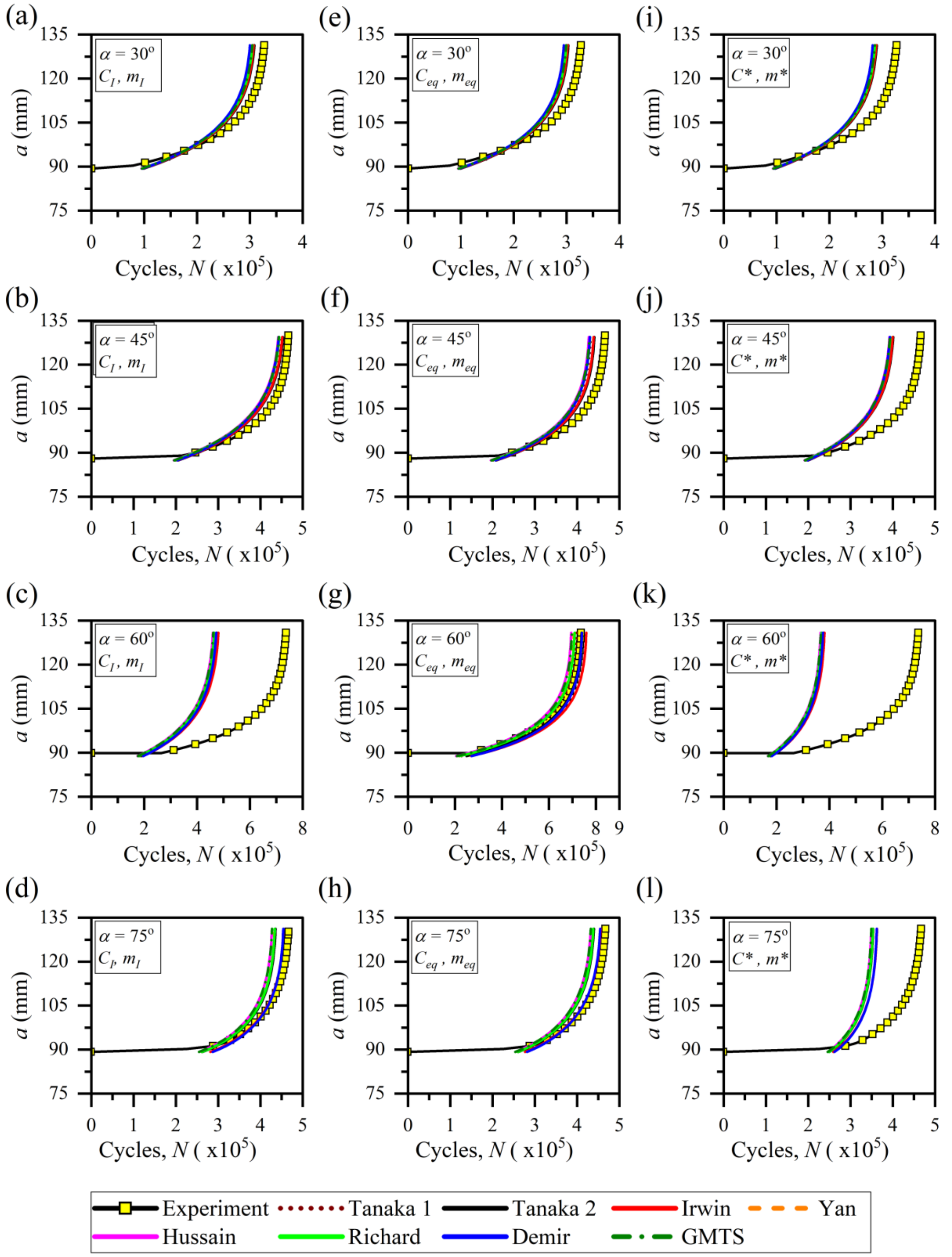

Fig. 8.7 Predicted fatigue life using C_I, m_I for: (a) $\alpha = 30°$, (b) $\alpha = 45°$, (c) $\alpha = 60°$, (d) $\alpha = 75°$. Predicted fatigue life using C_{eq}, m_{eq} for: (e) $\alpha = 30°$, (f) $\alpha = 45°$, (g) $\alpha = 60°$, (h) $\alpha = 75°$. Predicted fatigue life using C^*, m^* for: (i) $\alpha = 30°$, (j) $\alpha = 45°$, (k) $\alpha = 60°$, (l) $\alpha = 75°$.

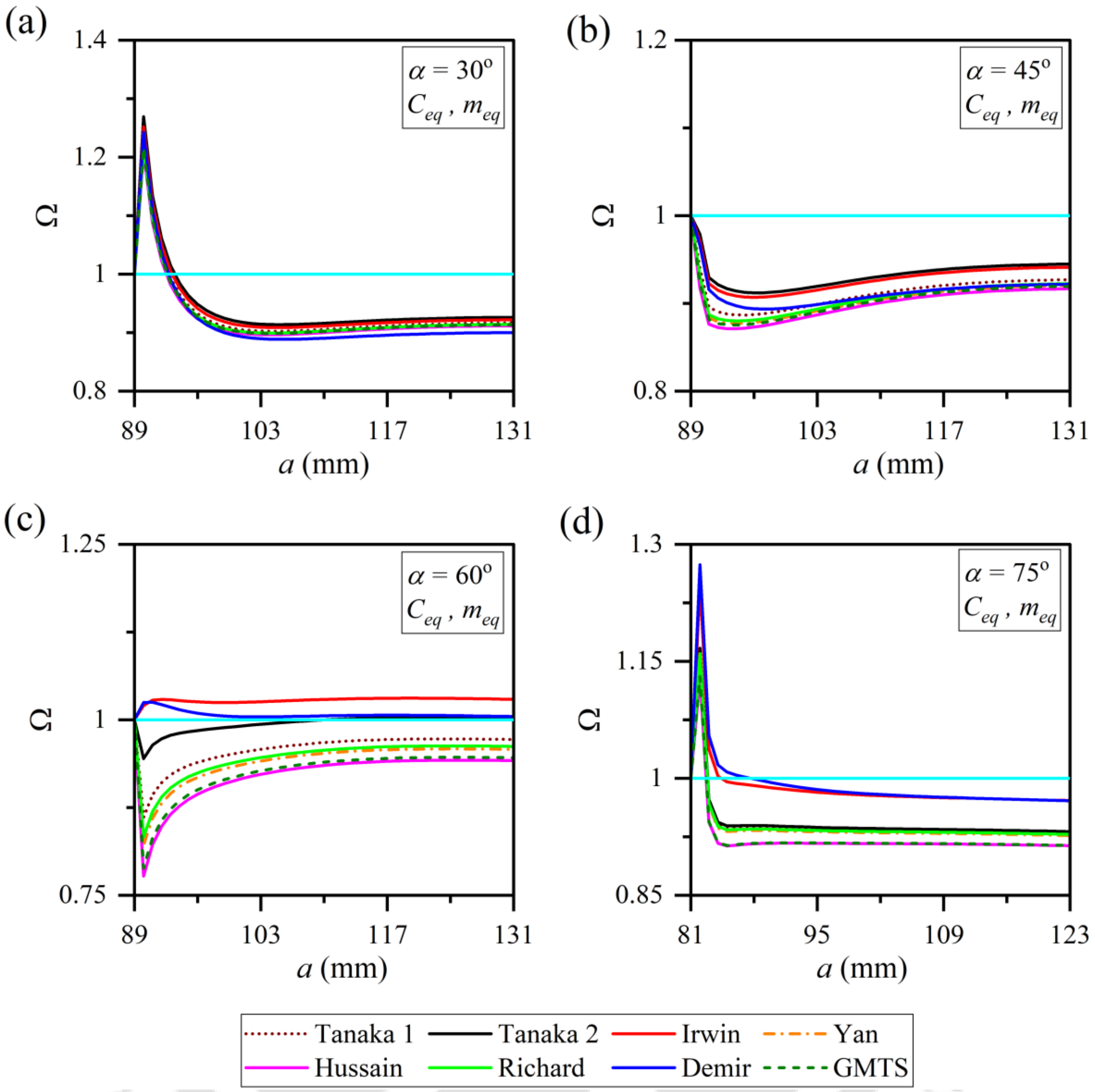

Fig. 8.8 The performance index of different ΔK_{eq} models for predicting fatigue life using C_{eq}, m_{eq} for: (a) $\alpha = 30°$. (b) $\alpha = 45°$. (c) $\alpha = 60°$. (d) $\alpha = 75°$.

8.5 Fractographic studies

Fractographic studies are essential to determine microscopic features like striations, secondary cracks, river line patterns, flat facets, etc. These features are the most typical attributes of fatigue fracture. The fractured surfaces of the SECC specimen have been observed under a Zeiss Sigma field emission scanning electron microscope.

Fig. 8.9 shows different features of the fracture surface of the CT specimen tested under mode I loading. In all the figures, the crack growth direction is mentioned at the top-left corner by a red color arrow mark. It can be observed that the striation marks spread over most of the fracture surfaces (Fig. 8.9b). The striation marks on the fracture surface are a good indicator of ductility [264]. To clearly distinguish the striation marks, SEM images at a magnification of 10,000× are shown in Fig. 8.9b. It has been observed that as the crack grows progressively, the spacing between striations marks increases with each cycle [265].

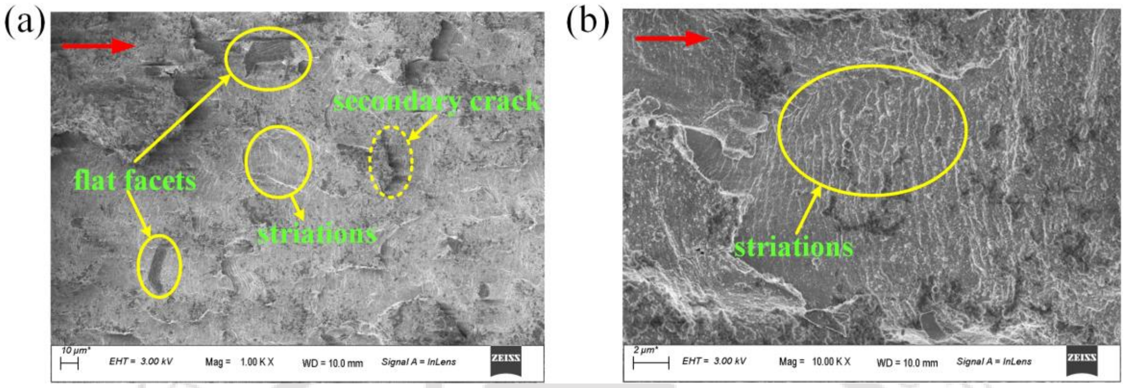

Fig. 8.9 SEM photographs of the fracture surface of CT specimen tested under mode I loading at (a) $a \approx 15.2\,\text{mm}$ and (b) $a \approx 17.8\,\text{mm}$.

The SEM images of the fractured surface of the SECC specimens tested under different loading angles, i.e., $\alpha = 30°$, 45°, 60°, and 75° are shown in Fig. 8.10. As can be observed from Fig. 8.10a,e,f, during the initial stages of the crack growth, the fracture surfaces exhibit a higher degree of roughness that can be attributed to the presence of the mode II loading component. Since the features of these fracture surfaces cannot be expressed in simple terms, they are called "featureless fracture surfaces" (Fig. 8.10a) [266]. The fracture surfaces at the later stage of crack growth appear relatively smoother. This can possibly be attributed to the continuous decrease in the mode II SIF K_{II} and corresponding increase in mode I SIF K_{I}, with the increasing crack length. The decrease in K_{II} reduces the rubbing and interaction between the opposing fracture surfaces, thereby producing comparatively smooth surfaces. The flat facets indicate the intergranular separation and grain boundary cracking (Fig. 8.9a and Fig. 8.10b,e,f,g) [267], and the irregular regions surrounding these flat facets can be associated with quasi-cleavage separation [268]. Singh et al. [257] have opined that the interaction of inclusions/hard particles with the propagating striations may be the reason for the generation of secondary cracks (Fig. 8.10). Peculiar features of fatigue fracture like the striation marks can be seen clearly in Fig. 8.10d,h. These morphological features are characteristic of the stable crack growth process in stage II of fatigue [257]. These observations agree with the result of the macroscopic crack growth.

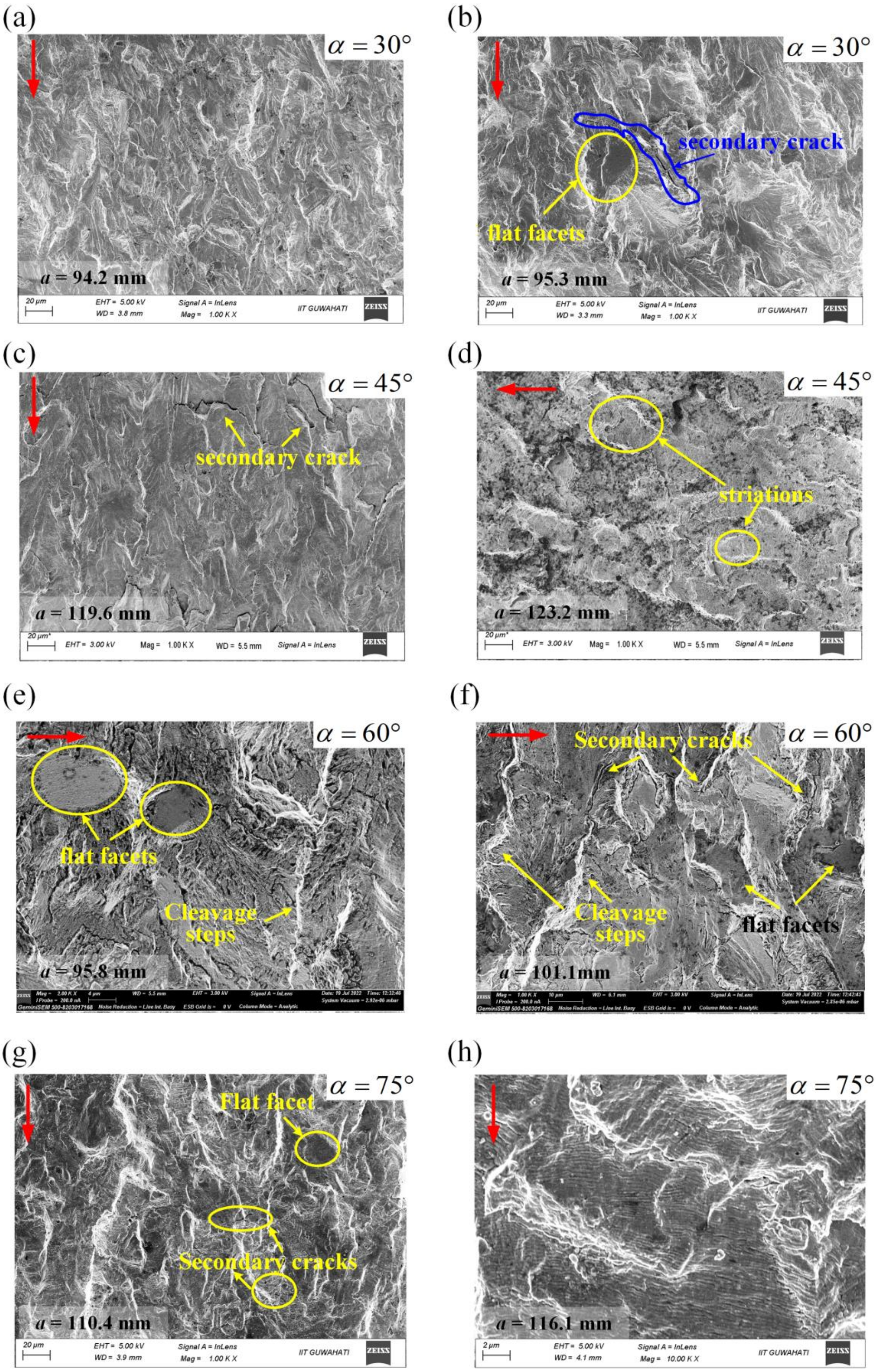

Fig. 8.10 SEM photographs of the fractured surface of SECC specimen for loading angles: (a,b) $\alpha = 30°$, (c,d) $\alpha = 45°$, (e,f) $\alpha = 60°$, and (g,h) $\alpha = 75°$ at different crack lengths.

8.6 Summary

The present work investigates the mixed mode (I/II) FCG characteristics of the AISI 304 steel using a newly proposed SECC specimen. The effect of Paris constants on the numerically predicted fatigue life (using modified Paris law) has also been studied by performing finite element FCG simulations. Also, the competence of selected ΔK_{eq} models has been investigated in terms of fatigue life prediction. The GMTS criterion has been used for the crack path prediction. The effect of three different types of Paris constants to predict fatigue life under mixed mode (I/II) loading conditions, viz., (a) using C and m calculated from the mode I FCG tests on standard CT specimen, (b) using average C_{eq} and m_{eq} values associated with each loading angle α, and (c) using $C*$ and $m* = m$, have been investigated. Practically, all ΔK_{eq} models have provided accurate life predictions when the mixed mode Paris constants $C_{\mathrm{eq}}, m_{\mathrm{eq}}$ are employed in the modified Paris law. Specifically, Tanaka 2 and Irwin ΔK_{eq} models provide fatigue life predictions close to the experimental fatigue life for all loading angles using mixed mode $C_{\mathrm{eq}}, m_{\mathrm{eq}}$. The GMTS-based ΔK_{eq} model provides a conservative prediction of fatigue life for all the loading angles. Fractographic analyses show that the fatigue fracture surfaces of AISI 304 steel are dominated by featureless regions and higher roughness at the initial crack growth stage. And, the stable crack growth region is dominated by striation marks for all mixed mode loading angles.

Chapter 9

Conclusions and scope of future work

This chapter introduces the key accomplishments of this dissertation along with some scope of future research studies which concludes the thesis.

9.1 Summary

The present work proposes a new experimental setup consisting of the single edge cracked circular (SECC) specimen and a new out-of-plane loading fixture (J-fixture) for conducting mixed mode (I/II), (I/III), and (I/II/III) fracture and fatigue crack growth studies on brittle and metallic materials. The efficacy of the proposed loading setup has been investigated by conducting a large number of static and FCG experiments on three different materials, viz., PMMA, AISI 304 steel, and Al 7075-T6 alloy. First, a detailed numerical and experimental analysis of mixed mode (I/II) and (I/III) fracture studies has been made with the added objective of studying the efficacy of the proposed SECC specimen setup in conducting mixed mode (I/II) and (I/III) static fracture tests using PMMA material. These studies have provided important observations on the application of various mixed mode fracture criteria in the prediction of crack kink and twist angles, and fracture locus. Further, these results also clearly demonstrated the applicability of the proposed specimen setup for conducting mixed mode fracture tests.

Secondly, the fatigue loading capabilities of the proposed specimen have been tested using specimens made of Al7075-T6 alloy and AISI 304 steel. In the context of mixed mode (I/II) FCG studies on Al 7075-T6 and AISI 304 steel, the present work has four objectives: (a) to study the effect of different Paris constants (viz., mode I constants (C, m) obtained from mode I FCG tests on the standard CT specimen, mixed mode Paris constants ($C_{\mathrm{eq}}, m_{\mathrm{eq}}$) obtained from mixed mode FCG tests on SECC specimen, and modified Paris constants (C^*, m^*) that is proposed by Ma et al. [162]) on the predicted mixed mode (I/II) fatigue life; (b) to study the competence of different equivalent SIF ΔK_{eq} models; (c) to investigate the GMTS criterion for prediction of both the crack initiation angle and fatigue life; and finally (d) to demonstrate the efficacy of the proposed SECC specimen for mixed mode fatigue fracture on metallic materials. All these objectives have been achieved using finite element FCG simulations and mixed mode FCG experimental studies. For this purpose, a series of mixed mode FCG experiments have been conducted on the SECC specimen made of Al 7075-T6 and AISI 304 steel. Multiple specimens have been used to study the reproducibility of the results. Modified Paris law has been employed for prediction of the mixed mode (I/II) fatigue life using selected ΔK_{eq} models with different sets of the Paris' constants and finite element simulations of FCG. The predicted life obtained from these models has been compared with the experimental results to assess the nature of the predictive capabilities of the selected ΔK_{eq} models. The results of the present study provide conclusive recommendations on the selection of the Paris' constants and ΔK_{eq} models for numerical prediction of the mixed mode (I/II) fatigue life of engineering components. Fractographic analysis has also been carried out to aid in understanding the results obtained in the present investigation. The salient conclusions from the present study have been summarized under two sections, viz., (a) specific conclusions and (b) general conclusions, which are as follows:

9.2 Specific conclusions

This section presents the specific conclusions drawn from different experimental and numerical work explained in previous chapters.

9.2.1 Conclusion from mixed mode (I/II) testing on PMMA under static loading conditions

- The proposed specimen is simple to fabricate and load using conventional uniaxial testing machines. No additional test fixtures are needed for loading the specimen under mixed mode (I/II). Mixed mode (I/II) loading can be easily imparted by simply rotating the specimen.
- The proposed specimen has most convenient arrangement for creation of precrack in PMMA and metals in the horizontal direction.
- A limitation of the proposed specimen is that it is incapable of producing pure mode II loading. Otherwise, all other mode mixities, including pure mode I, can be easily tested.
- The load-displacement curve of PMMA specimens is linear up to the point of fracture.
- Very good reproducibility in terms of crack growth angle and critical loads has been noticed under repeated tests.
- The thickness of the specimen has negligible effect on the crack kink angle θ_0 and fracture locus ($K_{\mathrm{I}} / K_{\mathrm{Ic}}$ vs $K_{\mathrm{II}} / K_{\mathrm{Ic}}$) under mixed mode (I/II) loading conditions.

- The crack under mixed mode (I/II) loading grows in a curvilinear path not parallel to the original crack axis. However, under mode I loading, crack propagates in a self-similar manner.
- Crack kink angle increases with increasing mode mixity or loading angle α.
- The prediction of the crack kink angle (crack growth angle) of the GMTS criterion, M and $G-$criteria are in very good agreement with the experimental values for all the loading angles considered here.
- No specific relationship between the average critical load and the loading angle α has been noticed. Indeed, it has been observed lowest critical load for $\alpha = 45°$ and highest for $\alpha = 75°$.
- Variation of the average critical load $P_{\mathrm{cr}}^{\mathrm{avg}}$ per unit thickness is nearly same for both the 6 mm and 10 mm plates. This is true for a given α.
- The prediction of fracture locus by $G-$criterion, ASED-criterion and GMTS-criterion are in good agreement with the experimental results for the entire range of mode mixity considered here.
- At higher mode mixities, the predicted crack kink angle and fracture locus of MTS criterion have shown significant deviations from the experimental values.
- For complete range of mode mixities, the GMTS criterion has shown superior performance than the MTS criterion in terms of crack kink angle and fracture locus for the SECC specimen.
- The SECC specimen can be recommended for investigating the mixed mode (I/II) fracture behavior of brittle materials like PMMA under static loading conditions.

9.2.2 Conclusions from mixed mode (I/III) tests on PMMA under static loading

- The new J-fixture provides a straightforward provision to apply out-of-plane load to the SECC specimen using any uniaxial testing machine.
- For $\alpha = 0°,\ 0° < \phi < 90°$ the test setup exerts mixed mode (I/III) loading onto the midplane of the SECC specimen. The loading angles $\alpha = 0°, \phi = 0°$ correspond to pure mode I, and $\alpha = 0°, \phi = 90°$ corresponds to pure mode III.

- Under mixed mode (I/III) loading, the mode I and mode III SIFs distribution along the thickness of the SECC specimen are symmetric and uniform with respect to the midpoint of the crack front.
- Coupling between Y_{III} and Y_{II} exists in mixed mode (I/III) problems.
- While the Y_{I} and Y_{III} remain nearly uniform, mode II SIF $Y_{\mathrm{II}} = 0$ at the midpoint and varies antisymmetric to the midpoint of the crack front with maximum values at both the free surfaces.
- The variation of Y_{I}, Y_{II} and Y_{III} are in accordance with the published results.
- FE analyses affirm that the combination of the SECC specimen and the new J-fixture is capable of producing pure mode I, pure mode III, and mixed mode (I/III) and (I/II/III) loading conditions.
- The proposed specimen setup can be used for investigating all possible combinations of mixed mode (I/III) loading conditions by keeping in-plane loading angle $\alpha = 0°$ and varying the out-of-plane loading angle ϕ.
- By keeping $\alpha \neq 0°$ and varying the out-of-plane loading angle ϕ from 0° to 90° produce desired mixed mode (I/II/III) loading onto the SECC specimen.
- The load-displacement plots of all (PMMA made SECC) specimens tested under mixed mode (I/III) are linear up to the point of final fracture.
- The mode I and mode III fracture toughness of the 12 mm thick PMMA sheet material is found to be equal to $K_{\mathrm{Ic}} = 1.41\ \mathrm{MPa}\sqrt{\mathrm{m}}$ and $K_{\mathrm{IIIc}} = 2.06\ \mathrm{MPa}\sqrt{\mathrm{mm}}$, respectively.
- K_{IIIc} is found 1.46 times higher than K_{Ic}.
- K_{I} at the moment of fracture i.e., K_{If} is found higher than K_{Ic}. Similar observation has also been made by other researchers.
- Mode III loading has a considerable effect on fracture surface. The fractured surface is smooth under the pure mode I loading. The fracture surfaces under mixed mode (I/III) loading are very rough with riverline pattern and herringbone fracture features. The fracture surface roughness increases with the increase in mode III component of loading.

- A straight crack front fragments into multiple daughter cracks and river line type features appear on the fractured surface under mixed mode (I/III) loading.
- The present experimental results of crack twist angles agree reasonably well with the theoretical predictions made by the MMPS criterion.
- The fracture locus obtained using the MMPS and Richard criteria agree reasonably well with the present experimental results for the pure mode III, and K_{IIIc} has been accurately predicted by both MMPS and Richards criteria.
- The fracture locus obtained for mixed mode (I/III) loading conditions does not agree well with the MMPS and Richard criteria.
- Except for the cases of pure mode I and pure mode III, the value of $K_{\mathrm{If}} / K_{\mathrm{Ic}}$ is greater than 1.0.

9.2.3 Conclusions from mixed mode (I/II) FCG experiments on Al 7075-T6 alloy and AISI 304 steel

- Nearly identical values of the Paris' material constants C and m are observed from repeated mode I FCG tests using the CT specimen made of Al 7075-T6 alloy and AISI 304 materials.
- All of the FCG experiments conducted under mode I conditions exhibit flat and elastic fatigue-fractured surfaces with crack growth in the direction of the axis of the crack. Thus, affirming the accuracy of the current experimental program and the design and fabrication of the specimens.
- The approximate fracture toughness value of Al 7075-T6 alloy is found to be equal to 39.7 $\mathrm{MPa}\sqrt{\mathrm{m}}$, and that of AISI 304 steel is 99.8 $\mathrm{MPa}\sqrt{\mathrm{m}}$.
- The mode I Paris material constants for Al 7075-T6 are equal to $C = 4.3316\times10^{-9}$ $(\mathrm{mm/cycle})/(\mathrm{MPa\ mm}^{m/2})$ and $m = 1.912$, and that of AISI 304 steel are equal to $C = 7.0487\times10^{-12}$ $(\mathrm{mm/cycle})/(\mathrm{MPa\ mm}^{m/2})$ and $m = 2.458$.
- Fractographic studies on the CT specimen clearly show increasing spacing between the striations, and these are formed perpendicular to the direction of the crack growth, indicating the Paris regime and the correctness of the experiments.

- As expected, the crack growth is not self-similar in all the mixed mode (I/II) FCG experiments on both materials (i.e., AISI 304 steel and Al 7075-T6 alloy), clearly indicating the presence of mixed mode (I/II) loading at the crack tip.
- In all the mixed mode (I/II) FCG experiments on both materials, the crack kink angle θ_0 increases with an increase in loading angle α, and the crack finally turns nearly perpendicular to the direction of the applied load.
- For both materials, the mixed mode fatigue life increased with an increase in the loading angle α due to a higher crack initiation life.
- For both materials, the GMTS criterion very accurately predicts crack kink angles θ_0 better than the MTS criterion for all three loading angles, i.e., $\alpha = 30°$, 45°, and 60°.
- For Al 7075-T6 alloy, the FCGR is higher in mixed mode (I/II) than in mode I for all the loading angles and for all selected ΔK_{eq} models.
- For AISI 304 steel, the mixed mode FCGR has the same order as the mode I FCGR for all the loading angles and for all selected ΔK_{eq} models.
- For both materials, except for the initial crack positions, the correlations of various ΔK_{eq} models with da/dN do not significantly differ from each other.
- In case of Al 7075-T6 alloy, the mixed mode Paris constants $C_{\mathrm{eq}}, m_{\mathrm{eq}}$ of each loading angle are significantly different from the mode I Paris constants $C_{\mathrm{I}}, m_{\mathrm{I}}$. On the other hand, only m_{eq} is of the same order as that of m_{I} in case of AISI 304 steel.
- The fatigue life predicted by all ΔK_{eq} models for a given set of Paris' constants is nearly close to each other.
- The results clearly show that the Paris' constants have more effect on the predicted fatigue life over the ΔK_{eq} models.
- The fatigue life computed using all selected ΔK_{eq} models and mixed mode Paris constants ($C_{\mathrm{eq}}, m_{\mathrm{eq}}$) agrees well with the experimental data for all the loading angles and both materials (Al 7075-T6 alloy and AISI 304 steel).

- More specifically, for Al 7075-T6 alloy, Richard's and Tanaka 1 ΔK_{eq} models have provided more accurate and consistent life predictions for all the loading angles. Similarly, on overall, the Irwin's model has provided accurate and consistent life predictions for AISI 304 steel.
- The results of the present investigation show that the GMTS ΔK_{eq} model provides a conservative prediction of fatigue life for all the loading angles and for both materials.
- For both materials, almost flat fracture surfaces have been observed in the fatigue fracture region in all the fractured SECC specimens, indicating small scale yielding conditions due to high cycle fatigue.
- Fractographic studies of both materials reveal that the stable crack growth region is dominated by the striations marks for all mixed mode loading configurations. Also, the spacing between striations decreases as the mode mixity angle increases due to the crack growth rate reduction.
- Fractographic studies of the specimens tested under mixed mode loading showed a rough fractured surface at the beginning. Afterward, a smooth surface of fatigue crack growth, indicating the presence of mode II at the beginning stages and mode I dominated crack growth in the later stage of crack propagation. This is true for both materials.
- Mixed mode (I/II) FCG results on AISI 304 steel and Al 7075-T6 again affirm the suitability of the proposed specimen for conducting mixed mode (I/II) FCG studies on metallic materials.

9.3 General conclusions

- It was found that the suggested testing setup with the SECC specimen and J-fixture works well for FCG studies and mixed mode (I/II), (I/III), and (I/II/III) fracture tests.
- Among the various criteria considered under mixed (I/II) loading, the GMTS criteria consistently outperforms in predicting crack kink angle and fracture locus, regardless of loading angle.

- The prediction of fracture locus by $G-$criterion, ASED-criterion and GMTS-criterion for mixed mode (I/II) fracture tests is in good agreement with the experimental results for the entire range of mode mixity.
- In mixed mode (I/III) fracture tests, crack twist angles agree reasonably well with the theoretical predictions made by the MMPS criterion.
- The fracture locus obtained using the MMPS and Richard criteria agree reasonably well with the present experimental results for the pure mode III.
- The fracture locus obtained for mixed mode (I/III) loading conditions does not agree well with the MMPS and Richard criteria.
- For mixed mode (I/III) loading, Y_{I} and Y_{III} are found nearly uniform and induced Y_{II} varies antisymmetrically along the crack front with $Y_{\mathrm{II}}=0$ at the midpoint of the front.
- In mixed mode (I/III) loading, K_{I} at the moment of fracture i.e., K_{If} is found higher than K_{Ic} and K_{IIIc} is found 1.46 times higher than K_{Ic}.
- In the context of fatigue life prediction, practically, all ΔK_{eq} models have provided very accurate mixed mode (I/II) life prediction when the mixed mode Paris constants $(C_{\mathrm{eq}}, m_{\mathrm{eq}})$ are employed in the modified Paris law.
- The mixed mode (I/II) fatigue results clearly show that the Paris constants have more effect on the predicted fatigue life over the ΔK_{eq} models.
- Fractographic studies reveal that the stable crack growth region is dominated by the striations marks for all the mode mixity loading angles.

9.4 Scope of future work

- The efficacy of the proposed specimen setup needs to be further examined for static mixed mode (II/III) and general mixed mode (I/II/III) fracture studies using metals and PMMA.
- The complete mixed mode (I/III) and (I/II/III) FCG studies on Al 7075-T6 alloy and AISI 304 steel can be performed, and it can be compared with present mixed

mode (I/II) FCG results to understand the different crack growth mechanism under such loading conditions.

- An empirical relation between the mixed mode (I/II) Paris constants (C_{eq}, m_{eq}) and the loading angle α can be developed for Al 7075-T6 so that further experiments for the Paris' constants can be avoided.
- The coupling effect between the mode II SIF and mode III SIFs can be explored further to develop a thorough understanding of fracture characteristics under general mixed mode (I/II/III) loading conditions.
- In the present work, a small qualitative description of the fracture surfaces has been provided. A comprehensive SEM analysis can be conducted to investigate the mechanisms behind sudden directional changes and crack kinking from the tip of pre-crack during mixed mode fatigue loading.
- A detailed examination of the fracture features using SEM images can be performed to get further insights into the origins of flat facet and the governing mechanisms of secondary cracks. The relationship between these features and external mixed mode loading conditions can be further explored.
- The present work can be extended to test the mixed mode fracture behaviour of 3D-printed materials using the proposed loading setup.

Appendix A

A.1 Crack-tip stress field equations

The analytical approach to determine the crack tip field equations, i.e., stress, strain, and displacement field, are given in this section. These field equations play an important role in characterizing the fracture process near the crack tip. The field equations are derived under the assumption of LEFM for quasi-static loading conditions. Two approaches are generally used to derive the crack tip field equations, viz., *Williams' asymptotic eigenfunction expansion method* [82] and the *generalized Westergaard approach* [269]. These two approaches are complementary, and the relationship between the coefficients of the stress field series solution obtained from the Williams method and that of the generalized Westergaard approach can be found in [270]. In the present work, the field equations are derived using the generalized Westergaard approach (as proposed by Sanford [271]).

A.1.1 Westergaard approach

In the conventional Westergaard approach, the crack tip field solutions are obtained by introducing a complex stress function $Z(z)$, where $z = x + iy$ and $i = \sqrt{-1}$. Accordingly, the Airy stress function can be defined in terms of the complex stress function $Z(z)$ as:

$$\Phi = \mathrm{Re}\,\bar{\bar{Z}} + y\,\mathrm{Im}\,\bar{Z} \tag{A.1}$$

where (Re) and (Im) denote the real and imaginary parts of the complex function, respectively, and $\bar{\bar{Z}}$, $\bar{Z}$ and Z' are defined as.

$$\bar{Z} = \frac{d\bar{\bar{Z}}}{dz}; \quad Z = \frac{d\bar{Z}}{dz}; \quad Z' = \frac{dZ}{dz} \tag{A.2}$$

As we know, the stress components can be calculated from the Airy stress function Φ as:

$$\sigma_{xx} = \frac{\partial^2 \Phi}{\partial y^2}; \quad \sigma_{yy} = \frac{\partial^2 \Phi}{\partial x^2}; \quad \tau_{xy} = -\frac{\partial^2 \Phi}{\partial x \partial y} \tag{A.3}$$

In Westergaard approach, $Z(z)$ is selected in such a way that it must be an analytical biharmonic function and satisfy the Cauchy-Reimann conditions given in Eq. (A.4)

$$\begin{aligned} \frac{\partial \operatorname{Im} \mathrm{Z}}{\partial y} &= \frac{\partial \operatorname{Re} \mathrm{Z}}{\partial x} = \operatorname{Re} Z' \\ \frac{\partial \operatorname{Re} \mathrm{Z}}{\partial y} &= -\frac{\partial \operatorname{Im} \mathrm{Z}}{\partial x} = -\operatorname{Im} Z' \end{aligned} \tag{A.4}$$

It is well established that the conventional form of the Westergaard stress function, in terms of a single complex stress function $Z(z)$, applies only to solving a limited range of mode I crack geometries and could not be used for any general crack problems. To overcome this drawback of the conventional Westergaard approach, Sanford [271] proposed a generalized form of the Westergaard function, which is applicable to a wider range of crack configurations. *In the generalized Westergaard formulation, two complex functions are used to define the Airy stress functions, viz., the standard Westergaard stress function* $Z(z)$ *, and an additional analytic function* $\mathrm{H}(z)$.

A.2 Mode I field equations

According to Sanford [271], the Airy stress function for mode I (Φ_{I}) can be defined as:

$$\Phi_{\mathrm{I}} = \operatorname{Re} \overline{\overline{Z}}_{\mathrm{I}}(z) + y \operatorname{Im} \overline{Z}_{\mathrm{I}}(z) + y \operatorname{Im} \overline{\mathrm{H}}_{\mathrm{I}}(z) \tag{A.5}$$

where $\mathrm{Z}_{\mathrm{I}}(z)$ and $\mathrm{H}_{\mathrm{I}}(z)$ are defined in series form as

$$\mathrm{Z}_{\mathrm{I}}(z) = \sum_{n=0}^{\infty} A_n z^{(n-1/2)} \;; \quad \mathrm{H}_{\mathrm{I}}(z) = \sum_{m=0}^{\infty} B_m z^m \tag{A.6}$$

Putting Eq. (A.5) and Cauchy-Reimann relations Eq. (A.4) in Eq. (A.3), the stress components for Mode I (in the absence of body forces) can be determined as:

$$\begin{aligned} \sigma_{xx} &= \operatorname{Re} \mathrm{Z}_{\mathrm{I}} - y \operatorname{Im} \mathrm{Z}_{\mathrm{I}}' - y \operatorname{Im} \mathrm{H}_{\mathrm{I}}' + 2 \operatorname{Re} \mathrm{H}_{\mathrm{I}} \\ \sigma_{yy} &= \operatorname{Re} \mathrm{Z}_{\mathrm{I}} + y \operatorname{Im} \mathrm{Z}_{\mathrm{I}}' + y \operatorname{Im} \mathrm{H}_{\mathrm{I}}' \\ \tau_{xy} &= -y \operatorname{Re} \mathrm{Z}_{\mathrm{I}}' - y \operatorname{Re} \mathrm{H}_{\mathrm{I}}' - \operatorname{Im} \mathrm{H}_{\mathrm{I}} \end{aligned} \tag{A.7}$$

Substituting the series form of $\mathrm{Z}_{\mathrm{I}}(z)$ and $\mathrm{H}_{\mathrm{I}}(z)$ from Eq. (A.6) into Eq. (A.7), we can get the mode I stress field equations for the whole domain as

$$\begin{Bmatrix} \sigma_{xx} \\ \sigma_{yy} \\ \tau_{xy} \end{Bmatrix} = \sum_{n=0}^{N} A_n r^{(n-\frac{1}{2})} \begin{Bmatrix} \cos(n-\tfrac{1}{2})\theta - (n-\tfrac{1}{2})\sin\theta \sin(n-\tfrac{3}{2})\theta \\ \cos(n-\tfrac{1}{2})\theta + (n-\tfrac{1}{2})\sin\theta \sin(n-\tfrac{3}{2})\theta \\ -(n-\tfrac{1}{2})\sin\theta \cos(n-\tfrac{3}{2})\theta \end{Bmatrix} + \sum_{m=0}^{M} B_m r^m \begin{Bmatrix} 2\cos m\theta - m\sin\theta \sin(m-1)\theta \\ m\sin\theta \sin(m-1)\theta \\ -m\sin\theta \cos(m-1)\theta - \sin m\theta \end{Bmatrix} \tag{A.8}$$

Under the assumption of plane stress conditions, the strain components can be calculated using the generalized Hooke's law as

$$\begin{aligned} E\varepsilon_{xx} &= (1-\nu)\operatorname{Re} \mathrm{Z}_{\mathrm{I}} - (1+\nu) y \operatorname{Im} \mathrm{Z}'_{\mathrm{I}} - (1+\nu) y \operatorname{Im} \mathrm{H}'_{\mathrm{I}} + 2\operatorname{Re} \mathrm{H}_{\mathrm{I}} \\ E\varepsilon_{yy} &= (1-\nu)\operatorname{Re} \mathrm{Z}_{\mathrm{I}} + (1+\nu) y \operatorname{Im} \mathrm{Z}'_{\mathrm{I}} + (1+\nu) y \operatorname{Im} \mathrm{H}'_{\mathrm{I}} - 2\nu \operatorname{Re} \mathrm{H}_{\mathrm{I}} \\ E\gamma_{xy} &= -2(1-\nu)\operatorname{Im} \mathrm{H}_{\mathrm{I}} - 2(1+\nu) y \operatorname{Re} \mathrm{Z}'_{\mathrm{I}} - 2(1+\nu) y \operatorname{Re} \mathrm{H}'_{\mathrm{I}} \end{aligned} \tag{A.9}$$

Substituting Eq. (A.6) in Eq. (A.9) we can get the mode I strain field equations as

$$\begin{aligned} \begin{Bmatrix} \varepsilon_{xx} \\ \varepsilon_{yy} \\ \gamma_{xy} \end{Bmatrix} = \sum_{n=0}^{N} \frac{A_n}{E} r^{(n-\frac{1}{2})} & \begin{Bmatrix} (1-v)\cos(n-\frac{1}{2})\theta - (n-\frac{1}{2})(1+v)\sin\theta\sin(n-\frac{3}{2})\theta \\ (1-v)\cos(n-\frac{1}{2})\theta + (n-\frac{1}{2})(1+v)\sin\theta\sin(n-\frac{3}{2})\theta \\ -(n-\frac{1}{2})(1+v)\sin\theta\cos(n-\frac{3}{2})\theta \end{Bmatrix} \\ + \sum_{m=0}^{M} \frac{B_m}{E} r^{m} & \begin{Bmatrix} 2\cos m\theta - (1+v) m \sin\theta \sin(m-1)\theta \\ (1+v) m \sin\theta\sin(m-1)\theta - 2v\cos m\theta \\ -2(1+v) m\sin\theta\cos(m-1)\theta - 2(1+v)\sin m\theta \end{Bmatrix} \end{aligned} \tag{A.10}$$

Integrating the strain components Eq. (A.9), the Mode I displacement components can be obtained as

$$\begin{aligned} Eu_{\mathrm{I}} &= (1-\nu)\operatorname{Re} \overline{\mathrm{Z}}_{\mathrm{I}} - (1+\nu) y \operatorname{Im} \mathrm{Z}_{\mathrm{I}} - (1+\nu) y \operatorname{Im} \mathrm{H}_{\mathrm{I}} + 2\operatorname{Re} \overline{\mathrm{H}}_{\mathrm{I}} \\ Ev_{\mathrm{I}} &= 2\operatorname{Im} \overline{\mathrm{Z}}_{\mathrm{I}} - (1+\nu) y \operatorname{Re} \mathrm{Z}_{\mathrm{I}} - (1+\nu) y \operatorname{Re} \mathrm{H}_{\mathrm{I}} + (1-\nu)\operatorname{Im} \overline{\mathrm{H}}_{\mathrm{I}} \end{aligned} \tag{A.11}$$

Substituting Eq. (A.6) into Eq. (A.11), we get the mode I displacement field equations as

$$\begin{aligned} \begin{Bmatrix} u_{\mathrm{I}} \\ v_{\mathrm{I}} \end{Bmatrix} = \sum_{n=0}^{N} \frac{A_n}{E} r^{(n+\frac{1}{2})} & \begin{Bmatrix} \dfrac{2(1-v)}{2n+1}\cos(n+\frac{1}{2})\theta - (1+v)\sin\theta\sin(n-\frac{1}{2})\theta \\ \dfrac{4}{2n+1}\sin(n+\frac{1}{2})\theta - (1+v)\sin\theta\cos(n-\frac{1}{2})\theta \end{Bmatrix} \\ + \sum_{m=0}^{M} \frac{B_m}{E} r^{(m+1)} & \begin{Bmatrix} \dfrac{2}{m+1}\cos(m+1)\theta - (1+v)\sin\theta\sin m\theta \\ \dfrac{1-v}{m+1}\sin(m+1) - (1+v)\sin\theta\sin m\theta \end{Bmatrix} \end{aligned} \tag{A.12}$$

Considering the terms corresponding to only the first three coefficients A_0, A_1 and B_0 in Eqs. (A.8), (A.10) and (A.12) the field equations can be written as:

$$\begin{aligned} \sigma_{xx} &= A_0 r^{-1/2} \cos\frac{\theta}{2}\left(1 - \sin\frac{\theta}{2}\sin\frac{3\theta}{2}\right) + 2B_0 + A_1 r^{1/2}\cos\frac{\theta}{2}\left(1+\sin^2\frac{\theta}{2}\right) \\ \sigma_{yy} &= A_0 r^{-1/2} \cos\frac{\theta}{2}\left(1 + \sin\frac{\theta}{2}\sin\frac{3\theta}{2}\right) + A_1 r^{1/2}\cos\frac{\theta}{2}\left(1-\sin^2\frac{\theta}{2}\right) \\ \tau_{xy} &= A_0 r^{-1/2} \sin\frac{\theta}{2}\cos\frac{\theta}{2}\cos\frac{3\theta}{2} - A_1 r^{1/2}\sin\frac{\theta}{2}\cos^2\frac{\theta}{2} \end{aligned} \tag{A.13}$$

$$\begin{aligned}
E\varepsilon_{xx} &= A_0 r^{-1/2}\cos\frac{\theta}{2}\left[(1-\nu)-(1+\nu)\sin\frac{\theta}{2}\sin\frac{3\theta}{2}\right]+2B_0+A_1 r^{-1/2}\cos\frac{\theta}{2}\left[(1-\nu)+(1+\nu)\sin^2\frac{\theta}{2}\right]\\
E\varepsilon_{yy} &= A_0 r^{-1/2}\cos\frac{\theta}{2}\left[(1-\nu)+(1+\nu)\sin\frac{\theta}{2}\sin\frac{3\theta}{2}\right]-2\nu B_0+A_1 r^{-1/2}\cos\frac{\theta}{2}\left[(1-\nu)-(1+\nu)\sin^2\frac{\theta}{2}\right]\\
2G\gamma_{xy} &= A_0 r^{-1/2}\left[\sin\theta\cos\frac{3\theta}{2}\right]-A_1 r^{1/2}\left[\sin\theta\cos\frac{\theta}{2}\right]
\end{aligned} \tag{A.14}$$

$$\begin{aligned}
u_I &= \frac{A_0}{2G}r^{1/2}\left[(\kappa-1)\cos\frac{\theta}{2}+\sin\theta\sin\frac{\theta}{2}\right]+\frac{A_1}{2G}r^{3/2}\left[\frac{\kappa-1}{3}\cos\frac{3\theta}{2}-\sin\theta\sin\frac{\theta}{2}\right]+\frac{B_0(\kappa+1)}{4G}r\cos\theta\\
v_I &= \frac{A_0}{2G}r^{1/2}\left[(\kappa+1)\sin\frac{\theta}{2}-\sin\theta\cos\frac{\theta}{2}\right]+\frac{A_1}{2G}r^{3/2}\left[\frac{\kappa+1}{3}\sin\frac{3\theta}{2}-\sin\theta\cos\frac{\theta}{2}\right]-\frac{B_0\nu(\kappa+1)}{4G}r\sin\theta
\end{aligned} \tag{A.15}$$

where

$$\begin{aligned}
\kappa &= \frac{3-\nu}{1+\nu}; &&\text{for plane stress and}\\
\kappa &= 3-4\nu; &&\text{for plane strain}
\end{aligned} \tag{A.16}$$

Equations (A.13), (A.14), and (A.15) represent the stress, strain, and displacements field equations, respectively, for a crack under mode I loading conditions at a point near the crack tip having coordinate (r,θ). The stress and strain components of the field equations (given in Eqs. (A.13) and (A.14)) show a square root singularity, i.e., for $r \to 0$, the stress and strain reach towards infinity. On the other hand, the displacement components Eq. (A.15) are finite near the crack tip and do not contain any singularity. These singular solutions (Eqs. (A.13) and (A.14)) characterize the crack tip in LEFM.

The mode I stress intensity factor K_{I} is formally defined as

$$K_{\mathrm{I}} = \lim_{r\to 0}\sqrt{2\pi r}\,\sigma_{yy}\Big|_{(\theta=0)} \tag{A.17}$$

which relates K_{I} to A_0 as

$$K_{\mathrm{I}} = \sqrt{2\pi}\,A_0 \tag{A.18}$$

The $T-$stress can be related to the coefficient B_0 as

$$T = 2B_0 \tag{A.19}$$

A.3 Mode II field equations

The stress, strain, and displacement field equations in pure mode II are of particular importance for analyzing the mixed mode (I/II) loading conditions. The Airy stress function for Mode II (Φ_{II}) is defined as [271]:

$$\Phi_{\mathrm{II}} = \operatorname{Im}\overline{\mathrm{H}}_{\mathrm{II}}(z) - y\operatorname{Re}\overline{\mathrm{H}}_{\mathrm{II}}(z) - y\operatorname{Re}\overline{\mathrm{Z}}_{\mathrm{II}}(z) \tag{A.20}$$

For Mode II, the $\mathrm{Z}_{\mathrm{II}}\left(z\right)$ and $\mathrm{H}_{\mathrm{II}}\left(z\right)$ are defined as

$$\mathrm{Z}_{\mathrm{II}}(z) = \sum_{n=0}^{\infty} C_n z^{(n-1/2)} \;\; ; \quad \mathrm{H}_{\mathrm{II}}(z) = \sum_{m=0}^{\infty} D_m z^m \tag{A.21}$$

Following the same procedure as adopted previously for the mode I loading and considering the terms corresponding to the first three coefficients C_0, C_1, and D_0, the mode II stress, strain, and displacement field equations can be written as in Eqs. (A.22), (A.23), and (A.24) , respectively.

$$\begin{aligned}
\sigma_{xx} &= C_0 r^{-1/2}\left(-\frac{1}{2}\sin\theta\cos\frac{3\theta}{2} - 2\sin\frac{\theta}{2}\right) + C_1 r^{1/2}\left(\frac{1}{2}\sin\theta\cos\frac{\theta}{2} + 2\sin\frac{\theta}{2}\right)\\
\sigma_{yy} &= C_0 r^{-1/2}\left(\frac{1}{2}\sin\theta\cos\frac{3\theta}{2}\right) + C_1 r^{1/2}\left(-\frac{1}{2}\sin\theta\cos\frac{\theta}{2}\right)\\
\tau_{xy} &= C_0 r^{-1/2}\left(\cos\frac{\theta}{2} - \frac{1}{2}\sin\theta\sin\frac{3\theta}{2}\right) + C_1 r^{1/2}\left(\cos\frac{\theta}{2} + \frac{1}{2}\sin\theta\sin\frac{\theta}{2}\right)
\end{aligned} \tag{A.22}$$

$$\begin{aligned}
E\varepsilon_{xx} &= -C_0 r^{-1/2}\sin\frac{\theta}{2}\left[(1+v)\cos\frac{\theta}{2}\cos\frac{3\theta}{2} + 2\right] + C_1 r^{1/2}\sin\frac{\theta}{2}\left[(1+v)\cos^2\frac{\theta}{2} + 2\right]\\
E\varepsilon_{yy} &= -C_0 r^{-1/2}\sin\frac{\theta}{2}\left[2v + (1+v)\cos\frac{\theta}{2}\cos\frac{3\theta}{2}\right] - C_1 r^{1/2}\sin\frac{\theta}{2}\left[(1+v)\cos^2\frac{\theta}{2} + 2v\right]\\
G\gamma_{xy} &= C_0 r^{-1/2}\cos(\frac{\theta}{2})\left[1 - \sin\frac{\theta}{2}\sin\frac{3\theta}{2}\right] - C_1 r^{1/2}\cos\frac{\theta}{2}\left[1 + \sin^2\frac{\theta}{2}\right]
\end{aligned} \tag{A.23}$$

$$\begin{aligned}
u_{\mathrm{II}} &= \frac{C_0}{2G} r^{1/2}\left[(\kappa+1)\sin\frac{\theta}{2} + \sin\theta\cos\frac{\theta}{2}\right] + \frac{C_1}{2G} r^{3/2}\left[\frac{(\kappa+1)}{3}\sin\frac{3\theta}{2} + \sin\theta\cos\frac{\theta}{2}\right] + \frac{D_0(\kappa+1)}{4G} r\sin\theta\\
v_{\mathrm{II}} &= \frac{C_0}{2G} r^{1/2}\left[(1-\kappa)\cos\frac{\theta}{2} + \sin\theta\sin\frac{\theta}{2}\right] + \frac{C_1}{2G} r^{3/2}\left[\frac{(1-\kappa)}{3}\cos\frac{3\theta}{2} + \sin\theta\sin\frac{\theta}{2}\right] - \frac{D_0(\kappa+1)}{4G} r\cos\theta
\end{aligned} \tag{A.24}$$

Similar to the case of Mode I, the stress and strain components of the field equations (given in Eqs. (A.22) and (A.23)) show a square root $r^{-1/2}$ singularity, i.e. for $r \to 0$, the stress and strain reach towards infinity. On the other hand, the displacement components (Eq. (A.24)) are finite near the crack tip and do not contain any singular term. The mode II stress intensity factor K_{II} is formally defined as

$$K_{\mathrm{II}} = \lim_{r\to 0} \sqrt{2\pi r}\; \tau_{xy}\Big|_{(\theta=0)} \tag{A.25}$$

which relates K_{II} to C_0 as a

$$K_{\text{II}} = \sqrt{2\pi}\, C_0 \tag{A.26}$$

A.4 Mode III field equations

As far as the mode III crack problem is concerned, the crack-tip field equations can be determined as explained below. Fig. A.1 shows a schematic of the crack under out-of-plane loading conditions. Here, a local coordinate system is located at the crack tip, with $x-$axis normal to the crack front, $y-$axis normal to the crack plane, and $z-$axis tangential to the crack front.

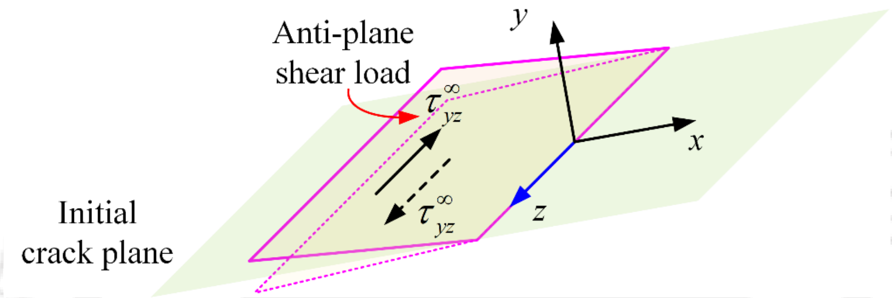

Fig. A.1 Crack under mode III loading and the position of local coordinate system.

Under the mode III loading conditions, the following displacement and stress conditions are satisfied at the crack flank surfaces:

$$\begin{aligned} &u_{\text{III}} = v_{\text{III}} = 0,\ w_{\text{III}} \neq 0, \quad \text{and} \\ &\sigma_{xx} = \sigma_{yy} = \sigma_{zz} = \tau_{xy} = 0,\ \tau_{xz} \neq 0, \tau_{yz} \neq 0 \end{aligned} \tag{A.27}$$

According to the Hooke's law, the out-of-plane shear stresses τ_{xz} and τ_{yz} can be written as

$$\tau_{xz} = G\gamma_{xz}\ ; \quad \tau_{yz} = G\gamma_{yz} \tag{A.28}$$

where, γ_{xz} and γ_{yz} are out-of-plane shear strain given by

$$\gamma_{xz} = \frac{1}{2}\frac{\partial w_{\text{III}}}{\partial x}; \quad \gamma_{yz} = \frac{1}{2}\frac{\partial w_{\text{III}}}{\partial y} \tag{A.29}$$

In the absence of body forces, the equilibrium equation can be written as:

$$\frac{\partial \tau_{xz}}{\partial x} + \frac{\partial \tau_{yz}}{\partial y} = 0 \tag{A.30}$$

Substituting Eqs. (A.28) and (A.29) into Eq. (A.30), we can get a Laplace's equation

$$\frac{\partial^2 w_{\mathrm{III}}}{\partial x^2}+\frac{\partial^2 w_{\mathrm{III}}}{\partial y^2}=\nabla^2 w_{\mathrm{III}}=0 \tag{A.31}$$

The above Laplace's equation can be solved using the complex variable method by assuming:

$$w_{\mathrm{III}}=\frac{1}{G}\left[g(z)+\bar{g}(\bar{z})\right] \tag{A.32}$$

where $g(z)=p(x,y)+iq(x,y)$ and $\bar{g}(\bar{z})=p(x,y)-iq(x,y)$. $\bar{g}(\bar{z})$ is the complex conjugate of $g(z)$. Putting Eq. (A.32) into Eq. (A.29), and using the chain rule of differentiation, we have

$$\begin{aligned}\gamma_{xz}&=\frac{1}{G}\left[g'(z)+\bar{g}'(\bar{z})\right]\\ \gamma_{yz}&=\frac{i}{G}\left[g'(z)-\bar{g}'(\bar{z})\right]\end{aligned} \tag{A.33}$$

Now the shear stress from Eq. (A.28) can be rewritten as

$$\tau_{xz}-i\tau_{yz}=2g'(z) \tag{A.34}$$

Let the function $g(z)$ be analytic and defined as

$$g(z)=\Omega z^{\lambda+1}\ ; \quad \text{where,} \quad \Omega=N+iQ \tag{A.35}$$

where N, Q and λ are undetermined constants. For finite displacements at the crack tip $(|z|=r=0), \lambda>-1$. Putting Eq. (A.35) into Eq. (A.33) yields

$$\tau_{xz}-i\tau_{yz}=2(\lambda+1)\Omega z^{\lambda}=2(\lambda+1)r^{\lambda}(N+iQ)(\cos\lambda\theta+i\sin\lambda\theta) \tag{A.36}$$

whence,

$$\begin{aligned}\tau_{xz}&=2(\lambda+1)r^{\lambda}(N\cos\lambda\theta-Q\sin\lambda\theta)\\ \tau_{yz}&=-2(\lambda+1)r^{\lambda}(N\sin\lambda\theta+Q\cos\lambda\theta)\end{aligned} \tag{A.37}$$

The traction free boundary conditions on the crack surface require that $\tau_{yz}=0$ on $\theta=\pm\pi$. Consequently,

$$\begin{aligned}N\sin\lambda\pi+Q\cos\lambda\pi&=0\\ N\sin\lambda\pi-Q\cos\lambda\pi&=0\end{aligned} \tag{A.38}$$

For non-trivial solutions, the determinant of the coefficients of Eq. (A.38) must be equal to zero, which yields:

$$\sin 2\lambda\pi = 0 \tag{A.39}$$

For $\lambda > -1$, Eq. (A.39) has the roots $\lambda = -1/2, n/2;$ for $n = 0,1,2,\ldots$. Of the infinite set of functions of the form of Eq. (A.35) that satisfies the boundary conditions for traction-free crack surfaces, the function with $\lambda = -1/2$ for which $N = 0$ provides the most significant contribution to the field equations. Hence, considering $\lambda = -1/2$, out-of-plane shear stress $\tau_{yz}, \tau_{\theta z}$ and the resultant displacement w_{III} become

$$\begin{aligned} \tau_{xz} &= -Q_0 r^{-1/2} \sin\frac{\theta}{2} \\ \tau_{yz} &= Q_0 r^{-1/2} \cos\frac{\theta}{2} \\ w_{\mathrm{III}} &= \frac{2Q_0 r^{1/2}}{G} \sin\frac{\theta}{2} \end{aligned} \tag{A.40}$$

The mode III stress intensity factor K_{III} is formally defined as

$$K_{\mathrm{III}} = \lim_{r\to 0} \sqrt{2\pi r}\; \tau_{zy}\Big|_{(\theta=0)} \tag{A.41}$$

which relates K_{III} to Q_0 as a

$$K_{\mathrm{III}} = \sqrt{2\pi}\, Q_0 \tag{A.42}$$

Appendix B

B.1 Convergence of computed mixed mode SIFs for 2D finite element simulations

Prior to the actual FCG simulations, an extensive mesh convergence study has been performed to find the appropriate mesh density. For this purpose, the SECC specimen shown in Fig. B.1a with $\alpha = 30°$ and $a / D_o = 0.55$ is considered. A reference load $P = 20\,\mathrm{kN}$ is applied to the specimen, and the variation of K_I and K_II are observed with respect to the size of the QPEs. Six different FE meshes with increasing mesh density or decreasing QPE sizes have been used to compute the SIFs (Fig. 9a). The variation of the computed K_I and K_II as a function of QPE size at the crack tip are shown in Fig. B.1b. It can be noticed from Fig. B.1b that as the meshes are refined the computed K_I and K_II are converging to a constant value. It can also be observed from Fig. B.1b that the values of K_I and K_II do not change significantly after the QPE size of 0.05 mm. Hence based on this analysis, a QPE size of 0.05 mm is found adequate for accurately estimating SIFs. Therefore, a QPE size of 0.05 mm is used in all the FE simulations of the present investigation.

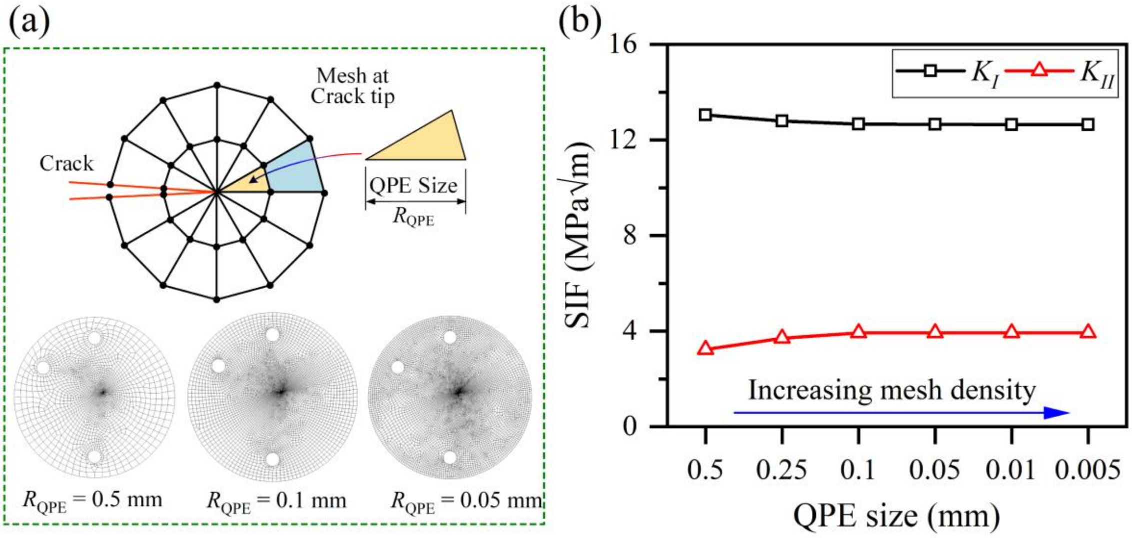

Fig. B.1 (a) Schematic of the mesh pattern at the crack tip showing QPE size and meshes at three different QPE sizes. (b) Results of the mesh convergence study.

B.2 Mesh convergence and verification of 3D finite element simulations used for mixed mode (I/II/III)

To verify the present 3D finite element simulation method, the mixed mode (I/II/III) results of Razavi and Berto [33] have been considered as the reference values. The mixed mode (I/II/III) simulations of Razavi and Berto [33] have been repeated, and the results of this verification study is shown in Fig. B.2. Two different 3D mixed mode (I/II/III) configurations have been simulated using the present method for the verification purpose: first, 3D pure mode I configuration $\alpha = 0°, \beta = 0°$, and second 3D pure mode III configuration $\alpha = 0°, \beta = 90°$.

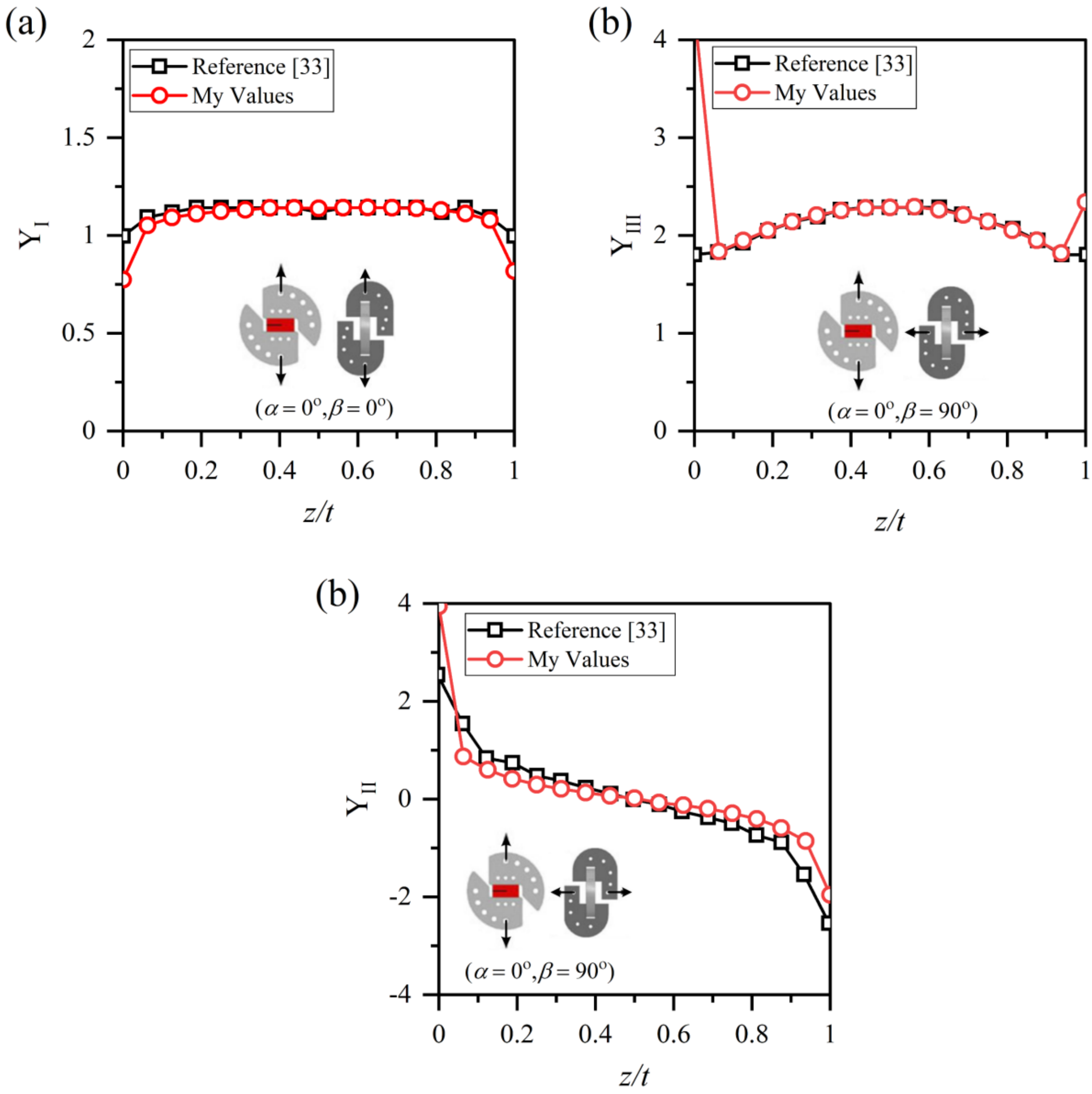

Fig. B.2 Results of the 3D FE mesh convergence and verification study. Comparison of normalized: (a) mode I SIFs, (b) mode II SIFs and (c) Mode III SIFs computed using present 3D finite element technique with the result of Razavi and Berto [33].

Here, the definition of loading angles α and β are kept same as used by Razavi and Berto [33], i.e., α is the loading angle in C-fixture and β is the loading angle in J-fixture. Here, $z/t = 0$ is the crack tip at front surface, and $z/t = 1$ is the crack tip at back surface of the CTS specimen. The material properties of PMMA: $E = 2900\,\text{MPa}$ and $\nu = 0.35$; and Steel: $E = 200\,\text{GPa}$ and $\nu = 0.3$, have been considered [33]. The thickness of the CTS specimen, C-fixture and J-fixture have been considered as 10 mm, 20 mm and 20 mm, respectively. The other dimensions of the CTS specimen and fixtures given in Ref. [33] have been considered for 3D meshing. All the 3D FE simulations have been performed in ANSYS® APDL. In Fig. B.2, the calculated geometry factors or normalized SIFs (along the normalized thickness direction z/t) using the current method are compared with the results of Razavi and Berto [33]. It can be seen from Fig. B.2 that the variation of the geometry factors, viz., $Y_{\text{I}}, Y_{\text{II}}$ and Y_{III} calculated using present 3D finite element method are in excellent agreement with the reference values. The results of the present analyses, shown in Fig. B.2, confirms the accuracy of the current 3D simulation technique used for the mixed mode (I/III) loading conditions. Based on this analysis, the size of wedge element $0.005a$ mm and global element size of 2 mm are found adequate for accurately estimating the SIFs. Therefore, a wedge element of size of $0.005a$ mm (a is the crack length) are used in all the mixed mode (I/II/III) FE simulations of the present investigation.

B.3 Verification of mixed mode (I/II) finite element fatigue crack growth simulation technique

To verify the effectiveness of the present fatigue crack growth simulation method, the FCG simulations of Sajith et al. [28] on CTS specimen made of AISI 316 steel has been repeated using the current method. For this purpose, the fatigue crack paths under three different loading angles ($\alpha = 30°$, 45° and 60°) on the CTS specimen are predicted using the present method. And the predicted paths (using the current method) are compared with the results of Sajith et al. [28]. The material properties $E = 192\,\text{GPa}$ and $\nu = 0.27$ of the AISI 316 steel have been taken from Sajith et al. [28]. As seen from Fig. B.3, the crack path predicted using the present simulation method are in excellent agreement with the reference crack paths [28] for all the loading angles. The maximum percentage error observed in the calculation of the *x*-coordinate and *y*-coordinate is below 1% for $\alpha = 30°$ and 60°. For $\alpha = 45°$ a maximum error of 3% and 1.5% have been observed in the calculation of the *x*-

coordinate and *y*-coordinate, respectively. This difference can be attributed to the error during the data extraction from the reference graphs. The results of the present analyses, shown in Fig. B.3, confirms the accuracy of the current simulation technique used in the present investigation for the SECC specimen.

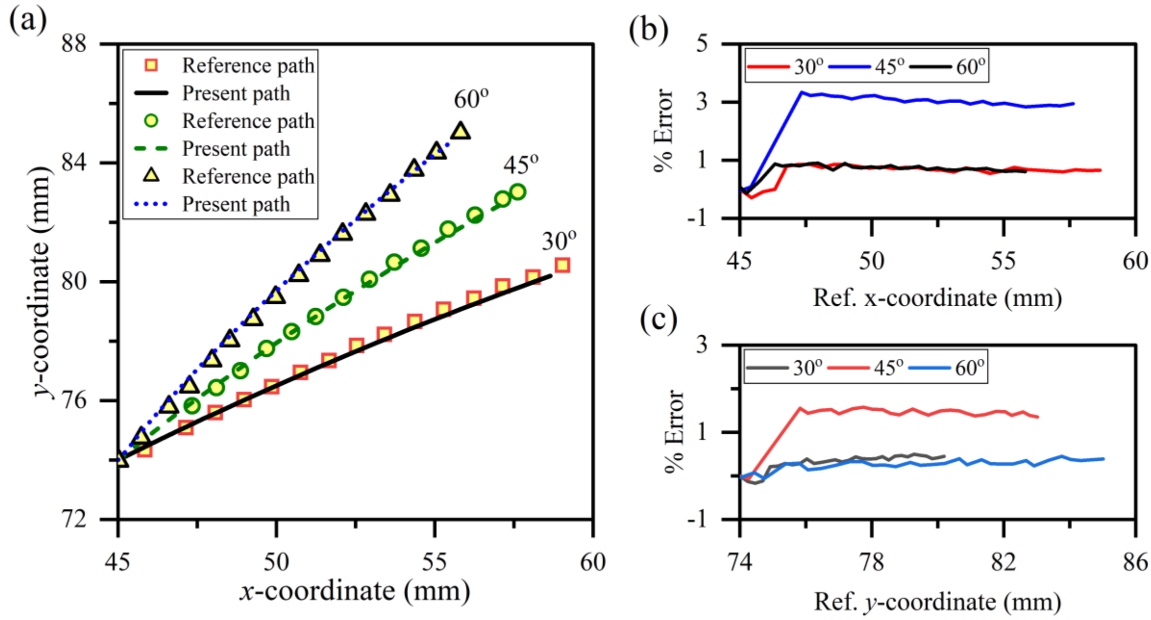

Fig. B.3 Comparison of results obtained using present FE fatigue crack growth simulation technique with Sajith et al. [28]. (a) Comparison of crack path obtained using present FE technique with the reference results. (b) Percentage error of calculated x – coordinate of crack path. (c) Percentage error of calculated y – coordinate of crack path.

References

[1] Kim TY, Kim HK. Mixed mode fatigue crack growth behavior of fully lower bainite steel. Mater Sci Eng A 2013;580:322–9.

[2] Qian J, Fatemi A. Fatigue crack growth under mixed-mode I and II loading. Fatigue Fract Eng Mater Struct 1996;19:1277–84.

[3] Srinivas V, Vasudevan P. Experimental observations on mixed mode fatigue crack propagation. Int J Press Vessel Pip 1993;56:319–29.

[4] Srinivas V, Vasudevan P. Studies of mixed mode crack propagation in D16AT Aluminium alloy. Eng Fract Mech 1993;45:415–30.

[5] Lin B, Mear ME, Ravi-Chandar K. Criterion for initiation of cracks under mixed-mode I + III loading. Int J Fract 2010;165:175–88.

[6] Richard HA. Development of fatigue crack growth in real structures. Eng Fract Mech 2008;75:331–40.

[7] Haghani R, Al-Emrani M, Heshmati M. Fatigue-prone details in steel bridges. Buildings 2012;2:456–76.

[8] Fonte M, Infante V, Reis L, Freitas M. Failure mode analysis of a diesel motor crankshaft. Eng Fail Anal 2017;82:681–6.

[9] Findlay SJ, Harrison ND. Why aircraft fail. Mater Today 2002;5:18–25.

[10] Broek D. The practical use of fracture mechanics. Dordrecht: Springer Netherlands; 1989.

[11] Tavares SMO, de Castro PMST. An overview of fatigue in aircraft structures. Fatigue Fract Eng Mater Struct 2017;40:1510–29.

[12] Broek D. The civil damage tolerance requirements in theory and practice, 1991, p. 73–86.

[13] Anderson TL (Ted L. Fracture mechanics : fundamentals and applications. Taylor & Francis; 2005.

[14] Zerbst U, Beretta S. Failure and damage tolerance aspects of railway components. Eng Fail Anal 2011;18:534–42.

[15] Zerbst U, Schödel M, Beier HT. Parameters affecting the damage tolerance behaviour of railway axles. Eng Fract Mech 2011;78:793–809.

[16] Qian J, Fatemi A. Mixed mode fatigue crack growth: A literature survey. Eng Fract Mech 1996;55:969–90.

[17] Erdogan F, Sih GC. On the crack extension in plates under plane loading and transverse shear. J Basic Eng 1963;85:519–25.

[18] Hussain M, Pu S, Underwood J. Strain energy release rate for a crack under combined mode I and mode II. Natl. Symp. Fract. Mech., vol. 560, 100 Barr Harbor Drive, PO Box C700, West Conshohocken, PA 19428-2959: ASTM International; 1974, p. 2-2–27.

[19] Richard HA, Schramm B, Schirmeisen N-H. Cracks on mixed mode loading – Theories, experiments, simulations. Int J Fatigue 2014;62:93–103.

[20] Schöllmann M, Richard HA, Kullmer G, Fulland M. A new criterion for the prediction of crack development in multiaxially loaded structures. Int J Fract 2002;117:129–41.

[21] Richard HA, Fulland M, Sander M. Theoretical crack path prediction. Fatigue Fract Eng Mater Struct 2005;28:3–12.

[22] Ayatollahi MR, Saboori B. Maximum tangential strain energy density criterion for general mixed mode I/II/III brittle fracture. Int J Damage Mech 2014;24:263–78.

[23] Wang J, Ren L, Xie LZ, Xie HP, Ai T. Maximum mean principal stress criterion for three-dimensional brittle fracture. Int J Solids Struct 2016;102–103:142–54.

[24] Richard HA. Specimens for investigating biaxial fracture and fatigue processes. Mechcanical Eng Publ 1989:217–29.

[25] Ayatollahi MR, Aliha MRM, Saghafi H. An improved semi-circular bend specimen for investigating mixed mode brittle fracture. Eng Fract Mech 2011;78:110–23.

[26] Banks-Sills L, Arcan M, Bortman Y. A mixed mode fracture specimen for mode II dominant deformation. Eng Fract Mech 1984;20:145–57.

[27] Demir O, Ayhan AO, İriç S. A new specimen for mixed mode-I/II fracture tests: Modeling, experiments and criteria development. Eng Fract Mech 2017;178:457–76.

[28] Sajith S, Shukla SS, Murthy KSRK, Robi PS. Mixed mode fatigue crack growth studies in AISI 316 stainless steel. Eur J Mech - A/Solids 2020;80:103898.

[29] Sajith S, Murthy KSR., Robi PS. Experimental and numerical investigation of mixed mode fatigue crack models in Aluminum 6061-T6. Int J Fatigue 2020:105285.

[30] Richard HA, Schirmeisen N, Eberlein A. Experimental investigations on mixed-mode-loaded cracks. 4th Int. Conf. Crack Paths, CD-Rom, Gaeta, Italy, 2012, p. 219–33.

[31] Richard HA, Eberlein A. Material characteristics at 3D-mixed-mode-loadings. Procedia Struct Integr 2016;2:1821–8.

[32] Zeinedini A. A novel fixture for mixed mode I/II/III fracture testing of brittle materials. Fatigue Fract Eng Mater Struct 2018:1–16.

[33] Razavi SMJ, Berto F. A new fixture for fracture tests under mixed mode I/II/III loading. Fatigue Fract Eng Mater Struct 2019;42:1874–88.

[34] Tanaka K. Fatigue crack propagation from a crack inclined to the cyclic tensile axis. Eng Fract Mech 1974;6:493–507.

[35] Biner SB. Fatigue crack growth studies under mixed mode loading. Int J Fatigue 2001;23:259–63.

[36] Demir O, Ayhan AO, Iric S, Lekesiz H. Evaluation of mixed mode-I/II criteria for fatigue crack propagation using experiments and modeling. Chinese J Aeronaut 2018;31:1525–34.

[37] Yan X, Du S, Zhang Z. Mixed-mode fatigue crack growth prediction in biaxially stretched sheets. Eng Fract Mech 1992;43:471–5.

[38] Rozumek D, Macha E. A survey of failure criteria and parameters in mixed-mode fatigue crack growth. Mater Sci 2009;45:190–210.

[39] Shlyannikov V, Fedotova D. Distinctive features of crack growth rate for assumed pure mode II conditions. Int J Fatigue 2021;147:106163.

[40] Sajith S, Krishna Murthy KSR, Robi PS. Prediction of accurate mixed mode fatigue crack growth curves using the Paris' law. J Inst Eng Ser C 2019;100:165–74.

[41] Floros D, Ekberg A, Larsson F. Evaluation of crack growth direction criteria on mixed-mode fatigue crack growth experiments. Int J Fatigue 2019;129:105075.

[42] Blažić M, Maksimović S, Petrović Z, Vasović I, Turnić D. Determination of fatigue crack growth trajectory and residual life under mixed modes. Stroj Vestnik/Journal Mech Eng 2014;60:250–4.

[43] Marques JB, Tavares SMO, de Castro PMST. Analysis of mode II and mixed mode I-II in fracture and fatigue: A numerical and experimental study. vol. 98. Springer International Publishing; 2019.

[44] Tavares SMO, Reis L, de Freitas M, de Castro PMST. Mixed mode fatigue and fracture in planar geometries: Observations on Keq and crack path modelling. Fatigue Fract Eng Mater Struct 2019;42:2441–56.

[45] Tamilselvan T, Lo KW, Gong YB, Zhao MM. A model for mixed-mode fatigue. J Test Eval 2005;33:188–96.

[46] Chang KJ. On the maximum strain criterion-a new approach to the angled crack problem. Eng Fract Mech 1981;14:107–24.

[47] Mirsayar MM. Mixed mode fracture analysis using extended maximum tangential strain criterion. Mater Des 2015;86:941–7.

[48] Mirsayar MM, Razmi A, Aliha MRMM, Berto F. EMTSN criterion for evaluating mixed mode I/II crack propagation in rock materials. Eng Fract Mech 2018;190:186–97.

[49] Lazzarin P, Zambardi R. A finite-volume-energy based approach to predict the static and fatigue behavior of components with sharp V-shaped notches. Int J Fract 2001;112:275–98.

[50] Smith DJ, Ayatollahi MR, Pavier MJ. The role of T -stress in brittle fracture for linear elastic materials under mixed-mode loading. Fatigue Fract Eng Mater Struct 2001;24:137–50.

[51] Lazzarin P, Berto F, Elices M, Gómez J. Brittle failures from U- and V-notches in mode I and mixed, I + II, mode: A synthesis based on the strain energy density averaged on finite-size volumes. Fatigue Fract Eng Mater Struct 2009;32:671–84.

[52] Mróz KP, Mróz Z. On crack path evolution rules. Eng Fract Mech 2010;77:1781–807.

[53] Pook LPP. Five decades of crack path research. Eng Fract Mech 2010;77:1619–30.

[54] Maiti SK, Smith RA. Criteria for brittle fracture in biaxial tension. Eng Fract Mech 1984;19:793–804.

[55] Akbardoost J, Ayatollahi MR. Experimental analysis of mixed mode crack propagation in brittle rocks: The effect of non-singular terms. Eng Fract Mech 2014;129:77–89.

[56] Kong XM, Schlüter N, Dahl W. Effect of triaxial stress on mixed-mode fracture. Eng Fract Mech 1995;52:379–88.

[57] Hua W, Dong S, Pan X, Wang Q. Mixed mode fracture analysis of CCBD specimens based on the extended maximum tangential strain criterion. Fatigue Fract Eng Mater Struct 2017;40:2118–27.

[58] Wei MD, Dai F, Xu NW, Liu Y, Zhao T. Fracture prediction of rocks under mode I and mode II loading using the generalized maximum tangential strain criterion. Eng Fract Mech 2017;186:21–38.

[59] Sih GC. Strain-energy-density factor applied to mixed mode crack problems. Int J Fract 1974;10:305–21.

[60] Ayatollahi MR, Moghaddam MR, Berto F. A generalized strain energy density criterion for mixed mode fracture analysis in brittle and quasi-brittle materials. Theor Appl Fract Mech 2015;79:70–6.

[61] Rashidi Moghaddam M, Ayatollahi MR, Berto F, Moghaddam MR, Ayatollahi MR, Berto F. Mixed mode fracture analysis using generalized averaged strain energy density criterion for linear elastic materials. Int J Solids Struct 2017;120:137–45.

[62] Nuismer RJ. An energy release rate criterion for mixed mode fracture. Int J Fract 1975;11:245–50.

[63] Hou C, Jin X, Fan X, Xu R, Wang Z. A generalized maximum energy release rate criterion for mixed mode fracture analysis of brittle and quasi-brittle materials. Theor Appl Fract Mech 2019;100:78–85.

[64] Wang Y, Wang W, Zhang B, Li C-Q. A review on mixed mode fracture of metals. Eng Fract Mech 2020;235:107126.

[65] Smith DJ, Ayatollahi MR, Davenport JCW, Swankie TD. Mixed mode brittle and ductile fracture of a high strength rotor steel at room temperature.Int J Fract 1998;94:235-250.

[66] Chang SH, Lee CI, Jeon S. Measurement of rock fracture toughness under modes I and II and mixed-mode conditions by using disc-type specimens. Eng Geol 2002;66:79–97.

[67] Hassan HA, Lewandowski JJ. A Effects of mixed mode loading on the fracture toughness of bulk metallic glass / W composites. Mater Sci Eng A 2013;586:413–7.

[68] Mirsayar MM, Joneidi VA, Petrescu RV V, Petrescu FIT, Berto F. Extended MTSN criterion for fracture analysis of soda lime glass. Eng Fract Mech 2017;178:50–9.

[69] Xeidakis GS, Samaras IS, Zacharopoulos DA, Papakaliatakis GE. Crack growth in a mixed-mode loading on marble beams under three point bending. Int J Fract 1996;79:197–208.

[70] Miao X-TT, Zhou C-YY, Lv F, He X-HH. Three-dimensional finite element analyses of T-stress for different experimental specimens. Theor Appl Fract Mech 2017;91:116–25.

[71] Amrollahi H, Baghbanan A, Hashemolhosseini H. Measuring fracture toughness of crystalline marbles under modes I and II and mixed mode I–II loading conditions using CCNBD and HCCD specimens. Int J Rock Mech Min Sci 2011;48:1123–34.

[72] Aliha MRM, Ashtari R, Ayatollahi MR. Mode I and mode II fracture toughness testing for a coarse grain marble. Appl Mech Mater 2006;5(6):181–188.

[73] Aliha MRM, Mousavi SS, Bahmani A, Linul E, Marsavina L. Crack initiation angles and propagation paths in polyurethane foams under mixed modes I/II and I/III loading. Theor Appl Fract Mech 2019;101:152–61.

[74] Marsavina L, Berto F, Negru R, Serban DA, Linul E. An engineering approach to predict mixed mode fracture of PUR foams based on ASED and micromechanical modelling. Theor Appl Fract Mech 2017;91:148–54.

[75] Ayatollahi MR, Aliha MRM. Mixed mode fracture in soda lime glass analyzed by using the generalized MTS criterion. Int J Solids Struct 2009;46:311–21.

[76] Ayatollahi MR, Aliha MRM, Hassani MM. Mixed mode brittle fracture in PMMA—An experimental study using SCB specimens. Mater Sci Eng A 2006;417:348–56.

[77] Ayatollahi MR, Aliha MRM. Fracture toughness study for a brittle rock subjected to mixed mode I/II loading. Int J Rock Mech Min Sci 2007;44:617–24.

[78] Ayatollahi MR, Aliha MRM. Analysis of a new specimen for mixed mode fracture tests on brittle materials. Eng Fract Mech 2009;76:1563–73.

[79] Aliha MRM, Bahmani A, Akhondi S. Mixed mode fracture toughness testing of PMMA with different three-point bend type specimens. Eur J Mech - A/Solids 2016;58:148–62.

[80] Aliha MRM, Berto F, Mousavi A, Razavi SMJ. On the applicability of ASED criterion for predicting mixed mode I+II fracture toughness results of a rock material. Theor Appl Fract Mech 2017;92:198–204.

[81] Hua W, Dong S, Fan Y, Pan X, Wang Q. Investigation on the correlation of mode II fracture toughness of sandstone with tensile strength. Eng Fract Mech 2017;184:249–58.

[82] Williams ML. The bending stress distribution at the base of a stationary crack. J Appl Mech 1957;79:109–14.

[83] Cornetti P, Sapora A, Carpinteri A. T-stress effects on crack kinking in finite fracture mechanics. Eng Fract Mech 2014;132:169–76.

[84] Du ZZ, Hancock JW. The effect of non-singular stresses on crack-tip constraint. J Mech Phys Solids 1991;39:555–67.

[85] Shlyannikov VNN. T-stress for crack paths in test specimens subject to mixed mode loading. Eng Fract Mech 2013;108:3–18.

[86] Ayatollahi MR, Saboori B. T-stress effects in mixed mode I/II/III brittle fracture. Eng Fract Mech 2015;144:32–45.

[87] Sapora A, Cornetti P, Mantič V. T -stress effects on crack deflection: Straight vs. curved crack advance. Eur J Mech - A/Solids 2016;60:52–7.

[88] Ayatollahi MR, Aliha MRM. On determination of mode II fracture toughness using semi-circular bend specimen. Int J Solids Struct 2006;43:5217–27.

[89] Aliha MRM, Ayatollahi MR. Analysis of fracture initiation angle in some cracked ceramics using the generalized maximum tangential stress criterion. Int J Solids Struct 2012;49:1877–83.

[90] Hou C, Wang Z, Liang W, Li J, Wang Z. Determination of fracture parameters in center cracked circular discs of concrete under diametral loading : A numerical

analysis and experimental results. Theor Appl Fract Mech 2016;85:355–66.

[91] Williams JG, Ewing PD. Fracture under complex stress - The angled crack problem. Int J Fract 1972;8:441–6.

[92] Yukio U, Kazuo I, Tetsuya Y, Mitsuru A. Characteristics of brittle fracture under general combined modes including those under bi-axial tensile loads. Eng Fract Mech 1983;18:1131–58.

[93] Aliha MRM, Hosseinpour GR, Ayatollahi MR. Application of cracked triangular specimen subjected to three-point bending for investigating fracture behavior of rock materials. Rock Mech Rock Eng 2013;46:1023–34.

[94] Ren L, Zhu Z, Yang Q, Ai T. Investigation on the applicability of several fracture criteria to the mixed mode brittle fractures. Adv Mech Eng 2013;2013:545108.

[95] Sih GC, Cha BCK. A fracture criterion for three-dimensional crack problems. Eng Fract Mech 1974;6:699–723.

[96] Yishu Z. A strain energy criterion for mixed mode crack propagation. Eng Fract Mech 1987;26:533–9.

[97] Yishu Z. Griffith's criterion for mixed mode crack propagation. Eng Fract Mech 1987;26:683–9.

[98] Lazarus V, Buchholz FG, Fulland M, Wiebesiek J. Comparison of predictions by mode II or mode III criteria on crack front twisting in three or four point bending experiments. Int J Fract 2008;153:141–51.

[99] Lazarus V, Leblond JB, Mouchrif SE. Crack front rotation and segmentation in mixed mode I + III or I + II + III. Part II: Comparison with experiments. J Mech Phys Solids 2001;49:1421–43.

[100] Chang J, Xu JQ, Mutoh Y. A general mixed-mode brittle fracture criterion for cracked materials. Eng Fract Mech 2006;73:1249–63.

[101] Sih GC. Mechanics of fracture initiation and propagation: surface and volume energy density applied as failure criterion. vol. 11. Springer Science & Business Media; 2012.

[102] Aliha MRM, Bahmani A. Rock fracture toughness study under mixed mode I/III loading. Rock Mech Rock Eng 2017;50:1739–51.

[103] Aliha MRM, Linul E, Bahmani A, Marsavina L. Experimental and theoretical fracture toughness investigation of PUR foams under mixed mode I+III loading. Polym Test 2018;67:75–83.

[104] Seifi R, Omidvar N. Fatigue crack growth under mixed mode I+III loading. Mar Struct 2013;34:1–15.

[105] Pham KH, Ravi-Chandar K. Further examination of the criterion for crack initiation under mixed-mode I+III loading. Int J Fract 2014;189:121–38.

[106] Pham KH, Ravi-Chandar K. On the growth of cracks under mixed-mode I + III loading. Int J Fract 2016;199:105–34.

[107] Berto F, Ayatollahi MR, Campagnolo A. Fracture tests under mixed mode I + III loading: An assessment based on the local energy. Int J Damage Mech 2017;26:881–94.

[108] Chang KJ. Further studies of the maximum stress criterion on the angled crack problem. Eng Fract Mech 1981;14:125–42.

[109] Theocaris PS, Andrianopoulos NP. The T-criterion applied to ductile fracture. Int J Fract 1982;20:125–30.

[110] Tsangarakis N. The dependence of mode III fracture initiation toughness on strength and microstructure. Eng Fract Mech 1984;19:903–9.

[111] Luo P-F, Huang FC. An experimental study on the mixed-mode crack tip deformation fields in polymethyl methacrylate. J Strain Anal Eng Des 2003;38:313–28.

[112] Ayatollahi MR, Sedighiani K. Mode I fracture initiation in limestone by strain energy density criterion. Theor Appl Fract Mech 2012;57:14–8.

[113] Zhong J, Wang J, Li X, Chu X. Experiments and discrete element simulations of crack initiation angle of mixed-mode I/II in PMMA material. Theor Appl Fract Mech 2023;125:103862.

[114] Richard HA, Benitz K. A loading device for the creation of mixed mode in fracture mechanics. Int J Fract 1983;22:55–8.

[115] Arcan M, Hashin Z, Voloshin A. A method to produce uniform plane-stress states with applications to fiber-reinforced materials. Exp Mech 1978;18:141–6.

[116] Demir O, Ayhan AO. Investigation of mixed mode-I/II fracture problems - Part 2: evaluation and development of mixed mode-I/II fracture criteria. Frat Ed Integrità Strutt 2016;10:340–9.

[117] Shetty DK, Rosenfield AR, Duckworth WH. Mixed-mode fracture in biaxial stress state: Application of the diametral-compression (Brazilian disk) test. Eng Fract Mech 1987;26:825–40.

[118] Chong KP, Kuruppu MD. Fracture toughness determination of layered materials. Eng Fract Mech 1987;28:43–54.

[119] Maccagno TM, Knott JF. The fracture behaviour of PMMA in mixed modes I and II. Eng Fract Mech 1989;34:65–86.

[120] Fett T, Gerteisen G, Hahnenberger S, Martin G, Munz D. Fracture tests for ceramics under mode-I, mode-II and mixed-mode loading. J Eur Ceram Soc 1995;15:307–12.

[121] Mahanty DK, Maiti SK. Experimental and finite element studies on mode I and mixed mode (I and II) stable crack growth—I. Experimental. Eng Fract Mech 1990;37:1237–50.

[122] Maiti SK, Mahanty DK. Experimental and finite element studies on mode I and mixed mode (I and II) stable crack growth—II. finite element analysis. Eng Fract Mech 1990;37:1251–75.

[123] De Oliveira Miranda AC, Meggiolaro MA, De Castro JTP, Martha LF. Fatigue life prediction of complex 2D components under mixed-mode variable amplitude loading. Int J Fatigue 2003;25:1157–67.

[124] Miranda ACO, Meggiolaro MA, Castro JTP, Martha LF, Bittencourt TN. Fatigue life and crack path predictions in generic 2D structural components. Eng Fract Mech 2003;70:1259–79.

[125] Miranda ACO, Meggiolaro MA, Castro JTP, Martha LF. Path and life predictions under mixed mode I-Mode II complex loading. Mech Solids Brazil 2007:421–32.

[126] Greer JM, Galyon Dorman SE, Hammond MJ. Some comments on the Arcan mixed-mode (I/II) test specimen. Eng Fract Mech 2011;78:2088–94.

[127] Manoharan M, Hirth JP, Rosenfield AR. A suggested procedure for combined mode I - mode III fracture toughness testing. J Test Eval 1990;18:106–14.

[128] Chandra Rao BSS, Srinivas M, Kamat S V. The effect of mixed mode I/III loading on the fracture toughness of Timetal 834 titanium alloy. Mater Sci Eng A 2008;476:162–8.

[129] Pook LP. The fatigue crack direction and threshold behaviour of mild steel under mixed mode I and III loading. Int J Fatigue 1985;7:21–30.

[130] Aliha MRM, Bahmani A, Akhondi S. Numerical analysis of a new mixed mode I/III fracture test specimen. Eng Fract Mech 2015;134:95–110.

[131] Pirmohammad S, Bayat A. Characterizing mixed mode I / III fracture toughness of asphalt concrete using asymmetric disc bend (ADB) specimen. Constr Build Mater 2016;120:571–80.

[132] Aliha MRM, Bahmani A, Akhondi S. A novel test specimen for investigating the mixed mode I + III fracture toughness of hot mix asphalt composites – Experimental and theoretical study. Int J Solids Struct 2016;90:167–77.

[133] Richard HA, Eberlein A, Kullmer G. Concepts and experimental results for stable and unstable crack growth under 3D-mixed-mode-loadings. Eng Fract Mech 2017;174:10–20.

[134] Richard HA, Kuna M. Theoretical and experimental study of superimposed fracture modes I, II and III. Eng Fract Mech 1990;35:949–60.

[135] Khatammanesh A, Farhangdoost K, Ghahremani Moghadam D, Masoudi Nejad R. An evaluation of the loading condition on mixed-mode stress intensity factors for CTST specimens made of 2024-T351 aluminum alloy. Eng Fail Anal 2021;130:105780.

[136] Bozkurt M, Ayhan AO, Yaren MF, İriç S. Finite element modeling and experimental studies on mixed mode-I/III fracture specimens. Frat Ed Integrita Strutt 2016;10:350–9.

[137] Ayhan AO, Demir O. A novel test system for mixed mode-I/II/III fracture tests – Part 1: Modeling and numerical analyses. Eng Fract Mech 2019;218:106597.

[138] Demir O, Ayhan AO, Iric S. A novel test system for mixed mode-I/II/III fracture tests – Part 2: Experiments and criterion development. Eng Fract Mech 2019;218:106597.

[139] Wei Z, Deng X, Sutton MA, Yan J, Cheng CS, Zavattieri P. Modeling of mixed-

mode crack growth in ductile thin sheets under combined in-plane and out-of-plane loading. Eng Fract Mech 2011;78:3082–101.

[140] Ayatollahi MR, Saboori B. A new fixture for fracture tests under mixed mode I/III loading. Eur J Mech A/Solids 2015;51:67–76.

[141] Hellier AK, Corderoy DJH, McGirr MB. A practical mixed Mode II/III fatigue test rig. Int J Fatigue 1987;9:95–101.

[142] Vojtek T, Pokluda J, Šandera P, Horníková J, Hohenwarter A, Pippan R. Analysis of fatigue crack propagation under mixed mode II + III in ARMCO iron. Int J Fatigue 2015;76:47–52.

[143] Saboori B, Ayatollahi MR. A novel test configuration designed for investigating mixed mode II/III fracture. Eng Fract Mech 2018;197:248–58.

[144] Ayatollahi MR, Karami J, Saboori B. Mixed mode II/III fracture experiments on PMMA using a new test configuration. Eur J Mech A/Solids 2019;77:103812.

[145] Merati AA, Hellier AK, Zarrabi K. On the mixed Mode II/III fatigue threshold behaviour for aluminium alloys 2014-T6 and 7075-T6. Fatigue Fract Eng Mater Struct 2012;35:2–12.

[146] Iida S, Kobayashi AS. Crack-propagation rate in 7075-T6 plates under cyclic tensile and transverse shear loadings. J Basic Eng Trans ASME 1969:764–9.

[147] Roberts R, Kibler JJ. Mode II fatigue crack propagation. J Basic Eng 1971:671–80.

[148] Paris PC, Gomez MP, Anderson WE. A rational analytic theory of fatigue. Trend Eng 1961;13:9–14.

[149] Chen WR, Keer LM. Fatigue crack growth in mixed mode loading. J Eng Mater Technol 1991;113:222–7.

[150] Pandey RK, Patel AB. Mixed-mode fatigue crack growth under biaxial loading. Int J Fatigue 1984;6:119–23.

[151] Patel AB, Pandey RK. Fatigue crack growth under mixed mode loading. Fatigue Eng Mater Struct 1981;4:65–77.

[152] Hoshide T, Socie DF. Mechanics of mixed mode small fatigue crack growth. Eng Fract Mech 1987;26:841–50.

[153] Srivastava YP, Garg SBL. Study on modified J-integral range and its correlation

with fatigue crack growth. Eng Fract Mech 1988;30:119–33.

[154] Chow CL, Lu TJ. Cyclic J-integral in relation to fatigue crack initiation and propagation. Eng Fract Mech 1991;39:1–20.

[155] Fatemi A, Socie DF. A critical plane approach to multiaxial fatigue damage including out-of-phase loading. Fatigue Fract Eng Mater Struct 1988;11:149–65.

[156] Reddy SC, Fatemi A, Mitchell MR, Landgraf RW. Small crack growth in multiaxial fatigue. ASTM STP 1992;1122:276–98.

[157] Socie DF, Hua CT, Worthem DW. Mixed mode small crack growth. Fatigue Fract Eng Mater Struct 1987;10:1–16.

[158] Albuquerque C, Silva ALL, De Jesus AMP, Calçada R. An efficient methodology for fatigue damage assessment of bridge details using modal superposition of stress intensity factors. Int J Fatigue 2015;81:61–77.

[159] He W, Liu J, Xie D. Numerical study on fatigue crack growth at a web-stiffener of ship structural details by an objected-oriented approach in conjunction with ABAQUS. Mar Struct 2014;35:45–69.

[160] Seo KJ, Choi BH, Lee JM, Shin SM. Investigation of the mixed-mode fatigue crack growth of a hot-rolled steel plate with a circular microdefect. Int J Fatigue 2010;32:1190–9.

[161] Zhang XB, Ma S, Recho N, Li J. Bifurcation and propagation of a mixed-mode crack in a ductile material. Eng Fract Mech 2006;73:1925–39.

[162] Ma S, Zhang XB, Recho N, Li J. The mixed-mode investigation of the fatigue crack in CTS metallic specimen. Int J Fatigue 2006;28:1780–90.

[163] Kim J-K, Kim C-S. Fatigue crack growth behaviour of rail steel under mode I and mixed mode loadings. Mater Sci Eng A338 2002;338:191–201.

[164] Ingraffea AR, Blandford GE, Liggett JA. Automatic modelling of mixed mode fatigue and quasi-static crack propagation using the boundary element method. Fract Mech Fourteenth Symp Theory Anal ASTM STP 791, J C Lewis G Sines, Eds, Am Soc Test Mater 1983:407–26.

[165] Wawrzynek PA, Ingraffea AR. An interactive approach to local remeshing around a propagating crack. Finite Elem Anal Des 1989;5:87–96.

[166] Yan AM, Nguyen-Dang H. Multiple-cracked fatigue crack growth by BEM. Comput Mech 1995;16:273–80.

[167] Leite PGP, Gomes G. Numerical simulation of fatigue crack propagation in mixed-mode (I+II) using the program BemCracker2D. Int J Struct Integr 2019;10:497–514.

[168] Alegre JM, Cuesta II. Some aspects about the crack growth FEM simulations under mixed-mode loading. Int J Fatigue 2010;32:1090–5.

[169] Lesiuk G, Smolnicki M, Mech R, Zięty A, Fragassa C. Analysis of fatigue crack growth under mixed mode (I + II) loading conditions in rail steel using CTS specimen. Eng Fail Anal 2020;109:104354.

[170] Lesiuk G, Kucharski P, Correia JAFO, De Jesus AMP, Rebelo C, Simões Da Silva L. Mixed Mode (I+II) Fatigue crack growth of long term operating bridge steel. Procedia Eng 2016;160:262–9.

[171] Horas CS, Alencar G, De Jesus AMP, Calçada R. Development of an efficient approach for fatigue crack initiation and propagation analysis of bridge critical details using the modal superposition technique. Eng Fail Anal 2018;89:118–37.

[172] Muzvidziwa M, Okazaki M, Suzuki K, Hirano S. Role of microstructure on the fatigue crack propagation behavior of a friction stir welded Ti-6Al-4V. Mater Sci Eng A 2016;652:59–68.

[173] Wang Q, Liu X, Wang W, Yang C, Xiong X, Fang H. Mixed mode fatigue crack growth behavior of Ni-Cr-Mo-V high strength steel weldments. Int J Fatigue 2017;102:79–91.

[174] Heirani H, Farhangdoost K. Effect of compressive mode I on the mixed mode I/II fatigue crack growth rate of 42CrMo4. J Mater Eng Perform 2018;27:138–46.

[175] Cao J, Li F, Ma X, Sun Z. Study of anisotropic crack growth behavior for aluminum alloy 7050-T7451. Eng Fract Mech 2018;196:98–112.

[176] Liu JY, Bao WJ, Zhao JY, Zhou CY. Fatigue crack growth behavior of CP-Ti cruciform specimens with mixed mode I-II crack under biaxial loading. Materials 2022;15:1926.

[177] Nasri K, Zenasni M. Fatigue crack growth simulation in coated materials using X-FEM. Comptes Rendus - Mec 2017;345:271–80.

[178] Dirik H, Yalçinkaya T. Crack path and life prediction under mixed mode cyclic variable amplitude loading through XFEM. Int J Fatigue 2018;114:34–50.

[179] Liu AF, Allison JE, Dittmer DF, Yamane JR. Effect of biaxial stresses on crack growth. Fract. Mech. Proc. Elev. Natl. Symp. Fract. Mech. Part I, ASTM International 1979;677:5.

[180] Shi J, Chopp D, Lua J, Sukumar N, Belytschko T. Abaqus implementation of extended finite element method using a level set representation for three-dimensional fatigue crack growth and life predictions. Eng Fract Mech 2010;77:2840–63.

[181] Srilakshmi R, Ramji M, Chinthapenta V. Fatigue crack growth study of CFRP patch repaired Al 2014-T6 panel having an inclined center crack using FEA and DIC. Eng Fract Mech 2015;134:182–201.

[182] Li CQ, Fu G, Yang W. Stress intensity factors for inclined external surface cracks in pressurised pipes. Eng Fract Mech 2016;165:72–86.

[183] Sadeghirad A, Chopp DL, Ren X, Fang E, Lua J. A novel hybrid approach for level set characterization and tracking of non-planar 3D cracks in the extended finite element method. Eng Fract Mech 2016;160:1–14.

[184] Broszeit E, Preussler T, Wagner M, Zwirlein O. Stress Hypotheses and material stresses in Hertzian contacts. Materwiss Werksttech 1986;17:238–46.

[185] Richard HA, Buchholz FG, Kullmer G, Schöllmann M. 2D- and 3D-mixed mode fracture criteria. Key Eng Mater 2003;251–252:251–60.

[186] Sander M, Richard HA. Experimental and numerical investigations on the influence of the loading direction on the fatigue crack growth. Int J Fatigue 2006;28:583–91.

[187] Sander M, Richard HA. Finite element analysis of fatigue crack growth with interspersed mode I and mixed mode overloads. Int J Fatigue 2005;27:905–13.

[188] Seifi R, Eshraghi M. Effects of mixed-mode overloading on the mixed-mode I+II fatigue crack growth. Arch Appl Mech 2013;83:987–1000.

[189] Borrego LP, Antunes F V., Costa JM, Ferreira JM. Mixed-mode fatigue crack growth behaviour in aluminium alloy. Int J Fatigue 2006;28:618–26.

[190] Mohanty JR, Verma BB, Ray PK. Evaluation of overload-induced fatigue crack

growth retardation parameters using an exponential model. Eng Fract Mech 2008;75:3941–51.

[191] Mohanty JR, Verma BB, Ray PK. Prediction of fatigue crack growth and residual life using an exponential model: Part I (constant amplitude loading). Int J Fatigue 2009;31:418–24.

[192] Varfolomeev I, Burdack M, Moroz S, Siegele D, Kadau K. Fatigue crack growth rates and paths in two planar specimens under mixed mode loading. Int J Fatigue 2014;58:12–9.

[193] Zarrinzadeh H, Kabir MZ, Deylami A. Experimental and numerical fatigue crack growth of an aluminium pipe repaired by composite patch. Eng Struct 2017;133:24–32.

[194] Li H, Yuan H, Li X. Assessment of low cycle fatigue crack growth under mixed-mode loading conditions by using a cohesive zone model. Int J Fatigue 2015;75:39–50.

[195] Peixoto DFC, de Castro PMST. Fatigue crack growth of a railway wheel. Eng Fail Anal 2017;82:420–34.

[196] Madia M, Beretta S, Schödel M, Zerbst U, Luke M, Varfolomeev I. Stress intensity factor solutions for cracks in railway axles. Eng Fract Mech 2011;78:764–92.

[197] Farjoo M, Pal S, Daniel W, Meehan PA. Stress intensity factors around a 3D squat form crack and prediction of crack growth direction considering water entrapment and elastic foundation. Eng Fract Mech 2012;94:37–55.

[198] Ghaffari MA, Pahl E, Xiao S. Three dimensional fatigue crack initiation and propagation analysis of a gear tooth under various load conditions and fatigue life extension with boron/epoxy patches. Eng Fract Mech 2015;135:126–46.

[199] Schöllmann M, Fulland M, Richard HA. Development of a new software for adaptive crack growth simulations in 3D structures. Eng Fract Mech 2003;70:249–68.

[200] Demir O, İriç S, Ayhan AO, Lekesiz H. Investigation of mixed mode - I/II fracture problems - Part 1: Computational and experimental analyses. Frat Ed Integrita Strutt 2016;35:330–9.

[201] Miranda ACO, Martha LF, Castro JTP. Curved fatigue cracks under complex

loading. Soc Automot Eng Inc 2001:1–11.

[202] Leonel ED, Venturini WS. Multiple random crack propagation using a boundary element formulation. Eng Fract Mech 2011;78:1077–90.

[203] Ayatollahi MR, Razavi SMJ, Yahya MY. Mixed mode fatigue crack initiation and growth in a CT specimen repaired by stop hole technique. Eng Fract Mech 2015;145:115–27.

[204] Singh I V., Mishra BK, Bhattacharya S, Patil RU. The numerical simulation of fatigue crack growth using extended finite element method. Int J Fatigue 2012;36:109–19.

[205] Grbović A, Kastratović G, Sedmak A, Eldweib K, Kirin S. Determination of optimum wing spar cross section for maximum fatigue life. Int J Fatigue 2019;127:305–11.

[206] Grbović A, Kastratović G, Sedmak A, Balać I, Popović MD. Fatigue crack paths in light aircraft wing spars. Int J Fatigue 2019;123:96–104.

[207] Martins RF, Ferreira L, Reis L, Chambel P. Fatigue crack growth under cyclic torsional loading. Theor Appl Fract Mech 2016;85:56–66.

[208] Yang Y, Vormwald M. Fatigue crack growth simulation under cyclic non-proportional mixed mode loading. Int J Fatigue 2017;102:37–47.

[209] Vormwald M, Hos Y, Freire JLF, Gonzáles GLG, Díaz JG. Crack tip displacement fields measured by digital image correlation for evaluating variable mode-mixity during fatigue crack growth. Int J Fatigue 2018;115:53–66.

[210] Xie Q, Qi H, Li S, Yang X, Shi D. Experimental and numerical investigation of mixed-mode fatigue crack growth in nickel-based superalloy at high temperature. Eng Fract Mech 2022;273:108736.

[211] Kim ST, Tadjiev D, Yang HT. Fatigue life prediction under random loading conditions in 7475-T7351 aluminum alloy using the RMS model. Int J Damage Mech 2006;15:89–102.

[212] Keprate A, Ratnayake RMC. Fatigue and fracture degradation inspection of offshore structures and mechanical items: The state of the art. Proc. ASME 2015 34th Int. Conf. Ocean. Offshore Arct. Eng. OMAE2015, 2017;1–13.

[213] Zhang P, Xie L qi, Zhou C yu, He X hua. Experimental and numerical investigation on fatigue crack growth behavior of commercial pure titanium under I-II mixed mode loading at negative load ratios. Int J Fatigue 2020;138:105700.

[214] Silva ALL, de Jesus AMP, Xavier J, Correia JAFO, Fernandes AA. Combined analytical-numerical methodologies for the evaluation of mixed-mode (I + II) fatigue crack growth rates in structural steels. Eng Fract Mech 2017;185:124–38.

[215] Sajith S. Experimental and numerical investigation of equivalent stress intensity factor models for fatigue life predictions. 2020.

[216] Berto F, Lazzarin P. A review of the volume-based strain energy density approach applied to V-notches and welded structures. Theor Appl Fract Mech 2009;52:183–94.

[217] Reimers P. Simulation of mixed mode fatigue crack growth. Comput Struct 1991;40:339–46.

[218] Jogdand PV, Murthy KSRK. A finite element based interior collocation method for the computation of stress intensity factors and T-stresses. Eng Fract Mech 2010;77:1116–27.

[219] Henshell RD, Shaw KG. Crack tip finite elements are unnecessary. Int J Numer Methods Eng 1975;9:495–507.

[220] Barsoum RS. On the use of isoparametric finite elements in linear fracture mechanics. Int J Numer Methods Eng 1976;10:25–37.

[221] Shih CF, de Lorenzi HG, German MD. Crack extension modeling with singular quadratic isoparametric elements. Int J Fract 1976;12:647–51.

[222] Ingraffea AR, Manu C. Stress-intensity factor computation in three dimensions with quarter-point elements. Int J Numer Methods Eng 1980;15:1427–45.

[223] Daimon R, Okada H. Mixed-mode stress intensity factor evaluation by interaction integral method for quadratic tetrahedral finite element with correction terms. Eng Fract Mech 2014;115:22–42.

[224] Bremberg D, Faleskog J. A numerical procedure for interaction integrals developed for curved cracks of general shape in 3-D. Int J Solids Struct 2015;62:144–57.

[225] Toshio N, Parks DM. Determination of elastic T-stress along three-dimensional

crack fronts using an interaction integral. Int J Solids Struct 1992;29:1597–611.

[226] Emran Ismail A, Jamian S, Kamarudin K, Khir M, Nor M, Ibrahim N, et al. An overview of fracture mechanics with ANSYS. Int J Integr Eng Spec Issue 2018;10:59–67.

[227] Branco R, Costa JD, Borrego LP, Macek W, Berto F. Notch fatigue analysis and life assessment using an energy field intensity approach in 7050-T6 aluminium alloy under bending-torsion loading. Int J Fatigue 2022;162:106947.

[228] Lesiuk G, Kucharski P, Correia JAFO, De Jesus AMP, Rebelo C, Simões da Silva L. Mixed mode (I+II) fatigue crack growth in puddle iron. Eng Fract Mech 2017;185:175–92.

[229] Gupta M, Alderliesten RC, Benedictus R. A review of T-stress and its effects in fracture mechanics. Eng Fract Mech 2015;134:218–41.

[230] Sajith S, Murthy K, Robi P. A simple technique for estimation of mixed mode (I/II) stress intensity factors. J Mech Mater Struct 2018;13:141–54.

[231] Sajjadi SH, Ostad Ahmad Ghorabi MJ, Salimi-Majd D. A novel mixed-mode brittle fracture criterion for crack growth path prediction under static and fatigue loading. Fatigue Fract Eng Mater Struct 2015;38:1372–82.

[232] Aliha MRM, Berto F, Bahmani A, Gallo P. Mixed mode I/II fracture investigation of Perspex based on the averaged strain energy density criterion. Phys Mesomech 2017;20:149–56.

[233] Courtin S, Gardin C, Bézine G, Hamouda HBH. Advantages of the J-integral approach for calculating stress intensity factors when using the commercial finite element software ABAQUS. Eng Fract Mech 2005;72:2174–85.

[234] Berto F, Lazzarin P, Kotousov A. On the presence of the out-of-plane singular mode induced by plane loading with KII = KI = 0. Int J Fract 2011;167:119–26.

[235] Doquet V, Bui QH, Bertolino G, Merhy E, Alves L. 3D shear-mode fatigue crack growth in maraging steel and Ti-6Al-4V. Int J Fract 2010;165:61–76.

[236] Kotousov A, Lazzarin P, Berto F, Pook LP. Three-dimensional stress states at crack tip induced by shear and anti-plane loading. Eng Fract Mech 2013;108:65–74.

[237] Kotousov A, Berto F, Lazzarin P, Pegorin F. Three dimensional finite element mixed

fracture mode under anti-plane loading of a crack. Theor Appl Fract Mech 2012;62:26–33.

[238] Zhu L, Li Q, Buchholz FG. Computational fracture analysis of an AFM-specimen under mixed mode loading conditions. J Mar Sci Appl 2011;10:105–12.

[239] Buchholz FG, Chergui A, Richard HA. Fracture analyses and experimental results of crack growth under general mixed mode loading conditions. Eng Fract Mech 2004;71:455–68.

[240] Richard HA, Eberlein A. 3D-mixed-mode-loading: material characteristic values and criteria's validity. Frat Ed Integrità Strutt 2016;37:80–6.

[241] Aliha MRM, Kucheki HG, Asadi MM. On the use of different diametral compression cracked disc shape specimens for introducing mode III deformation. Fatigue Fract Eng Mater Struct 2021;44:3135–51.

[242] Kudari SK, Maiti B, Ray KK. The effect of specimen geometry on plastic zone size: A study using the J integral. J Strain Anal Eng Des 2007;42:125–36.

[243] Yishu Z. Experimental study on mixed mode crack propagation. Eng Fract Mech 1989;34:891–9.

[244] Eberlein A, Richard HA. Crack front segmentation under combined mode I- and mode III-loading. Frat Ed Integrita Strutt 2016;10:1–7.

[245] Knauss WG. An observation of crack propagation in anti-plane shear. Int J Fract Mech 1970;6:183–7.

[246] Hull D. Tilting cracks: the evolution of fracture surface topology in brittle solids. Int J Fract 1993;62:119–38.

[247] Pham KH, Ravi-Chandar K. The formation and growth of echelon cracks in brittle materials. Int J Fract 2017;206:229–44.

[248] Pons AJ, Karma A. Helical crack-front instability in mixed-mode fracture. Nature 2010;464:85–9.

[249] Cooke L, Pollard DD, Cooke ML, Pollard DD. Fracture propagation paths under mixed mode loading within rectangular blocks of polymethyl methacrylate. J o Geophys Res 1996;101:3387–400.

[250] Torabi AR, Ayatollahi MR, Torabi M, Rahimi AS. Crack growth onset in thin

aluminum sheets under mixed mode I/II loading: A new form of the Equivalent Material Concept. Thin-Walled Struct 2019;144:106337.

[251] Jones R, Tamboli D. Implications of the lead crack philosophy and the role of short cracks in combat aircraft. Eng Fail Anal 2013;29:149–66.

[252] Molent L, Barter SA. A comparison of crack growth behaviour in several full-scale airframe fatigue tests. Int J Fatigue 2007;29:1090–9.

[253] Yoder G, Cooley L, Crooker T. Procedures for precision measurement of fatigue crack growth rate using crack-opening displacement techniques. Fatigue Crack Growth Meas. Data Anal.: ASTM International 1981;85-102.

[254] Zhao T, Zhang J, Jiang Y. A study of fatigue crack growth of 7075-T651 aluminum alloy. Int J Fatigue 2008;30:1169–80.

[255] Fageehi YA, Alshoaibi AM. Numerical simulation of mixed-mode fatigue crack growth for compact tension shear specimen. Adv Mater Sci Eng 2020;2020:5426831.

[256] Cina B, Kaatz T. A systematic study of the fractography of fatigue in high strength aluminium alloys. Fatigue Eng Mater Struct 1979;2:85–95.

[257] Singh AK, Datta S, Chattopadhyay A, Riddick JC, Hall AJ. Fatigue crack initiation and propagation behavior in Al – 7075 alloy under in-phase bending-torsion loading. Int J Fatigue 2019;126:346–56.

[258] Dwibedi S, Bag S. Influence of process parameters on microstructural evolution, solidification mode, and impact strength in joining of stainless steel thin sheets. Adv Mater Process Technol 2021;00:1–16.

[259] Que Z, Huotilainen C, Seppänen T, Lydman J, Ehrnstén U. Effect of machining on near surface microstructure and the observation of martensite at the fatigue crack tip in PWR environment of 304L stainless steel. J Nucl Mater 2022;558:153399.

[260] Smudde CM, San Marchi CW, Hill MR, Gibeling JC. Effects of residual stress on orientation dependent fatigue crack growth rates in additively manufactured stainless steel. Int J Fatigue 2023;169:145266.

[261] Kumar P, Jayaraj R, Zhu Z, Narayan RL, Ramamurty U. Role of metastable austenite in the fatigue resistance of 304L stainless steel produced by laser-based powder bed fusion. Mater Sci Eng A 2022;837:142744.

[262] Biner SB. Fatigue crack growth studies under mixed-mode loading. Int J Fatigue 2001;23:259–63.

[263] Amato D, Yarullin R, Shlyannikov V, Citarella R. Numerical and experimental investigation of mixed-mode crack growth in aluminum alloys. Fatigue Fract Eng Mater Struct 2022;45:2854–72

[264] Jogi BF, Brahmankar PK, Nanda VS, Prasad RC. Some studies on fatigue crack growth rate of aluminum alloy 6061. J Mater Process Technol 2008;201:380–4.

[265] Cagle MS, Bryan KE, Dantin M, Furr WM, Giri D, Huddleston B, et al. Characterization and modeling of the fatigue behavior of 304L stainless steel using the MultiStage Fatigue (MSF) Model. Int J Fatigue 2021;151:106319.

[266] Kimura M, Yamaguchi K, Hayakawa M, Kobayashi K, Matsuoka S, Takeuchi T. Fatigue fracture mechanism maps for a type 304 stainless steel. Metall Mater Trans A Phys Metall Mater Sci 2004;35 A:1311–6.

[267] Gao M, Wei RP. Morphology of corrosion fatigue cracks produced in 3.5% NaCl solution and in hydrogen for a high purity metastable austenitic (Fe18Cr12Ni) steel. Scr Metall Mater 1992;26:1175–80.

[268] Tsay LW, Liu YC, Young MC, Lin DY. Fatique crack growth of AISI 304 stainless steel welds in air and hydrogen. Mater Sci Eng A 2004;374:204–10.

[269] Westergaard HM. Bearing pressures and cracks: Bearing pressures through a slightly waved surface or through a nearly flat part of a cylinder, and related problems of cracks. J Appl Mech 1939;6:A49–53.

[270] Ramesh K, Gupta S, Srivastava AK. Equivalence of multi-parameter stress field equations in fracture mechanics. Int J Fract 1996;79:R37–41.

[271] Sanford RJ. A critical re-examination of the westergaard method for solving opening-mode crack problems. Mech Res Commun 1979;6:289–94.

List of Publications

Publications from the Present Thesis Work

International Journals Publications

1. **S. S. Shukla**, and K. S. R. K. Murthy (2023). Mixed-mode (I/II) fatigue crack growth studies on AL 7075-T6 aluminium alloy using single edge cracked circular specimen. *International Journal of Fatigue*.176:107895.
2. **S. S. Shukla**, K. S. R. K. Murthy and S. Sajith (2023). Mixed mode (I/III) fracture studies using a new specimen setup. *International Journal of Mechanical Sciences*.243:108036.
3. **S. S. Shukla** and K. S. R. K. Murthy (2023). Mixed Mode (I/II) Fracture Studies in PMMA using Single Edge Cracked Circular Specimen. *Nano World Journal*.9:S621-S625
4. **S. S. Shukla**, S. Sajith and K. S. R. K. Murthy (2022). A new simple specimen for mixed-mode (I/II) fracture and fatigue tests: Numerical and experimental studies. *European Journal of Mechanics / A Solids*. 94:104566.
5. **S. S. Shukla,** and K. S. R. K. Murthy. Mixed-mode (I/II) fatigue crack growth studies on AISI 304 steel using single edge cracked circular specimen. *(Manuscript ready to be communicated)*

International Conferences Publications

1. **S. S. Shukla** and K. S. R. K. Murthy (2023). Investigation of the effect of Paris constants in predicted mixed mode (I/II) fatigue life using a new specimen. *14th International Conference on Mechanical Engineering (ICME-2023)*, 18-19 December, Bangladesh University of Engineering & Technology, Dhaka, Bangladesh. (*Selected for presentation*)
2. **S. S. Shukla**, P. B. Kumar and K. S. R. K. Murthy (2022). Effect of Stress Ratio on the Mixed Mode (I/II) Fatigue Crack Growth in Al 7075-T6. *8th Asian Conference on Mechanics of Functional Materials and Structures, ACMFMS-109*, 11-14 December, IIT Guwahati, Guwahati, India.
3. **S. S. Shukla** and K. S. R. K. Murthy (2022). Mixed mode (I/II) Fracture Studies in PMMA using Single Edge Cracked Circular Specimen. *International*

Conference on Innovations in Mechanical and Materials Engineering, IMME-2022, 4-6 November, MNNIT Allahabad, Prayagraj, India.

4. **S. S. Shukla**, Sandipan Baruah and K. S. R. K. Murthy (2021). Experimental and numerical analyses of mixed mode (I/II) crack growth. *12th International Conference on Structural Integrity and Failure (SIF2021)*, 5-8 December, Monash University, Melbourne, Australia.
5. **S. S. Shukla** and K. S. R. K. Murthy (2019). Numerical analysis of a semi-elliptical surface cracked plate under tension. *1st International Conference on manufacturing, material science and engineering (ICMMSE-2019)*, 16-17 August, CMR Institute of Technology, Hyderabad.

Book chapters

1. **S. S. Shukla**, P. B. Kumar and K. S. R. K. Murthy. Effect of stress ratio on the mixed mode (I/II) fatigue crack growth in Al 7075-T6. *Recent Advances in Mechanics of Functional Materials and Structures: A Springer book series Lecture Notes in Mechanical Engineering* edited by Poonam Kumari, S. K. Dwivedy. (In Press)

Other Publications

1. S. Sajith, **S. S. Shukla**, K. S. R. K. Murthy and P. S. Robi (2020). Mixed mode fatigue crack growth studies in AISI 316 stainless steel. *European Journal of Mechanics / A Solids*.80:103898.

About the Author

Mr. Shiv Sahaya Shukla was born to Mr. Onkar Nath Shukla and Mrs. Nirmala Shukla in the year 1993. He went to Jawahar Navodaya Vidyalaya Unnao, Uttar Pradesh, for his schooling and completed his Class – X and Class – XII from the Central Board of Secondary Education (CBSE) Board in the year 2008 and 2010, respectively, securing first division in both the examinations. He completed the Bachelor’s degree (B.Tech.) in Mechanical Engineering from Tezpur University, Assam, India, in 2015, securing first division. Just after completing his B.Tech., he joined the Department of Mechanical Engineering at the Indian Institute of Technology Guwahati (IIT Guwahati) as a regular research scholar in the year 2015. His areas of research are experimental and numerical fracture and fatigue crack growth studies, failure analysis, fracture mechanics, surface cracks, and 2D and 3D finite element methods.